

LES HOUCHES 2013: PHYSICS AT TEV COLLIDERS

NEW PHYSICS WORKING GROUP REPORT

**G. Brooijmans¹, R. Contino^{2,3}, B. Fuks^{3,4}, F. Moortgat³, P. Richardson⁵, S. Sekmen^{3,6} and
A. Weiler^{3,7} (convenors)**

A. Alloul⁸, A. Arbey^{3,9}, J. Baglio¹⁰, D. Barducci^{11,12}, A. J. Barr¹³, L. Basso^{4,14},
M. Battaglia^{3,15}, G. Bélanger¹⁶, A. Belyaev^{11,12}, J. Bernon¹⁷, A. Bharucha¹⁸, O. Bondu³,
F. Boudjema¹⁶, E. Boos¹⁹, M. Buchkremer²⁰, V. Bunichev¹⁹, G. Cacciapaglia²¹, G. Chalons¹⁷,
E. Conte⁸, M. J. Dolan²², A. Deandrea²¹, K. De Causmaecker^{3,23}, A. Djouadi²⁴, B. Dumont¹⁷,
J. Ellis^{3,25}, C. Englert²⁶, A. Falkowski²⁴, S. Fichet²⁷, T. Flacke²⁸, A. Gaz²⁹, M. Ghezzi^{30,31},
R. Godbole³², A. Goudelis¹⁶, M. Gouzevitch²¹, D. Greco², R. Grober¹⁰, C. Grojean³³,
D. Guadagnoli¹⁶, J. F. Gunion³⁴, B. Herrmann¹⁶, J. Kalinowski³⁵, J.H. Kim^{28,36}, S. Kraml¹⁷,
M. E. Krauss³⁷, S. Kulkarni¹⁷, S.J. Lee^{28,38}, S.H. Lim^{28,36}, D. Liu^{2,39}, F. Mahmoudi^{3,40},
Y. Maravin⁴¹, A. Massironi⁴², L. Mitzka³⁷, K. Mohan³², G. Moreau²⁴, M. M. Mühlleitner¹⁰,
D.T. Nhung¹⁰, B. O’Leary³⁷, A. Oliveira^{21,43}, L. Panizzi^{11,12}, D. Pappadopulo⁴⁴, S. Patariaia⁴⁵,
W. Porod³⁷, A. Pukhov¹⁹, F. Riva², J. Rojo³, R. Rosenfeld⁴³, J. Ruiz-Álvarez²¹, H. Rzehak¹⁴,
V. Sanz⁴⁶, D. Sengupta^{17,47}, M. Spannowsky⁵, M. Spira⁴⁸, J. Streicher¹⁰, N. Strobbe⁴⁹,
A. Thamm², M. Thomas¹¹, R. Torre^{50,51}, W. Waltenberger⁵², K. Walz¹⁰, A. Wilcock⁵,
A. Wulzer⁵⁰, F. Würthwein⁵³, C. Wymant¹⁶

Abstract

We present the activities of the “New Physics” working group for the “Physics at TeV Colliders” workshop (Les Houches, France, 3–21 June, 2013). Our report includes new computational tool developments, studies of the implications of the Higgs boson discovery on new physics, important signatures for searches for natural new physics at the LHC, new studies of flavour aspects of new physics, and assessments of the interplay between direct dark matter searches and the LHC.

Acknowledgements

We would like to heartily thank the funding bodies, the organisers (G. Bélanger, F. Boudjema, S. Gascon, P. Gras, D. Guadagnoli, J.P. Guillet, G. Hamel de Monchenault, B. Herrmann, S. Kraml, G. Moreau, E. Pilon, P. Slavich and D. Zerwas), the staff and the other participants of the Les Houches workshop for providing a stimulating and lively environment in which to work.

- ¹ Physics Department, Columbia University, New York, NY 10027, USA
- ² Institut de Théorie des Phénomènes Physiques, EPFL, 1015 Lausanne, Switzerland
- ³ Physics Department, CERN, CH-1211 Geneva 23, Switzerland
- ⁴ Institut Pluridisciplinaire Hubert Curien/Département Recherches Subatomiques, Université de Strasbourg/CNRS-IN2P3, 23 rue du Loess, F-67037 Strasbourg, France
- ⁵ Institute for Particle Physics Phenomenology, University of Durham, Durham, DH1 3LE, United Kingdom
- ⁶ Department of Physics, Florida State University, Tallahassee, Florida 32306, USA
- ⁷ Deutsches Elektronen-Synchrotron DESY, D-22607 Hamburg, Germany
- ⁸ Groupe de Recherche de Physique des Hautes Énergies (GRPHE), Université de Haute-Alsace, IUT Colmar, 34 rue du Grillenbreit BP 50568, 68008 Colmar Cedex, France
- ⁹ Centre de Recherche Astrophysique de Lyon, Observatoire de Lyon, Saint-Genis Laval Cedex, F-69561, France; CNRS, UMR 5574; Ecole Normale Supérieure de Lyon, France; Université de Lyon, Université Lyon 1, F-69622 Villeurbanne Cedex, France
- ¹⁰ Institut für Theoretische Physik, Karlsruher Institut für Technologie KIT, 76131 Karlsruhe, Germany
- ¹¹ School of Physics and Astronomy, University of Southampton, Highfield, Southampton SO17 1BJ, UK
- ¹² Particle Physics Department, Rutherford Appleton Laboratory, Chilton, Didcot, Oxon OX11 0QX, UK
- ¹³ Denys Wilkinson Building, Department of Physics, Oxford, OX1 3RH, UK
- ¹⁴ Physikalisches Institut, Albert-Ludwigs-Universität Freiburg D-79104 Freiburg, Germany
- ¹⁵ University of California at Santa Cruz, Santa Cruz Institute of Particle Physics, CA 95064, USA
- ¹⁶ LAPTh, Univ. de Savoie, CNRS, 9 Chemin de Bellevue, B.P. 110, Annecy-le-Vieux 74941, France
- ¹⁷ LPSC, Université Grenoble-Alpes, CNRS/IN2P3, 53 Avenue des Martyrs, F-38026 Grenoble, France
- ¹⁸ Physik Department T31, Technische Universität München, James-Franck-Straße 1, D-85748 Garching, Germany
- ¹⁹ Skobeltsyn Institute of Nuclear Physics, Moscow State University, Moscow 119991, Russia
- ²⁰ Centre for Cosmology, Particle Physics and Phenomenology (CP3), Université catholique de Louvain, Chemin du Cyclotron, 2, B-1348, Louvain-la-Neuve, Belgium
- ²¹ Université de Lyon, F-69622 Lyon, France; Université Lyon 1, Villeurbanne; CNRS/IN2P3, UMR5822, Institut de Physique Nucléaire de Lyon, F-69622 Villeurbanne Cedex, France
- ²² Theory Group, SLAC National Accelerator Laboratory, Menlo Park, CA 94025, USA
- ²³ Theoretische Natuurkunde, IIHE/ELEM and International Solvay Institutes, Vrije Universiteit Brussel, Pleinlaan 2, B-1050 Brussels, Belgium
- ²⁴ Laboratoire de Physique Théorique, CNRS – UMR 8627, Université de Paris-Sud 11, F-91405 Orsay Cedex, France
- ²⁵ Theoretical Particle Physics and Cosmology Group, Department of Physics, King's College London, London WC2R 2LS, UK
- ²⁶ SUPA, School of Physics and Astronomy, University of Glasgow, Glasgow G12 8QQ, UK
- ²⁷ International Institute of Physics, UFRN, Av. Odilon Gomes de Lima, 1722 - Capim Macio - 59078-400 - Natal-RN, Brazil
- ²⁸ Department of Physics, Korea Advanced Institute of Science and Technology, 335 Gwahak-ro, Yuseong-gu, Daejeon 305-701, Korea
- ²⁹ University of Colorado, Boulder, CO 80309-0390, USA
- ³⁰ Dipartimento di Fisica, Università di Torino and INFN, Torino, Italy
- ³¹ Dipartimento di Fisica, Università di Roma La Sapienza" and INFN, Sezione di Roma, Italy
- ³² Centre for High Energy Physics, Indian Institute of Science, Bangalore, India
- ³³ ICREA at IFAE, Universitat Autònoma de Barcelona, E-080193 Bellaterra, Spain
- ³⁴ Department of Physics, University of California, Davis, CA 95616, USA
- ³⁵ Instytut Fizyki Teoretycznej UW, Hoza 69, PL-00681 Warsaw, Poland
- ³⁶ Center for Theoretical Physics of the Universe, IBS, Daejeon, Korea
- ³⁷ Institut für Theoretische Physik und Astrophysik, Universität Würzburg, 97074 Würzburg, Germany
- ³⁸ School of Physics, Korea Institute for Advanced Study, Seoul 130-722, Korea
- ³⁹ State Key Laboratory of Theoretical Physics, Institute of Theoretical Physics, Chinese Academy of Sciences, Beijing, People's Republic of China
- ⁴⁰ Clermont Université, Université Blaise Pascal, CNRS/IN2P3, LPC, BP 10448, F-63000 Clermont-Ferrand, France
- ⁴¹ Physics Department, Kansas State University, Manhattan, KS 66506, USA.

- ⁴² Northeastern University, Boston, MA - USA
- ⁴³ ICTP South American Institute for Fundamental Research & Instituto de Física Teórica
UNESP - Universidade Estadual Paulista - Rua Dr. B. T. Ferraz 271, 01140-070, São Paulo, SP, Brazil
- ⁴⁴ Department of Physics, University of California, Berkeley, USA and Theoretical Physics Group, Lawrence
Berkeley National Laboratory, Berkeley, USA
- ⁴⁵ Bergische Universität Wuppertal, 42119 Wuppertal, Germany
- ⁴⁶ Department of Physics and Astronomy, University of Sussex, Brighton BN1 9QH, UK
- ⁴⁷ Department of High Energy Physics, Tata Institute of Fundamental Research, 1 Homi Bhabha Road, Mumbai
400005, India.
- ⁴⁸ Paul Scherrer Institut, CH-5232 Villigen PSI, Switzerland
- ⁴⁹ Department of Physics and Astronomy, Ghent University, Belgium
- ⁵⁰ Dipartimento di Fisica e Astronomia, Università di Padova and INFN, Padova, Italy
- ⁵¹ SISSA, Trieste, Italy
- ⁵² HEPHY Vienna, ÖAW, Nikolsdorfer Gasse 18, 1050 Wien, Austria
- ⁵³ University of California, San Diego, 9500 Gilman Drive, La Jolla, CA 92093, USA

Contents

Introduction	6
<i>G. Brooijmans, R. Contino, B. Fuks, F. Moortgat, P. Richardson, S. Sekmen, A. Weiler</i>	
Tools	8
1 Updates and Extensions of the Program HDECAY	9
<i>A. Djouadi, J. Kalinowski, M. Mühlleitner, M. Spira</i>	
2 eHDECAY - a Fortran Code for the Computation of Higgs Decays in the Effective Lagrangian Approach	13
<i>R. Contino, M. Ghezzi, C. Grojean, M. Mühlleitner, M. Spira</i>	
3 NMSSMCALC - a Fortran Package for Higher Order Higgs Boson Masses and Higgs Decay Widths in the Real and the Complex NMSSM	18
<i>J. Baglio, R. Grober, M. Mühlleitner, D.T. Nhung, H. Rzehak, M. Spira, J. Streicher, K. Walz</i>	
The Higgs Boson	24
4 The Theoretical Uncertainties in Higgs Signal Strength Fits	25
<i>S. Fichet, G. Moreau</i>	
5 Testing Custodial Symmetry and CP Properties of the 125 GeV Higgs Boson	30
<i>J. Bernon, B. Dumont, J. F. Gunion, S. Kraml</i>	
6 Probing Higgs Physics with Vector-Boson Scattering	39
<i>A. Belyaev, E. Boos, V. Bunichev, Y. Maravin, A. Pukhov, R. Rosenfeld, M. Thomas</i>	
7 Probing the Structure of Top-Higgs Interactions at the LHC	48
<i>F. Boudjema, R. Godbole, D. Guadagnoli, K. Mohan</i>	
8 A Realistic Analysis of Non-Resonant BSM Higgs Pair Production	55
<i>A. J. Barr, M. J. Dolan, C. Englert, M. M. Mühlleitner, M. Spannowsky</i>	
9 Resonant Higgs Pair Production in Vector Boson Fusion at the LHC	59
<i>A. Belyaev, O. Bondu, A. Massironi, A. Oliveira, R. Rosenfeld, V. Sanz</i>	
10 Strong Double Higgs Production at the LHC in the $4b$ and $2b2W$ Final States	68
<i>O. Bondu, A. Oliveira, R. Contino, M. Gouzevitch, A. Massironi, J. Rojo</i>	
11 Triple Gauge Couplings at LEP revisited	79
<i>A. Falkowski, S. Fichet, K. Mohan, F. Riva, V. Sanz</i>	
Natural Models	86
12 Model Independent Analyses of Vector-Like Quarks	87
<i>D. Barducci, L. Basso, A. Belyaev, M. Buchkremer, G. Cacciapaglia, A. Deandrea,</i>	

T. Flacke, J.H. Kim, S.J. Lee, S.H. Lim, F. Mahmoudi, L. Panizzi, and J. Ruiz-Álvarez

13 Cornering Compressed Supersymmetric Spectra with Monotops 105

B. Fuks, P. Richardson, A. Wilcock

14 Constraining Natural Supersymmetry from the LHC Stop and Sbottom Search Results at 8 TeV 111

J. Bernon, G. Chalons, E. Conte, B. Dumont, B. Fuks, A. Gaz, S. Kraml, S. Kulkarni, L. Mitzka, S. Pataraiia, W. Porod, S. Sekmen, D. Sengupta, N. Strobbe, W. Waltenberger, F. Würthwein, C. Wymant

15 Reviving Minimal Left-Right Supersymmetry in the Light of LHC Data 128

A. Alloul, L. Basso, B. Fuks, M. E. Krauss, W. Porod

16 Benchmark Models for Spin-1 Resonances in Composite Higgs Theories 135

R. Contino, D. Greco, C. Grojean, D. Liu, D. Pappadopulo, A. Thamm, R. Torre, A. Wulzer

Flavour 152

17 Indirect Constraints on Non-Minimal Flavour Violating Supersymmetry 153

K. De Causmaecker, B. Fuks, B. Herrmann, F. Mahmoudi, B. O'Leary, W. Porod, S. Sekmen, N. Strobbe

18 Effects of CP Violation in MSSM Scenarios 159

A. Arbey, J. Ellis, R. M. Godbole, F. Mahmoudi

Dark Matter 166

19 Dark Matter Effective Field Theory at Colliders 167

A. Arbey, M. Battaglia, G. Bélanger, A. Goudelis, F. Mahmoudi, S. Pukhov

20 The Interplay of the LHC and Direct Dark Matter Detection in Unravelling Natural Supersymmetry at the Focus Point 172

D. Barducci, S. Belyaev, A. Bharucha, W. Porod and V. Sanz

Introduction

G. Brooijmans, R. Contino, B. Fuks, F. Moortgat, P. Richardson, S. Sekmen, A. Weiler

This document is the report of the New Physics session of the 2013 Les Houches Workshop “Physics at TeV Colliders”. The discovery of a Higgs boson in the first run of the Large Hadron Collider (LHC) has led to a substantial refocusing of the searches for new physics. As a consequence, the leading search areas now lie in the investigation of deviations from the Standard Model predictions in Higgs boson production and decay, as well as in the probe of so-called “natural” models in which new physics eliminates, or at the very least attenuates, the hierarchy problem introduced by the existence of a Higgs boson at the electroweak scale. During the workshop, which brings together theorists and experimenters, a substantial number of ideas around these topics were discussed, and for a number of these in-depth studies were initiated. This report describes the results of those studies.

A first section presents progress specific to the software tools crucial in predicting Higgs boson properties in various models. The first contribution details new ingredients to HDECAY, a widely used program allowing one to calculate Higgs boson decay widths and branching ratios both in and beyond the Standard Model. The two other contributions in the “Tools” section of this document introduce packages dedicated to the computation of Higgs boson properties in an effective Lagrangian approach for the introduction of new physics effects, as well as in the specific case of the Next-to-Minimal Supersymmetric Standard Model.

The second section of this report shows various examples of how to use the existence of the Higgs boson to probe new physics. Its first contribution weighs the relative importance of experimental and theoretical uncertainties in extracting the Higgs boson couplings to Standard Model particles. The next three contributions exploit single-Higgs production: the first of these addresses a way to assess the custodial symmetry and CP properties primarily in the HWW and HZZ vertices, the second one investigates a possible measurement of the contributions of longitudinal and transverse vector boson polarizations in Higgs boson production via vector boson fusion, and the third one analyzes the $t\bar{t}H$ coupling. Next, three studies focus on Higgs-boson pair production: the first of these assumes a non-resonant scenario, whereas the second and third ones postulate a resonant production channel in the vector boson fusion mode. The last contribution in this section re-examines constraints on triple gauge couplings obtained at the LEP collider in a form that can be readily combined with direct Higgs boson results.

In the third section, multiple “natural” models of new physics are studied. Vector-like quarks are predicted in many new physics scenarios, and the first contribution in this section sets up three simplified models that encapsulate all the relevant vector-like quark phenomenology for the LHC. A second contribution studies the phenomenology of vector resonances in composite Higgs theories, converging on a simple benchmark model for searches at colliders. The other three contributions examine specific supersymmetric (SUSY) scenarios. One investigates monotop signatures for cases where sparticle masses are close to the electroweak scale, but have escaped detection because the SUSY spectrum is compressed. A second one examines how existing searches for stops and sbottoms can be used to form a coherent picture of constraints on third generation squarks, and a third one takes as an example left-right SUSY to investigate how results of searches for new charged gauge bosons should be presented to extract constraints on various models.

Section four tackles flavour and CP violation. One contribution evaluates the constraints

on non-minimal flavour violating effects from the Higgs boson discovery and several flavour and electroweak observables, and a second one uses the data from the Higgs boson discovery, direct dark matter searches and electric dipole moment (EDM) constraints in determining how CP-violating effects in the Minimal Supersymmetric Standard Model could be discovered.

Finally, the fifth section studies the interplay between direct dark matter searches and collider physics. This includes a contribution on using dark matter effective field theory in interpreting dark matter searches at colliders, and a second one on the interplay between direct dark matter detection and the LHC in the specific case of the far focus point of natural SUSY.

The meeting in Les Houches fostered a large number of discussions between theorists and experimenters, but, as mentioned above, in-depth studies could only be completed for a number of the generated ideas on the required timescale. It is clear however that even those that could not converge to a written contribution have paid off through the breadth of searches conducted by experimenters, their ways of presenting their results, and theorists' further understanding of the constraints imposed on experiments. We expect that many more future results will benefit from the discussions held at the workshop.

Tools

Contribution 1

Updates and Extensions of the Program HDECAY

A. Djouadi, J. Kalinowski, M. Mühlleitner, M. Spira

Abstract

The program HDECAY determines the decay widths and branching ratios of the Higgs bosons within the Standard Model (with 3 and 4 generations) and its minimal supersymmetric extension, including the dominant higher-order corrections. New theoretical developments are briefly discussed and the new ingredients incorporated in the program are summarized.

1 INTRODUCTION

The search strategies for Higgs bosons searches at LEP, Tevatron, LHC and future e^+e^- linear colliders (LC) exploit various Higgs boson decay channels. The strategies depend not only on the experimental setup (hadron versus lepton colliders) but also on the theoretical scenarios: the Standard Model (SM) or some of its extensions such as the Minimal Supersymmetric Standard Model (MSSM) or variants as e.g. including a 4th generation. It is of vital importance to have reliable predictions for the branching ratios of the Higgs boson decays for these theoretical models.

The current version of the program HDECAY [1, 2] can be used to calculate Higgs boson partial decay widths and branching ratios within the SM with 3 and 4 generations, the MSSM and fermiophobic Higgs models and includes:

- All decay channels that are kinematically allowed and which have branching ratios larger than 10^{-4} , i.e. the loop mediated, the three body decay modes and in the MSSM the cascade and the supersymmetric decay channels [3, 4, 5].
- All relevant higher-order QCD corrections to the decays into quark pairs and to the loop mediated decays into gluons are incorporated [6].
- Double off-shell decays of the CP-even Higgs bosons into massive gauge bosons which then decay into four massless fermions, and all important below-threshold three- and four-body decays [7].
- In the MSSM, the complete radiative corrections in the effective potential approach with full mixing in the stop/sbottom sectors; it uses the renormalization group improved values of the Higgs masses and couplings and the relevant next-to-leading-order corrections are implemented [8, 9, 10, 11].
- In the MSSM, all the decays into supersymmetric (SUSY) particles (neutralinos, charginos, sleptons and squarks including mixing in the stop, sbottom and stau sectors) when they are kinematically allowed [12, 13, 14]. The SUSY particles are also included in the loop mediated

$\gamma\gamma$ and gg decay channels.

The program, written in FORTRAN, provides a very flexible and convenient use, fitting to all options of phenomenological relevance. The basic input parameters, fermion and gauge boson masses and their total widths, coupling constants and, in the MSSM, soft SUSY-breaking parameters can be chosen from an input file. In this file several flags allow switching on/off or changing some options [*e.g.* choosing a particular Higgs boson, including/excluding the multi-body or SUSY decays, or including/excluding specific higher-order QCD corrections].

2 UPDATES

Since the release of the original version of the program a number of improvements and new theoretical calculations have been implemented. The following points summarize the most important modifications of HDECAY after its release and beyond the updates summarized in Ref. [15]:

- Inclusion of the full mass effects to $H \rightarrow gg, \gamma\gamma$ at next-to-leading order in QCD within the Standard Model [16].
- Inclusion of the leading electroweak corrections to all effective down-type fermion Yukawa couplings, i.e. for the μ, τ, s, b according to [17, 18, 19, 20, 21]. In this context the sneutrino masses of the first two generations are allowed to be different from the third generation.
- Inclusion of the two-loop QCD corrections to the top decays [22, 23, 24, 25, 26, 27, 28].
- Inclusion of the full CKM mixing effects in charged Higgs and top decays. This required the appropriate extension of the `hdecay.in` input file.
- Inclusion of running mass effects and $\Delta_{b/s}$ corrections to the Yukawa couplings in charged Higgs decays into b and s quarks, where $\Delta_{b/s}$ denotes the leading SUSY-QCD and SUSY-electroweak corrections to the effective bottom/strange Yukawa couplings.
- Addition of the charged Higgs decays $H^+ \rightarrow t\bar{d}/t\bar{s}/c\bar{d}$.
- Inclusion of charm loop contributions in the gluonic Higgs decays, $\phi \rightarrow gg$, for the SM and MSSM.
- Inclusion of bottom mass effects and double off-shell decays in $H \rightarrow hh/AA/AZ/H^+W^-/t\bar{t}$, $A \rightarrow hZ$ and $H^+ \rightarrow t\bar{b}$.
- Extension of HDECAY to the general Two Higgs Doublet model (2HDM) [29]. This required the extension of the `hdecay.in` input file and the inclusion of several new decay modes that are not possible within the MSSM. The input file allows to work with two different set-ups for the 2HDM.
- Inclusion of rescaled Higgs couplings to SM particles according to the effective interaction Lagrangian

$$\begin{aligned} \mathcal{L}_{int} = & - \sum_{\psi} c_{\psi} m_{\psi} \bar{\psi} \psi \frac{H}{v} + 2c_W m_W^2 W^{+\mu} W_{\mu}^{-} \frac{H}{v} + c_Z m_Z^2 Z^{\mu} Z_{\mu} \frac{H}{v} \\ & + \left\{ \frac{\alpha_s}{8\pi} c_{gg} G^{a\mu\nu} G_{\mu\nu}^a + \frac{\alpha}{8\pi} c_{\gamma\gamma} F^{\mu\nu} F_{\mu\nu} + \frac{\sqrt{\alpha\alpha_2}}{4\pi} c_{Z\gamma} F^{\mu\nu} Z_{\mu\nu} \right\} \frac{H}{v} \end{aligned} \quad (1)$$

where $G^{a\mu\nu}$, $F^{\mu\nu}$ and $Z^{\mu\nu}$ are the field strength tensors of the gluon, photon and Z -boson fields. The couplings α , α_2 and α_s are the electromagnetic (in the Thompson limit), isospin ($g^2 = 4\pi\alpha_2$) and strong couplings, respectively, v is the Higgs vacuum expectation value and H the Higgs boson field. Note that we added novel point-like couplings of the Higgs boson to gluons, photons and Z bosons affecting the Higgs decays $H \rightarrow gg/\gamma\gamma/Z\gamma$. Electroweak corrections are only kept in the SM part of the individual decay amplitudes, i.e. the parts for $c_\psi = c_W = c_Z = 1$ and $c_{gg} = c_{\gamma\gamma} = c_{Z\gamma} = 0$, while QCD corrections have been included in all parts of the decays widths, since the dominant parts factorize. This approach deviates from the general addition of dimension-six operators as pursued in Ref. [30] where additional tensor structures have been added at the dimension-six level.

The above rescaling of the Higgs couplings modifies e.g. the Higgs decay widths into quarks as

$$\Gamma(H \rightarrow q\bar{q}) = \frac{3G_F M_H}{4\sqrt{2}\pi} \bar{m}_q^2(M_H) c_b \{c_b + \delta_{elw}\} \left\{ 1 + \delta_{QCD} + \frac{c_t}{c_b} \delta_t \right\} \quad (2)$$

where δ_{elw} denotes the electroweak corrections, δ_{QCD} the pure QCD corrections and δ_t the top-quark induced QCD corrections with the latter involving the top Yukawa coupling instead of the bottom one. The coefficient is expressed in terms of the Fermi constant G_F , the Higgs mass M_H and the running $\overline{\text{MS}}$ bottom mass \bar{m}_q at the scale of the Higgs mass.

The gluonic Higgs decay, taken as an example of a case with a novel tensor structure involving the point-like coupling factor c_{gg} , is given by

$$\begin{aligned} \Gamma(H \rightarrow gg) = & \frac{G_F \alpha_s^2 M_H^3}{36\sqrt{2}\pi^3} \left[\left| \sum_{Q=t,b,c} c_Q A_Q(\tau_Q) \right|^2 c_{eff}^2 \kappa_{soft} \right. \\ & + \delta_{elw} \left(\sum_{Q,Q'=t,b,c} c_Q A_Q(\tau_Q) A_Q^*(\tau_{Q'}) \right) c_{eff}^2 \kappa_{soft} \\ & + 2 \operatorname{Re} \left(\sum_{Q=t,b,c} c_Q A_Q^*(\tau_Q) \frac{3}{2} c_{gg} \right) c_{eff} \kappa_{soft} + \left| \frac{3}{2} c_{gg} \right|^2 \kappa_{soft} \\ & \left. + \sum_{Q,Q'=t,b} c_Q A_Q^*(\tau_Q) c_{Q'} A_{Q'}(\tau_{Q'}) \kappa^{NLO}(\tau_Q, \tau_{Q'}) \right], \quad (3) \end{aligned}$$

where $\tau_Q = 4m_Q^2/M_H^2$ and δ_{elw} denotes the electroweak corrections [31, 32, 33, 34, 35]. The loop function $A_Q(\tau_Q)$ is normalized to unity for large quark masses and can be found in Ref. [16]. The contributions c_{eff} and κ_{soft} denote the QCD corrections originating from the effective Lagrangian in the heavy top quark limit,

$$\mathcal{L}_{eff} = c_{eff} \frac{\alpha_s}{12\pi} G^{a\mu\nu} G_{\mu\nu}^a \frac{H}{v} \quad (4)$$

and the residual corrections due to diagrams involving gluon exchange and light-quark contributions, respectively. They are included up to the next-to-next-to-next-to-leading order (NNNLO) [36, 37, 38, 39, 40, 41, 42, 43]. At the next-to-leading order (NLO), they are given by [36, 37],

$$c_{eff} = 1 + \frac{11}{4} \frac{\alpha_s}{\pi}, \quad \kappa_{soft} = 1 + \left(\frac{73}{4} - \frac{7}{6} N_F \right) \frac{\alpha_s}{\pi} \quad (5)$$

with $N_F = 5$ light quark flavours. Finally κ^{NLO} represents the finite top and bottom mass effects at NLO beyond the limit of heavy quarks, i.e. beyond the terms contained in c_{eff} and κ_{soft} [16].

All other Higgs decay modes are treated analogously in the case of rescaled Higgs couplings.

The logbook of all modifications and the most recent version of the program can be found on the web page <http://people.web.psi.ch/spira/proglist.html>.

Contribution 2

eHDECAY - a Fortran Code for the Computation of Higgs Decays in the Effective Lagrangian Approach

R. Contino, M. Ghezzi, C. Grojean, M. Mühlleitner, M. Spira

Abstract

We present the Fortran code eHDECAY. It is based on a modification of the program HDECAY [1, 2], in which the full list of leading bosonic operators of the Higgs effective Lagrangian has been implemented. This has been done for a linear and a non-linear realization of the electroweak symmetry and for two benchmark composite Higgs models. In the decay widths all the relevant QCD corrections have been included. The electroweak corrections on the other hand can only be implemented in a consistent way for the linear realization in the vicinity of the Standard Model (SM).

1 INTRODUCTION

After the discovery of a new boson by the ATLAS [44] and CMS [45] collaborations, any hint of the existence of new additional particles is still lacking. The approach of the Higgs sector in terms of an effective Lagrangian allows us to parametrize our ignorance of New Physics (NP) beyond the SM (BSM), and thereby to describe the properties of the new boson and to investigate its nature. In Ref. [30] we have reviewed in detail the low-energy effective Lagrangian for a light Higgs-like boson. In order to investigate the effective Lagrangian beyond tree-level a multiple expansion has been performed in the SM coupling parameter α/π and in powers of E/M , with E being the energy of the process and M the NP scale, where new massive states appear. If the Higgs-like boson is part of a weak doublet there is an additional expansion parameter $v/f \ll 1$ with $f \equiv M/g_*$ and g_* the typical NP coupling. The weak scale is defined in terms of the Fermi constant G_F by $v \equiv 1/(\sqrt{2}G_F)^{1/2} \approx 246$ GeV. In Ref. [46] the relation between the non-linear and the linear effective Lagrangian approach has been discussed. Furthermore, the implementation in the Fortran code eHDECAY has been presented in detail. In this contribution, using the example of the Higgs boson decay into two gluons, the importance of the higher order QCD corrections and of the mass effects in the corrections shall be discussed. The program can be downloaded from the url: <http://www.itp.kit.edu/~maggie/eHDECAY/>.

2 HIGHER ORDER CORRECTIONS AND MASS EFFECTS

As the leading part of the QCD corrections in general factorizes with respect to the expansion in the number of fields and derivatives of the effective Lagrangian, they can be included by taking over the results from the SM. The electroweak (EW) corrections, on the contrary, require dedicated computations that are not available at present. They can only be implemented in the framework of the Strongly Interacting Light Higgs Lagrangian (SILH) [47], in which the coupling deviations from the SM are small, and up to orders v/f . In the following the higher order

QCD corrections and the mass effects shall be discussed for the non-linear implementation. We denote by c_ψ the modification of the Higgs couplings to fermions in terms of the SM coupling and by c_{gg} the effective Higgs coupling to gluons. Hence, with h denoting the scalar field, the related effective Lagrangian reads

$$\mathcal{L}_{\psi,G} = - \sum_{\psi=u,d,l} c_\psi \bar{\psi} \psi \frac{h}{v} + \frac{c_{gg}}{2} G_{\mu\nu}^a G^{a\mu\nu} \frac{h}{v}. \quad (1)$$

Here $G_{\mu\nu}^a$ denotes the field strength tensor for gluons,

$$G_{\mu\nu}^a = \partial_\mu G_\nu^a - \partial_\nu G_\mu^a + g_S f^{abc} G_\mu^b G_\nu^c, \quad a, b, c = 1, \dots, 8, \quad (2)$$

with the strong coupling constant g_S and the gluon field G_μ . The decay rate into gluons implemented in eHDECAY in the framework of the non-linear Lagrangian is then given by

$$\begin{aligned} \Gamma(gg)|_{NL} = & \frac{G_F \alpha_s^2 m_h^3}{4\sqrt{2}\pi^3} \left[\left| \sum_{q=t,b,c} \frac{c_q}{3} A_{1/2}(\tau_q) \right|^2 c_{eff}^2 \kappa_{soft} \right. \\ & + 2 \operatorname{Re} \left(\sum_{q=t,b,c} \frac{c_q}{3} A_{1/2}^*(\tau_q) \frac{2\pi c_{gg}}{\alpha_s} \right) c_{eff} \kappa_{soft} + \left| \frac{2\pi c_{gg}}{\alpha_s} \right|^2 \kappa_{soft} \\ & \left. + \frac{1}{9} \sum_{q,q'=t,b} c_q A_{1/2}^*(\tau_q) c_{q'} A_{1/2}(\tau_{q'}) \kappa^{NLO}(\tau_q, \tau_{q'}) \right], \quad (3) \end{aligned}$$

where $\tau_q = 4m_q^2/m_h^2$ and the loop function

$$A_{1/2}(\tau) = \frac{3}{2}\tau[1 + (1 - \tau)f(\tau)], \quad (4)$$

which is normalized to 1 in the limit of large quark masses. In the decay width we use the pole masses for the top, bottom and charm quarks, $m_t = 172.5 \text{ GeV}$, $m_b = 4.75 \text{ GeV}$ and $m_c = 1.42 \text{ GeV}$, and α_s is computed up to the next-to-next-to-next-to-leading order (N³LO) at the scale m_h for $N_F = 5$ active flavours, $\alpha_s = 0.114$. The function $f(\tau)$ is given by

$$f(\tau) = \begin{cases} \arcsin^2 \frac{1}{\sqrt{\tau}} & \tau \geq 1 \\ -\frac{1}{4} \left[\ln \frac{1 + \sqrt{1 - \tau}}{1 - \sqrt{1 - \tau}} - i\pi \right]^2 & \tau < 1. \end{cases} \quad (5)$$

The QCD corrections have been taken into account up to N³LO QCD in the limit of heavy loop-particle masses. The effect from soft gluon radiation, given by the coefficient κ_{soft} , factorizes in this limit. The corrections from hard gluon and hard quark exchange with virtuality $q^2 \gg m_t^2$ are encoded in the coefficient c_{eff} . Namely, for $m_h \ll 2m_t$ the top quark can be integrated out, leading to the effective five-flavour Lagrangian

$$\mathcal{L}_{eff} = -2^{1/4} G_F^{1/2} C_1 G_{a\mu\nu}^0 G_a^{0\mu\nu} h. \quad (6)$$

The superscript 0 denotes the bare fields. The dependence on the top quark mass m_t is included in the coefficient function C_1 . We then have for κ_{soft} and c_{eff} ,

$$\kappa_{soft} = \frac{\pi}{2m_h^4} \operatorname{Im} \Pi^{GG}(q^2 = m_h^2) \quad (7)$$

$$c_{eff} = -\frac{12\pi C_1}{\alpha_s^{(5)}(m_h)}, \quad (8)$$

with the vacuum polarization $\Pi^{GG}(q^2)$ induced by the gluon operator. The N³LO expressions for C_1 [39, 40, 41, 42] in the on-shell scheme and for $\text{Im } \Pi^{GG}$ have been given in Ref. [43]. The next-to-leading order (NLO) expressions for κ_{soft} and c_{eff} read [36, 37, 38]

$$\kappa_{soft}^{NLO} = 1 + \frac{\alpha_s}{\pi} \left(\frac{73}{4} - \frac{7}{6} N_F \right), \quad c_{eff}^{NLO} = 1 + \frac{\alpha_s}{\pi} \frac{11}{4}, \quad (9)$$

in agreement with the low-energy theorem [48, 49, 50]. Here α_s is evaluated at the scale m_h and computed for $N_F = 5$ active flavours. In eHDECAY it is consistently computed up to N³LO. The additional mass effects at NLO [16] in the top and bottom loops are taken into account by the function $\kappa^{NLO}(\tau_q, \tau_{q'})$, in the last line of Eq. (3). This function quantifies the difference between the NLO QCD corrections for the top (bottom) contribution taking into account finite mass effects in the loop, and the result for the top (bottom) contribution in the limit of a large loop particle mass. These mass effects shall be discussed in the following.

In order to investigate the mass effects in the NLO QCD corrections we choose a scenario for $m_h = 125$ GeV with SM bottom- and charm-couplings, *i.e.* $c_b = c_c = 1$ and a modified top quark coupling $c_t = 0.85$. Note, that at the LHC with 300 fb^{-1} the top quark coupling can be determined with a precision of about 15% [51, 52, 53]. Furthermore, we set the effective Higgs-gluon-gluon coupling to zero, $c_{gg} = 0$. In Table 1 we show at leading order (LO) and at N³LO the total Higgs decay width into gluons, as well as the individual contributions from the top- and bottom-loops, and the top-bottom interference. Note, that the total gluonic decay width includes the charm loop contribution as well. The N³LO QCD corrections are computed

	Γ_{tt} [GeV]	Γ_{bb} [GeV]	Γ_{tb} [GeV]	Γ_{tot}^{gg} [GeV]
LO	1.433×10^{-4}	2.174×10^{-6}	-2.028×10^{-5}	1.217×10^{-4}
N ³ LO w/o	2.674×10^{-4}	4.056×10^{-6}	-3.785×10^{-5}	2.271×10^{-4}
N ³ LO w/	2.682×10^{-4}	3.768×10^{-6}	-3.509×10^{-5}	2.304×10^{-4}
K , w/o	1.87	1.87	1.87	1.87
K , w/	1.87	1.73	1.73	1.89

Table 1: The total partial decay width for the Higgs decay into gluons Γ_{tot}^{gg} and the individual contributions from the top and bottom loops with the corresponding interferences. The scenario is given by $c_t = 0.85$, $c_b = c_c = 1$ and $c_{gg} = 0$. At LO (1st line), at N³LO without inclusion of the mass effects in the top and bottom loops at NLO QCD (2nd line) and with the inclusion of the mass effects (3rd line). The 4th and 5th line are the K -factors without and with inclusion of the NLO top and bottom mass effects.

in the limit of large loop particle masses (2nd line in the Table) and taking into account finite quark mass effects at NLO in the top and bottom loops (3rd line). This means, that in the first case we set $\kappa^{NLO} = 0$ in Eq. (3). As expected, the higher order corrections are large, with the N³LO QCD corrections increasing the total width by almost up to 90%. The results in Table 1 furthermore show, that the mass effects at NLO QCD are relevant for the bottom loop where they amount to 8%, while they are negligible for the top loop.

The K -factor is defined as the ratio between the decay width at N³LO and at LO. It is shown for the individual contributions and the total gluonic decay width, without the NLO bottom and top mass effects (4th line) and including them through the function κ^{NLO} (5th line). Taking into account finite masses in the NLO QCD loops has an 8% effect on the K -factor for the bottom loop contribution, while for the K -factor of the total width it is only 1%.

Setting also $c_t = 1$, hence taking the SM-limit, the LO width and the N³LO QCD width, including mass effects at NLO, amount to

$$\begin{aligned}\Gamma^{\text{LO}}(h^{SM} \rightarrow gg) &= 1.724 \times 10^{-4} \text{ GeV} \\ \Gamma^{\text{N}^3\text{LO QCD}}(h^{SM} \rightarrow gg) &= 3.259 \times 10^{-4} \text{ GeV} .\end{aligned}\quad (10)$$

The 15% decrease in the top-Yukawa couplings hence decreases the total SM width (without EW corrections) by 30%. Note, that at a future e^+e^- collider the Higgs decay rate into gluons will be accessible with a precision of a few percent through a measurement of the branching ratio [54, 55]. To be consistent with the non-linear approach, in Eq. (10) no electroweak corrections have been included. Including electroweak corrections, the SM width is changed by $\sim 5\%$,

$$\Gamma_{\text{EW}}^{\text{N}^3\text{LO QCD}}(h^{SM} \rightarrow gg) = 3.424 \times 10^{-4} \text{ GeV} .\quad (11)$$

We now investigate a scenario with a non-vanishing effective Higgs coupling to gluons, $c_{gg} = 0.001$, and SM-like Yukawa couplings, $c_t = c_b = c_c = 1$. In a composite Higgs scenario with fully composite right-handed top quark, for example, we expect c_{gg} to be of the order of $\alpha_s/(4\pi) m_t^2/m_*^2$, where m_* denotes the mass of the top partners [30]. This leads to a c_{gg} of order 0.001 for a top partner mass in the TeV range. A value of $c_{gg} = 0.001$ furthermore corresponds to the contribution of a top squark with a mass value of about the top quark mass in a *natural* supersymmetric scenario¹. The total partial decay width for $m_h = 125$ GeV into a gluon pair is given in Table 2 and, separately, the quark loop and the effective Higgs- gg contributions with their interference term. The quark loop contribution stems from the sum of the top-, bottom- and charm-quark contributions. Shown are the contributions at LO and at N³LO without and with NLO bottom and top quark loop mass effects. As can be inferred from Table 2 and Eq. (10) a non-vanishing $c_{gg} = 0.001$ increases the total N³LO SM width by 33%. The K -factor for the individual contribution from the effective Higgs- gg coupling is 1.53 and roughly 20% smaller than the one for the quark loops. This can be traced back to the factor $c_{\text{eff}}^2 = 1.22$ in the N³LO corrections to the quark loop contributions, cf. Eq. (3). In fact, the K -factors without mass effects for the quark loops in Tables 1 and 2 are given by $c_{\text{eff}}^2 \kappa_{\text{soft}} = 1.87$, and the K -factor for the effective Higgs- gg - contribution is given by $\kappa_{\text{soft}} = 1.53$. The K -factor 1.81 for the total width Γ_{tot}^{gg} is due to the relative weight of the long distance and short distance contributions. The inclusion of finite mass effects in the NLO QCD corrections, finally, again has a negligible effect on the total N³LO K -factor, being $\mathcal{O}(1\%)$.

In summary, the inclusion of finite top and bottom quark masses in the N³LO QCD corrections, has an effect of 8% on the individual bottom quark contribution, while the over-all K -factor is changed by 1% only in scenarios close to the SM. A non-vanishing effective Higgs-gluon-gluon coupling can significantly change the total width, also for small coupling values. This is to be expected, as the decay at leading order is already loop-mediated.

¹Applying the Higgs low-energy theorem, for the light stop contribution in the decoupling limit we have $c_{gg} = \frac{\alpha_s}{24\pi} (m_{\tilde{t}_1}^2/m_{\tilde{t}_1}^2 + m_{\tilde{t}_2}^2/m_{\tilde{t}_2}^2 - \sin^2(2\theta_{\tilde{t}})\delta m^4/(4m_{\tilde{t}_1}^2 m_{\tilde{t}_2}^2))$ [56, 57], with $m_{\tilde{t}_{1,2}}$ denoting the masses of the two stops, $\theta_{\tilde{t}}$ the stop mixing angle and δm^2 the squared mass difference of the two stops.

	Γ_{qq} [GeV]	Γ_{gg} [GeV]	Γ_{qq-gg} [GeV]	Γ_{tot}^{gg} [GeV]
LO	1.72×10^{-4}	5.13×10^{-6}	5.91×10^{-5}	2.37×10^{-4}
N ³ LO w/o	3.22×10^{-4}	7.84×10^{-6}	9.99×10^{-5}	4.29×10^{-4}
N ³ LO w/	3.26×10^{-4}	7.84×10^{-6}	9.99×10^{-5}	4.33×10^{-4}
<i>K</i> -factor w/o	1.87	1.53	1.69	1.81
<i>K</i> -factor w/	1.89	1.53	1.69	1.83

Table 2: The total partial decay width Γ_{tot}^{gg} for the Higgs decay into gluons and the individual contributions from the sum over the quark loops, the effective Higgs-*gg* coupling and the interference of these two contributions. The scenario is given by $c_t = c_c = c_b = 1$ and $c_{gg} = 0.001$. At LO (1st line), at N³LO without inclusion of the mass effects in the top and bottom loops at NLO QCD (2nd line) and with the inclusion of the mass effects (3rd line). The 4th and 5th line are the *K*-factors without and with inclusion of the NLO top and bottom mass effects.

CONCLUSIONS

We have presented the program eHDECAY which is based on an extension of the Fortran code HDECAY to include the full list of leading bosonic operators of the Higgs effective Lagrangian. The higher-order QCD corrections have been consistently included both in the linear and the non-linear approach. Electroweak corrections have been implemented only for the linear realization of the electroweak symmetry, in the vicinity of the SM, as their inclusion in the general case would require dedicated calculations not available at present. Taking the example of the Higgs decay into gluons we have discussed mass effects in the NLO QCD corrections as well as the inclusion of an effective Higgs coupling to gluons.

ACKNOWLEDGEMENTS

RC, MM and MS would like to thank the organisers of Les Houches for the very nice atmosphere of the workshop.

Contribution 3

NMSSMCALC - a Fortran Package for Higher Order Higgs Boson Masses and Higgs Decay Widths in the Real and the Complex NMSSM

J. Baglio, R. Grober, M. Muhlleitner, D.T. Nhung, H. Rzehak, M. Spira, J. Streicher, K. Walz

Abstract

We present the Fortran package NMSSMCALC. It provides the loop-corrected Higgs boson masses and calculates their decay widths including the dominant higher order corrections as well as off-shell effects in the CP-conserving and the CP-violating Next-to-Minimal Supersymmetric Extension of the Standard Model (NMSSM). Special emphasis is put on the inclusion of the supersymmetric-QCD and supersymmetric-electroweak corrections to the decay widths into quark and lepton pair final states, which have been evaluated for the first time for the NMSSM during the development of this tool.

1 INTRODUCTION

The discovery of the Higgs boson by the LHC experiments ATLAS [44] and CMS [45] in 2012 has been followed by an intense research program in order to determine its properties and to pin down its true nature. While the boson looks very Standard Model (SM)-like, there is still room for interpretations within models beyond the SM (BSM), in particular supersymmetric (SUSY) extensions have been intensely studied. In order to catch up with the increasing amount of data and precision of the experimental measurements, the theory predictions have to become more refined, necessarily including higher order corrections. This is also essential for the proper distinction between different models. The program package NMSSMCALC [58, 59] complies with these requirements by providing the loop-corrected masses for the neutral Higgs sector of the NMSSM [60, 61, 62, 63, 64, 65, 66, 67, 68, 69, 70, 71, 72, 73, 74, 75]. It furthermore computes the decay widths of the neutral and charged NMSSM Higgs bosons including the dominant higher order corrections as well as possibly important off-shell decays. It is the first package which includes at this level of precision not only the CP-conserving but also the CP-violating case. The program package can be downloaded from the url: <http://www.itp.kit.edu/~maggie/NMSSMCALC/>.

2 PROGRAM DESCRIPTION

The Model: In the NMSSM an additional singlet superfield \hat{S} is introduced compared to the minimal supersymmetric extension of the SM (MSSM). The μ parameter is generated dynamically when the scalar component of \hat{S} , which couples to the two Higgs doublets \hat{H}_u and \hat{H}_d via $\lambda\hat{S}\hat{H}_u\hat{H}_d$, acquires a vacuum expectation value (VEV) v_s . A massless axion is prevented by breaking the Peccei-Quinn symmetry [76, 77] explicitly through the introduction of a cubic

coupling for \hat{S} , $\kappa\hat{S}^3/3$, in the scale-invariant superpotential. The MSSM μ -term as well as the tadpole and bilinear terms of the singlet superfield are assumed to be zero in the superpotential. Mixing between the sfermion generations is neglected and the soft SUSY breaking terms linear and quadratic in the singlet field are set to zero. We denote by $\tan\beta$ the ratio of the absolute values of the two vacuum expectation values, v_u and v_d , of the scalar components of the two Higgs doublets \hat{H}_u and \hat{H}_d , which can be complex in the CP-violating NMSSM. At tree-level the Higgs sector of the NMSSM can be described by $\tan\beta$, by the two NMSSM specific couplings λ and κ , by the soft SUSY breaking trilinear couplings A_λ ¹ and A_κ and by the vacuum expectation value v_s of the singlet field. In case of CP-violation the parameters λ and κ and, as mentioned above, the VEVs can be complex, while they are real in the CP-conserving case. All soft-SUSY breaking mass parameters of the scalar fields are real, however, the soft SUSY breaking gaugino mass parameters and trilinear couplings can be complex, if CP-violation is assumed. The phases of the Yukawa couplings, which are complex in general, are reabsorbed by a redefinition of the quark fields. After electroweak (EW) symmetry breaking three degrees of freedom of the Higgs doublet fields are absorbed to give masses to the massive gauge bosons, so that we are left with seven Higgs bosons. In the CP-conserving case, there are three CP-even Higgs bosons H_i ($i = 1, 2, 3$) and two CP-odd Higgs bosons A_j ($j = 1, 2$) as well as two charged Higgs states H^\pm . They are ordered by ascending mass with $M_{H_1} \leq M_{H_2} \leq M_{H_3}$ and $M_{A_1} \leq M_{A_2}$. In the CP-violating NMSSM there are no mass eigenstates with definite CP quantum numbers. The five neutral mass eigenstates are denoted by H_i ($i = 1, \dots, 5$) and ordered by ascending mass.

The input and output files of the program package feature the SUSY Les Houches Accord (SLHA) [78, 79]. The input file is named `inp.dat` and must contain the specification of the model (CP-conserving or violating) and the SLHA SM input parameters, which have been extended by the W boson pole mass which is used in the mass and decay width calculations. The values for $\tan\beta$, for the NMSSM specific parameters and for the soft SUSY breaking masses and trilinear couplings have to be provided in the SLHA block `EXTPAR`. In the CP-violating case the input has to be supplemented by the block `IMEXTPAR` with the imaginary parts of the corresponding real parameters, and by a newly introduced block with the phase φ_u . The phases φ_u and φ_s describe the phase differences between the three vacuum expectation values $\langle H_u^0 \rangle$, $\langle H_d^0 \rangle$ and $\langle S \rangle$ of the neutral components of the Higgs doublet and singlet fields. In a second input file, `bhdecay.in`, the CKM parameters and several flags for the calculation of the decay widths are set.

The package consists of a wrap file `nmssmcalc.f` and three main files: (i) `CalcMasses.F` for the calculation of the one-loop corrected NMSSM Higgs boson masses in the real and the complex NMSSM. They are obtained in the Feynman-diagrammatic approach in two different renormalisation schemes both in the real and in the complex NMSSM. Details can be found in Refs. [59, 80, 81, 82]. (ii) `bhdecay.f`, which computes the NMSSM Higgs boson decay widths and branching ratios in the real NMSSM. (iii) `bhdecay_c.f`, providing the decay widths and branching ratios of CP-violating NMSSM Higgs bosons.

The wrap file reads in the input parameters for the Higgs mass calculation from `inp.dat` and calls `CalcMasses.F` to which it then passes on the input values. The latter calculates the loop-corrected neutral Higgs boson masses, which are written out together with the mixing angles in an SLHA output file `slha.in`. Subsequently `nmssmcalc.f` calls `bhdecay.f` (in the CP-violating case `bhdecay_c.f`), which reads in `slha.in` and computes all NMSSM Higgs decay

¹The trilinear coupling A_λ can be traded for the charged Higgs boson mass M_{H^\pm} .

widths and branching ratios. They are written out in an SLHA output file `slha_decay.out`. Sample input and output files can be found on the program webpage. Note, that the user can also specify the names of the input file and of the output files, provided by the mass and decay routines, in the command line when running the program.

The decay widths have been implemented including the dominant higher order QCD corrections. In addition, the higher order SUSY-QCD corrections and the approximate SUSY-electroweak corrections at one-loop level are included in the Higgs boson decays into fermion pairs. The decays into stop and sbottom pairs contain the SUSY-QCD corrections in the case of the CP-conserving NMSSM. Off-shell decays are taken into account in the decays into massive gauge boson pairs, into gauge and Higgs boson final states, into Higgs pairs and into heavy quark pairs. In this context bottom quark mass effects in the off-shell decays into top quark final states tt^* for the neutral Higgs bosons and into the top-bottom final state t^*b for the charged Higgs boson have been calculated and implemented. Note, that EW corrections beyond the approximate SUSY-EW contributions are not included in general, as this would require further missing calculations, due to the additional NMSSM singlet field compared to the MSSM.

3 SUSY CORRECTIONS TO FERMIONIC DECAYS

In the decays into fermion final states the SUSY-QCD and the SUSY-EW corrections become important in parts of the parameter space. The dominant contributions can be resummed and included in effective Yukawa couplings [17, 18, 19, 20, 21, 83, 84, 85, 86, 87, 88], by deriving them from an effective Lagrangian. In the NMSSM care has to be taken to properly take into account the singlet contribution. For the bottom-Yukawa part *e.g.* the corresponding effective Lagrangian is given by (see [83, 85] in the case of the MSSM)

$$\mathcal{L}_{\text{eff}} = -y_b \bar{b}_R \left[(1 + \Delta_1) H_d + \frac{\lambda^* e^{i\varphi_u} (1 + \Delta_1) \Delta_b}{\mu_{\text{eff}}^* \tan \beta} S^* H_u^* \right] b_L + h.c. , \quad (1)$$

where H_d , H_u and S are the scalar components of \hat{H}_d , \hat{H}_u and \hat{S} , respectively. The Yukawa coupling is denoted by y_b , and the indices L, R denote the left- and right-chiral projections of the bottom quarks. In the case of the CP-conserving NMSSM $\varphi_u = 0$ and also λ and μ_{eff} are real. The corrections Δ_b and Δ_1 include the SUSY-QCD and SUSY-EW corrections inducing a modification of the relation between the bottom quark mass m_b and the Yukawa coupling y_b . The explicit expressions for the CP-conserving and CP-violating case can be found in [59]. Also the corrections for the neutral Higgs boson decays into strange quark and lepton pair final states, respectively, as well as for the charged Higgs decays into up/charm/top and bottom quark pair and into up/charm/top and strange quark pair can be found there.

4 HIGGS BOSON PHENOMENOLOGY

In this section we discuss some interesting features in the NMSSM Higgs boson phenomenology which can be investigated by applying our program package NMSSMCALC.

Higgs boson masses in the complex NMSSM: We first analyse the impact of non-vanishing complex phases, *i.e.* CP-violation, on Higgs boson phenomenology, in particular the Higgs boson masses. Contrary to the MSSM, in the NMSSM CP-violation already appears at tree-level, described by a non-vanishing phase φ_y given by

$$\varphi_y = \varphi_\kappa - \varphi_\lambda + 2\varphi_s - \varphi_u , \quad (2)$$

where φ_κ , φ_λ and φ_s denote the phases of κ , λ and the VEV of the singlet field S , respectively. In Fig. 1 (left) we show the tree-level masses and the loop-corrected masses of the neutral Higgs bosons H_2 and H_3 . The input parameters are given by

$$\begin{aligned} \tan \beta &= 2, & \text{Re}(\lambda) &= 0.65, & \text{Re}(\kappa) &= 0.085, \\ A_\kappa &= -95 \text{ GeV}, & M_{H^\pm} &= 500 \text{ GeV}, & \text{Re}(\mu_{\text{eff}}) &= 200 \text{ GeV}, \end{aligned} \quad (3)$$

with the effective μ parameter $\mu_{\text{eff}} = \lambda v_s \exp(i\varphi_s)/\sqrt{2}$. The real parts of the parameters are denoted by Re , and we have set $\varphi_s = 0$. The soft SUSY breaking gaugino mass parameters $M_{1,2,3}$ as well as the left- and right-handed soft SUSY breaking mass parameters of the lepton sector and correspondingly of the quark sector for the three different generations have been chosen as

$$\begin{aligned} M_1 &= 150 \text{ GeV}, & M_2 &= 340 \text{ GeV}, & M_3 &= 1 \text{ TeV}, \\ M_{\tilde{E}_{R1,2}} &= M_{\tilde{L}_{1,2}} = M_{\tilde{D}_{R1,2,3}} = M_{\tilde{Q}_{1,2}} = 1.5 \text{ TeV}, \\ M_{\tilde{U}_{R1,2}} &= 1 \text{ TeV}, & M_{\tilde{U}_{R3}} &= M_{\tilde{Q}_3} = 700 \text{ GeV}, & M_{\tilde{E}_{R3}} &= M_{\tilde{L}_3} = 250 \text{ GeV}. \end{aligned} \quad (4)$$

The soft SUSY breaking trilinear couplings are set to, ($U \equiv u, c, t$, $D \equiv d, s, b$, $L \equiv e, \mu, \tau$)

$$\text{Re}(A_U) = 300 \text{ GeV}, \quad A_D = A_L = 1.5 \text{ TeV}. \quad (5)$$

We furthermore include CP-violation at tree-level by choosing a non-vanishing phase φ_u and non-zero imaginary parts for λ and κ , respectively. Additionally, we choose an imaginary part for A_U which enters through loop-corrections in the masses (only A_t induces a non-negligible effect, though). Hence,

$$\varphi_u = 0.1, \quad \text{Im}(\lambda) = 0.1, \quad \text{Im}(\kappa) \in [0.04, \dots, 0.07], \quad \text{Im}(A_U) = -50 \text{ GeV}. \quad (6)$$

Keeping φ_u and $\text{Im}(\lambda)$ constant, we vary $\text{Im}(\kappa)$ and hence φ_y . From the dashed lines in Fig. 1 (left) we see that CP-violation at tree-level clearly has an impact on the mass values. With increasing $\text{Im}(\kappa)$ the masses of the next-to-lightest H_2 and of the third lightest H_3 approach each other, before departing from each other again. The one-loop corrections increase the masses by up to 10%, as can be inferred from the full lines. Also here the strong dependence on the complex phase persists. Interestingly, for $\text{Im}(\kappa) \approx 0.054$ the two masses are almost degenerate and both close to 126 GeV. In this case the two Higgs bosons would build up the signal observed at the LHC. At this value of $\text{Im}(\kappa)$ in fact, H_2 and H_3 interchange their roles, as explained below when discussing Fig. 1 (right).

In Fig. 1 (right) we show the amount of CP-violation $r_{\text{CP}}^{i=2,3}$ of H_2 and H_3 , respectively. For the boson H_i it is quantified by the loop-corrected mixing matrix elements \mathcal{R}_{ij} as

$$r_{\text{CP}}^i \equiv (\mathcal{R}_{i1})^2 + (\mathcal{R}_{i2})^2 + (\mathcal{R}_{i3})^2, \quad i = 1, \dots, 5. \quad (7)$$

The 5×5 matrix \mathcal{R} rotates the interaction to the loop-corrected mass eigenstates H_i where the ordering is such that the first three (last two) columns correspond to the CP-even (CP-odd) components of H_u, H_d and S . A pure CP-even (CP-odd) state corresponds to $r_{\text{CP}}^i = 1$ (0).

From Fig. 1 (right) it can be inferred, that the initially CP-even-like H_3 becomes more and more CP-even-like with increasing $\text{Im}(\kappa)$, reaching its maximum value of almost one at the point where H_2 and H_3 are nearly mass degenerate. Subsequently, it develops a CP-odd

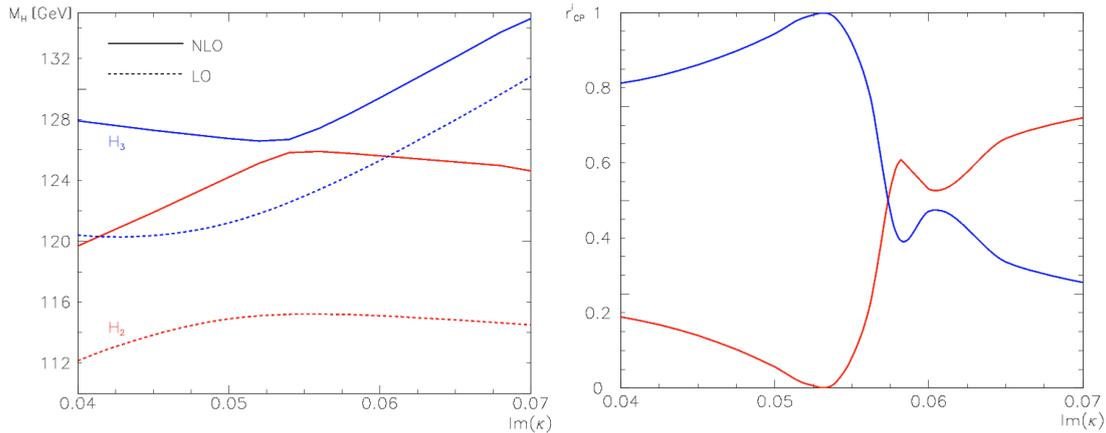


Figure 1: Left: Higgs boson masses M_{H_2} (red/light grey) and M_{H_3} (blue/dark grey) as function of $\text{Im}(\kappa)$ at LO (dashed) and NLO (full). Right: The amount of CP-violation r_{CP}^i for H_2 (red/light grey) and H_3 (blue/dark grey) as function of $\text{Im}(\kappa)$.

component which increases with $\text{Im}(\kappa)$. The next-to-lightest H_2 shows the opposite behaviour. Being initially CP-odd-like, this component increases until H_2 is almost purely CP-odd-like at $\text{Im}(\kappa) \approx 0.054$. Beyond this point H_2 and H_3 interchange their roles, with H_2 being more and more CP-even-like. Finally, we note that in the limit of CP-conservation we have $M_{H_2} = 115.8$ GeV and $M_{H_3} = 125.5$ GeV, with a CP-odd H_2 and a CP-even H_3 . Hence H_3 plays the role of the 125 GeV resonance, discovered at CERN, while for the CP-violating case with $\text{Im}(\kappa) = 0.07$ this role is taken over by H_2 .

This discussion shows that non-vanishing CP-violating phases can have an important impact on Higgs boson phenomenology, in particular if CP-violation is already present a tree-level. *SUSY corrections to decays into fermions:* In order to discuss the impact of the SUSY-QCD and SUSY-EW corrections on the Higgs decays into fermions we take a toy scenario with large values of $\tan \beta$ and μ_{eff} for which these corrections become sizeable. We keep the same parameter set as in the previous scenario with the exception that we set all imaginary parts and phases to zero, so that we are in the CP-conserving case. Furthermore we change $\tan \beta$, λ , M_{H^\pm} and μ_{eff} to

$$\tan \beta = 30, \quad \lambda = 0.1, \quad M_{H^\pm} = 150 \text{ GeV}, \quad \mu_{\text{eff}} = 500 \text{ GeV}. \quad (8)$$

This leads to a mass spectrum with the second lightest Higgs boson having a mass of 125 GeV. As expected, due to the large value of $\tan \beta$ and μ_{eff} SUSY corrections in the decays into fermions become important. In the H_2 decays they can increase the partial decay width by up to $\sim 15\%$ in the τ lepton final state and reduce the decay width into bottom quarks by up to 8% . In the H^\pm decays the corrections become even more important, reaching up to $\sim 15\%$ in the $\tau\nu_\tau$ final state and $\sim 18\%$ in the decays into bottom charm or bottom up.

CONCLUSIONS

We have presented the program package NMSSMCALC for the computation of the higher order corrected NMSSM Higgs boson masses and decay widths in the CP-conserving and the CP-violating cases. For the computation of the decay widths it is at present the most-up-to-date

program tool, which includes besides the most important QCD corrections also SUSY-QCD and SUSY-EW corrections for the decays into fermion pairs, not only for the real but also the complex NMSSM. In application of our package we have discussed the impact of complex phases on Higgs boson phenomenology, which can be considerable. In a toy example the importance of the SUSY-QCD and SUSY-EW corrections for the decays into fermionic final states has been demonstrated.

ACKNOWLEDGEMENTS

MM and MS would like to thank the organisers of Les Houches for the great and fruitful atmosphere of the workshop.

The Higgs Boson

Contribution 4

The Theoretical Uncertainties in Higgs Signal Strength Fits

S. Fichet, G. Moreau

Abstract

We carry out fits of a simple anomalous Lagrangian to latest Higgs data using various statistical treatments of theoretical uncertainties. We discuss the discrepancies obtained from frequentist and Bayesian statistics, and from employing either Gaussian or uniform priors. Slight discrepancies appear between fits with Gaussian and uniform priors. One also observes differences between frequentist and Bayesian both because of the regions definition and because of the treatment of nuisance parameters. These various discrepancies do not have a significant impact on the conclusions of the fits. We point out that as the LHC will collect more data, the frequentist and Bayesian treatments of nuisance parameters will converge and the dependence on theoretical uncertainty priors will increase.

1 INTRODUCTION

In addition to the recent discovery of a resonance around 125.5 GeV [44, 45] that is most probably the Brout-Englert-Higgs boson, the ATLAS and CMS collaborations have provided a long list of production and decay rate measurements. This precious list of data constitutes a new source of information on physics beyond the Standard Model (SM). Indeed, deviations of the observed Higgs boson rates with respect to their SM predictions may reveal the presence of underlying new physics (NP), while the absence of such deviations translates as constraints on NP models. A large amount of Higgs coupling studies has already been realized, with so far no significant signs from unknown physics. However, given the far-reaching implications of such results, it is mandatory to take carefully into account all the possible sources of uncertainty. In this contribution we carry out a global fit to the available data, taking into account the potentially significant uncertainties present on the theoretical side. In particular we implement the possibility of a flat prior distribution for the theoretical error and carry out both frequentist and Bayesian treatments.

2 Likelihood function and theoretical uncertainties

The results from Higgs searches are given in terms of signal strengths $\mu(X, Y)$, the ratio of the observed rate for some process $X \rightarrow h \rightarrow Y$ relative to the prediction for the SM Higgs,

$$\mu(X, Y) = \frac{N_{obs}}{[\sigma(X \rightarrow h) \mathcal{B}(h \rightarrow Y) \varepsilon^{XY} \mathcal{L}]_{SM}}. \quad (1)$$

We use the full dataset collected so far with luminosities of $\mathcal{L} \sim 5 \text{ fb}^{-1}$ at the center of mass energy $\sqrt{s} = 7 \text{ TeV}$ and $\mathcal{L} \sim 20 \text{ fb}^{-1}$ at $\sqrt{s} = 8 \text{ TeV}$ [89, 90, 91]. Here \mathcal{B} is the branching ratio of the decay and the coefficient $\varepsilon^{XY} \in [0, 1]$ characterizes the efficiency of event selection for a given subcategory. An experimental channel is defined by its final state ($\gamma\gamma$, ZZ , WW , $b\bar{b}$, $\tau\tau$) and is often divided into subchannels having different sensitivity to the various production processes. The accessible production mechanisms at the LHC are *i*) gluon-gluon Fusion (ggF), *ii*) Vector Boson Fusion (VBF), *iii*) associated production with an electroweak gauge boson $V = W, Z$ (Vh), and *iv*) associated production with a $t\bar{t}$ pair (tth). The theoretical signal strengths for Higgs searches can be expressed as (see [92, 93, 94] for more details)

$$\bar{\mu}(X, Y) = \frac{[\sigma(X \rightarrow h) \mathcal{B}(h \rightarrow Y) \varepsilon^{XY}]_{NP}}{[\sigma(X \rightarrow h) \mathcal{B}(h \rightarrow Y) \varepsilon^{XY}]_{SM}}. \quad (2)$$

In all generality, efficiencies in the SM with and without higher order operators are not necessarily the same, *i.e.* $\varepsilon_{NP} \neq \varepsilon_{SM}$, because kinematic distributions can be modified in a non-trivial way by new physics effects.

The model of new physics we adopt consists of a modification of the Standard Model tree-level couplings,

$$\mathcal{L}_h^{tree} = c_V \frac{h}{v} 2m_W^2 W_\mu^+ W_\mu^- + c_V \frac{h}{v} m_Z^2 (Z_\mu)^2 - c_f \sum_f \frac{h}{v} m_f \bar{\Psi}_{fL} \Psi_{fR} + h.c., \quad (3)$$

by the parameters (c_V, c_f) . The theoretical signal strengths are thus function of these anomalous couplings, *i.e.* $\bar{\mu}(c_V, c_f)$. Note these deviations to the SM are not the most general ones. Indeed, assuming the existence of new physics at a mass scale somewhat higher than the EW scale, the effects of new physics are captured in a low-energy effective Lagrangian, which in turn induces a peculiar pattern of anomalous couplings [94]. However we limit ourselves to the two dimensional subset (c_V, c_f) because our focus is on the statistical methods rather than the effective Lagrangian. The efficiencies are not modified in this simple case.

Given the released experimental information, the likelihood we are able to reconstruct is a product of Gaussians. Although experimental systematics are in principle included in these data, the non-trivial correlations among subchannels they induce are most of the time not available. They will not be discussed further in this work. Labeling by I the various independent subsets of channels, the likelihood reads

$$L_0 \propto \prod_I e^{-(\bar{\mu}_I - \mu_I)^2 / 2(\Delta_I^{\text{ex}})^2}, \quad (4)$$

where Δ_I^{ex} denotes the experimental uncertainties.

Let us turn to the picture of theoretical uncertainties. The leading theoretical uncertainties come from the QCD prediction of the Higgs production cross sections. At the proton level, they come from parton distribution function (PDF) errors. At the parton level they originate from the lack of knowledge of the higher order contributions in the perturbative expansion, and can be equivalently recast into the dependence on the QCD renormalization scale. Besides cross sections, this same source of uncertainty also affects the branching ratios. As they affect the predicted quantities, it turns out that these theoretical uncertainties approximately cancel in the predicted signal strengths $\bar{\mu}$, because they appear both in the numerator and the denominator.

Instead the experimental signal strength μ gets fully affected as no cancellation occurs. Here we will parametrize the theoretical errors on experimental signal strengths under the form

$$\mu_I \rightarrow \mu_I \times \left(1 + \delta_I \frac{\Delta_I^{\text{th}}}{\mu_I}\right), \quad (5)$$

where the δ_I are nuisance parameters, and the Δ_I^{th} set the magnitudes of the error in a given subchannel.

We adopt two different statistical frameworks, the one of Bayesian statistics and the one of (so-called) hybrid frequentist statistics. In both of these arguably well-defined frameworks, a probability density function (*pdf*) is associated with all input parameters. From now we denote it as the “prior” *pdf*. The prior *pdf* multiplies the likelihood, such that one has to deal with the distribution

$$L_0(c_V, c_f, \delta_I) p(c_V, c_f, \delta_I), \quad (6)$$

called “posterior” in Bayesian statistics. The parameters of interest c_V , c_f will be given a uniform prior. Our focus is rather on the nuisance parameters which are modeling the theoretical uncertainties. We give the same probability distributions to all of the δ_I ’s. It is clear that theoretical uncertainties may induce new correlations among the various subchannels. However we take the study of such correlations to be beyond the scope of the present contribution, and leave it for future work [95]. Here we rather focus on the various discrepancies related to the statistical framework.

Apart from conceptual differences, in practice there are two differences between frequentist and Bayesian statistics that lead to potentially different results for Higgs fits. First, nuisance parameters are integrated over in the Bayesian framework, while the likelihood is instead maximized with respect to them in the frequentist framework. Second, the frequentist confidence regions and Bayesian credible regions have different definitions (*c.f.* [96]). It is therefore necessary to discuss the impact of these differences on Higgs fits.

A widespread practice in the community is to combine theoretical uncertainties in quadrature with the experimental uncertainties, that is make the following replacement in Eq.(4),

$$(\Delta_I^{\text{ex}})^2 \rightarrow \Delta_I^2 \equiv (\Delta_I^{\text{ex}})^2 + (\Delta_I^{\text{th}})^2. \quad (7)$$

We stress that this approach actually amounts to assume a Gaussian prior for the δ_I ’s, under the form

$$p(\delta_I) \propto e^{-\delta_I^2/2}. \quad (8)$$

This is true in both frequentist and Bayesian frameworks. We emphasize that a Gaussian prior is however not particularly motivated in order to model the uncertainties. A uniform prior over an appropriate interval may for example seem more objective. In any case, the prior dependence of the fit needs to be controlled. In addition, in case of a prior other than Gaussian, the frequentist and Bayesian approaches also differ at the level of marginalization itself, *i.e.* the marginalized likelihoods are no longer identical.

All these aspects constitute motivations to compare both frequentist with Bayesian fits and Gaussian with uniform priors. Before turning to numerical results, it is instructive to consider the behavior of these fits in various limits. First, in the limit $\Delta_I^{\text{th}} \rightarrow 0$ at fixed Δ_I^{ex} , the interval of δ_I shrinks to zero, *i.e.* $p(\delta_I)$ tends to a Dirac peak, *i.e.* δ_I is set to zero. In that limit, the difference between fits based on the various prior shapes vanishes, and the only remaining difference

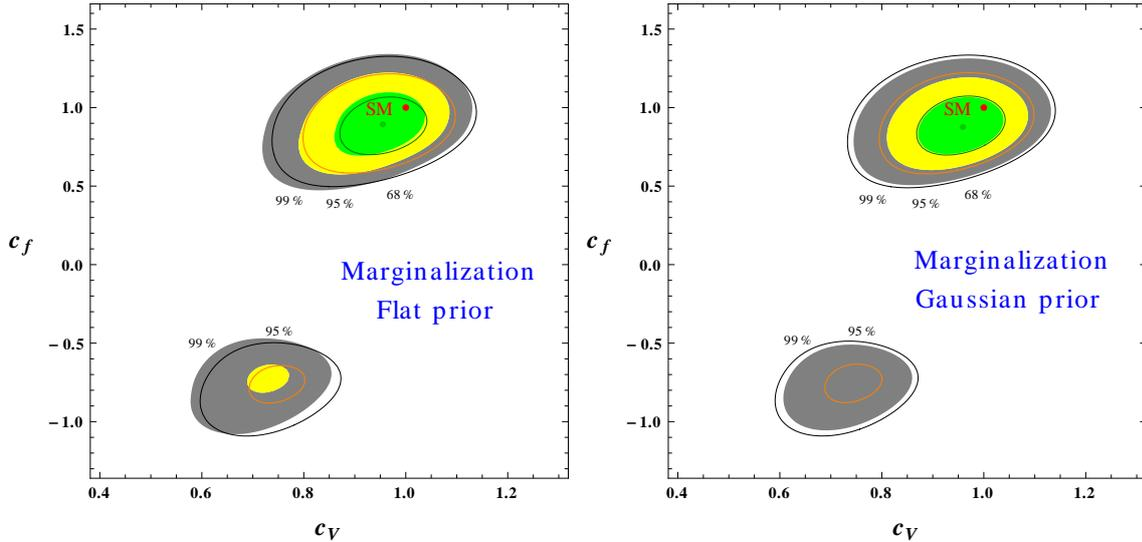


Figure 1: The 68.27%, 95.45%, 99.73% confidence level (CL) (from marginalized frequentist likelihoods) and Bayesian credible (from posteriors) regions are shown respectively as colored regions and contour levels in the (c_V, c_f) plane. The green point is the frequentist best-fit location. Left and right panels respectively correspond to the flat and Gaussian prior case. The SM prediction point is also displayed [in red].

between frequentist and Bayesian fits comes from the definition of the best-fit regions. Second, in the “high statistics limit” $\Delta_I^{\text{ex}} \rightarrow 0$ at fixed Δ_I^{th} , the L_0 likelihood function of Eq.(4) tends to a Dirac peak, so that there is no more difference between frequentist and Bayesian treatments of nuisance parameters. Indeed, in this limit, the likelihoods take the form

$$L \propto \prod_I p(\delta_I) \Big|_{\delta_I = (\bar{\mu}_I / \mu_I - 1) / (\Delta_I^{\text{th}} / \mu_I)} \quad (9)$$

The marginalized likelihoods therefore depend maximally on the prior for δ , such that the issue of theoretical uncertainties will become dominantly important as the LHC accumulates more data.

3 Numerical results

The marginalized frequentist likelihood and Bayesian posteriors with either flat or Gaussian prior are shown in Fig. 1. First of all, we can observe that the frequentist and Bayesian approaches give very similar outcome. This shows explicitly the fact that the two approaches have reached a certain degree of convergence since the priors on c_V, c_f are already dominated by the data¹.

For the Gaussian case, even though the likelihood functions are exactly the same, we observe that the 95.45%CL region is still present in the Bayesian fit, while it disappears in the frequentist case – this difference being only induced by the definition of the best-fit regions. It turns out from the right figure that the Bayesian regions are more conservative. For the flat prior

¹Notice however that this statement depends on the model under consideration. In particular with the present data, a global fit of the dimension 6 effective Lagrangian still has some weakly constrained directions in the operator space [94].

case, one can see that the difference between frequentist and Bayesian treatments of nuisance parameters leads to slightly different positions and shapes for the best-fit regions.

For a given statistical approach (either frequentist or Bayesian), small differences are observed between the flat and Gaussian priors. As discussed in the previous Section, the smallness of these discrepancies is related to the fact that we are currently in the regime where experimental uncertainties are large with respect to theoretical uncertainties, *i.e.* $\Delta_I^{\text{ex}} \gg \Delta_I^{\text{th}}$. This situation will change with future and more accurate LHC data.

CONCLUSIONS

In this contribution we discuss the discrepancies induced on Higgs fits from various statistical treatments of theoretical uncertainties, using the most recent data available. We present and compare results obtained from frequentist and Bayesian statistics, and from employing either Gaussian or uniform priors. Discrepancies between frequentist and Bayesian are observed in the Gaussian case because of the regions definition. In the flat prior case, further discrepancies appear because of the treatment of nuisance parameters. These discrepancies do not have a significant impact on the conclusions of the fits. It is worth pointing out that in the limit of high statistics, the frequentist and Bayesian treatments of nuisance parameters converge, while the theoretical uncertainty prior dependence increases. The study of the impact from correlations induced by theoretical uncertainties is left for further work [95].

ACKNOWLEDGEMENTS

S. Fichet thanks the University of Orsay/France for hospitality offered as some of the work contained in these proceedings was performed there. The authors also acknowledge the organizers of the “Les Houches” Workshop for the perfect organization and friendly atmosphere during the Workshop.

Contribution 5

Testing Custodial Symmetry and CP Properties of the 125 GeV Higgs Boson

J. Bernon, B. Dumont, J. F. Gunion, S. Kraml

Abstract

Performing a fit to all publicly available data, we analyze the extent to which the latest results from the LHC and Tevatron constrain the couplings of the 125 GeV Higgs boson. In particular, we test custodial symmetry through HWW and HZZ coupling modifications and study possible CP-violating contributions. Moreover, we consider consequences for the $Z\gamma$ channel.

1 INTRODUCTION

That the mass of the Higgs boson is about 125 GeV is a very fortunate circumstance in that we can detect it in many different production and decay channels [44, 45]. Indeed, many distinct signal strengths, defined as production \times decay rates relative to Standard Model (SM) expectations, $\mu_i \equiv (\sigma \times \text{BR})_i / (\sigma \times \text{BR})_i^{\text{SM}}$, have been measured with unforeseeable precision already with the 7–8 TeV LHC run [90, 97]. From these signal strengths one can obtain information about the couplings of the Higgs boson to electroweak gauge bosons and fermions (of the third generation), and loop-induced couplings to photons and gluons.

Fits to various combinations of reduced Higgs couplings (*i.e.* Higgs couplings to fermions and gauge bosons relative to their SM values) have been performed by the experimental collaborations themselves as well as in a large number of theoretical papers, see *e.g.* Ref. [98] and references therein. In Ref. [98] some of us combined the information provided by ATLAS, CMS and the Tevatron experiments on the $\gamma\gamma$, $ZZ^{(*)}$, $WW^{(*)}$, $b\bar{b}$ and $\tau\tau$ final states including the error correlations among various production modes. The five theoretically “pure” production modes which are accessible are gluon–gluon fusion (ggF), vector boson fusion (VBF), associated production with a W or Z boson (WH and ZH, commonly denoted as VH), and associated production with a top-quark pair (ttH). The scheme conveniently adopted by the experimental collaborations is to group these five modes into just two effective modes, ggF + ttH and VBF + VH, and present contours of constant likelihood for particular final states in the $\mu(\text{ggF} + \text{ttH})$ versus $\mu(\text{VBF} + \text{VH})$ plane. Using this information, we obtained “combined likelihood ellipses”, which can be used in a simple, generic way to constrain non-standard Higgs sectors and new contributions to the loop-induced processes, provided they have the same Lagrangian structure as the SM.

In particular, these likelihoods can be used to derive constraints on a model-dependent choice of generalized Higgs couplings, the implications of which we studied in Ref. [98] for several well-motivated models. In this contribution, we go a step further and study to which extent the current global coupling fit can test i) custodial symmetry and ii) possible CP-violating contributions.

2 TESTING CUSTODIAL SYMMETRY

We fit the latest Higgs data using the following parametrization of the Higgs couplings:

$$\mathcal{L} = g \left[C_W m_W W^\mu W_\mu + C_Z \frac{m_Z}{\cos \theta_W} Z^\mu Z_\mu - C_U \frac{m_t}{2m_W} \bar{t}t - C_D \frac{m_b}{2m_W} \bar{b}b - C_D \frac{m_\tau}{2m_W} \bar{\tau}\tau \right] H. \quad (1)$$

We set $C_W, C_Z > 0$ by convention and use $\text{sgn}(C_U) = \text{sgn}(C_D) = 1$ unless explicitly mentioned. For convenience, we define C_{WZ} as the ratio of the HWW coupling to the HZZ coupling,

$$C_{WZ} \equiv \frac{C_W}{C_Z}. \quad (2)$$

We define C_g and C_γ to be the ratio of the Hgg and $H\gamma\gamma$ couplings to their SM values. In this paper we do not consider potential BSM loop contributions ΔC_g and ΔC_γ from new particles in the $gg \rightarrow H$ and $H \rightarrow \gamma\gamma$ loops and, therefore, C_g and C_γ are simply computed in terms of the parameters appearing in Eq. (1).

Our aim is to obtain confidence level (CL) intervals on C_{WZ} . For that, the signal strengths μ in the various observed channels are used to compute a χ^2 :

$$\chi^2 = \sum_k \frac{(\bar{\mu}_k - \mu_k)^2}{\Delta\mu_k^2}, \quad (3)$$

where k runs over all available production \times decay channels, μ_k is the experimental signal strength for the channel k , and $\bar{\mu}_k$ is the predicted signal strength from the set of reduced couplings C_i . Whenever the 2D information ($\mu_{\text{ggF}+\text{ttH}}, \mu_{\text{VBF}+\text{VH}}$) is available, a Gaussian fit is performed and the correlation between the two signal strengths is obtained and taken into account. Details on this procedure are explained in Ref. [98] (see also the discussion in Ref. [99]).

When the experimental result is only given for VH production and not for WH and ZH separately, we combine the calculated signal strengths for a given decay mode as:

$$\bar{\mu}_{\text{VH}} = \frac{\sigma(pp \rightarrow ZH)}{\sigma(pp \rightarrow VH)} \bar{\mu}_{\text{ZH}} + \frac{\sigma(pp \rightarrow WH)}{\sigma(pp \rightarrow VH)} \bar{\mu}_{\text{WH}}. \quad (4)$$

For the VBF production mode, we compute a reduced C_{VBF} coupling as

$$C_{\text{VBF}}^2 = \frac{C_Z^2 \sigma(\text{ZBF}) + C_W^2 \sigma(\text{WBF}) + C_Z C_W \sigma(\text{interference})}{\sigma(\text{ZBF}) + \sigma(\text{WBF}) + \sigma(\text{interference})}, \quad (5)$$

where the cross sections are obtained with VBFNLO [100].

For validation, we first compare our fits using only CMS or ATLAS data to the results of fits performed by the CMS [97] and ATLAS [101] collaborations themselves. For CMS, two cases are considered. First, custodial symmetry and universal fermion couplings to the Higgs boson are assumed, *i.e.* $C_V \equiv C_Z = C_W$ and $C_F \equiv C_U = C_D$. Second, a universal fermion coupling C_F is assumed while C_{WZ} and C_Z are scanned over. For ATLAS, the scan has been performed over C_F , C_{WZ} and C_Z , for different signs of C_F . The results are displayed in Fig. 1. Since we do not have access to the full experimental information, our fits naturally somewhat differ from the ones done by the collaborations. Nonetheless, as one can see, our fits provide a very good approximation.

Next, we fit the Higgs couplings to W and Z bosons using the full data sets available from the LHC and Tevatron, *i.e.* combining all available results. We consider the cases that a) the fermionic couplings C_U and C_D are as in the SM, *i.e.* $C_U = C_D = 1$ and b) the fermionic couplings are allowed to vary independently. The results are reported in the 2D plane of C_W versus C_Z plane in Fig. 2. When the fermionic couplings are set to their SM values, no correlation is seen between C_W and C_Z . The situation is different when C_U and C_D are varied independently. Indeed, when C_W takes values larger (smaller) than 1, the signal strengths $\mu(H \rightarrow WW)$ and $\mu(H \rightarrow \gamma\gamma)$ become large (small) and thus deviate considerably from the experimental values. When C_D is allowed to deviate from one, the total width of the observed state can be made larger (smaller) in order to decrease (increase) the signal strengths $\mu(H \rightarrow WW)$, $\mu(H \rightarrow \gamma\gamma)$ and $\mu(H \rightarrow ZZ)$ while keeping an acceptable rate for $H \rightarrow b\bar{b}$ and $H \rightarrow \tau\tau$. Finally, to accommodate the measured $H \rightarrow ZZ$ value, C_Z is preferably larger than 1. This leads to the observed correlation between C_W and C_Z . Note that in case a) the best fit for C_W is slightly below unity while that for C_Z it is slightly above unity. In case b) the best fits for values C_W and C_Z are both slightly above unity. The corresponding 68% and 95.4% CL intervals for C_W and C_Z are given in Table 1.

	C_W : 1 σ range	C_Z : 1 σ range	C_W : 2 σ range	C_Z : 2 σ range
$C_U = C_D = 1$	[0.94, 1.06]	[0.99, 1.17]	[0.87, 1.11]	[0.89, 1.26]
$C_U, C_D > 0$	[0.96, 1.15]	[1.04, 1.27]	[0.87, 1.24]	[0.91, 1.39]

Table 1: 68% and 95.4% CL intervals of C_W and C_Z in two different scenarios.

The $\Delta\chi^2$ profile of C_{WZ} is shown in Fig. 3, for the cases $C_U = C_D = 1$ (red line), varying $C_U, C_D > 0$ (orange line) and varying $C_U, C_D < 0$ (blue line). The corresponding 68% and 95.4% CL intervals for C_{WZ} and the χ^2 at the best-fit points are listed in Table 2. The first two scenarios are compatible at the 1 σ level with the SM. The best-fit case is obtained when C_U and C_D are positive and varied independently. The best-fit point for this scenario is: $C_U = 0.90$, $C_D = 1.02$, $C_Z = 1.18$, $C_{WZ} = 0.90$, $C_W = 1.06$ with a χ^2_{\min} of 15.70 for 20 degrees of

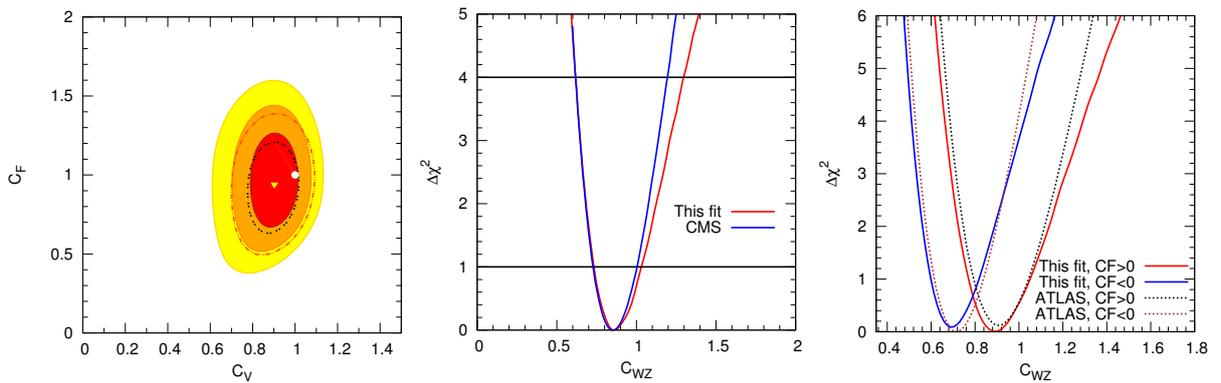


Figure 1: Left plot: Fit of C_V and C_F . The dashed lines are the 68% and 95.4% CL contours as reported by the CMS collaboration in Fig. 6 of Ref. [97], while the red, orange and yellow regions are the 68%, 95.4% and 99.7% CL regions of our fit. Middle plot: Fit of C_{WZ} while C_Z and $C_F > 0$ are profiled over with comparison to the CMS fit, Fig. 7 of Ref. [97]. Right plot: Fit of C_{WZ} while C_Z and C_F are profiled over with comparison to the ATLAS fit, Fig. 11 of Ref. [101].

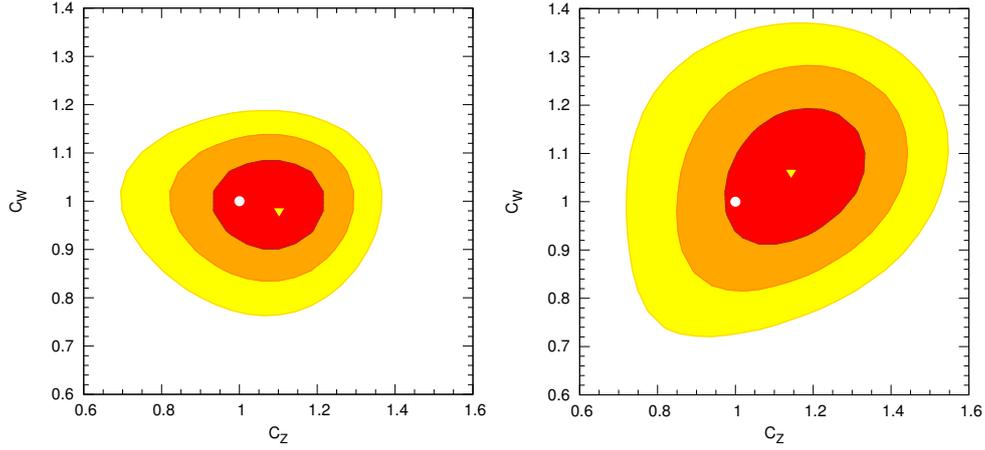


Figure 2: C_W, C_Z fit assuming $C_U = C_D = 1$ (left) and varying $C_U, C_D > 0$ (right). The red, orange and yellow regions are respectively the 68%, 95.4%, and 99.7% CL regions. The white point shows the SM expectation while the yellow triangle shows the best-fit point: $(C_W = 0.980, C_Z = 1.102)$ (left) and $(C_W = 1.061, C_Z = 1.143)$ (right).

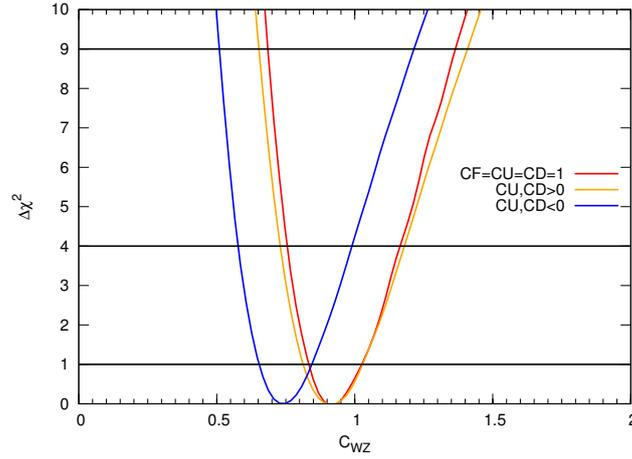


Figure 3: 1-dimensional fit of C_{WZ} for three different choices of fermionic couplings; when free, C_U and C_D are profiled over.

freedom.

	1σ range	2σ range	$\chi_{\min}^2/\text{ndof}$
$C_U = C_D = 1$	[0.83, 1.02]	[0.76, 1.16]	16.87/22 = 0.77
$C_U, C_D > 0$	[0.81, 1.03]	[0.73, 1.18]	15.70/20 = 0.79
$C_U, C_D < 0$	[0.65, 0.84]	[0.58, 0.99]	18.84/20 = 0.94

Table 2: 68% and 95.4% CL intervals of C_{WZ} and $\chi_{\min}^2/\text{ndof}$ in three different scenarios.

Even though the SM unity values of C_W and C_Z are compatible with the experimental data already at the 1σ level, this fit cannot exclude values greater than unity. Of course, values above

unity can only be realized if the H of Eq. (1) has a component coming from triplet or higher Higgs representations. Differences between C_W and C_Z are of course severely constrained from the precise measurement of the Peskin–Takeuchi T parameter at LEP. It is however still possible to obtain $C_W \neq C_Z$ in an effective approach at the price of a fine-tuned cancellation between operators [102]. Another possibility would be to generate an apparent splitting between C_W and C_Z from the tensor couplings $H(Z_{\mu\nu})^2$ and $HW_{\mu\nu}^+W_{\mu\nu}^-$ [94].

3 TESTING CP-VIOLATING ADMIXTURES

The Higgs coupling to vector bosons has the general form

$$VVH : \quad C_V \frac{gM_V^2}{m_W} g^{\mu\nu} , \quad (6)$$

where as above C_V measures the departure from the SM: $C_V = 1$ for a pure scalar (CP-even) state with SM-like couplings and $C_V = 0$ for a pure pseudoscalar (CP-odd) state. Above, we found that C_V is always well compatible with 1. However, this does not mean that CP is conserved in the Higgs sector. Likewise, $C_V \neq 1$ would not automatically be an indication of CP violation (although $C_V > 1$ would require higher Higgs representations). Instead, it is possible that two or more states of an enlarged Higgs sector share the couplings to W and Z bosons between them. (In this case, the squared couplings of each state H_i to gauge bosons should sum to unity, $\sum_i (C_V^i)^2 = 1$.) For testing CP mixing, one would need to exploit angular distributions, see Refs. [103, 104] for reviews.

A more decisive test of a possible CP-odd admixture comes from the fermion sector because of the general scalar and pseudo–scalar structure of the Higgs coupling to fermions [103, 104]. Concretely, we have

$$f\bar{f}H : \quad -\bar{f}(v_f + ia_f\gamma_5)f \frac{gm_f}{2m_W} , \quad (7)$$

where in the SM one has $v_f = 1$ and $a_f = 0$, while a purely CP-odd Higgs would have $v_f = 0$ and $a_f = 1$. In the notation of Eq. (1), $v_f = \text{Re}(C_F)$ and $a_f = \text{Im}(C_F)$, $F = U, D$, and the normalisation of the coupling, $\text{Re}(C_F)^2 + \text{Im}(C_F)^2 = |C_F|^2$, should be taken arbitrary as in the previous section. Effects of CP mixing will show up at loop level, in particular in the $gg \rightarrow H$ and $H \rightarrow \gamma\gamma$ rates. A test of the CP properties of the observed Higgs boson from a global fit to the signal strengths was first presented in Ref. [93]. Following Ref. [93], at leading order the Higgs rates normalized to the SM expectations can be written as

$$\begin{aligned} \frac{\Gamma(H \rightarrow \gamma\gamma)}{\Gamma(H \rightarrow \gamma\gamma)|_{\text{SM}}} &\simeq \frac{|\frac{1}{4}C_W A_1^+[m_W] + (\frac{2}{3})^2 \text{Re}(C_U)|^2 + |(\frac{2}{3})^2 \frac{3}{2} \text{Im}(C_U)|^2}{|\frac{1}{4}A_1^+[m_W] + (\frac{2}{3})^2|^2} , \\ \frac{\sigma(gg \rightarrow H)}{\sigma(gg \rightarrow H)|_{\text{SM}}} &= \frac{\Gamma(H \rightarrow gg)}{\Gamma(H \rightarrow gg)|_{\text{SM}}} \simeq |\text{Re}(C_U)|^2 + |\frac{3}{2} \text{Im}(C_U)|^2 , \end{aligned} \quad (8)$$

with $A_1^+[m_W] \simeq -8.34$ for $M_H = 125.5$ GeV. For convenience, the contribution of the b quark has been omitted in the above equations but is taken into account in the numerical analyses. Note that a pure pseudoscalar state not only implies $\text{Re}(C_U) = 0$, but also $C_W = C_Z = 0$; this is clearly excluded, as VBF production as well as $H \rightarrow ZZ$ and WW decays (4ℓ and $2\ell 2\nu$ signals) have been observed; besides, there would be no W boson contribution to the $H \rightarrow \gamma\gamma$ rate.

A CP-odd admixture to the observed state at 125.5 GeV is however still an interesting possibility and would necessarily indicate an enlarged Higgs sector. To test this possibility, we include $\text{Re}(C_U)$ and $\text{Im}(C_U)$ as independent parameters and perform the following fits:

- i) free $\text{Im}(C_U)$ and C_V while $|C_U|^2 = C_D = 1$,
- ii) free $\text{Re}(C_U)$, $\text{Im}(C_U)$ and C_V while $C_D = 1$,
- iii) free $\text{Re}(C_U)$, $\text{Im}(C_U)$, C_D , C_W and C_Z .

The results are shown in Figs. 4 and 5.¹ The best-fit points and the corresponding $\chi^2_{\text{min}}/\text{ndof}$ are given in Table 3. Upper limits on a given parameter are computed from the 1-dimensional $\Delta\chi^2$ distribution obtained by profiling over all other parameters of the fit.

In the $(1 - C_V^2, \text{Im}(C_U))$ plane, Fig. 4, we see that relaxing the $|C_U|^2 = 1$ constraint does not affect much the $1 - C_V^2$ parameter but enhances considerably the maximal possible value of $\text{Im}(C_U)$ at 68% and 95% CL, as also seen in Table 4. In fit i) the best fit point actually has $\text{Im}(C_U) = 0$ and $C_V = 1.03$, which corresponds to a pure scalar. In fit ii) the best fit point has $\text{Re}(C_U) = 0.72$ and $\text{Im}(C_U) = 0.35$, which would indicate a CP-violating contribution with an overall reduced $|C_U| = 0.8$, while C_V remains very SM-like. (Note however the SM values $\text{Im}(C_U) = 1 - C_V^2 = 0$ are perfectly compatible with data at the 1σ level.) Moreover, fit ii) gives a 95.4% CL upper bound of $1 - C_V^2 < 0.26$ and $\text{Im}(C_U) < 0.64$. This is a direct bound on a possible CP-odd admixture to the observed 125.5 GeV state.

Without custodial symmetry, in fit iii), the best-fit point corresponds to a non-vanishing value, $\text{Im}(C_U) = 0.52$, which is even larger than the CP-even component, $\text{Re}(C_U) = 0.42$. The reduced value $|C_U| = 0.67$ is compensated by an enhanced $C_Z = 1.15$ (which with custodial symmetry this does not work because C_W is more constrained than C_Z). Overall, there is still an upper bound of $\text{Im}(C_U) < 0.69$ (0.80) at 95.4% (99.7%) CL.

The correlation between the possible CP-even and CP-odd components of C_U , without constraining $|C_U|$ to unity, is illustrated in Fig. 5. Note in particular that a pure CP-odd coupling to the top quark, *i.e.* $\text{Re}(C_U) = 0$, is compatible with the experimental data at the 1.6σ level in fit ii) and at the 1σ level in fit iii). The SM values $\text{Re}(C_U) = 1$ and $\text{Im}(C_U) = 0$ are nonetheless still within the 68% CL region. Note finally that the quality of the fits, *i.e.* the $\chi^2_{\text{min}}/\text{ndof}$, is roughly the same in all fits considered here.

Fit	$\text{Re}(C_U)$	$\text{Im}(C_U)$	C_D	C_W	C_Z	$\chi^2_{\text{min}}/\text{ndof}$
i)	1.00	0.00	1.00	1.03		17.43/22 = 0.79
ii)	0.72	0.35	1.00	1.04		16.14/21 = 0.77
iii)	0.42	0.52	1.05	0.98	1.15	14.67/19 = 0.77

Table 3: Best-fit points and $\chi^2_{\text{min}}/\text{ndof}$ in the three different fits with CP-violating contributions.

¹Our analysis extends that of Ref. [93] in that it 1) includes the latest data and 2) uses the 2D information including correlations in the $(\mu_{\text{ggF}+\text{ttH}}, \mu_{\text{VBF}+\text{VH}})$ plane, instead of signal strengths per cut categories.

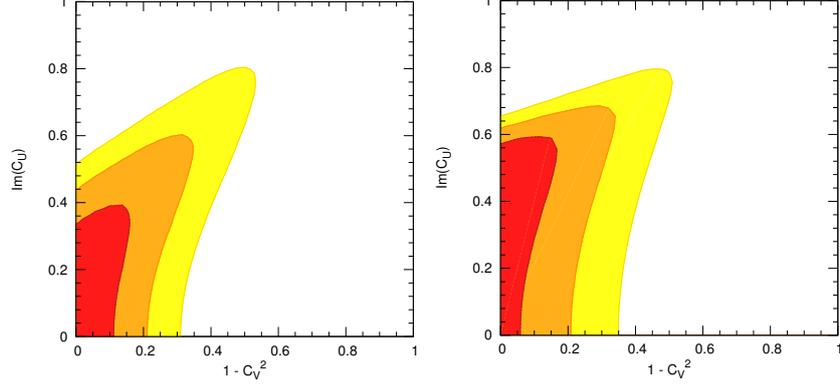


Figure 4: 68% (red), 95.4% (orange) and 99.7% (yellow) CL best-fit regions in the $(1 - C_V^2, \text{Im}(C_U))$ plane, on the left for fit i), on the right for fit ii). In both cases, the best-fit point lies in the $1 - C_V^2 < 0$ region.

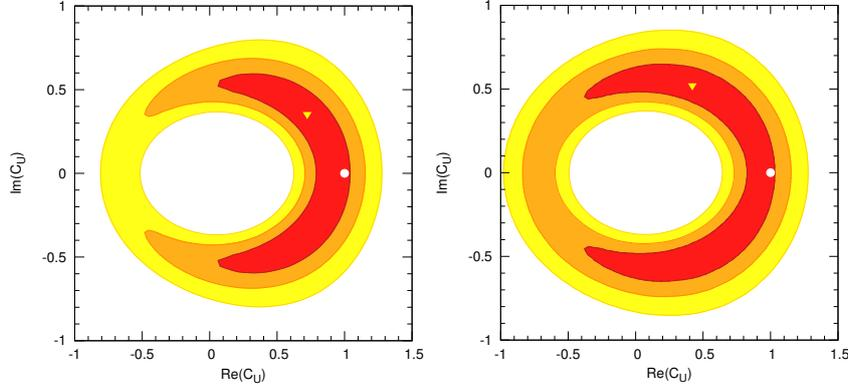


Figure 5: 68% (red), 95.4% (orange) and 99.7% (yellow) CL best-fit regions in the $(\text{Re}(C_U), \text{Im}(C_U))$ plane, on the left for fit ii) with $C_V \equiv C_W = C_Z$, on the right for fit iii) with free C_W and C_Z . The white point shows the SM expectation while the yellow triangle shows the best-fit point.

Fit	1σ	2σ	3σ
i)	0.28	0.50	0.72
ii)	0.55	0.64	0.75
iii)	0.61	0.69	0.80

Table 4: Upper bounds on $|\text{Im}(C_U)|$ at the 1, 2 and 3σ levels when profiling over all other parameters in fits i)–iii).

4 PREDICTIONS FOR $H \rightarrow Z\gamma$

Analogously to Eq. (8), we can write the partial width of the $H \rightarrow Z\gamma$ decay, normalized to its SM expectation, as

$$\frac{\Gamma(H \rightarrow Z\gamma)}{\Gamma(H \rightarrow Z\gamma)|_{\text{SM}}} \simeq \frac{\left| 2\frac{v_t}{c_W} \text{Re}(C_U) B_{1/2}^+[m_t] + C_W B_1^+[m_W] \right|^2 + 4 \left| 2\frac{v_t}{c_W} \text{Im}(C_U) B_{1/2}^-[m_t] \right|^2}{\left| 2\frac{v_t}{c_W} B_{1/2}^+[m_t] + B_1^+[m_W] \right|^2}, \quad (9)$$

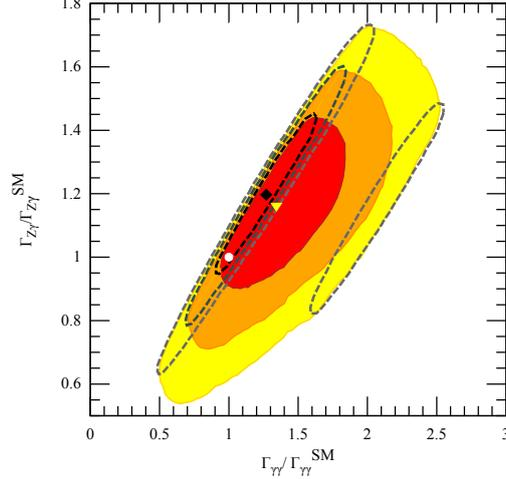


Figure 6: Fit of $\text{Re}(C_U)$, $\text{Im}(C_U)$ and C_V shown in the $(\Gamma_{\gamma\gamma}/\Gamma_{\gamma\gamma}^{\text{SM}}, \Gamma_{Z\gamma}/\Gamma_{Z\gamma}^{\text{SM}})$ plane. The red, orange and yellow regions are the 68%, 95.4% and 99.7% CL regions, respectively. The yellow triangle marks the best fit point, while the white point is the SM expectation. Overlaid are for comparison the 68% (dashed black), 95.4% (dashed dark gray) and 99.7% (dashed light gray) CL contours for the CP-conserving case with $\text{Im}(C_U) = 0$.

with $v_t = 2I_t^3 - 4Q_t s_W^2$, $B_{1/2}^+[m_t] \simeq -0.35$, $B_1^+[m_W] \simeq 5.78$, and $B_{1/2}^-[m_t] \simeq 0.54$ for $m_H = 125.5$ GeV, see Refs. [4, 5]. This allows us to make a prediction for $H \rightarrow Z\gamma$ based on the fits presented above. As an example, Fig. 6 illustrates how the strong correlation between $H \rightarrow \gamma\gamma$ and $H \rightarrow Z\gamma$ is relaxed when allowing for a non-vanishing $\text{Im}(C_U)$, which affects the $\gamma\gamma$ mode more strongly than the $Z\gamma$ mode.

5 CONCLUSIONS AND OUTLOOK

Using all publicly available results from the LHC and Tevatron experiments, we investigated the extent to which custodial symmetry and CP violation can be tested in a global Higgs coupling fit. We found that the equality between the reduced C_W and C_Z couplings and their compatibility with the SM value of unity hold at 68% CL. However, this analysis does not exclude values of C_W, C_Z greater than 1 and the possibility that the observed H boson contains a component coming from Higgs representations higher than doublets or singlets thus still remains. Moreover, we observed that the present experimental data allows for a sizeable CP-odd contribution, $\text{Im}(C_U)$, in the coupling to the top quark, although the SM still remains compatible with the data at 68% CL. A limit of $1 - C_V^2 < 0.26$ at 95.4% CL has been derived for the CP-odd admixture to the 125.5 GeV observed state. Alternatively, this means that a pure CP-odd component acting as the observed state is excluded at more than 4σ . From the fermionic sector, however, we found that a pure CP-odd component is compatible at the 1σ level with the experimental data while the SM CP-even component lies in the same region as well. In addition, when allowing for a non-vanishing $\text{Im}(C_U)$ we found that the correlation between $\gamma\gamma$ and $Z\gamma$ decay modes is significantly relaxed.

It is important to recognize that the kinds of fits that we have performed on the observed H boson data do not take into account constraints that may be present in the context of particular models. For example, in the case of two Higgs doublet models (2HDMs) plus singlets, the CP-

violating component of the Htt coupling, a_t (Eq. (7)), must be zero if $C_V = 1$. More generally, sum rules [105, 106] imply that the size of a_t is limited by the extent to which C_V deviates from unity. Thus, it could happen that more precise data will yield fits to the properties of the H boson that violate the 2HDM+singlets sum rules, thereby requiring higher Higgs representations, even if $C_V = 1$ with high precision. In any case, in order to discuss fits within a given model context, it is necessary to employ a parametrization of the various C_i of Eq. (1) appropriate to that model, which will automatically guarantee that all sum rules and related constraints are enforced. For 2HDMs, this was done in Ref. [107].

Last but not least we note that two of us are currently developing a new version of our code for fitting the Higgs likelihood, which is entirely written in Python and is intended for public release in Spring 2014 [108]. This new code is modular and has all the experimental results stored in a flexible XML database that includes the full likelihoods in the 2D plane $(\mu_{\text{ggF}+\text{ttH}}, \mu_{\text{VBF}+\text{VH}})$ when available [109, 110, 111] instead of a Gaussian approximation. The new code moreover provides a rather general and user-friendly way of specifying the model input in terms of reduced couplings, or cross sections and branching fractions, or signal strengths directly. In all cases, there is the option to include the effects of invisible or undetected decay modes in the fit.

ACKNOWLEDGEMENTS

This work was supported in part by the PEPS-PTI project “LHC-itools”, by IN2P3 under contract PICS FR–USA No. 5872 and by the US DOE grant DE-SC-000999. J.B. is supported by the “Investissements d’avenir, Labex ENIGMASS”.

Contribution 6

Probing Higgs Physics with Vector-Boson Scattering

A. Belyaev, E. Boos, V. Bunichev, Y. Maravin, A. Pukhov, R. Rosenfeld, M. Thomas

Abstract

We suggest the combination of two main observables which provides a unique sensitivity to the ratio of the longitudinal versus transverse polarizations of the W and Z bosons in the vector-boson scattering processes. Therefore, the analysis we present also provides the sensitivity to the Higgs boson couplings to the gauge bosons and consequently to the theory underlying the Higgs sector. We conclude that the analysis of vector boson fusion provides a model independent and robust method to study the Higgs boson couplings to the gauge bosons.

1 Introduction

The historical discovery of a Higgs-like particle at the LHC [44, 45] ushered a new era in the determination of the properties of the electroweak symmetry breaking (EWSB) sector. Since the longitudinal polarizations of the electroweak gauge bosons (V_L 's, $V = W^\pm, Z$) have their origin in the EWSB sector, determining their interactions, especially in the study of $V_L V_L$ scattering, is of fundamental importance to unravel the mechanism of EWSB. In particular, we now know that $V_L V_L$ scattering is at least partially unitarized by the Higgs-like particle.

This importance has been known for many years. The first calculations of $V_L V_L$ scattering were performed in the context of the so-called Effective W Approximation (EWA) [112, 113, 114] with the use of the Equivalence Theorem (ET) [115], that states that at high energies the amplitudes for $V_L V_L$ scattering can be calculated using the corresponding degrees of freedom in the EWSB sector. The first realistic study of $V_L V_L$ scattering in a strongly coupled EWSB sector but assuming ET and EWA and adopting several unitarization prescriptions were performed in the 1990's [116, 117] (see also [118]). Basic techniques such as as forward jet tagging, central jet vetoing, and cuts on the transverse momenta were introduced to select processes with vector boson fusion (VBF). The first studies that went beyond the EWA performing a complete calculation of WW scattering were [119, 120].

One of the most difficult issues in extracting the physics of EWSB from VV scattering is the so-called transverse pollution, that is, the irreducible background coming from the transversely polarized gauge bosons. Much work has been done to devise cuts that can reduce the transverse pollution and this is the subject of this contribution. Below we start with a brief review of the most recent developments in these efforts.

In the gauge boson rest frame the distribution of transverse and longitudinal polarizations are given by:

$$P_{\pm}(\cos \theta^*) = \frac{3}{8}(1 \pm \cos \theta^*)^2, \quad P_L(\cos \theta^*) = \frac{3}{4}(1 - \cos^2 \theta^*), \quad (1)$$

where θ^* is the angle between the fermion in the decay products and the gauge boson boost to its rest frame. It is worth clarifying the meaning of the the P_{\pm} symbol in connection to the transverse polarisation of the vector boson and the polarisation of the respective fermion from its decay which defines the θ^* angle. The P_+ distribution takes place when the polarisation of the vector boson V and the respective fermion ψ coincide, i.e. P_+ corresponds to the (V_{left}, ψ_{left}) or $(V_{right}, \psi_{right})$ case. On the other hand, the P_- distribution takes place when the polarisation of the vector boson V and the respective fermion ψ are opposite, i.e. P_- corresponds to the (V_{left}, ψ_{right}) or (V_{right}, ψ_{left}) case.

Han *et al.* [121] proposed to directly reconstruct the 4-momenta of the decay products of the gauge boson and hence measure the $\cos \theta^*$ distribution and fit it to

$$P(\cos \theta^*) = f_L P_L(\cos \theta^*) + f_+ P_+(\cos \theta^*) + f_- P_-(\cos \theta^*) \quad (2)$$

with $f_L + f_- + f_+ = 1$. They show that the fit is robust against full hadronization. Doroba *et al.* [122] proposed a new variable to isolate $W_L W_L$ scattering in same-sign WW production. This variable is related to the observation that W_L 's tend to be emitted at smaller angles with respect to the initial quarks and hence the final quarks are more forward. Therefore, they require a small transverse momenta of the forward jets in order to improve W_T rejection. The jet substructure techniques used by Han *et al.* to reconstruct hadronically decaying gauge bosons were recently further improved in [123], where a multivariate W jet tagging method is employed. They also used the cuts suggested by Doroba *et al.* [122]. Freitas and Gainer [124] showed that the significance of the VBF signal can be increased by using the matrix element method but further investigation including showering and detector simulation is still required to quantify their findings. More recently, Chang *et al.* [125] used WW scattering to study the sensitivity to additional Higgs bosons in a complete calculation without relying on EWA, employing the usual selection cuts to maximize the VBF contribution.

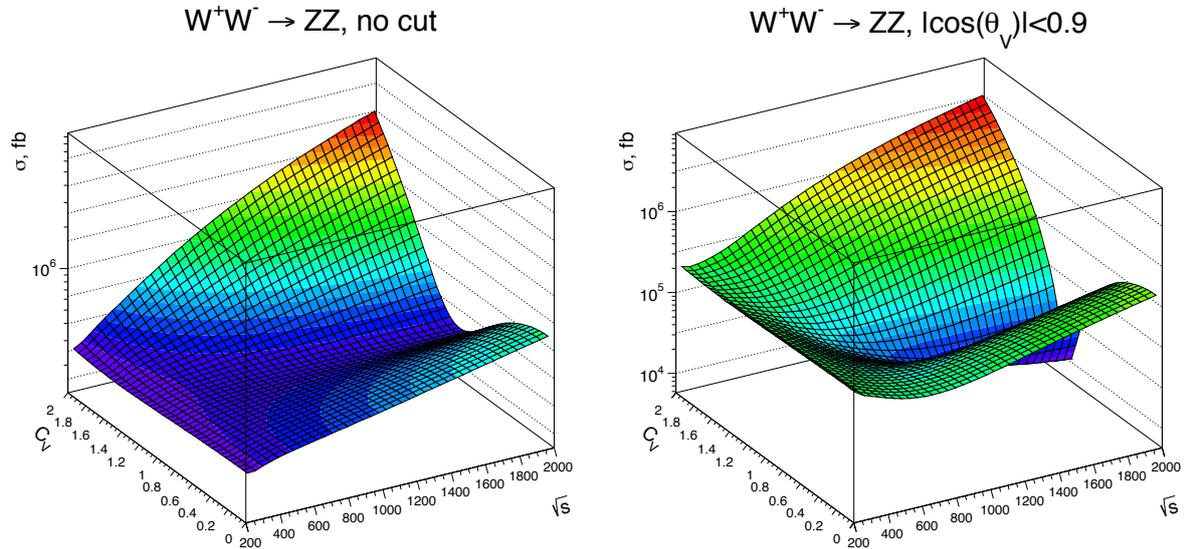


Figure 1: Total $W^+W^- \rightarrow ZZ$ without cuts (left plot) and with $|\cos(\theta_Z)| < 0.9$ (right plot) as a function of center-of-mass energy \sqrt{s} and anomalous coupling c_V .

In this Les Houches contribution, we study the sensitivity of VV scattering to new physics.

We focus on possible deviations of the Higgs coupling to electroweak gauge bosons from its SM value, parameterized by an anomalous coefficient c_V , normalised such that $c_V = 1$ in the SM. This corresponds to adding the contribution of higher dimensional effective operators to the SM lagrangian, such as $\partial_\mu(H^\dagger H)\partial^\mu(H^\dagger H)$ (see, *e.g.*, [47]). The extreme case of a Higgsless case corresponds to $c_V = 0$. In particular, our goal is to devise optimal cuts capable of selecting the contribution from the longitudinally polarized gauge bosons and hence increasing the sensitivity to c_V .

One important point to stress is that the current way to measure c_V is from direct Higgs production in gluon fusion through the decay $H \rightarrow VV^*$, which is somewhat model dependent because of the loop-induced gluon-gluon-Higgs coupling. In contrast, the method proposed here relies only on VV scattering and therefore the measurement of c_V in this case is more model-independent.

In order to motivate our work, we show in the left panel of Fig. 1 the total cross section for $W^+W^- \rightarrow ZZ$ as a function of center-of-mass energy \sqrt{s} and anomalous coupling c_V without any cuts. One can see an increase for $c_V \neq 1$ due to the non-cancellation of the growth with energy of $V_L V_L$ scattering. This behaviour is enhanced when a simple angular cut such as $|\cos(\theta_Z)| < 0.9$ is applied, since it tends to select the longitudinal polarizations, as demonstrated in the right panel of the figure.

This contribution is organized as follows. In the next Section we discuss in a parton level analysis the selection criteria we propose to implement in order to enhance the contribution from the longitudinally polarized gauge bosons. In Section 3 a preliminary analysis is performed to understand whether the efficiency of the proposed criteria survive at the full $2 \rightarrow 6$ level at the LHC. Finally, we conclude the study in Section 4.

2 Analysis at the $VV \rightarrow VV$ level

Let us consider the properties of vector boson scattering in the $VV \rightarrow VV$ process, where $V = W^\pm, Z$. In Fig. 2 we present differential cross section for $VV \rightarrow VV$ process with respect to the scattering angle of the gauge boson V for $\sqrt{s} = 1$ TeV. Due to the t - and u -channels corresponding to the exchange of an electroweak gauge boson (as exemplified in Fig. 3) or a Higgs boson, the angular distributions are peaked in the forward-backward directions, as seen in Fig. 2. The processes on the left plots have symmetric final state and hence the distributions are symmetric, while this is not the case for the right plots. The incoming W^+ boson tends eventually to scatter in the forward direction, as shown in the right plots, and the incoming W^- or Z bosons tend to scatter in the backward direction because of the presence of the t -channel diagrams. In the absence of a Higgs boson ($c_V = 0$), the relative contribution from the longitudinally polarized gauge bosons increases resulting in a larger cross section and an angular distribution less depleted in the central region, as shown by the red curves in Fig. 2. This provides the first important observation: the forward-backward regions in $VV \rightarrow VV$ scattering are mainly related to the transversely polarized gauge bosons while the differences in the longitudinally polarized bosons are mainly pronounced in the central region.

In order to proceed further we decay one of the final state EW bosons and analyse the angular distribution in $\cos\theta^*$ of the charged fermion, which is sensitive to the degree of polarization of the parent EW gauge boson. The results for two different angular cuts in $\cos\theta_V$ are shown in Fig. 4. The difference between the SM and a higgsless model is more dramatic, with a change in the shape of the distributions, and it increases as the angular cut becomes tighter,

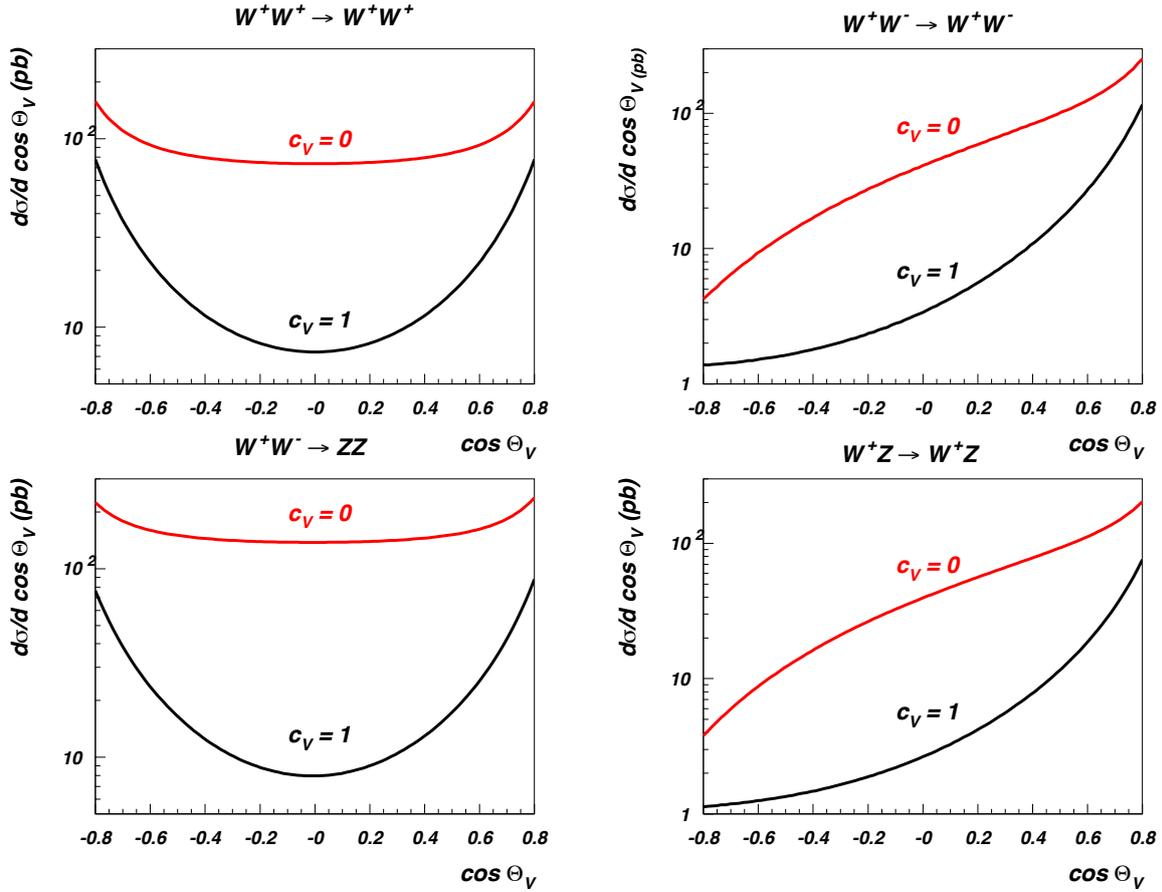


Figure 2: $\cos \theta_V$ angular distributions for $VV \rightarrow VV$ process for $\sqrt{s} = 1$ TeV with (black curves, $c_V = 1$, SM case) and without Higgs boson (red curves, $c_V = 0$).

since we are selecting more longitudinally polarized gauge bosons in this case. This observation makes this variable a very important one to discriminate between longitudinal and transversely polarized gauge bosons. In Fig. 5 we recover the degree of polarization of the parent EW gauge boson by performing a fit using Eq. 2. In the left plot we show that in the higgsless case, one can enrich the fraction of longitudinally polarized gauge bosons by performing cuts on $\cos \theta_V$, at the expense of reducing the number of events of course. In the right plot we show how the fraction of longitudinally polarized gauge boson increases with the center-of-mass energy, reaching almost 100% in the $c_V = 0$ case.

3 LHC sensitivity to longitudinal vector boson scattering and Higgs boson couplings to gauge bosons

In this section we study the LHC sensitivity to probe the fraction of longitudinal polarisation of the gauge bosons produced in the vector boson fusion (VBF), which will provide in turn the sensitivity to the Higgs boson couplings to gauge bosons. In this contribution and in this section in particular we present our study on the process $pp \rightarrow jjZZ \rightarrow e^+e^-\mu^+\mu^-jj$ ($p = u, \bar{u}, d, \bar{d}$, $j = u, \bar{u}, d, \bar{d}$) and the respective LHC sensitivity to HVV coupling.

The matrix element for the complete set of diagrams for this process was evaluated using

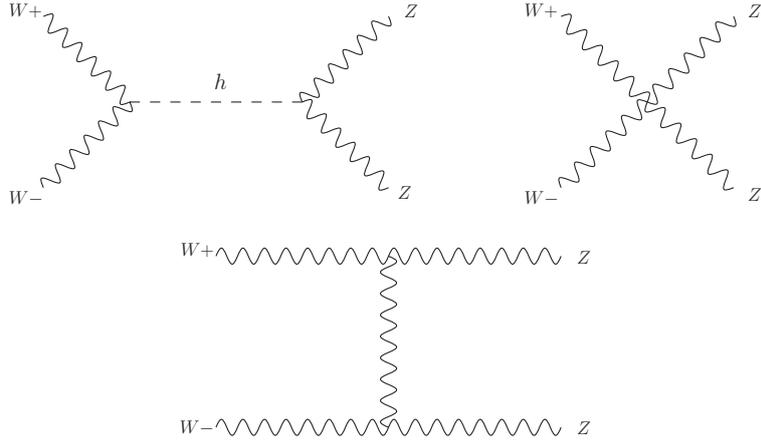


Figure 3: Diagrams contributing to the $W^+, W^- \rightarrow Z, Z$ process.

MADGRAPH package [126], which was also used for the event simulation. For this parton level study we have used the following initial kinematic cuts:

$$\begin{aligned} \text{Acceptance cuts: } p_T^j &> 30 \text{ GeV}, |\eta_j| < 4.5 \\ p_T^e &> 20 \text{ GeV}, |\eta_e| < 2.5 \\ p_T^\mu &> 20 \text{ GeV}, |\eta_e| < 2.5 \end{aligned} \quad (3)$$

$$\text{VBF cuts: [127]} \quad \Delta\eta_{jj} > 4, E_j > 300 \text{ GeV} \quad (4)$$

$$\text{Z boson ID cuts: } |M_{ee,\mu\mu} - M_Z| \leq 10 \text{ GeV} \quad (5)$$

In our calculations we have been using CTEQ6L1 PDF parameterisation and QCD scale fixed to M_Z . The cross section for this process was found to be 0.0298 fb including Higgs boson exchange and 0.0362 fb when Higgs boson contribution was removed. The cross section of this process is quite low since it includes leptonic decay for both Z -bosons. For the case of semi-leptonic decays of Z -bosons, the cross section is about 40 times larger. Moreover one can estimate that including WW and WZ processes with semi-leptonic decay would lead to the event rate which is about a factor of 250 higher than the one mentioned above for $pp \rightarrow jjZZ \rightarrow e^+e^-\mu^+\mu^-jj$. We will keep this in mind when estimating prospect of our results.

For the $pp \rightarrow jjZZ \rightarrow e^+e^-\mu^+\mu^-jj$ processes let us assume an integrated luminosity of 1.5 ab^{-1} , which is being discuss as one of the high luminosity benchmarks at the future LHC13TeV, for which we will have about 50 events from this process for analysis. We start our analysis with a presentation of the invariant mass distribution of the ZZ pair which is derived from the four-lepton invariant mass, M_{4l} , presented in Fig. 6. The left (right) figure presents the M_{4l} distribution for $|\cos\theta_V| < 0.9(0.5)$ cuts respectively. One can see that the $c_V = 0$ distribution presented by the red histogram is visibly above the the $c_V = 1$ distribution presented by the blue histogram. One can also see the slight effect of increasing the $|\cos\theta_V|$ cut from 0.9 to 0.5: the difference between $c_V = 0$ and $c_V = 1$ become bigger especially in the region of higher M_{4l} where the $c_V = 0$ case is enhanced by the longitudinal vector boson scattering process. At the same time the difference between the $c_V = 0$ and $c_V = 1$ cases become slightly smaller in the lower M_{4l} region where the cross section is dominated by the transverse vector boson scattering.

It is also worth clarifying the details of how the angle θ_V of vector boson scattering in the VV mass fame was deduced for the $pp \rightarrow jjZZ \rightarrow e^+e^-\mu^+\mu^-jj$ process. First of

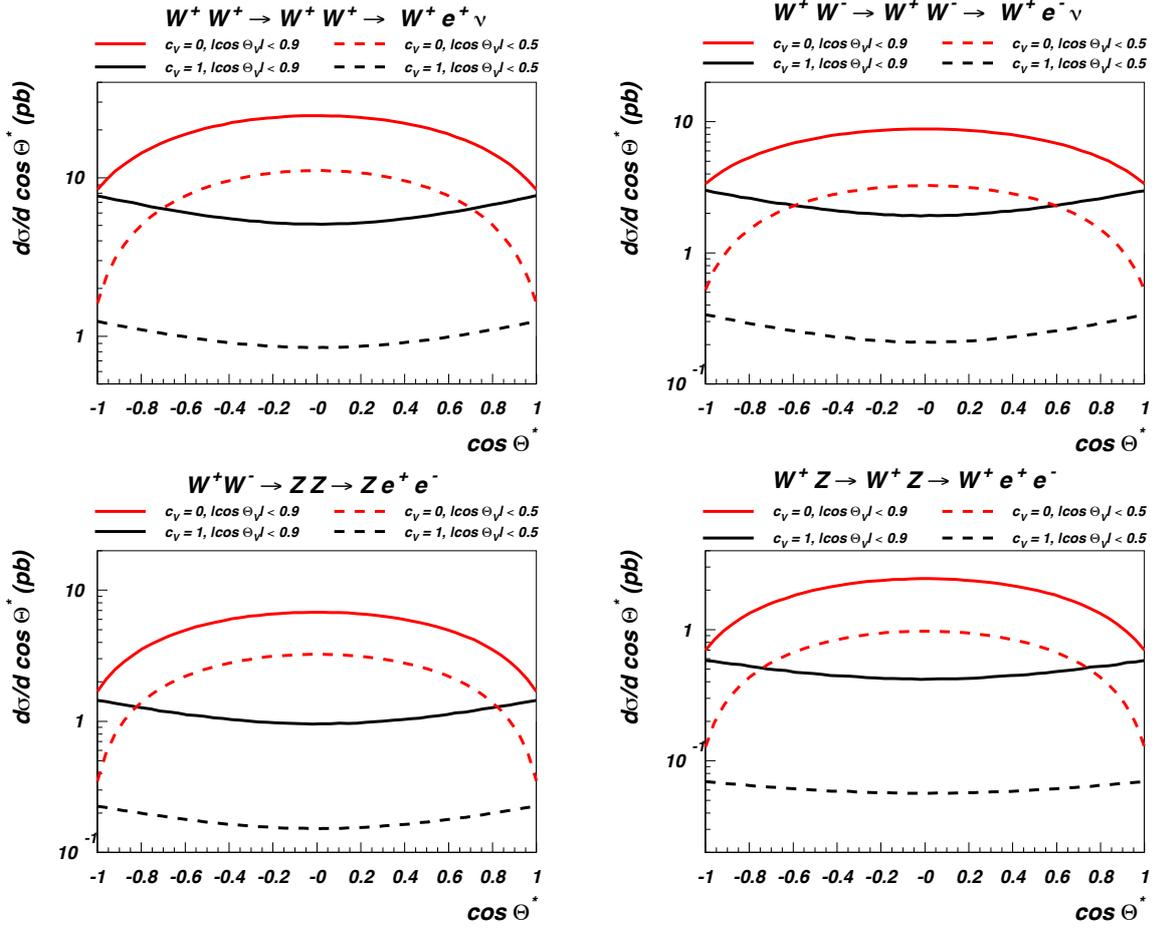


Figure 4: $\cos \theta^*$ angular distributions for $VV \rightarrow VV \rightarrow Vll(Vl\nu)$ process for $\sqrt{s} = 1$ TeV with (black curves, $c_V = 1$, SM case) and without Higgs boson (red curves, $c_V = 0$).

all we find the momenta p_1 and p_2 of the initial quarks q_1, q_2 in the $q_1 q_2 \rightarrow q_3 q_4 ZZ$ process from a) total invariant mass of the final state particles and b) from the total momentum of the final state particle along the z-axis. Then we find two pairs of the final and initial quarks, say, (q_1, q_3) and (q_2, q_4) with the minimal angle between them in the centre-of-mass frame. This will give us access to the four momentum of each virtual vector bosons, p_1^V, p_2^V in the initial state: $p_1^V = q_3 - q_1$ and $p_2^V = q_4 - q_2$ which allows us to calculate the θ_V angle in the centre-of-mass frame of the $VV \rightarrow VV$ scattering.

At the next step we study the ability of a cut on M_{4l} to increase the sensitivity to longitudinal VV scattering and the consequent sensitivity to the HVV coupling. In Fig. 7 we present the effect of the M_{4l} cut on the $\cos(\theta_V)$ distribution by comparing the case when no M_{4l} cut is applied (left) with the distributions after cutting for $M_{4l} > 500$ GeV. One can see the dramatic effect of the M_{4l} cut which aimed to reject events with the transversely polarised scattering which is background in the case of our study. Indeed, after applying the $M_{4l} > 500$ GeV cut one can see that a difference in the middle of the $\cos(\theta_V)$ distribution – i.e. in the central region of the VV scattering between $c_V = 0$ and $c_V = 1$ cases, becomes very pronounced which reproduces the results at the level of $VV \rightarrow VV$ scattering which we found in Section 2

Finally, we perform an analysis of the $\cos(\theta^*)$ distribution and present the respective re-

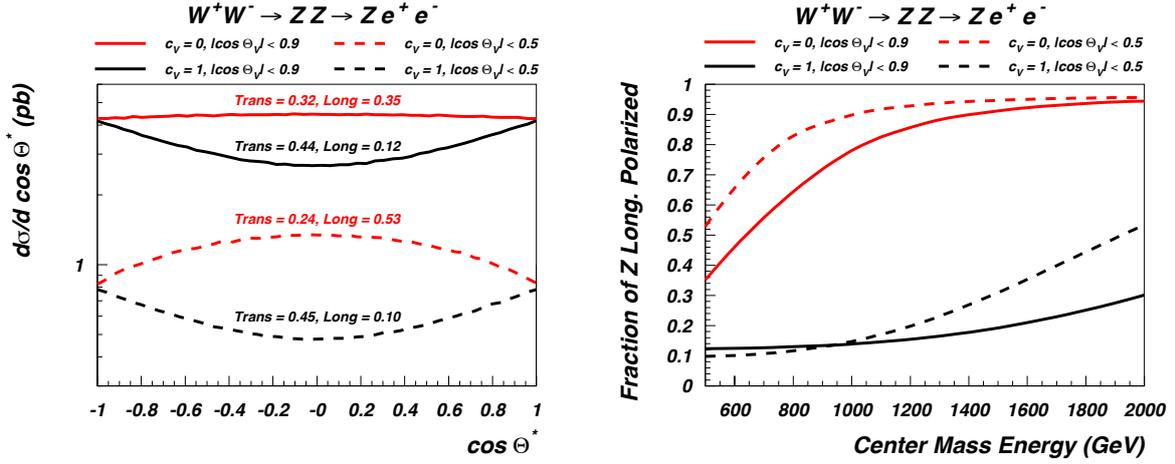


Figure 5: Left: Fitting parameter results of the Z boson polarization at $\sqrt{s} = 0.5$ TeV (Left and Right polarizations were fitted separately but results were identical to accuracy given in plot.) Right: Fraction of the Z bosons which are longitudinal as a function of energy for $c_V = 0, 1$ with $|\cos \theta_V| < 0.9$ and 0.5 .

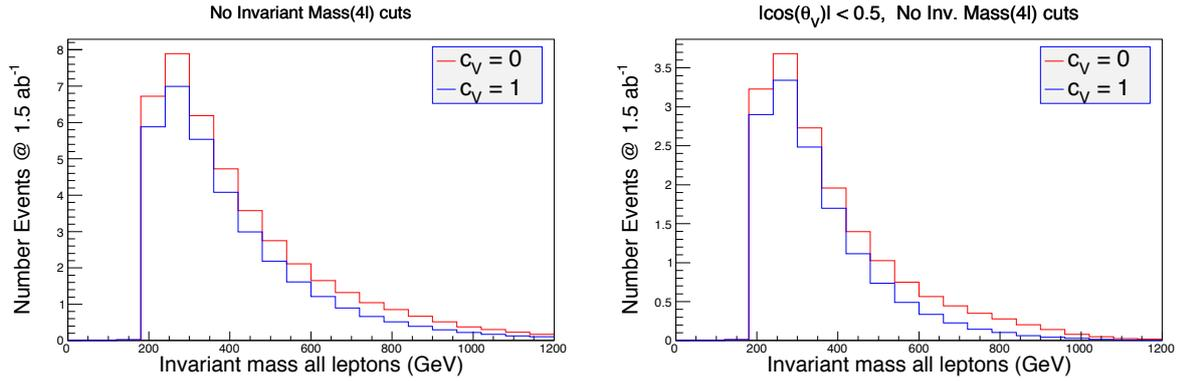


Figure 6: Four-lepton invariant mass distribution, M_{4l} for 1.5 ab^{-1} @LHC13TEV representing the invariant mass of the vector-boson scattering in $pp \rightarrow jjZZ \rightarrow e^+e^-\mu^+\mu^-jj$ process: left (right) frames present the M_{4l} distribution for $|\cos \theta_V| < 0.9(0.5)$ cuts respectively. The red histogram is for $c_V = 0$, the blue one represents $c_V = 0$ (SM) case.

sults in Fig. 8. The $\cos(\theta^*)$ is defined with respect to the electron in the centre-of-mass of the e^+e^- system and the direction of the boost to this system. There are four frames in Fig. 8 presenting $\cos(\theta^*)$ distributions for four different cases of kinematic cuts, aimed to consequently increase the fraction of the longitudinal polarisation of the Z -bosons in the $c_V = 0$ case and enhance the difference between the $c_V = 0$ and $c_V = 1$ cases: a) $|\cos(\theta_V)| < 0.9$; b) $|\cos(\theta_V)| < 0.5$; c) $|\cos(\theta_V)| < 0.9$ and $M_{4l} > 500$ GeV; d) $|\cos(\theta_V)| < 0.5$ and $M_{4l} > 500$ GeV. For each case we fit the $\cos(\theta^*)$ distribution using the standard fitting routines of ROOT package [128], and for each of $c_V = 0$ and $c_V = 1$ we find the fraction of the longitudinal and transverse Z -bosons. One can see that the $\cos(\theta_V)$ cut has a much smaller effect than the M_{4l} cut on enhancing the sensitivity to the difference between the $c_V = 0$ and $c_V = 1$ cases. Among the four cuts, the biggest difference between the fraction of the longitudinally polarised (LP) Z -bosons

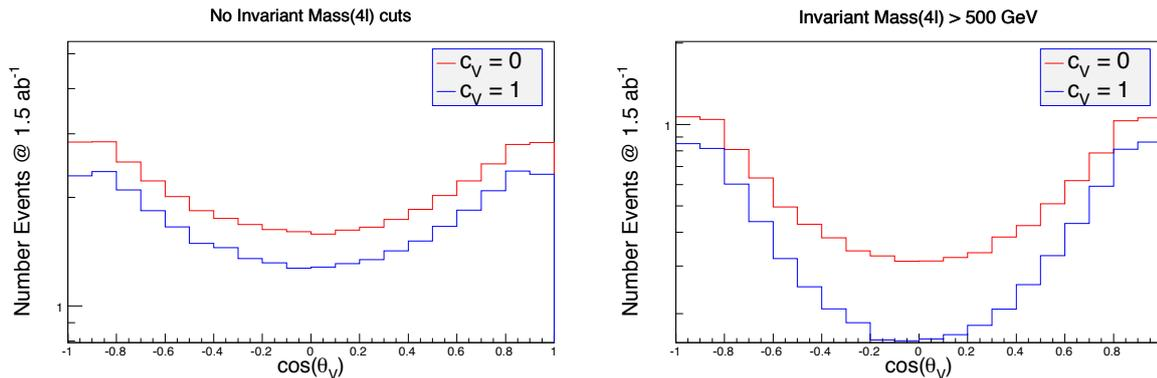


Figure 7: The $\cos(\theta_V)$ distribution for 1.5 ab^{-1} @LHC13TEV for $pp \rightarrow jjZZ \rightarrow e^+e^-\mu^+\mu^-jj$ process. Left: no M_{4l} cut applied, Right: the distributions after $M_{4l} > 500 \text{ GeV}$ cut.

for $c_V = 0$ and $c_V = 1$ is for the cut d): the fit gives $\text{LP}=0.34$ for $c_V = 0$ and $\text{LP}=0.05$ for $c_V = 1$ (SM). At the same time due to the lack of statistics, the fit error (which we do not present in plots), is quite large: it varies from about 100% for cut a) statistics to around 300% in case of cuts d) statistics where the events rate is reduced by factor of 9. At the same time we should stress that including semi-leptonic channels as well as a complete set of processes — ZZ, WW, WZ — will increase the statistics by a factor of about 250, which will decrease the statistical fit error down to about 2.5% level for 1.5 ab^{-1} integrated luminosity and to about 10% even for 100 fb^{-1} integrated luminosity. The sensitivity to c_V parameter is eventually expected to be similar. Moreover the optimisation of the M_{4l} and $\cos(\theta_V)$ cuts as well as involving the total cross section as another variable for discrimination of different c_V scenarios will be able to improve the accuracy of the c_V measurement even further.

4 Conclusions

In this contribution we present our preliminary results of the LHC sensitivity to the HVV couplings via the vector boson fusion process. This sensitivity is *independent* of that which can be deduced from direct Higgs searches at the LHC. Moreover, the measurement of the HVV coupling ($V = Z, W^\pm$) is not quite trivial from direct searches: it is derived from several production processes and it depends on all other Higgs couplings, including couplings to new particles. However only one Higgs coupling, HVV , enters the VBF process, so it could be measured in a much more model-independent way from VBF process.

The VBF process provides a unique sensitivity to the HVV coupling since the Higgs boson provides a unitarisation of the $VV \rightarrow VV$ amplitudes, so any deviation from $c_V = 1$ will lead to an enhancement of the cross section of the longitudinal VV scattering. We have found an important correlation of the longitudinally polarised vector boson fraction (FL) and the vector boson scattering angle θ_V in the VV centre-of-mass frame and well as a FL correlation with the invariant mass of the VV system, M_{VV} . Using a combination of θ_V , M_{VV} and θ^* observables for the $pp \rightarrow jjZZ \rightarrow e^+e^-\mu^+\mu^-jj$ process, chosen as an example for this preliminary study, we have performed a fit of the θ^* distribution to find the FL value, and have demonstrated an important sensitivity of the VBF to the HVV coupling given that statistics will be high enough.

For a combination of semi-leptonic channels as well as complete set of processes —

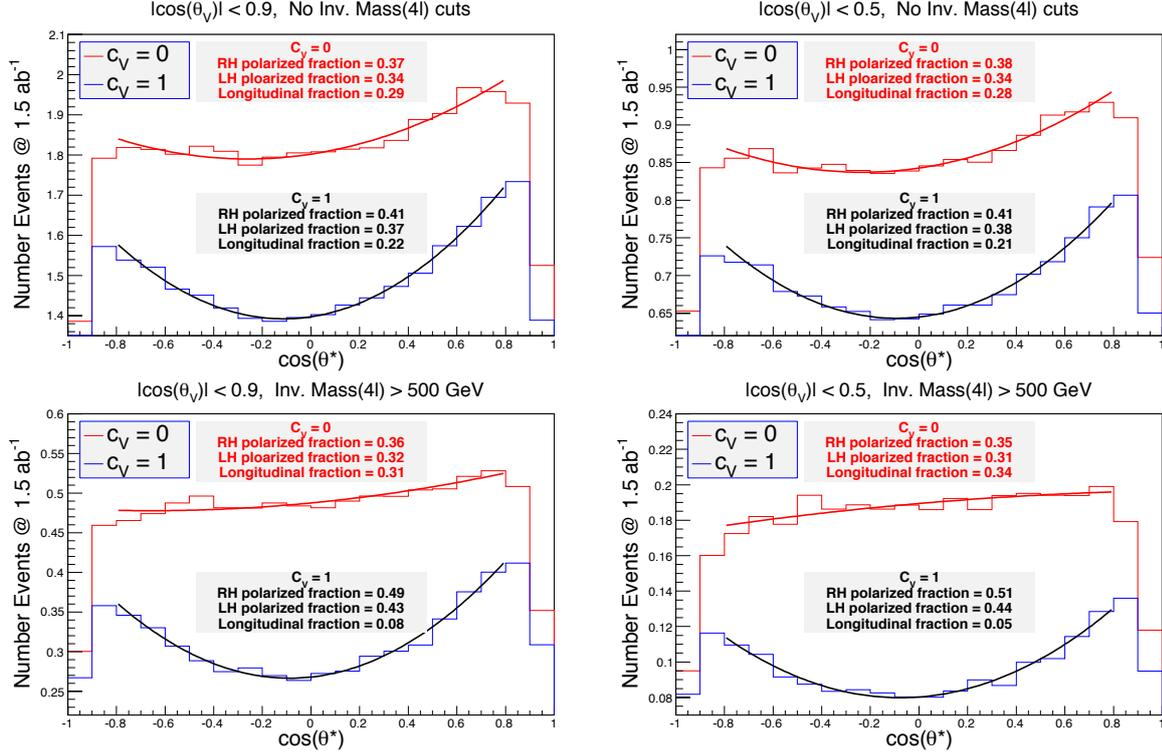


Figure 8: The $\cos(\theta^*)$ distribution for $pp \rightarrow jjZZ \rightarrow e^+e^-\mu^+\mu^-jj$ process for 1.5 ab^{-1} @LHC13TEV for four different sets of cuts: a) (top-left) $|\cos(\theta_V)| < 0.9$; b) (top-right) $|\cos(\theta_V)| < 0.5$; c) (bottom-left) $|\cos(\theta_V)| < 0.9$ and $M_{4l} > 500 \text{ GeV}$ d) (bottom-right) $|\cos(\theta_V)| < 0.5$ and $M_{4l} > 500 \text{ GeV}$.

ZZ, WW, WZ — which will increase statistics by a factor about 250, one could expect VBF sensitivity to the c_V coupling at a level of 10% or better even with 100 fb^{-1} @LHC13TEV.

One should also note that VBF provides not only an independent and precise way to measure the HVV coupling, but it is also robust against systematic errors since it relies not only on the absolute cross section measurement but also on the *shape* of the $\cos(\theta^*)$ distribution.

Acknowledgements

We thank the Les Houches workshop organisers for an unprecedentedly creative atmosphere which allowed us to generate ideas for this contribution. We acknowledge the use of IRIDIS HPC Facility at the University of Southampton for this study. AB is supported in part by the NExT Institute and MCT is supported by an STFC studentship grant. RR is supported in part by grants from CNPq and Fapesp. EB, VB, and AP are partially supported by RFBR grant 12-02-93108 and NSh grant 3042.2014.2.

Contribution 7

Probing the Structure of Top-Higgs Interactions at the LHC

F. Boudjema, R. Godbole, D. Guadagnoli, K. Mohan

Abstract

We investigate the methods to explore the nature of the $t\bar{t}h$ coupling at the LHC. To that end we focus on the associated production of the Higgs boson with a $t\bar{t}$ pair. We analyze the feasibility of this process for determining the CP properties of the coupling of the Higgs boson to the top quark. We first show the constraints implied by the Higgs rates from the currently available LHC data. We then focus on specific kinematic observables that can be used to determine the coupling itself.

1 Introduction

The 7-8 TeV runs of the LHC have led to the discovery of a 125 GeV boson [45, 44, 97, 90]. The properties measured so far show very good consistency with those expected for the Standard-Model (SM) Higgs boson. Despite the fact that these runs have not revealed any sign of physics beyond the SM (in particular, production of new particles), the fact remains that the SM cannot address a few pressing questions, such as the baryon asymmetry of the universe, nor does the SM provide a candidate for Dark Matter. These issues call for New Physics. Furthermore, the observation of a 125 GeV boson as well as the absence so far of New Physics at the TeV scale form a puzzle from the point of view of Naturalness. Probing the Higgs sector is therefore of utmost importance, and crucial is in particular a precise determination of its couplings to other particles. One of the most important couplings of the Higgs boson is to the top quark, the heaviest SM particle. Not only is this coupling responsible for the main production channel of the SM Higgs boson at the LHC but the interaction with the top quark also has important consequences on spontaneous symmetry breaking within the SM – notably, vacuum stability arguments – as well as beyond the SM – supersymmetry, for instance, where the top quark drives electroweak symmetry breaking in some scenarios. Yet a *direct* measurement of the Higgs-top coupling is lacking.

In this note, we focus our attention on the possibility of a direct determination of the Higgs-top coupling. The Higgs-top coupling can generally be parametrized in the form

$$\mathcal{L}_{t\bar{t}h} = g_{t\bar{t}h} \bar{t}(a + ib\gamma_5)\phi t, \quad (1)$$

where $g_{t\bar{t}h} = m_t/v$ normalizes the coupling to the SM strength. The coefficients a and b are assumed to be real. In the SM, where the Higgs boson is a scalar, $a = 1$ and $b = 0$. For a pure pseudoscalar $a = 0$ and $b \neq 0$. A Higgs boson with mixed CP properties is realized if both $a \neq 0$ and $b \neq 0$. The exact values of these coefficients will depend on the specific model. Here we are interested in a model-independent approach to determine the nature of the interaction from data.

Note that the electron and neutron dipole moments [129] as well as the decay and production rates of the Higgs boson measured at the LHC [93, 130] provide important constraints on the strength of the a, b coefficients in Eq. (1). However, an unambiguous determination of them is only possible by measuring directly Higgs production in association with a top and anti-top quark ($t\bar{t}h$ production). In order to illustrate this point, in the following section we determine the constraints that Higgs rates can place on a and b using currently available data. We then proceed to analyze $t\bar{t}h$ production at LHC and construct some observables that could be used to determine the nature of the $t\bar{t}h$ interaction itself.

2 Indirect probes of an anomalous $t\bar{t}h$ coupling

Within the SM, and with Higgs and top masses as measured, there are four main production modes of the Higgs boson at the LHC: gluon fusion, vector-boson fusion (VBF), Higgs production in association with a W/Z boson (VH) and Higgs production in association with a $t\bar{t}$ pair. The gluon-fusion production mode has the largest cross-section at the LHC, and the dominant contribution to this process comes from a top loop. The Higgs decay to two photons has also a contribution due to a top loop, although the dominant one comes from a W -boson loop. ATLAS and CMS have already put indirect constraints on the value of a , assuming that there are no other sources contributing to the effective couplings $gg \rightarrow h$ or $h \rightarrow \gamma\gamma$. At 95% confidence level these constraints read [90, 131]

$$\begin{aligned} a &\in [-1.2, -0.6] \cup [0.6, 1.3] && \text{ATLAS,} \\ a &\in [0.3, 1.0] && \text{CMS.} \end{aligned}$$

In the rest of this section we extend this analysis by allowing in the fit both a and b couplings in Eq. (1). As customary, the signal strength measured in a particular channel i at the LHC is defined as

$$\hat{\mu}_i = \frac{n_{exp}^i}{(n_S^i)^{SM}}, \quad (2)$$

where n_{exp}^i is the number of events observed in the channel i and $(n_S^i)^{SM}$ is the expected number of events as predicted in the SM. In order to contrast specific model predictions with the experimentally derived $\hat{\mu}_i$ we define (as usual)

$$\mu_i = \frac{n_S^i}{(n_S^i)^{SM}} = \frac{\sum_p \sigma_p \epsilon_p^i}{\sum_p \sigma_p^{SM} \epsilon_p^i} \times \frac{BR_i}{BR_i^{SM}}. \quad (3)$$

Here n_S^i corresponds to the expected number of events predicted in the hypothesized model under consideration; σ_p corresponds to the cross-section in the p^{th} production mode, i.e. the cross-section for Higgs production in one of the four production modes listed earlier; BR_i is the branching ratio of the Higgs boson in the i^{th} channel; ϵ_p^i is the efficiency of the p^{th} production mode to the selection cuts imposed in the i^{th} channel. Note that the efficiencies in the numerator and denominator of Eq. (3) are taken to be the same. This is true at leading order for the gluon fusion process.

Besides direct $t\bar{t}h$ production, which will be discussed separately in the next section, the a and b couplings contribute to two main quantities, namely Higgs production from a gluon-gluon pair and Higgs decay into two photons. We discuss these quantities in turn. The ratio of the

decay width of the Higgs boson to two photons to the SM decay width, at leading order and neglecting the small contribution from lighter fermions, can be written in the form [5]

$$\frac{\Gamma(h \rightarrow \gamma\gamma)}{\Gamma(h \rightarrow \gamma\gamma)^{SM}} = \frac{|\kappa_W A_W^a(\tau_W) + a \frac{4}{3} A_t^a(\tau_t)|^2 + |b \frac{4}{3} A_t^b(\tau_t)|^2}{|A_W^a(\tau_W) + \frac{4}{3} A_t^a(\tau_t)|^2}. \quad (4)$$

Here A_j^i corresponds to the form factors defined below

$$\begin{aligned} A_t^a(\tau) &= \frac{2}{\tau^2}(\tau + (\tau - 1)f(\tau)), \\ A_W^a(\tau) &= -\frac{1}{\tau^2}(2\tau^2 + 3\tau + 3(2\tau - 1)f(\tau)), \\ A_t^b(\tau) &= \frac{2}{\tau}f(\tau) \end{aligned} \quad (5)$$

with $\tau_i = \frac{m_h^2}{4m_i^2}$ and

$$f(\tau) = \begin{cases} \arcsin^2 \sqrt{\tau} & \text{for } \tau \leq 1 \\ -\frac{1}{4} \left[\log \frac{1+\sqrt{1-\tau^{-1}}}{1-\sqrt{1-\tau^{-1}}} - i\pi \right]^2 & \text{for } \tau > 1 \end{cases}. \quad (6)$$

κ_W is a multiplicative factor that rescales the SM $HW^\mu W_\mu$ coupling (for the SM $\kappa_W = 1$). Similarly, for Higgs boson production through gluon fusion, neglecting the small b -quark contribution and at leading order, one could write

$$\frac{\sigma(gg \rightarrow h)}{\sigma(gg \rightarrow h)^{SM}} = \frac{\Gamma(h \rightarrow gg)}{\Gamma(h \rightarrow gg)^{SM}} = a^2 + b^2 \frac{|A_t^b(\tau_t)|^2}{|A_t^a(\tau_t)|^2}. \quad (7)$$

Combining both ATLAS and CMS data [90, 132, 133, 134, 135, 136] we determine the best-fit values of a and b by minimizing the χ^2 defined as

$$\chi^2 = \sum_{i=(p,d)} \frac{(\mu_i - \hat{\mu}_i)^2}{(\sigma_i^{exp})^2}, \quad (8)$$

where the sum is over each of the production (ggF, VBF, Vh, tth) and decay ($h \rightarrow ZZ^*$, WW^* , $\gamma\gamma$, $b\bar{b}$, $\tau\tau$) modes and σ_i^{exp} is the experimental error. We adopt this Gaussian approximation rather than a full-fledged likelihood analysis, since our objective is to obtain approximate allowed ranges for non-SM couplings. Note that our fits for a alone are in reasonable agreement with ATLAS and CMS fits, and that we have not taken into account recent data on $t\bar{t}h$ production [137, 138, 139, 140, 141] and we do plan on doing so in the future. However the large errors these measurements come with imply that they will not strongly affect the fit. The fit results are displayed in Fig. 1, with the 1, 2 and 3σ regions being shown in orange, green, and blue respectively. The best-fit point is given by the black dot. While the a coupling is constrained fairly well, already within this limited amount of data, it is immediately evident that the constraint to the pseudoscalar coupling to fermions, b , is still fairly loose. Values of $|b|$ even above 2 are still allowed.

These results can be easily understood by looking at Eqs. (4) – (7). In $gg \rightarrow h$ the a and b coefficients enter quadratically, weighed by the loop functions A_t^a and A_t^b respectively. Therefore, while $gg \rightarrow h$ production is useful to constrain the overall $|a|^2$ and $|b|^2$ magnitudes,

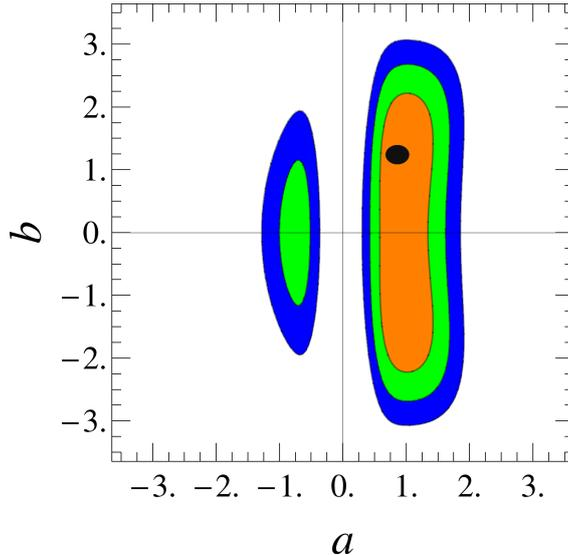


Figure 1: Two-dimensional fit to the Higgs-top couplings a and b in Eq. (1) using Higgs decay and production rates from ATLAS and CMS data.

it is unable to distinguish a versus b effects. Including the $h \rightarrow \gamma\gamma$ decay channel substantially improves the discriminating power. The important point is that, in this decay channel, the scalar-coupling contribution, contrary to the pseudoscalar contribution, interferes with the W boson contribution. In particular, for $a > 0$, as in the SM, this interference is destructive. On the other hand, for a negative, the branching ratio gets enhanced with respect to the SM by both the scalar and the pseudoscalar contributions, thus making $\Gamma(h \rightarrow \gamma\gamma)$ too large. This is the reason why the $a > 0$ and $a < 0$ allowed regions are completely separated in Fig. 1, and why the $a < 0$ allowed region is smaller. Specifically, $a = 0$ does not fit the data either because in this case the W loop is too large and cannot obviously be compensated by the b contribution, irrespective of the value of b . In conclusion, from these data alone the constraints on b are expected to be (and remain) much looser than those on a , as confirmed by our Fig. 1.

One must therefore resort to a more direct approach to determine the Higgs-top coupling, also to exclude the presence of additional contributions not accounted for by a and b . This will be discussed in the following section.

3 Associated production of the Higgs with a $t\bar{t}$ pair

Of the four production modes ($gg \rightarrow h; Vh; VV \rightarrow h; t\bar{t}h$, with $V = W^\pm, Z$) of the Higgs boson at the LHC, $t\bar{t}h$ production has the smallest cross-section. The complicated final state of the process, with the top quark decaying to a bottom quark and a W boson, which in turn may decay either hadronically or leptonically, and the large backgrounds to the process make this a difficult channel to study at the LHC. However, as accentuated in the discussion in the previous section, $t\bar{t}h$ production is necessary, among the other reasons, in order to unambiguously determine the parity of the Higgs coupling to the top quark.

In this section we wish to point out the major differences that a scalar versus a pseudoscalar coupling case entails for $t\bar{t}h$ production at the LHC. As a first step we consider observables suitable for the dileptonic decay mode, i.e. with both the top and anti-top quarks decaying leptonically. We will comment on analogous observables that can be constructed for other decay

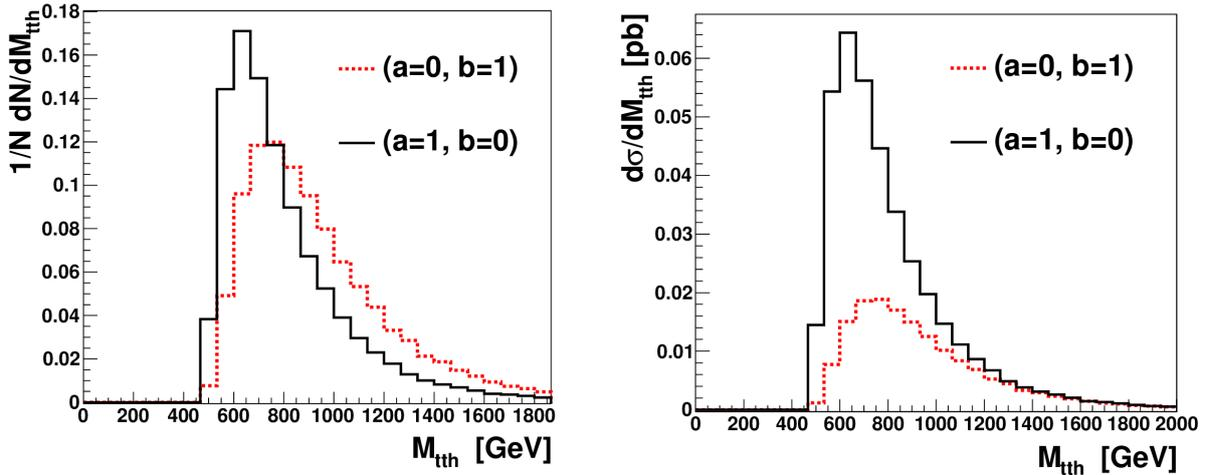


Figure 2: (Left panel) The invariant-mass distribution of the $t\bar{t}h$ system, normalized to unity. (Right panel) The differential cross-section with respect to the invariant mass distribution of the $t\bar{t}h$ system.

modes of the top.

The first distribution we consider is the production cross-section near threshold. It has been pointed out that the threshold behavior of the cross-section for a scalar versus a pseudoscalar Higgs boson is very different at an e^+e^- collider [142, 143, 144]. More specifically, the *rate* of increase of the cross-section with the centre of mass energy of the collision is suppressed in the case of the pseudoscalar Higgs coupling by a factor of ρ , where $\rho = (\sqrt{s} - 2m_t - m_h)/\sqrt{s}$ parametrizes the proximity to the production threshold. This factor can be easily understood from arguments of parity and angular-momentum conservation [144]. The same behavior is observed in the quark-initiated process of a pp collision, which is a spin-1, s -channel mediated process, but this contribution is negligible at the LHC. This being said, the dominant gg -initiated Higgs-production cross-section does also exhibit a faster rise at threshold for the scalar than for the pseudoscalar case, even if this rise is not as pronounced as in the case of s -channel spin-1 production. Similar considerations on parity and orbital angular momentum hold here, the difference being that more partial waves contribute in the gg -initiated process.

In the left panel of Fig. 2 we show the normalized invariant mass distributions of the $t\bar{t}h$ system for the pseudoscalar ($a = 0, b = 1$) and scalar ($a = 1, b = 0$) cases. We see that the rate of increase of the cross-section with the invariant mass of the $t\bar{t}h$ system is much more rapid for the scalar than for the pseudoscalar case. This is an important distinguishing feature and could be used to probe the nature of the Higgs-top quark coupling. The right panel of Fig. 2 shows the same distribution, but normalized to the total cross-section (i.e. $d\sigma/dM_{t\bar{t}h}$). We observe that for the same magnitude of the coupling strength, the cross-section for the pseudoscalar case is suppressed in comparison to scalar $t\bar{t}h$ production.

Looking at the form of the Lagrangian in Eq. (1) one expects that the nature of the Higgs-top coupling should also affect spin correlations between the top and anti-top quarks, which in turn are passed on to the kinematic distributions of their decay products. In Fig. 3 we show $\Delta\phi^{\bar{t}\bar{t}}(\ell^+, \ell^-)$, defined as the difference between the azimuthal angle of the ℓ^+ momentum in the rest frame of the top quark and the azimuthal angle of the ℓ^- momentum evaluated in the

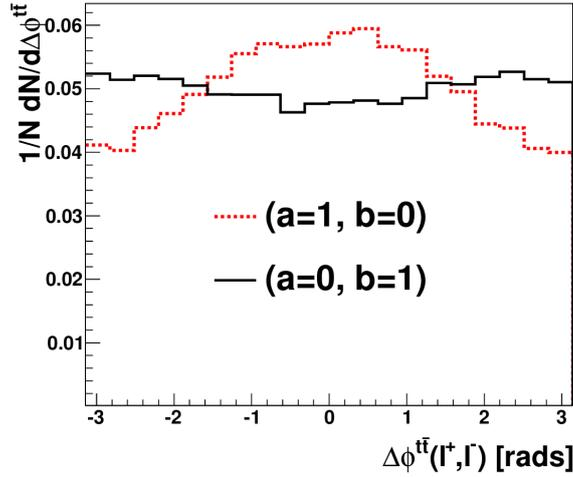


Figure 3: Difference in the azimuthal angles of the lepton momenta, with the ℓ^+ momentum evaluated in the rest frame of the top quark and the ℓ^- momentum evaluated in the rest frame of the anti-top quark.

rest frame of the anti-top quark [145]¹. It is evident that the information about the nature of the coupling is indeed encoded in the t and \bar{t} polarizations and hence in the spin correlations between them. Such an angle is however hard to reconstruct, in particular because it requires reconstruction of the top and anti-top momenta in presence of two escaping particles (the ν 's). We therefore explore a similar observable in more convenient frames.

Results are presented in Fig. 4. The left panel shows the azimuthal angle difference between the ℓ^+ and ℓ^- with the lepton momenta evaluated in the rest frame of the Higgs boson. The right panel shows the azimuthal angle difference between the top and anti-top ($\Delta\phi(t, \bar{t})$) quarks evaluated in the lab frame. These observables are more straightforward to reconstruct at the LHC. Furthermore, it is easy to find proxies of these distributions suitable for hadronic and semi-leptonic decays of the top quark. In particular, in semileptonic or fully hadronic decays one may replace one or respectively both leptons with the parent W boson, and define azimuthal-angle observables accordingly, namely as $\Delta\phi(W^\pm, \ell^\mp)$ for the semileptonic case, and $\Delta\phi(W^\pm, W^\mp)$ for the hadronic case, with momenta evaluated in the rest frame of the Higgs boson. Although not shown here, we have checked that these distributions are similar to the dilepton distribution shown in Fig. 4.

¹In constructing the ℓ^\pm momenta as described, we keep fixed for all events the choice of the x and y axes, and the z axis is chosen, as customary, to lie along the beam direction. While individually the azimuthal angles for the ℓ^+ and ℓ^- momenta do depend on the choice of the x and y axes, their difference, as in $\Delta\phi$, does not. $\Delta\phi$ depends only on the choice of the beam axis. One can construct $\Delta\phi$ from the following formula

$$\cos(\Delta\phi^{t\bar{t}}(\ell^+, \ell^-)) = \frac{(\hat{z} \times \vec{p}_{\ell^-}^{\bar{t}}) \cdot (\hat{z} \times \vec{p}_{\ell^+}^t)}{|\vec{p}_{\ell^-}^{\bar{t}}| |\vec{p}_{\ell^+}^t|}, \quad (9)$$

that shows dependence only on the \hat{z} direction. In this formula, the superscripts t (\bar{t}) indicate that the given momentum is calculated in the rest frame of the t (\bar{t}). Analogous relations apply for the other $\Delta\phi$ definitions to follow.

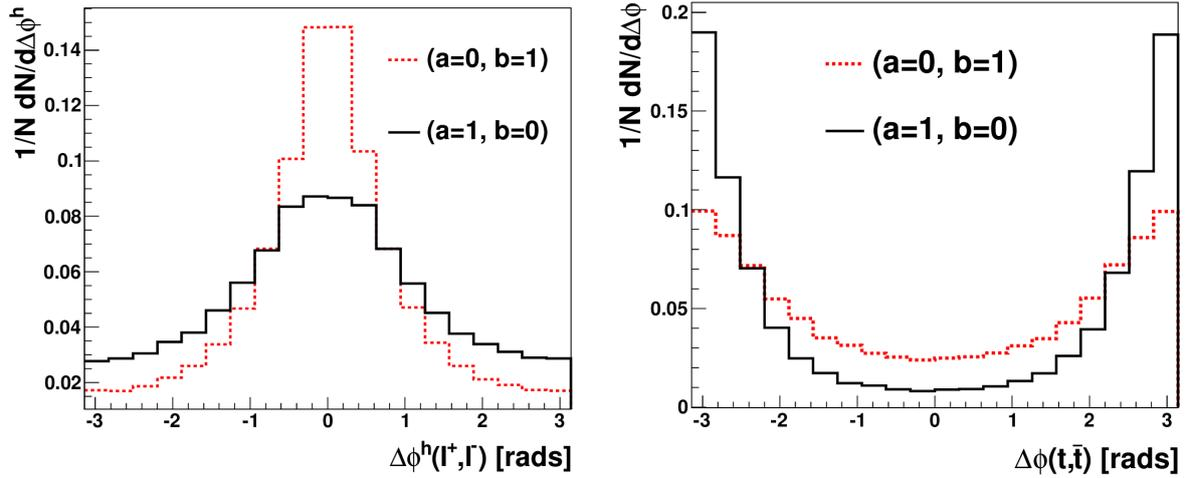


Figure 4: (Left panel): Difference in the azimuthal angles of the lepton momenta, with both momenta evaluated in the rest frame of the Higgs boson. (Right panel): Azimuthal angle difference between the top and anti-top quarks in the lab frame.

Conclusions

We have considered the general Higgs-top quark coupling and have explored the possibility to probe this coupling in a model-independent framework. We find that the information provided by the Higgs rates does not suffice to provide conclusive evidence about the nature (scalar versus pseudoscalar) of the coupling. One must therefore resort to a more direct method of probing the coupling. We investigated some of the possible kinematic observables that could be used to this end. We find that the information about the nature of the coupling is encoded in the threshold behaviour of the cross-section as well as in kinematic distributions that reflect the $t\bar{t}$ spin correlations, which are affected by the parity of the $t\bar{t}h$ coupling. We also note that it is possible to extract information about this coupling by using these distributions to construct asymmetries.

Acknowledgements

KM acknowledges the financial support from CSIR India, the French CMIRA and ENIGMASS Labex and LAPTh, Annecy-le-Vieux for hospitality while part of this work was done. RG wishes to thank the Department of Science and Technology, Government of India, for support under grant no. SR/S2/JCB-64/2007.

Contribution 8

A Realistic Analysis of Non-Resonant BSM Higgs Pair Production

A. J. Barr, M. J. Dolan, C. Englert, M. M. Mühlleitner, M. Spannowsky

Abstract

After the Higgs boson discovery the question of the relation of the symmetry breaking potential to the TeV scale is more pressing than ever. Models that invoke the notion of TeV-scale compositeness are potential solutions that interpret the Higgs boson as a pseudo-Nambu-Goldstone mode of a strongly interacting sector that allows to postpone the hierarchy problem to a higher scale. In these scenarios the Higgs potential, induced by a Coleman-Weinberg type mechanism, can be dramatically different from the Standard Model (SM). Multi-Higgs production provides the only direct avenue to analyze the Higgs potential directly. We therefore perform a realistic hadron-level analysis of the di-Higgs final state in the $b\bar{b}\tau^+\tau^-$ channel for the representative MCHM4 benchmark model, that makes new physics contributions to di-Higgs production most transparent.

1 Introduction

The end of Run I of the LHC has left a changed landscape in particle physics, which theorists are still coming to terms with. The discovery of the Higgs boson with mass 125 GeV [44, 45] has provided final confirmation of the realisation of the Higgs mechanism, in the process obliterating any number of Higgsless theories constructed by theorists. At the same time, and despite a multitude of searches performed by the ATLAS and CMS experiments, no evidence of Beyond-the-Standard-Model (BSM) physics has yet emerged from the LHC. However, according to the vague dictates of the naturalness criterion signs of BSM physics should emerge at the higher energies available in Run II: new states are expected around the TeV scale in order to solve the hierarchy problem. Along with softly-broken supersymmetry, new strong interactions are the only other construction which can solve the hierarchy problem in a way which leads to testable predictions. One of the most prominent among these scenarios is the interpretation of the observed Higgs boson as a Pseudo-Nambu Goldstone of a strongly-interacting sector [146, 147, 148, 149, 150, 151].

A generic prediction of such models is the existence of new resonances which are partners of the Standard Model top quark. These can drastically alter Higgs phenomenology. In the first instance, the top partners can propagate in the one-loop triangle diagram associated with Higgs production from gluon fusion. However, composite Higgs models also predict the existence of higher dimensional $HHt\bar{t}$ interactions whose effects can only be accessed in di-Higgs production. Multi-Higgs production thus emerges as one of the most attractive means of probing the composite Higgs scenario. In this contribution to the Les Houches proceedings we study the di-

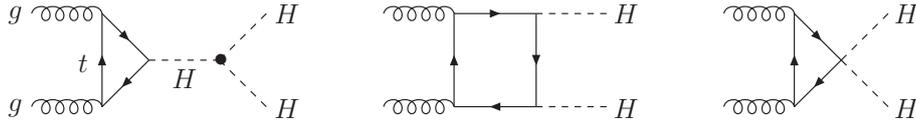


Figure 1: Representative Feynman diagrams entering double Higgs production in MCHM4.

Higgs phenomenology and LHC14 prospects of one particular realisation of the Pseudo-Nambu Goldstone-ism (pNG) paradigm, the so-called MCHM4 model which we now briefly discuss.

2 The Model

Composite Higgs models are based upon the idea that the Higgs boson could be a bound state of a strongly interacting sector rather than a fundamental scalar. Such a state can be naturally lighter than the other states associated with the strongly interacting sector if the Higgs is the pNG of a large global symmetry \mathcal{G} associated with the strong dynamics which is then dynamically broken to a smaller subgroup \mathcal{H} at a scale f . The SM gauge group $SU(2)_L \times U(1)_Y$ is then gauged into \mathcal{H} , and the coset \mathcal{H}/\mathcal{G} is required to contain an $SU(2)_L$ doublet, which can be associated with the SM Higgs boson. The Higgs potential is generated at loop-level and breaks electroweak symmetry. Deviations from SM Higgs phenomenology are parametrised by the dimensionless quantity $\xi = v/f$, with the SM-like behaviour being realised in the limit $\xi \rightarrow 0$ (and infinitely heavy top partners). A recent review of the status of composite Higgs models can be found in Ref. [152].

The simplest such model is given by a strong sector with the gauge symmetry $\mathcal{G} = SO(5) \times U(1)_X$ which is broken down to $\mathcal{H} = SO(4) \times U(1)_X$. Since $SO(4)$ is isomorphic to $SU(2)_L \times SU(2)_R$ the SM gauge group $SU(2)_L \times U(1)_Y$ can easily be embedded. In the minimal composite Higgs model MCHM4 [153] the Standard Model fermions transform as spinorial representations of $SO(5)$. This leads to *universal* rescalings of all the Higgs couplings and of the trilinear Higgs coupling by $\sqrt{1-\xi}$. Note, that this is not the case in other composite Higgs scenarios. Furthermore, there are also direct four-point couplings between two Higgs bosons and two fermions, $HHf\bar{f}$, whose coefficients are proportional to $\xi m_f/v^2$. They therefore vanish in the SM limit of $\xi \rightarrow 0$. While the MCHM4 and associated models have a rich and varied phenomenology, these facts are sufficient for our study of the di-Higgs phenomenology.

2.1 Simulation results

Our analysis is a re-evaluation of Ref. [155] adapted to the MCHM4 model as introduced in the previous section. The phenomenology of the Higgs decays in MCHM4 remains unmodified with respect to the SM, as a consequence of the global re-scalings of the SM-like couplings, i.e. all the partial decay widths and hence also the total Higgs width decrease by $1-\xi^2$ so that the Higgs branchings ratios remain identical to SM case. Therefore there is a strict discrimination between single Higgs phenomenology and double Higgs phenomenology in MCHM4, especially because of the novel $HHt\bar{t}$ couplings introduced in the previous section. This is the reason why we choose to work in MCHM4, even if this model suffers from electroweak precision constraints due to breaking of custodial isospin symmetry.¹ We consider only gluon-induced HH production [160] in the following as this is the dominant contribution to HH

¹These constraints can be weakened somewhat by new heavy fermions [156, 157, 158, 159].

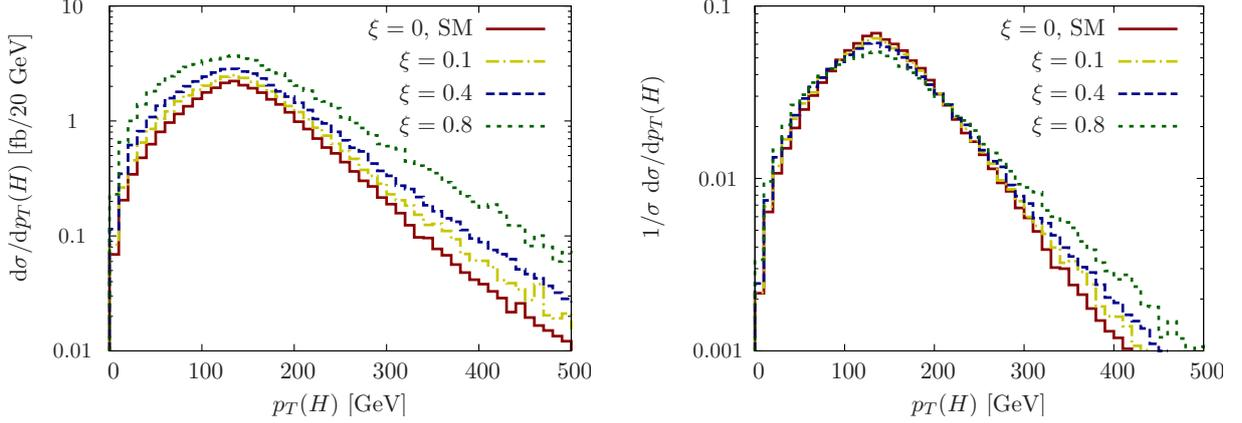


Figure 2: Comparison of the inclusive Higgs transverse momentum spectrum for different values of ξ , a total K factor estimate is included [154]. We also show a shape-comparison in the right panel. It demonstrates the standard lore of composite scenarios: there are large deviations when the characteristic new physics scale starts to get resolved.

production at the 14 TeV LHC run; representative Feynman diagrams that contribute to this process in MCHM4 are depicted in Fig. 1.

Events are generated using an MCHM4-adapted framework of Refs. [155, 161] in the Les Houches event standard and subsequently showered and hadronized with HERWIG++ [162]. The cross-sections then agree with those obtained in Ref. [163]. We report results directly in relation to the SM limit, $\xi = 0$. Since QCD corrections to di-Higgs production are driven by soft gluon emission [164, 165, 166] we expect this ratio to be robust against modified higher order QCD effects which could in principle modify the total K factor away from $K \simeq 2$ [154, 167], especially when heavy top partners are included to the picture [168].

The simulation incorporates detector resolution effects based on the ATLAS “Kraków” parameterisation [169], which implements a conservative estimate of the expected detector performance during the high-luminosity LHC run with a target of $3/\text{ab}$. We account for the effects of pile-up (with a mean number of pp collisions $\mu = 80$), and include $\sum E_T$ -dependent resolutions for jets and missing transverse momentum.

We include both leptonic and hadronic τ candidates and assume that events pass the trigger in the presence of two τ s with $p_T > 40$ GeV or one τ with $p_T > 60$ GeV. The τ efficiencies and fake rates are based on Ref. [169], jets are reconstructed using the anti- k_t algorithm [170, 171] with radial parameter 0.6. We require exactly two reconstructed τ leptons as well as exactly two jets which need to pass b tags. Furthermore, the b -tagged jets have to reconstruct the Higgs mass within a 25 GeV window. Separating $H \rightarrow \tau^+\tau^-$ from $Z \rightarrow \tau^+\tau^-$ is one of the main obstacles of this analysis. To reflect the corresponding systematics, we discuss results for an optimistic and a pessimistic estimate on the reconstruction of the invariant τ -pair mass. The former is performed without \cancel{p}_T resolution, demanding $100 \text{ GeV} < m_{\tau\tau} < 150 \text{ GeV}$ while the latter includes a conservative treatment of the \cancel{p}_T resolution and requires $80 \text{ GeV} < m_{\tau\tau} < 130 \text{ GeV}$ thus including a dominant² background contribution from $Z \rightarrow \tau^+\tau^-$. Further details can be found in [155].

²It is shown in Ref [155] that the background from $t\bar{t} \rightarrow b\bar{b}\tau\tau\nu\nu$ can be greatly reduced using a selection on the kinematic variable m_{T2}

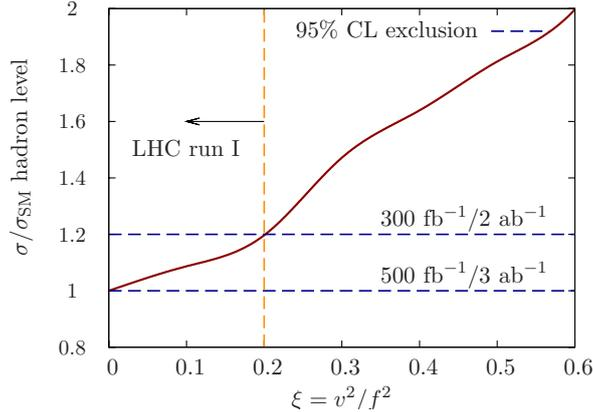


Figure 3: Double Higgs production cross section of MCHM4 in the full hadron-level analysis of $HH \rightarrow b\bar{b}\tau^+\tau^-$. For the two luminosities at each dashed line, see text.

Performing the analysis we find that trigger criteria and the event selection do not induce a notable bias: the event selection efficiencies are almost independent of ξ . The dominant discriminating power, hence, results from the modified cross section, that results from an enhancement over the entire relevant Higgs p_T range, see Fig. 2. Additional sensitivity to ξ comes from the relative increase of harder events for larger values of ξ .

The combined result of the described analysis is shown in Fig. 3, where we show the 95% CL constraints that are expected for a measurement in the $HH \rightarrow b\bar{b}\tau^+\tau^-$ channel. The different values of the integrated luminosity reflect our two choices of including the systematics of the τ pair reconstruction. We also include the current constraint on these model classes from Higgs data, $\xi \lesssim 0.2$. Fig. 3 excellently demonstrates that di-Higgs production is an excellent tool to constrain the parameter region of composite Higgs models with the LHC target luminosity of 3/ab. We expect quantitatively improved result for, e.g., MCHM5 [172], which exhibits a strong dependence on ξ , in particular when additional dynamical top partners are taken into account [173, 174].

Conclusions

Di-Higgs production in composite Higgs scenarios is significantly enhanced over the SM. In this article, we have adapted a hadron-level analysis of $pp \rightarrow HH \rightarrow b\bar{b}\tau^+\tau^-$ to the MCHM4 model. It is expected that sensitivity to a SM-like cross section can be obtained at the LHC 14 TeV with high luminosity. As a consequence, the LHC will become sensitive to deviations that are apparent when the Higgs boson emerges as part of a strongly interacting sector with a parametrically suppressed mass. In the absence of a signal, i.e. an enhancement of the di-Higgs cross section, the majority of the parameter space of the MCHM4 can be excluded. Since it is known that other composite models often exhibit an even larger sensitivity in the di-Higgs final state, this result is rather general.

Acknowledgements

We thank the organizers of the 2013 Les Houches workshop for keeping a well stocked bar for the duration of our stay.

Contribution 9

Resonant Higgs Pair Production in Vector Boson Fusion at the LHC

A. Belyaev, O. Bondu, A. Massironi, A. Oliveira, R. Rosenfeld, V. Sanz

Abstract

We examine resonant Higgs pair production at the LHC in vector boson fusion. This channel directly tests the couplings of the longitudinally polarized gauge bosons to new physics and therefore it is important as a test to any new model. In particular, we use as benchmark a model of warped extra dimensions where a KK-graviton can be produced on-shell through vector boson fusion and subsequently decays into a pair of Higgs bosons. We concentrate on the final state with 4 b quarks and 2 jets and devise cuts to decrease the irreducible QCD and EW backgrounds. We did not include effects of showering and hadronization in this preliminary analysis. For this reason we do not impose any cuts that relies on the reconstruction of either the resonance or the Higgs masses, cuts which would significantly reduce the SM backgrounds. Although our results are over-pessimistic at this point, we believe that there is great potential in this channel once a more realistic analysis with appropriate cuts is performed.

1 INTRODUCTION

In the Standard Model (SM), the production of a pair of Higgs bosons (H) is the only way to directly examine the Higgs self-coupling λ . Production of such pairs can proceed either via gluon fusion (GF) or vector boson fusion (VBF).

In the case of the SM, this coupling is predicted once the Higgs mass is known. Following the LHC discovery [45, 175, 44], the self coupling is determined to be:

$$\lambda_{SM} = \frac{m_h^2}{2v^2} \approx 0.13. \quad (1)$$

This in turn predicts a rather small Higgs pair production cross section for a centre of mass energy of $\sqrt{s} = 14$ TeV : $\sigma(pp \rightarrow gg \rightarrow hh + X) \approx 30$ fb and $\sigma(pp \rightarrow (WW, ZZ) \rightarrow hh + X) \approx 3$ fb [176, 177].

There exist several models Beyond the Standard Model (BSM) which predict different values for this coupling and that can lead to enhanced cross sections for Higgs pair production, both for the case of GF [178, 173] and VBF [179] processes.

However, even larger enhancements arise if there are new particles with masses within LHC reach that can decay on-shell into a Higgs boson pair, leading to the possibility of resonant Higgs boson pair production. Such a production process was studied in the context of

the MSSM[177], NMSSM[180], and 2-Higgs doublet models[181], where the resonances are identified with heavy Higgses. Models with Warped Extra Dimensions (WED) of the Randall-Sundrum type [182, 183] also contain particles that can contribute to resonant Higgs pair production, namely the radion and the KK-graviton.

A recent study was performed to demonstrate the feasibility of detection of resonant Higgs pair production in GF in the final state with 4 bottom quarks. This study featured a new tagging algorithm, that was developed in order to deal with the different boosting regimes of the decaying Higgses [184]. The benchmark model used in this study was a Randall-Sundrum (RS) model where the radion or the KK-graviton can decay into a Higgs boson pair.

The present contribution uses the same benchmark model, focusing on the KK-graviton contribution, to study resonant double Higgs production via vector boson fusion. The VBF signature, with the handle of two extra high- p_T jets could make this channel competitive with the GF searches. The couplings of the longitudinally polarized gauge bosons to the resonance play a crucial role and hence can be sensitive to details of the model.

2 THE MODEL

We write the couplings of the radion (r) and the KK-graviton ($G_{\mu\nu}$, later denoted by G) at the linear level with matter as (see, e.g. [185] and references therein):

$$\mathcal{L} = -\frac{c_i}{\Lambda} G_{\mu\nu} T_i^{\mu\nu} - \frac{d_i}{\sqrt{6}\Lambda} r T_i \quad (2)$$

where Λ is the compactification scale, $T_i^{\mu\nu}$ is the energy-momentum tensor of species i , T_i is its trace, and the coefficients c_i and d_i are related to the overlap of the 5D profiles of the corresponding particles. The compactification scale can be related to the curvature κ and the size L of the compact extra dimension as:

$$\Lambda = e^{-\kappa L} \bar{M}_{Pl}, \quad (3)$$

where $\bar{M}_{Pl} = 2.43 \times 10^{18}$ GeV is the reduced Planck mass. In order to solve the hierarchy problem one must have κL about 35. An important quantity that will be used to characterize the model is $\tilde{\kappa}$ defined as

$$\tilde{\kappa} \equiv \frac{\kappa}{\bar{M}_{Pl}} \quad (4)$$

The mass of the first KK-graviton resonance M_G is given by

$$M_G = x_1 \tilde{\kappa} \Lambda, \quad (5)$$

where $x_1 = 3.83$.

Since in models of warped extra dimensions the profiles of both the radion and the KK-graviton are peaked towards the infrared (IR) brane we assume that the dominant couplings are with particles that are also mostly localized in the IR, namely the Higgs boson (H), the longitudinal components of the electroweak gauge bosons (W_L and Z_L) and the right-handed top quark (t_R) [186, 187], in which case we take $c = d = 1$ for these particles. The coupling to the transverse polarizations of the gauge bosons (which we denote c_g) is suppressed due to the fact that their wave function is flat in the extra dimension and for definiteness we use $c_g = 0.0137$ (this value corresponds to $\kappa L = 35$ and has a very mild dependence on M_G).

This fixes the couplings that are relevant for resonant Higgs pair production in VBF. In the following we concentrate only on the KK-graviton G contribution. The model was implemented in MadGraph 5 [126] using a modified version of the FeynRules RS implementation in [188] and checked with CalcHEP [189].

Fig. 1 shows the total cross section for the GF and VBF production of a KK-graviton at the LHC13 as a function of its mass for fixed $\tilde{\kappa} = 0.1$. Typically the GF cross section is one order of magnitude larger than the corresponding VBF one.

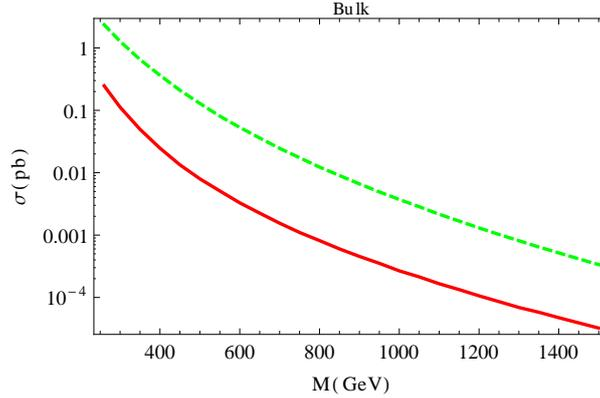


Figure 1: Production cross section of KK-graviton (in pb) as a function of its mass with at the LHC13 with $\tilde{\kappa} = 0.1$ for the GF (dashed green line) and VBF (solid red line) processes.

We show in Fig. 2 the branching ratios of the KK-graviton as a function of its mass, compared with the analytical predictions of [185]. The branching ratios are insensitive to the parameter $\tilde{\kappa}$. The total width for KK-graviton in all the suitable parameter space is less than 5 GeV [190]. Since the cross section results are not sensitive to the KK-graviton width, we keep it fixed at 1 GeV in what follows.

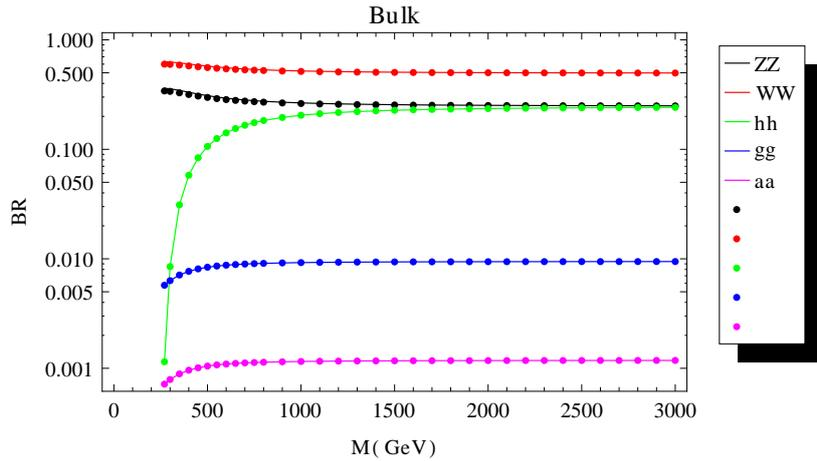


Figure 2: Branching ratios for bulk KK-graviton assuming no coupling with top quark. The solid lines represent analytical calculations and the dots are the numerical results from the model implementation.

We will focus in the rest of this contribution on the process $pp \rightarrow Gjj$, where the two jets come from vector boson fusion (see Fig. 3 (left)). It should be noted that KK-graviton

production in association with a W or Z boson (see Fig. 3 (right)) can in principle lead to the same final state. The cross section of the former is expected to be larger than the latter, and the kinematics of the two processes are expected to differ, leading to possibly different final selections. In principle these two contributions can not be separated but imposing specific cuts can favour one over the other. For instance, requiring $M_{jj} > 100$ GeV reduces the contribution from the associated production process.

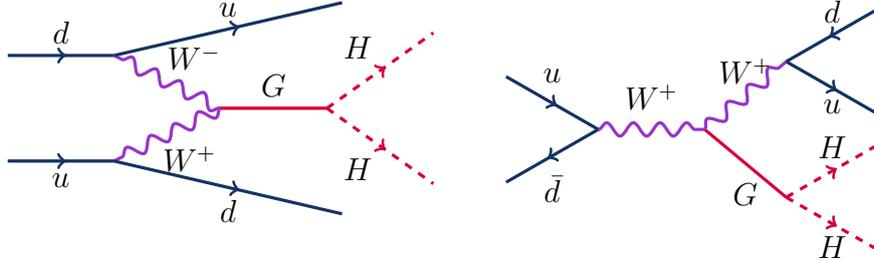


Figure 3: Examples of Feynman diagrams for Higgs pair production via a bulk KK-graviton resonance in the VBF (left) and associated production (right) cases.

3 SIGNAL GENERATION AND VBF CUTS

We will now focus on studying the VBF production process $pp \rightarrow Gjj$ following the model described in the previous section, for the prospect of the HL-LHC, assuming proton-proton collisions at a centre of mass energy of $\sqrt{s} = 13$ TeV for an integrated luminosity of $L = 3 \text{ ab}^{-1}$.

We generated 20k signal events in the model setting $\tilde{\kappa} = 0.1$ and varying the KK-graviton mass M_G from 260 to 1450 GeV. Only light quarks u and d in the proton and as final state jets have been considered. The KK-graviton was required to be produced on-shell and further decayed into a pair of Higgs bosons in Madgraph, with a mass of $m_H = 125$ GeV.

The following cuts were used for signal generation:

$$p_T^j > 10 \text{ GeV}, \quad M_{jj} > 100 \text{ GeV}, \quad |\eta_j| < 5, \quad \Delta R(jj) > 0.01 \quad (6)$$

$$p_T^b > 20 \text{ GeV}, \quad |\eta_b| < 2.5 \quad (7)$$

We will further concentrate on the decay of both Higgs bosons into b-quarks, leading to a $b\bar{b}b\bar{b}jj$ final state. Assuming SM branching fractions, this decay final state would represent roughly 33% of the total amount of Higgs boson pairs produced.

4 BACKGROUNDS FOR $b\bar{b}b\bar{b}jj$ FINAL STATE

To study potential detection of this channel at the LHC13, several processes leading to the same final state have to be considered, and will constitute an irreducible background. Three types of irreducible background have been considered :

- QCD production of four b -quarks and two additional jets. This is the background with the largest cross section; however it does not exhibit the same kinematics and can be kept under control using appropriate cuts. These events were generated with Alpgen [191].

- The Standard Model VBF production of Higgs boson pairs, with the Higgs boson decaying into b -quarks. Even though this background is the most similar to our signal in terms of kinematics, the di-Higgs pair production cross section is small and it does not have a resonant structure. These events were generated with Madgraph.
- Electroweak background producing Z bosons pairs decaying to b -quarks in association with jets. These events were generated with Madgraph.

Table 1 summarizes the different samples used, along with the expected cross-sections and number of generated events.

Process	Generator	σ (pb)	Number of events
QCD $bbbbjj$	Alpgen	148	500k
EWK $Z(b\bar{b})b\bar{b}jj$	Madgraph	1.46	200k
EWK $Z(b\bar{b})Z(b\bar{b})jj$	Madgraph	0.06	210k
VBF SM $H(b\bar{b})H(b\bar{b})jj$	Madgraph	2.71×10^{-4}	50k

Table 1: Background samples and the corresponding cross sections used for the analysis.

The cuts performed at the generator level for the QCD background were:

$$p_T^j > 20 \text{ GeV}, \quad |\eta_j| < 5, \quad \Delta R(jj) > 0.3, \quad \Delta R(bj) > 0.3, \quad p_T^b > 20 \text{ GeV}, \quad |\eta_b| < 2.5, \\ \Delta R(bb) > 0.1 \quad (8)$$

and for the electroweak background were:

$$p_T^j > 20 \text{ GeV}, \quad |\eta_j| < 5, \quad \Delta R(jj) > 0.3, \quad \Delta R(bj) > 0.4, \quad p_T^b > 20 \text{ GeV}, \quad |\eta_b| < 2.5, \\ \Delta R(bb) > 0.1, \quad M_{jj} > 100 \text{ GeV}. \quad (9)$$

The $\Delta R(bb)$ is relaxed with respect to the default value in order to take into account the case of a boosted Higgs. The M_{jj} cut, design to favour the VBF topology, was implemented only in the Madgraph generated background since it is not straightforward to do so in Alpgen.

5 RECONSTRUCTION OF THE PROCESS $pp \rightarrow G \rightarrow HHjj \rightarrow b\bar{b}b\bar{b}jj$

We cluster the “jets” with the anti- k_T 5 algorithm using FastJet3 [170]. This procedure makes sense even at a parton level preliminary analysis, since two partons that are close enough can cluster on a jet.

Following [184] we base the reconstruction algorithm for event selection on the number of jets per event. For the presence of jets with non-trivial substructure and high invariant mass, we use the mass drop definition of a fat jet [192]. We describe below the analysis flow we adopted.

We require at least two jets in the event after b and fat jet-tagging. The VBF jets are chosen as the pair that holds the largest invariant mass among the non-tagged jets. In this preliminary study we are considering only events with four b 's and assuming perfect b -tag performance. In deriving our results we use more realistic cuts on the VBF jets:

$$p_T^j > 30 \text{ GeV}, \quad M_{jj} > 400 \text{ GeV}, \quad |\eta_j| < 4.7 \quad (10)$$

After this first selection we reconstruct the Higgses from the remaining jets. We also take advantage of the fact that the di-Higgs system is boosted by using the following cuts:

$$M_{HH} > 250 \text{ GeV}, \quad p_T^{HH} > 60 \text{ GeV}, \quad \Delta\eta(HH) < 2 \quad (11)$$

We follow closely [184] and classify events by the number of mass-drop tagged jets (fat jets). We define mass drop by the tagger parameters:

$$\mu = 0.67, \quad y_{cut} = 0.09, \quad M_{\text{fat jet}} > 120 \text{ GeV} \quad (12)$$

We detail below event selection and classification of our tagging algorithm.

- If the two hardest jets in the event are found fat and satisfy the di-Higgs quality requirements of equation (11) the event is assigned to the **2-tag**.
- If one of the two fat jets do not pass quality requirements or only one of the jets among the two hardest is fat, then events with fewer than three jets after cuts are discarded. We then apply eqs. 6 and 7 and if the event passes those cuts it is assigned to **1-tag** sample.
- If the event is not assigned as **2-tag** or **1-tag** sample, we check the event can be classified as being two resolved Higgses.

Events with fewer than six jets passing the basic cuts are discarded. To select the Higgs candidates we pair the four non-VBF jets i, j, k, l minimizing the mass difference $|M_{ij} - M_{kl}|$. If the two reconstructed Higgs candidates satisfy the cuts (11) the event is classified as belonging to the **0-tag** sample.

We are now ready to discuss the preliminary parton level results.

6 RESULTS

We first discuss the general properties of the bulk graviton signal hypothesis. In figure (4) we show the pseudo-rapidity difference among the two VBF jets. The kinematics of the VBF jets in the signal differ from the case of the Standard Model VBF Higgs production, which tend to be more central. This is due to the fact that the KK-graviton vertices with massive vector bosons have a particular p_T dependence, and from the fact that the graviton is a spin 2 particle while the SM Higgs is a scalar. This effect has been already explored e.g. in reference [193].

We present the cut flow of our analysis in Table 2, where we show the impact of the cuts on the VBF jets system (10) and on di-Higgs system (11). To visually complement the cut flow we also display the parton level signal reconstructed efficiency separated by the number of mass drop tags in Fig. 5. In this figure we see that for KK-graviton mass hypothesis larger than 1 TeV there is a systematic increase of events with two tags, meaning the two b -quarks products of each one of the Higgses start to merge in one jet. This change of behaviour at 1 TeV is expected from calculating the distance radius between two partons giving the boost of their mother particle [184].

At very low mass ($M_G < 400 \text{ GeV}$) both Higgses are not very boosted, so there is larger probability of jets to superpose. We loose a large portion of the signal due this effect, due to for example the intrinsic mis-tag of events caused by an accidental merging of the b 's of the two different Higgses.

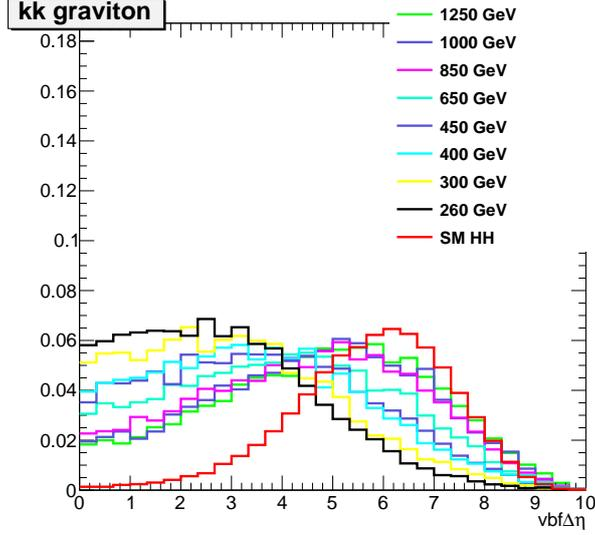


Figure 4: Separation in pseudo rapidity between the two VBF jets $\Delta\eta(jj)$. No additional cuts applied, the different contributions have been normalized to the same area.

Sample	basic cuts (eqs. 7,6)	jet merging (akt5)	$M_{jj} > 400$ GeV	$M_{HH} > 250$ GeV	$p_T^{HH} > 60$ GeV	$\Delta\eta_{HH} < 2$
1450 GeV	0.53	0.49	0.44	0.44	0.41	0.35
1250 GeV	0.52	0.47	0.43	0.43	0.40	0.35
1050 GeV	0.52	0.48	0.44	0.44	0.40	0.35
850 GeV	0.51	0.47	0.42	0.42	0.39	0.34
650 GeV	0.51	0.43	0.39	0.39	0.36	0.33
450 GeV	0.54	0.38	0.34	0.34	0.32	0.30
400 GeV	0.55	0.33	0.29	0.29	0.28	0.26
300 GeV	0.58	0.17	0.14	0.14	0.13	0.12
260 GeV	0.60	0.09	0.07	0.07	0.07	0.07
SM $H(bb)H(bb)jj$	0.41	0.38	0.36	0.36	0.30	0.12
$Z(bb)bbjj$	0.50	0.36	0.14	0.10	7.91E-02	4.55E-02
$Z(bb)Z(bb)jj$	0.62	0.51	0.17	0.12	9.66E-02	6.61E-02
$bbbbjj$	0.70	0.20	0.11	6.73E-02	5.49E-02	4.55E-02

Table 2: Cut flow on signal and BKG. The displayed numbers are efficiencies.

The most powerful variables for background rejection in this channel are related with its resonant character and rely on reconstructing the resonance. However, since we performed only a parton-level study without showering we restrain ourselves of using such variables and our results are possibly over-pessimistic. We present our results for the significance of the signal in Table 3.

To demonstrate the discovery potential of the channel despite our preliminary sensitivity results and push the need of a higher simulation level study we also display the parton level distributions of the mass of the leading reconstruct Higgs and the reconstructed di-Higgs resonance in Fig. 6.

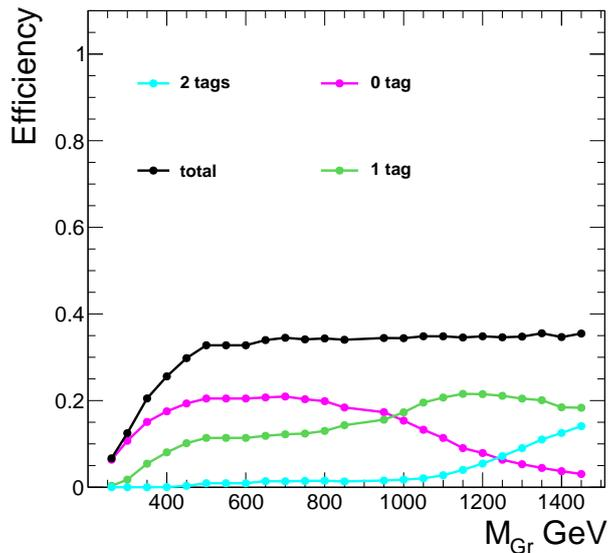


Figure 5: Parton level number separation on number of mass drops after analysis flow.

	$pp \rightarrow G(HH)jj$ σ (pb)	$\sigma \times \text{eff.}$ (pb)	Nevents (3000/fb)	S/\sqrt{B}
1450 GeV	6.91E-06	8.17E-07	2.45E+00	7.74E-06
1250 GeV	1.86E-05	2.14E-06	6.41E+00	2.03E-05
1050 GeV	7.87E-05	9.13E-06	2.74E+01	8.66E-05
850 GeV	2.63E-04	3.00E-05	9.01E+01	2.85E-04
650 GeV	1.28E-03	1.40E-04	4.20E+02	1.33E-03
450 GeV	8.87E-03	8.80E-04	2.64E+03	8.34E-03
400 GeV	1.41E-02	1.20E-03	3.60E+03	1.14E-02
300 GeV	1.55E-02	6.42E-04	1.93E+03	6.09E-03
260 GeV	5.72E-03	1.27E-04	3.80E+02	1.20E-03

Table 3: Cross section and events for HL-LHC, after all selections of Table 2. The parameters used are $\tilde{\kappa} = 0.1$ and $\kappa L = 35$. The S/\sqrt{B} ratio is calculated only with respect to the EW backgrounds and without the cut on resolution the mass of the Higgses and KK-graviton candidates.

7 CONCLUSIONS

The VBF production of a Higgs pair is sensitive to new physics that couple to the longitudinally polarized gauge bosons. Hence it is complementary to Higgs pair production via gluon fusion. We performed a first preliminary parton level study on the search for a bulk KK-graviton resonance at a HL-LHC using the di-Higgs channel with a VBF topology. We prospect the HL-LHC significance of such signal. After basic event quality cuts we do not find a large significance. However, one should note that our results are obtained using the signal and background efficiencies without applying cuts on resonance resolution (on both Higgs and KK-Graviton). We believe that applying such cuts at the parton level study would produce over-optimistic results. In this sense the numbers in Table 3 are a gross underestimate of the significance and a complete analysis based on more a realistic simulation that allows us to make more accurate predictions needs to be performed to rightly assess the detectability of a VBF resonant Higgs pair produc-

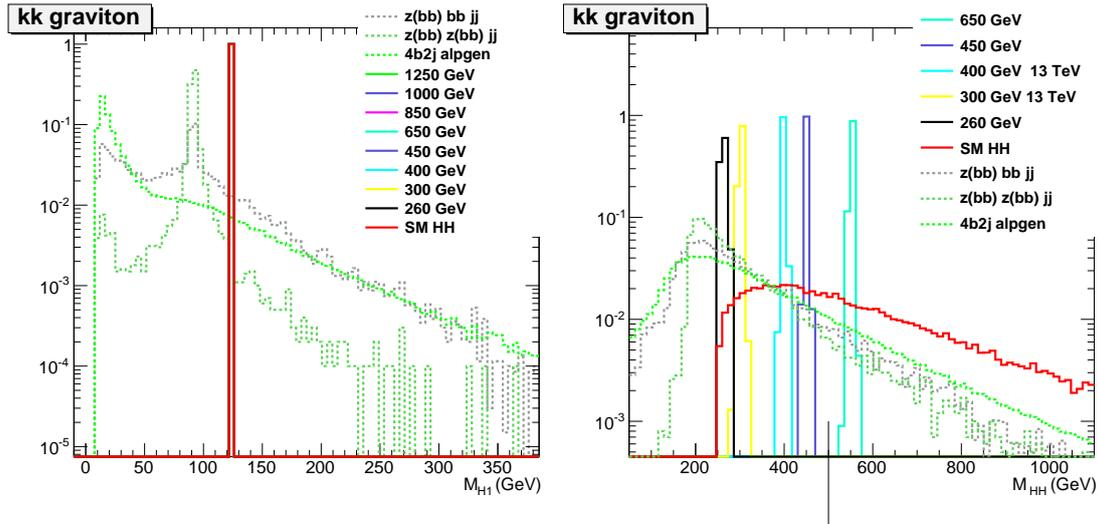


Figure 6: Parton level distributions of reconstructed objects with no cuts applied. Distributions are shape normalized. **Left:** Leading reconstructed Higgs. **Right:** Reconstructed bulk KK-graviton. Those distributions are only for illustration.

tion.

ACKNOWLEDGEMENTS

We thank M. Gouzevich and J. Rojo for valuable discussions on the QCD backgrounds. We acknowledge the use of IRIDIS HPC Facility at the University of Southampton for this study. AB is supported in part by the NExT Institute and MCT is supported by an STFC studentship grant. RR is supported in part by grants from CNPq and Fapesp (2011/11973-4).

Contribution 10

Strong Double Higgs Production at the LHC in the $4b$ and $2b2W$ Final States

O. Bondu, A. Oliveira, R. Contino, M. Gouzevitch, A. Massironi, J. Rojo

Abstract

The measurement of Higgs pair production will be one of the cornerstones of the LHC physics program in the next years. Double Higgs production via vector boson fusion, in particular, is sensitive to the strong interactions of a composite Higgs boson, and allows a direct extraction of the $hhVV$ quartic interaction. In this contribution we study the feasibility of probing strong double Higgs production via vector boson fusion at the 13 TeV LHC in the $4b$ and $2b2W$ final states. By performing a simple parton-level analysis, we find that, although experimentally challenging, these final states lead to a good sensitivity on New Physics. Our results are encouraging and motivate more realistic analyses to include parton shower, jet reconstruction and b -tagging efficiencies.

1 Introduction

The measurement of double Higgs production will be one of the main physics goals of the LHC program in its upcoming high-energy and high-luminosity phase. Double Higgs production is directly sensitive to the Higgs trilinear coupling, and thus provides information on the scalar potential responsible for electroweak symmetry breaking. It is also sensitive to the underlying strength of the Higgs interactions at high energies, and can test the composite nature of the Higgs boson [47, 179].

In the Standard Model (SM), the dominant mechanism for the production of two Higgs bosons at the LHC is gluon fusion (see Ref. [154] and references therein), analogously to single Higgs production. For a center-of-mass energy $\sqrt{s} = 14$ TeV, the recently computed next-to-next to leading order (NNLO) total cross section is approximately 40 fb [165]. Feasibility studies in the case of a light Higgs boson have been performed for several different final states, including $b\bar{b}\gamma\gamma$ [194, 195], $b\bar{b}\tau^+\tau^-$ [196, 155, 161, 197], $b\bar{b}W^+W^-$ [161, 198] and $b\bar{b}b\bar{b}$ [196, 161, 184, 199]. Another relevant production mode for Higgs boson pairs at the LHC is vector boson fusion (VBF), where a soft emission of two vector bosons from the incoming protons is followed by the hard $VV \rightarrow hh$ scattering ($V = W, Z$). In the SM, the leading order (LO) rate of this channel is small, around 1 fb at $\sqrt{s} = 14$ TeV. The full NNLO calculation recently performed in Ref. [200] has shown that the total cross section is perturbatively very stable, with a NNLO/LO K-factor deviating from 1 by only $\sim 10\%$. The production rate can be however strongly enhanced in theories where the Higgs is a composite pseudo Nambu-Goldstone boson (pNGB) of new strong dynamics at the TeV scale [146]. In those theories the Higgs anomalous couplings imply a growth of the $VV \rightarrow hh$ cross section with the partonic center-of-mass energy, $\sigma \propto \hat{s}/f^4$, where f is the pNGB decay constant. The enhanced sensitivity to the

underlying strength of the Higgs interactions thus makes double Higgs production via VBF a key process to test the nature of the electroweak symmetry breaking dynamics.

A first detailed study of double Higgs production via VBF at the LHC was performed in Ref. [179] for a Higgs mass $m_h = 180$ GeV by focussing on the $4W$ final state. In this work we want to revisit the feasibility of observing this process at the LHC for $m_h = 125$ GeV. Although a realistic final state simulation of all Higgs pair production channels can be now achieved up to next-to-leading order (NLO) matched to parton showers in the MadGraph5_aMCatNLO framework [164], we will keep our analysis as simple as possible and work at the parton level. We will consider the two final states with the largest branching fractions: $hh \rightarrow 4b$ and $hh \rightarrow 2b2W$. We will compute the relevant backgrounds for these final states and devise simple kinematic cuts to isolate the signal at the LHC with 300 fb^{-1} as well as at its future High-Luminosity upgrade to 3 ab^{-1} . In each case, we will study the sensitivity to New Physics (NP) in a way as model independent as possible. As we will show, a High-Luminosity upgrade of the LHC (HL-LHC) is essential in order to make a detailed study of double Higgs production, although already at 300 fb^{-1} important information can be obtained on the Higgs anomalous couplings in the most favorable NP scenarios.

The outline of this paper is as follows. In Sect. 2 we present our modeling of signal and background. Sections 3 and 4 contain our analysis of Higgs pair production via VBF respectively for the $4b$ and $2W2b$ final states. In Sect. 5 we conclude and discuss future directions for these studies.

2 Theoretical modeling of signal and background

In this section we discuss the theoretical modeling of signal and background events for Higgs pair production via vector boson fusion at the LHC for the two final states under consideration

$$pp \rightarrow hhjj \rightarrow 4bjj \quad (1)$$

$$pp \rightarrow hhjj \rightarrow 2W2bjj \rightarrow l^+l^- \cancel{E}_T 2bjj, \quad (2)$$

where j , b and $l = e, \mu$ stand respectively for jets (from light quarks and gluons), b -tagged jets and light charged leptons (electrons and muons). For simplicity, in the following we will refer to the $l^+l^- \cancel{E}_T 2bjj$ final state as $2W2bjj$, always assuming the leptonic decay of the W bosons. We set $m_h = 125$ GeV and assume a collider center-of-mass energy $\sqrt{s} = 13$ TeV. All events are generated at the parton level, without any shower or hadronization effect. No detector simulation or inclusion of underlying event and pileup corrections is attempted: in this first feasibility study we want to explore the most optimistic scenario. For this reason, we will also assume perfect b -jet tagging and omit the related identification efficiencies in our estimates. As our starting point, we impose the following selection cuts to all signal and background samples

$$\begin{aligned} p_{Tj} \geq 25 \text{ GeV}, \quad p_{Tb} \geq 25 \text{ GeV}, \quad p_{Tl_1} \geq 20 \text{ GeV}, \quad p_{Tl_2} \geq 10 \text{ GeV} \\ |\eta_j| \leq 4.5, \quad |\eta_b| \leq 2.5, \quad |\eta_l| \leq 2.5 \\ \Delta R_{jb} \geq 0.4, \quad \Delta R_{bb} \geq 0.2, \quad \Delta R_{jl} \geq 0.4, \quad \Delta R_{bl} \geq 0.4, \quad \Delta R_{ll} \geq 0.4, \end{aligned} \quad (3)$$

$$m_{jj} \geq 500 \text{ GeV}, \quad \Delta R_{jj} \geq 4.0. \quad (4)$$

The cuts of Eq. (3) are simple acceptance requirements, while those of Eq. (4) are specifically designed to isolate the VBF signal. The $hhjj$ process also follows from gluon-gluon fusion at

NNLO, but we expect this contribution to be subdominant compared to the VBF process after the cuts of Eq. (4). In practice, in a realistic analysis one will have to classify events by jet topology and isolate the VBF and gluon-fusion initiated contributions. The value of ΔR_{jb} has been chosen so as to reproduce the jet reconstruction of a cone algorithm with minimum cone size $R = 0.4$. The looser cut on ΔR_{bb} is motivated by the recent development of jet substructure techniques that provide the possibility to discriminate the $h \rightarrow b\bar{b}$ decay over the background even when the two prongs of the Higgs decay end up in the same jet [192].

The signal event samples have been generated with MadGraph5 [126], including the decays of the Higgs bosons into the relevant final states. We have used the NNPDF2.1LO PDF set [201] with dynamically generated renormalization and factorization scales (default choice in MadGraph5). Anomalous Higgs couplings have been parametrized according to the effective Lagrangian for non-linearly realized $SU(2)_L \times U(1)_Y$. Specifically, we have rescaled the couplings of the Higgs to vector bosons and the Higgs trilinear coupling as follows [179]

$$c_V g_{hVV}^{SM} hVV, \quad c_{2V} g_{hhVV}^{SM} hhVV, \quad c_3 g_{hhh}^{SM} hhh, \quad (5)$$

where g_i^{SM} are the corresponding SM couplings, so that the Standard Model limit is recovered by setting $c_V = c_{2V} = c_3 = 1$. In the case of composite Higgs theories where the electroweak symmetry is linearly realized at high energies and the Higgs boson is part of an $SU(2)_L$ doublet, the coefficients c_V , c_{2V} and c_3 deviate from 1 at order $(v/f)^2$. In general, one expects $O(g_*^2 v^2/m_*^2)$ corrections, where g_* is the Higgs coupling strength to new states and m_* is their mass. For simplicity we have neglected the direct contribution of new states, such as vector and scalar resonances, to the scattering amplitude (see for example Ref. [202] for an analysis in the case of composite Higgs theories). Eq. (5) has been implemented by a suitable modification of the Standard Model UFO [203] file in Madgraph5.¹ We have chosen to explore the following range of Higgs couplings:

$$\begin{aligned} 0.5 &\leq c_V \leq 1.5 \\ 0.0 &\leq c_{2V} \leq 2.0 \\ 0.0 &\leq c_3 \leq 2.0. \end{aligned} \quad (6)$$

While this is a reasonable choice, useful for the illustrative purposes of this work, one should keep in mind that current Higgs searches at the LHC typically set slightly more stringent bounds on $\Delta c_V = 1 - c_V$ at the level of 0.10–0.20, depending on the assumptions made (see for example Refs. [204, 205, 206]). Tighter limits on Δc_V come from electroweak precision tests in absence of additional NP contributions to the electroweak observables, see for example Ref. [207]. The couplings c_{2V} and c_3 have instead no direct experimental determination so far. Double Higgs production via VBF is the only process at the LHC that can give access to the coupling c_{2V} , while c_3 can in principle be extracted also from di-Higgs production via gluon-fusion.

In Table 1 we collect the cross sections of the signal in the Standard Model and in various BSM scenarios after the selections cuts of Eqs. (3) and (4). Branching fractions to the two final states under consideration are included assuming that they are not modified compared to their SM value: $\text{BR}(hh \rightarrow b\bar{b}b\bar{b}) = 0.333$, and $\text{BR}(hh \rightarrow b\bar{b}WW \rightarrow b\bar{b}l^+\nu l^-\bar{\nu}) = 1.17 \cdot 10^{-2}$ [208, 209, 145]. In the SM case, we also report the value of the $pp \rightarrow hhjj$ cross section with undecayed Higgs bosons both before cuts and after applying the cuts of Eqs. (3), (4) to the two jets. One can see that in the latter case (selection cuts applied only to the VBF jets) the SM

¹We are grateful to Benjamin Fuks for assistance with this implementation.

Model	Final state	Cross section [fb]	$N_{\text{ev}} (\mathcal{L} = 3 \text{ ab}^{-1})$
SM (no cut)	$hhjj$	0.83	2500
SM	$hhjj$	0.12	360
SM	$hhjj \rightarrow 4bjj$	0.049	150
$c_V = 0.5$		0.54	1600
$c_V = 1.5$		2.72	8100
$c_{2V} = 0$		1.23	3700
$c_{2V} = 2$		0.78	2300
$c_3 = 0$		0.14	420
$c_3 = 2$		0.042	130
SM	$hhjj \rightarrow l^+l^- \cancel{E}_T 2bjj$	$8.6 \cdot 10^{-4}$	2.6
$c_V = 0.5$		$2.0 \cdot 10^{-3}$	6
$c_V = 1.5$		$9.8 \cdot 10^{-2}$	290
$c_{2V} = 0$		$1.9 \cdot 10^{-2}$	54
$c_{2V} = 2$		$1.1 \cdot 10^{-2}$	33
$c_3 = 0$		$2.4 \cdot 10^{-3}$	7
$c_3 = 2$		$7.4 \cdot 10^{-4}$	2.2

Table 1: Cross sections for Higgs pair production in the vector-boson fusion channel at the LHC with $\sqrt{s} = 13 \text{ TeV}$. All numbers have been obtained after applying the basic selection cuts of Eqs. (3), (4) except for the first row, where no cut is applied. Branching fractions to the two final states under consideration are included assuming that they are not modified compared to their SM value, except for the first two rows where the cross section for undecayed Higgs bosons is reported. The last column indicates the corresponding number of events for an integrated luminosity $\mathcal{L} = 3 \text{ ab}^{-1}$. The final cross sections and number of signal and background events expected after all the analysis cuts is summarized in Tables 2 and 3.

signal cross section is 0.12 fb before Higgs decays, which corresponds to about 36 Higgs boson pairs produced in the VBF channel with $\mathcal{L} = 300 \text{ fb}^{-1}$ and to about 360 Higgs pairs with $\mathcal{L} = 3 \text{ ab}^{-1}$. These integrated luminosities correspond to the expectations for the future LHC runs and the possible High-Luminosity upgrade respectively.² Our LO MadGraph5 computation is in good agreement with the recent calculation of Ref. [200] within scale uncertainties. One can also see from Table 1 that the event yields are much larger in the $4bjj$ final state than in the $2b2Wjj$ one, the latter being suppressed by the leptonic branching fraction of the W bosons. In the $4bjj$ final state, we expect about 150 events in the SM with $\mathcal{L} = 3 \text{ ab}^{-1}$ after basic selection cuts, with event rates that can be higher by up to a factor ~ 50 in the most optimistic BSM scenarios.

For the $4bjj$ final state, we have considered three types of backgrounds: the QCD (non-resonant) $pp \rightarrow 4bjj$ production, and the resonant $pp \rightarrow Z(bb)bbjj$ and $pp \rightarrow Z(bb)Z(bb)jj$ processes with respectively one and two Z bosons decaying to $b\bar{b}$. To generate the QCD $4bjj$ events, we have used the ALPGEN parton level event generator [191], while $Z(bb)bbjj$ and $Z(bb)Z(bb)jj$ events have been generated with MadGraph5³. The $Z(bb)Z(bb)jj$ background

²Most likely, a High-Luminosity LHC will run at the higher center-of-mass energy $\sqrt{s} = 14 \text{ TeV}$. The impact of going from 13 to 14 TeV is however less important than that of a factor 10 increase in luminosity.

³These samples were also used in the contribution ‘‘Resonant Higgs Pair Production in Vector Boson Fusion

turns out to be much smaller than the other two after applying our analysis cuts and will be then neglected in the following. The cross sections of $4bjj$ and $Z(bb)bbjj$ after the selection cuts of Eqs. (3), (4) are reported in Table 2 in the σ_I column.

In the case of the $2W2bjj$ final state, the dominant background comes from the SM process $pp \rightarrow WWb\bar{b}jj$, with the subsequent leptonic decay of the W bosons. The bulk of its cross section (about 3/4 of the total) is dominated by the $pp \rightarrow t\bar{t}jj$ process, which is much easier to generate due to the smaller final state multiplicity. We have simulated both $WWb\bar{b}jj$ and $t\bar{t}jj$ events with MadGraph5. The corresponding cross sections after the selection cuts of Eqs. (3), (4) are reported in Table 3 in the σ_I column.

As a final remark, we stress that all the above backgrounds have been generated at the parton level. Once shower and detector effects are included, additional backgrounds will have to be included which can be potentially important, like for example $pp \rightarrow 4j2b$ where two light jets are mistagged as b -jets. Their estimate is beyond the scope of this work and is left for a future analysis.

3 Double Higgs production via VBF in the $4bjj$ final state

In this section we discuss our analysis of Higgs pair production via VBF in the $4bjj$ final state.

As shown in Table 2, after the basic selection cuts of Eqs. (3), (4) the QCD $4bjj$ process is by far the largest background. As a first way to reduce it, we can exploit the peculiar kinematics of the signal, where two pairs of b -jets come from the decay of the Higgs bosons. We construct the two Higgs candidates by identifying the two b -jet pairs $(bb)_1$ and $(bb)_2$ that minimize the dijet mass difference [184]. Their invariant masses are then required to lie in a window within 15% of the nominal Higgs mass ($m_h = 125$ GeV in our study)

$$|m_{(bb)_i} - m_h| \leq 0.15 m_h, \quad (i = 1, 2), \quad (7)$$

which roughly corresponds to the hadronic jet mass resolution in ATLAS and CMS. The cross sections of signal and background after this cut are reported in Table 2 in the σ_{II} column.

A further reduction of the background can be obtained by imposing a harder cut on the invariant mass of the VBF jets

$$m_{jj} \geq 800 \text{ GeV}, \quad (8)$$

which has a much steeper distribution for the $4bjj$ background than for the signal, see the left plot of Fig. 1. Requiring an additional stronger cut on the ΔR separation of the two VBF jets does not help, since its distribution is highly correlated with that of m_{jj} , as illustrated in the right plot of Fig. 1.⁴ The cross sections of signal and background after the additional VBF cut of Eq. (8) are summarized in Table 2 in the σ_{III} column.

Although Eqs. (7) and (8) are very efficient in suppressing the $4bjj$ background without reducing the signal, at this stage the signal-over-background ratio (S/B) is still quite small. This indicates that an analysis of Higgs pair production via VBF in the decay channel $hh \rightarrow 4b$ is rather challenging, in agreement with the estimate of Ref. [179]. There is however one more feature of the signal that can be exploited to isolate it from the background. In the case of anomalous Higgs couplings to the vector bosons, more specifically for $(c_V^2 - c_{2V}) \neq 0$, the cross

at the LHC" by A. Belyaev, O. Bondu, A. Massironi, A. Oliveira, R. Rosenfeld and V. Sanz, appearing in these proceedings.

⁴We thank Mauro Moretti for an important discussion on this point.

Sample	σ_I [fb]	σ_{II} [fb]	σ_{III} [fb]	σ_{IV} [fb]	$N_{ev} = \sigma_{IV} \cdot \mathcal{L}$
SM	0.04895	0.04894	0.04254	0.002263	6.788
$c_V = 0.5$	0.5424	0.5424	0.4869	0.1958	587.5
$c_V = 1.5$	2.717	2.717	2.393	0.6798	2039
$c_{2V} = 0$	1.237	1.237	1.101	0.3865	1160
$c_{2V} = 2$	0.7863	0.7861	0.713	0.3275	982.5
$c_3 = 0$	0.14	0.14	0.1186	0.003405	10.21
$c_3 = 2$	0.04156	0.04155	0.03687	0.001795	5.385
$4bjj$	7138	133.8	59.81	0.1185	355.5
$Zbbjj \rightarrow 4bjj$	126.8	1.918	1.039	< 0.0024	< 7

Table 2: Cut-flow for the analysis in the $4b2j$ final state. Cross sections are reported for the signal and backgrounds after sequentially imposing: the selection cuts of Eqs. (3), (4) (σ_I); the Higgs reconstruction cut of Eq. (7) (σ_{II}); the VBF cut of Eq. (8) (σ_{III}); the cut of Eq. (9) (σ_{IV}). At each stage all the previous cuts are also imposed. The values of the signal cross sections σ_I are the same as those reported in Table 1. The last column shows the expected number of events after all cuts, $N_{ev} = \sigma_{IV} \cdot \mathcal{L}$, for an integrated luminosity $\mathcal{L} = 3 \text{ ab}^{-1}$. Notice that b -tagging efficiencies have not been included.

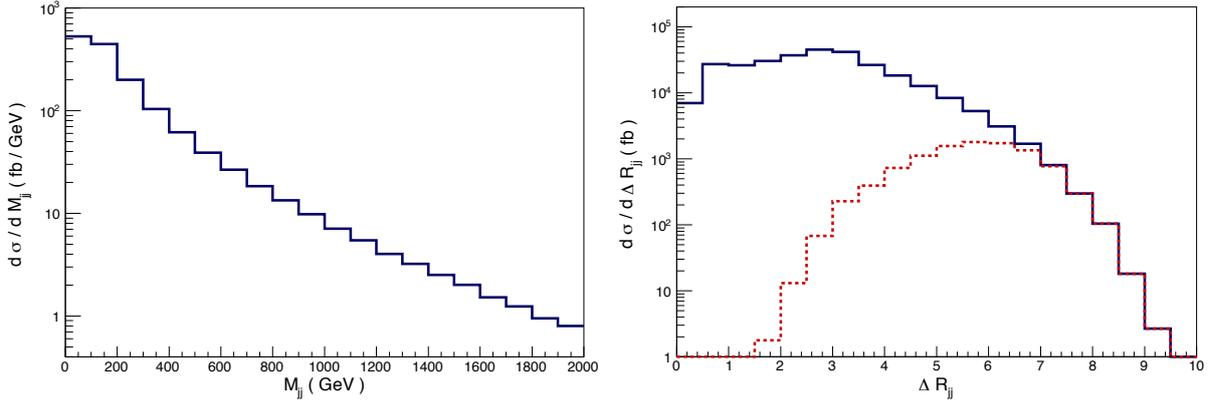


Figure 1: Distribution of the invariant mass m_{jj} (left plot) and separation ΔR_{jj} (right plot) of the two light jets in the QCD background $4bjj$. The blue solid curves are obtained after the selection cuts of Eqs. (3), (4); the dashed red curve in the right plot is obtained after imposing the additional VBF cut of Eq. (8). The $4bjj$ events have been simulated with the ALPGEN parton-level generator.

section of the underlying $VV \rightarrow hh$ scattering grows with the partonic energy. This is indeed the distinctive prediction of theories with strong EWSB dynamics [47]. After convoluting over the luminosities of the two initial vector bosons, such energy growth leads to an invariant mass distribution of the di-Higgs system which is much flatter than for the SM case. This is clearly shown in Fig. 2, where the distribution of the invariant mass of the four b -jet system, m_{4b} , is plotted for various BSM scenarios by normalizing it to the SM case. As expected, in the case of modified Higgs trilinear coupling, the m_{4b} distribution is affected mostly at threshold, and does not significantly differ from the SM case away from it. In the case of the background, on the other hand, the cross section steeply falls at large m_{4b} , see Fig. 3.⁵ It is then clear

⁵Although we have generated more than 10 million $4bjj$ events with ALPGEN, at very large m_{4b} invariant

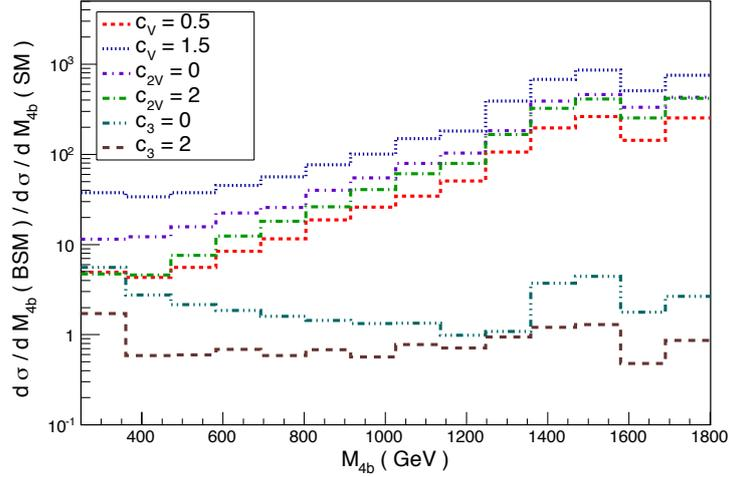


Figure 2: Invariant mass distribution of the $4b$ system after the basic selection cuts of Eqs. (3), (4) for the signal in various BSM scenarios. All curves are normalized to the SM signal.

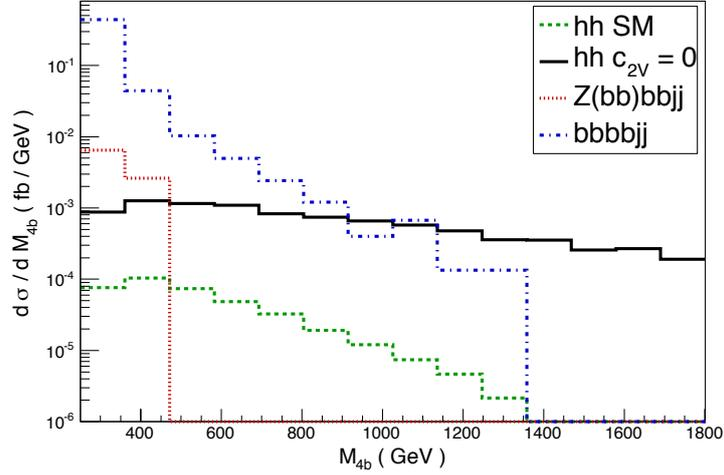


Figure 3: Invariant mass distribution of the $4b$ system after the basic selection cuts of Eq. (3), (4) and the additional cuts of Eqs. (7), (8), for the signal and the background. The abrupt fall-off of the dotted red and dot-dashed blue curves around their end points is due to the limited statistics of our background event samples.

that the invariant mass m_{4b} can be used as a way to enhance the sensitivity on the signal in the case of anomalous c_V and c_{2V} couplings. Although a realistic analysis will make use of the whole differential distribution to maximize the signal significance and extract the Higgs couplings, here we apply a simple cut on m_{4b} as a way to quantify the fraction of events with large di-Higgs invariant mass and estimate the significance of the signal. We require:

$$m_{4b} \geq 1000 \text{ GeV} . \quad (9)$$

The signal and background cross sections obtained after this cut are reported in Table 2 in

masses we are limited by statistics, and the corresponding distribution has a steep fall-off near its end point. This however occurs in a region where the BSM signal is much larger than the QCD background, so our estimates are not affected.

the σ_{IV} column. The corresponding number of events expected for an integrated luminosity $\mathcal{L} = 3 \text{ ab}^{-1}$ is shown in the last column of the same Table.

Our results indicate that a simple cut-and-count analysis of the $4bjj$ final state is inadequate to isolate the SM signal from the overwhelming QCD background. The possibilities of extracting the Higgs trilinear coupling are also quite limited in this channel, even in a High-Luminosity phase of the LHC. On the other hand, the invariant mass distribution of the di-Higgs system can be used to uncover the signal in the case of strong double Higgs production, implying in particular that a potentially interesting reach on the coupling c_{2V} can be obtained with sufficiently large integrated luminosity.

4 Double Higgs production via VBF in the $2b2Wjj$ final state

Next we discuss our analysis for the $2b2Wjj$ final state.

As for the study of the $4bjj$ channel, it is useful to impose additional cuts, besides those of Eqs. (3), (4), that exploit the kinematic of the signal, where two Higgs bosons are produced on-shell and then decay. We require the following set of Higgs-reconstruction cuts:

$$|m_{bb} - m_h| \leq 0.15 m_h \quad (10)$$

$$m_{ll} \leq 70 \text{ GeV} \quad (11)$$

$$m_T(WW) \leq 125 \text{ GeV} .$$

The transverse mass $m_T(WW)$ is defined as

$$m_T(WW) \equiv \left(\left(\sqrt{m_{ll}^2 + |\vec{p}_{Tll}|^2} + \sqrt{m_{ll}^2 + |\vec{p}_{Tmiss}|^2} \right)^2 - |\vec{p}_{Tll} + \vec{p}_{Tmiss}|^2 \right)^{1/2} , \quad (12)$$

where \vec{p}_{Tll} and m_{ll} are respectively the transverse momentum and the invariant mass of the ll system, and \vec{p}_{Tmiss} is the missing transverse momentum. The cross sections of signal and background after imposing Eqs. (10) and (11) are shown in Table 3 in the column σ_{II} . The cuts on m_{ll} and on the transverse mass $m_T(WW)$ exploit the fact that in the signal the lepton pair and the missing energy come from the decay of the second Higgs (see for example Refs. [179, 210, 211]). The invariant mass m_{ll} tends to be small due to the spin correlation of the two leptons implied by the decay of a spin-0 particle, see Fig. 4. The $m_T(WW)$ distribution has instead a sharp kinematic edge at m_h . A further refinement of the Higgs reconstruction could be obtained by imposing a lower cut on the transverse momentum of the ll system, which might be useful to eliminate additional soft backgrounds not considered in this analysis. A lower cut on the transverse missing energy would also help. Here we try to keep our strategy as simple as possible, and do not attempt any further optimization of the Higgs reconstruction.

At this stage the background is still overwhelming the signal, and its largest component is $t\bar{t}jj$. A large reduction can be however obtained by selecting events where the $llbb$ system is very energetic. In particular, we impose:

$$m_{2b2l} \geq 500 \text{ GeV} \quad (13)$$

$$p_{Tbb} \geq 200 \text{ GeV} . \quad (14)$$

Sample	σ_I [fb]	σ_{II} [fb]	σ_{III} [fb]	$N_{ev} = \sigma_{III} \cdot \mathcal{L}$
SM	0.0008607	0.0005184	$4 \cdot 10^{-5}$	0.1
$c_V = 0.5$	0.0020	0.0012	$4.5 \cdot 10^{-4}$	1.4
$c_V = 1.5$	0.098	0.059	0.01508	45.2
$c_{2V} = 0.0$	0.019	0.011	0.003421	10.3
$c_{2V} = 2.0$	0.011	0.0063	0.002688	8.1
$c_3 = 0.0$	0.0024	0.0014	$6.0 \cdot 10^{-5}$	0.2
$c_3 = 2.0$	0.00074	0.00044	$2.4 \cdot 10^{-5}$	0.1
$WWbbjj$	788.1	14.86	–	–
$t\bar{t}jj \rightarrow WWbbjj$	779.7	14.52	< 0.0020	< 6.2

Table 3: Cut-flow for the analysis in the $2b2Wjj$ final state. Cross sections are reported for the signal and backgrounds after sequentially imposing: the selection cuts of Eqs. (3), (4) (σ_I); the Higgs reconstruction cuts of Eqs. (10), (11) (σ_{II}); the cuts of Eq. (13) (σ_{III}). At each stage all the previous cuts are also imposed. The values of the signal cross sections σ_I are the same as those reported in Table 1. The $t\bar{t}jj$ background appearing in the last line is included as a resonant subprocess of the $WWbbjj$ background. The last column shows the expected number of events after all cuts, $N_{ev} = \sigma_{III} \cdot \mathcal{L}$, for an integrated luminosity $\mathcal{L} = 3 \text{ ab}^{-1}$. Notice that b -tagging efficiencies have not been included.

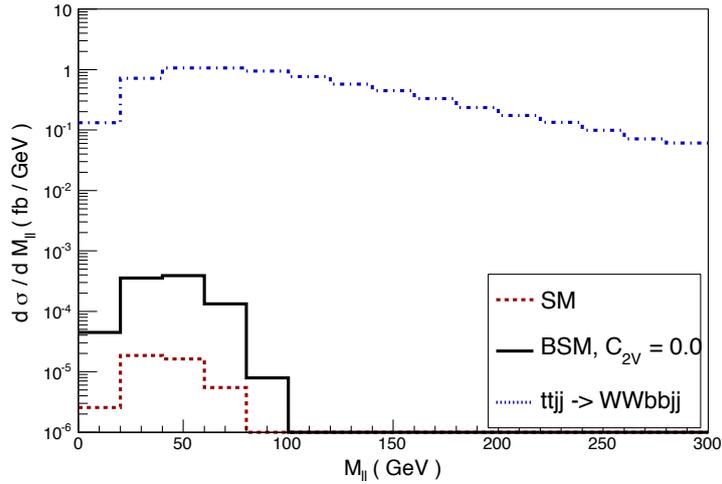


Figure 4: Invariant mass distribution of the ll system for the signal and the background after the selection cuts of Eqs. (3), (4), and the cut of Eq. (10).

The cut on the invariant mass of the $bbll$ system, m_{2b2l} , is quite efficient to suppress the background at the cost of a moderate reduction of the signal, see Fig. 5. The cut on the transverse momentum of the bb pair, p_{Tbb} , is strongly correlated with m_{2b2l} in the case of the signal and helps reducing the $t\bar{t}jj$ background.

After imposing Eqs. (13), (14) the cross sections are those reported in the column σ_{III} of Table 3. Although the number of generated events is too small in the case of the $WWbbjj$ background to allow us to get an precise calculation of its cross section after all cuts, a good estimate comes from the $t\bar{t}jj \rightarrow WWbbjj$ subprocess. It is reasonable to expect that the latter will account for the bulk of the $WWbbjj$ rate even after imposing Eqs. (13), (14). Under this assumption, Table 3 shows that despite the small number of events, in the case of strong

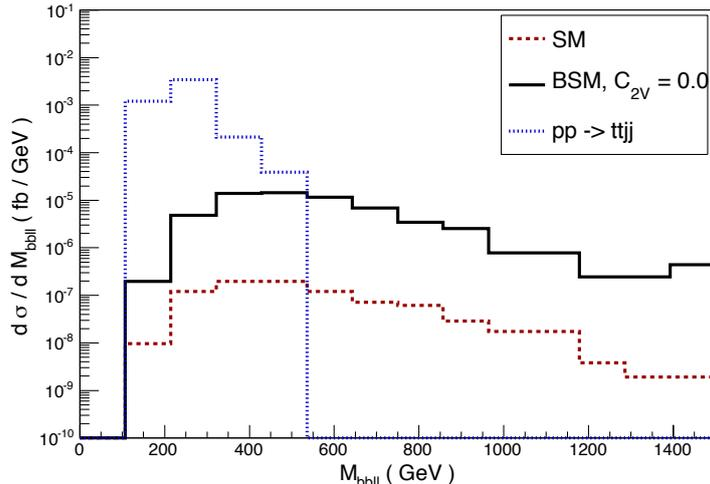


Figure 5: Invariant mass distribution of the $b\bar{b}l\bar{l}$ system for the signal and the background after the cuts of Eqs. (3), (4), (10), (11) and (14). The abrupt fall-off of the dotted blue curve around its end point is due to the limited statistics of our $t\bar{t}jj$ event sample.

double Higgs production the $2b2W$ channel offers a good sensitivity on c_V and c_{2V} . Isolating the SM signal or extracting the Higgs trilinear coupling, on the other hand, seems extremely challenging, even at a High-Luminosity phase of the LHC.

5 Conclusions and outlook

We have explored the feasibility of measuring Higgs pair production in the vector boson fusion channel at the LHC. While Higgs pair production via gluon fusion is key to pin down the Higgs self-coupling, c_3 , the VBF channel is especially sensitive to anomalous Higgs couplings to vector bosons, c_V and c_{2V} . Modifications of these couplings from their SM values imply a growth with the energy of the $VV \rightarrow hh$ partonic cross section, which in turn leads to potentially large enhancements of the production rate at the LHC. A previous study assumed a Higgs mass of $m_h = 180$ GeV and focused on the $hh \rightarrow 4W$ decay mode, concluding that the vector boson fusion channel is extremely challenging due to the large background and the small signal rates, even in the most optimistic BSM scenarios [179].

In this work we have revisited this process for a $m_h = 125$ GeV Higgs boson and concentrated on the $hh \rightarrow 4b$ and $hh \rightarrow 2b2W$ final states, which are those with the largest branching fractions. We performed a parton level analysis and followed a simple cut-and-count strategy. Our main results are summarized in Tables 2 and 3. We find that isolating the SM signal over the background is extremely challenging, if not impossible, in both channels. In the case of anomalous c_V and c_{2V} couplings, on the other hand, the signal can be more easily uncovered due to the larger rate and to a much harder spectrum of di-Higgs invariant mass that follows from the energy growth of the underlying partonic scattering. Our analysis suggests that a good sensitivity on c_{2V} can be obtained at the High-Luminosity LHC with 3 ab^{-1} . The sensitivity on c_3 , on the other hand, is extremely limited, and a measurement of this couplings seems rather challenging in the $4b$ and $2W2b$ decay modes even with high luminosity. In general, the $4b$ channel has a larger signal rate but it is plagued by a sizable QCD background. The $2b2W$ final state is cleaner and can lead to a large S/B in the most optimistic BSM scenarios, but it is characterized by smaller rates due to the leptonic branching ratios of the W bosons.

While our analysis was performed at the parton level and was intended to give a first assessment on the feasibility of observing di-Higgs production via VBF, it is clear that a more detailed estimate will require a more sophisticated simulation with hadronization and jet reconstruction. A realistic b -tagging algorithm is also required, since the finite light-jet mistag rates could substantially enhance the QCD backgrounds. In any case, jet substructure techniques and methods such as scale-invariant tagging that allow one to merge the boosted and resolved regimes, have the potential to help the S/B discrimination even in this more realistic scenario.⁶ We plan to present this work in a future publication, where we will determine the exact ranges of the c_V and c_{2V} parameters than can be explored at the HL-LHC.

In any case, it is clear that even at the HL-LHC, the measurement of Higgs pair production in the vector boson fusion channel is very challenging. In this sense, a future circular collider at 100 TeV would substantially increase the production rates and allow one to access a wider variety of final states like $2b2\gamma$ or $2b2\tau$, with complementary BSM sensitivity. As an additional goal of our future publication, we plan to study this process at $\sqrt{s} = 100$ TeV, and assess what is the reach in terms of BSM physics.

Let us finally mention that in this work we have only considered the non-resonant production of Higgs boson pairs in the VFB channel. Resonant production via the exchange of a new massive states could also increase substantially the event rates, and lead to a similar boosted final state topologies as the ones we find in the effective field theory approach.

Acknowledgments

We are grateful to Olivier Mattelaer for assistance with the Madgraph5 simulations and to Mauro Moretti and Fulvio Piccinini for assistance with the ALPGEN simulations. The work of R.C. was partly supported by the ERC Advanced Grant No. 267985 *Electroweak Symmetry Breaking, Flavour and Dark Matter: One Solution for Three Mysteries (DaMeSyFla)*.

⁶In addition, a suitable optimization of the jet radius R can be used to improve the performance of the kinematic reconstructions of the Higgs mass in the $b\bar{b}$ final state minimizing the contamination from QCD radiation, underlying event and pile-up [212].

Contribution 11

Triple Gauge Couplings at LEP revisited

A. Falkowski, S. Fichet, K. Mohan, F. Riva, V. Sanz

Abstract

We study the constraints on anomalous triple couplings of electroweak gauge bosons imposed by WW cross section measurements at LEP. We give the bounds on all eleven CP-even and CP-odd anomalous couplings when only one coupling is switched on at a time. Then we move to the effective theory approach with the Standard Model supplemented by dimension-6 operators. For the three coefficients of CP-even dimension-6 operators that modify the triple gauge couplings we provide a simultaneous fit including correlations.

1 Introduction

Triple gauge couplings (TGCs) of electroweak (EW) gauge bosons can be probed in collisions where a pair of gauge bosons is produced. This program started in the second phase of the LEP experiment (once the center of mass energy was sufficient for W^+W^- production), and has continued at the Tevatron and the LHC. The early motivation for this measurement was to establish the $SU(2)_L \times U(1)_Y$ symmetry structure of EW self-interactions. From the modern perspective, the study of TGCs is yet another precision test of the Standard Model (SM) that could potentially reveal the existence of new physics.

In the SM, the self-interactions of EW gauge bosons arise from the non-abelian structure of the field-strength tensor in the gauge kinetic terms:

$$\mathcal{L}^{\text{SM}} \supset -\frac{1}{4}W_{\mu\nu}^i W_{\mu\nu}^i, \quad W_{\mu\nu}^i = \partial_\mu W_\nu^i - \partial_\nu W_\mu^i + g_L \epsilon^{ijk} W_\mu^j W_\nu^k, \quad (1)$$

where W_μ^i, B_μ are the gauge fields $SU(2)_L \times U(1)_Y$, and the corresponding gauge couplings are denoted g_L, g_Y . It follows that the TGCs in the SM are given by $\mathcal{L}_{\text{TGC}}^{\text{SM}} = -g_L \epsilon^{ijk} \partial_\mu W_\nu^i W_\mu^j W_\nu^k$. After EW symmetry breaking, this leads to interactions between two charged and one neutral boson of the SM:

$$\mathcal{L}_{\text{TGC}}^{\text{SM}} = i \sum_{V=\gamma,Z} g_{WWV} [(W_{\mu\nu}^+ W_\mu^- - W_{\mu\nu}^- W_\mu^+) V_\nu + V_{\mu\nu} W_\mu^+ W_\nu^-], \quad (2)$$

whereas interactions between 3 neutral gauge bosons are absent in the SM Lagrangian. The coupling strength is uniquely fixed by the gauge couplings: $g_{WW\gamma} = e$, and $g_{WWZ} = eg_L/g_Y$, where $e \equiv g_L g_Y / \sqrt{g_L^2 + g_Y^2}$ is the electric charge. Going beyond the SM, TGCs between two

charged and one neutral boson can be generally parametrized as

$$\begin{aligned}
\mathcal{L}_{\text{TGC}} &= \sum_{V=\gamma,Z} g_{WW\gamma} (\mathcal{L}_{\text{TGC}}^+ + \mathcal{L}_{\text{TGC}}^-), \\
\mathcal{L}_{\text{TGC}}^+ &= i(1 + \delta g_1^V) (W_{\mu\nu}^+ W_\mu^- - W_{\mu\nu}^- W_\mu^+) V_\nu + i(1 + \delta\kappa_V) V_{\mu\nu} W_\mu^+ W_\nu^- \\
&\quad + i \frac{\lambda_V}{m_W^2} W_{\mu\nu}^+ W_{\nu\rho}^- V_{\rho\mu} - g_5^V \epsilon_{\mu\nu\rho\sigma} (W_\mu^+ \partial_\rho W_\nu^- - \partial_\rho W_\mu^+ W_\nu^-) V_\sigma, \\
\mathcal{L}_{\text{TGC}}^- &= i\tilde{\kappa}_V \tilde{V}_{\mu\nu} W_\mu^+ W_\nu^- + i \frac{\tilde{\lambda}_V}{m_W^2} W_{\mu\nu}^+ W_{\nu\rho}^- \tilde{V}_{\rho\mu} - \tilde{g}_4^V W_\mu^+ W_\nu^- (\partial_\mu V_\nu + \partial_\nu V_\mu),
\end{aligned} \tag{3}$$

where $V_{\mu\nu} = \partial_\mu V_\nu - \partial_\nu V_\mu$, $\tilde{V}_{\mu\nu} = \epsilon_{\mu\nu\rho\sigma} \partial_\rho V_\sigma$. The unbroken electromagnetic gauge invariance implies $\delta g_1^\gamma = g_4^\gamma = g_5^\gamma = 0$. We split these interactions into the CP-even (+) and CP-odd (-) parts.¹ The first five terms in $\mathcal{L}_{\text{TGC}}^+$ are C- and P-even, and follow the standard parametrization of Ref. [213, 214].² The last term proportional to g_5^V is C- and P-odd. The first two terms in $\mathcal{L}_{\text{TGC}}^-$ are C-even and P-odd, while the last one is C-odd and P-even. At the end of the day, we have 6 CP-even and 5 CP-odd couplings characterizing anomalous TGCs. The CP-even operators interfere with the SM amplitudes, therefore their effects show up at the linear order in the coupling, while the CP-odd couplings show up only at the quadratic order. In the SM limit all these couplings are zero at tree level³.

Constraints on anomalous TGCs can be translated into constraints on masses and couplings of new physics models. In some scenarios these constraints are complementary to those provided by direct searches and other precision studies. Basically, TGCs can be generated by loops of any particles with EW charges. For example, in the MSSM one can generate TGCs via loops of sfermions, gauginos and Higgses [215, 216]. Light supersymmetric particles could evade direct constraints due to lack of missing energy as in RPV SUSY, or small cross sections, as in electroweakino production, yet they could be constrained by precise measurements of TGCs. See [216] for TGCs in warped extra dimensions, composite Higgs, and their interplay with Higgs, EW precision physics and direct searches.

The effect of new physics is very transparent in the effective theory approach to physics beyond the SM (BSM). At the leading order in the effective theory expansion there are three operators associated with CP-even deformations of EW TGCs, and two more with CP-odd ones. Of these five operators, two affect *only* the self-couplings of EW gauge bosons, and can be probed *only* via precision measurements of TGCs. Further three operators affect both the self-couplings and the couplings to the Higgs boson, leading to important synergy between the Higgs and TGC studies. Finally, two of these operators contribute to the Peskin-Takeuchi S-parameter [217] leading to an interplay between the TGC and precision constraints from the Z-pole observables.

In this article we revisit the bounds on TGCs from the measurements of the total and differential W^+W^- production at LEP-2. We use the combined results from all four LEP collaborations [218]. We extract bounds on anomalous TGCs for all the 11 couplings in Eq. (3). In this case, due to a large number of parameters and large degeneracies, we restrict to a one-by-one fit where only one anomalous coupling is switched on at a time. We then move to

¹C acts as $W^\pm \rightarrow -W^\mp$, $V \rightarrow -V$. P acts as $V_0 \rightarrow V_0$, $V_i \rightarrow -V_i$, $\partial_i \rightarrow -\partial_i$.

²The couplings [214] are related to the ones in Eq. (3) by $\kappa_V = 1 + \delta\kappa_V$, $g_1^Z = 1 + \delta g_1^Z$. Note that we take the sign of g_{WWV} opposite to that of Ref. [214] because we use a different convention to define covariant derivatives: $D = \partial - igV$, as opposed to $D = \partial + igV$ in Ref. [213]. This corresponds to flipping the sign of all gauge fields.

³SM loops contribute to TGCs [215].

the parametrization of the TGCs in terms of the dimension-6 operators beyond the SM. We present constraints on the coefficients of the three CP-even operators contributing to anomalous TGCs, including their correlation. Previously, equivalent fits were performed by LEP's DELPHI collaboration [219], but no combined LEP constraints were available in this form. Our result is given in the form that can be readily combined with the Higgs results and other precision experiments.

2 One-by-one constraints on anomalous TGCs

In this section we derive bounds on TGCs in the case when only one anomalous coupling is switched on at a time. In Ref. [218] the LEP collaborations report combined measurements of the $e^-e^+ \rightarrow W^-W^+$ cross sections at different center-of-mass energies \sqrt{s} . We use the total cross sections for eight values of \sqrt{s} from Table 5.3 of Ref. [218], and the corresponding correlation matrix ρ from Table E.3 of Ref. [218]. We also use the differential cross section as function of the scattering angle between W^- and e^- for four values of averaged \sqrt{s} listed in Table 5.6 of Ref. [218]. For the differential cross sections the correlation matrix is not given; we assume these measurements are uncorrelated with each other and with the total cross section measurement.⁴ We collectively denote the measured central values of these observables as σ_{exp}^I , and the experimental errors as $\Delta\sigma_{\text{exp}}^I$. To compare these results with theoretical predictions, we first compute analytically these cross sections at tree level as function of the anomalous couplings in Eq. (3). The result can be split as $\sigma_{\text{LO}}^I = \sigma_{\text{LO,SM}}^I + \delta\sigma_{\text{LO}}^I$, where $\sigma_{\text{LO,SM}}^I$ is the tree-level SM cross-section, and $\delta\sigma_{\text{LO}}^I$ is the shift of the cross section due to anomalous TGCs that depends linearly (interference terms) and quadratically (new physics squared terms) on these couplings. In principle, the $e^-e^+ \rightarrow W^-W^+$ cross section could be affected by other deformations of the SM, for example modifications of the Z-boson mass and couplings to fermions, or the mixing between the $U(1)_Y$ and $SU(2)_L$ gauge bosons. These are however strongly constrained by other precision measurements, especially by the Z-pole constraints from LEP-1 and SLC [220]. Taking into account these constraints, these deformations have negligible effects on the WW production at LEP. To evaluate $\delta\sigma_{\text{LO}}^I$ we take the SM gauge couplings $g_L = 0.650$, $g_Y = 0.358$, and the masses $m_Z = 91.1876$ GeV, $m_W = 80.385$ GeV. Then the theoretical prediction is taken $\sigma_{\text{th}}^I = \sigma_{\text{NLO,SM}}^I + \delta\sigma_{\text{LO}}^I$.

For the SM NLO predictions $\sigma_{\text{SM,NLO}}^I$ we use the results from the RACOONWW code [221] that we borrow from from Table E.4 (total cross section) and Fig. 5.4 (differential cross section) of Ref. [218]. Finally, we construct the χ^2 function:

$$\chi^2 = \sum_{IJ} \frac{\sigma_{\text{NLO,SM}}^I + \delta\sigma_{\text{LO}}^I - \sigma_{\text{exp}}^I}{\Delta\sigma_{\text{exp}}^I} \rho_{IJ} \frac{\sigma_{\text{NLO,SM}}^J + \delta\sigma_{\text{LO}}^J - \sigma_{\text{exp}}^J}{\Delta\sigma_{\text{exp}}^J}. \quad (4)$$

Minimizing this χ^2 we obtain the central values, 1σ error and the 95% CL intervals for the anomalous TGCs when only one such coupling is present at a time. For the CP-even ones we find

$$\begin{aligned} \delta g_1^Z &= -0.10_{-0.05}^{+0.05}, & -0.19 < \delta g_1^Z < 0.00, \\ \delta \kappa_\gamma &= -0.03_{-0.04}^{+0.04}, & -0.10 < \delta \kappa_\gamma < 0.04, \end{aligned}$$

⁴This is clearly not a realistic assumption. Note however that the differential cross section measurements use a smaller subset of the data than the total cross section measurements, therefore it is not trivial to estimate the correlation between these observables.

$$\begin{aligned}
\delta\kappa_Z &= -0.07_{-0.04}^{+0.04}, & -0.14 < \delta\kappa_Z < 0.01, \\
\lambda_\gamma &= -0.05_{-0.04}^{+0.04}, & -0.12 < \lambda_\gamma < 0.04, \\
\lambda_Z &= -0.08_{-0.04}^{+0.04}, & -0.15 < \lambda_Z < 0.00, \\
g_5^Z &= -0.10_{-0.09}^{+0.09}, & -0.28 < g_5^Z < 0.08.
\end{aligned} \tag{5}$$

The fit to the LEP WW data can be improved by $\Delta\chi^2 \approx 4$ with respect to the SM if one of the anomalous couplings $\delta g_{1,Z}$, $\delta\kappa_Z$, or λ_Z is present. Note however that generic models beyond the SM will induce several anomalous couplings rather than just one. In the one-by-one fit the results depend very weakly on whether the quadratic corrections in anomalous couplings to the WW observables are kept or neglected.

For the CP-odd anomalous couplings we find

$$\begin{aligned}
\tilde{\kappa}_\gamma &= 0.00_{-0.15}^{+0.15}, & |\tilde{\kappa}_\gamma| < 0.24, \\
\tilde{\kappa}_Z &= 0.00_{-0.11}^{+0.11}, & |\tilde{\kappa}_Z| < 0.17, \\
\tilde{\lambda}_\gamma &= 0.00_{-0.12}^{+0.12}, & |\tilde{\lambda}_\gamma| < 0.18, \\
\tilde{\lambda}_Z &= 0.00_{-0.09}^{+0.09}, & |\tilde{\lambda}_Z| < 0.14, \\
\tilde{g}_4^Z &= 0.00_{-0.20}^{+0.20}, & |\tilde{g}_4^Z| < 0.32.
\end{aligned} \tag{6}$$

In this case $\delta\sigma_{LO}^I$ depends only quadratically on the anomalous couplings, which is the reason why the constraints are weaker than for the CP-even ones. Apparently, the fit to the WW LEP data cannot be improved at all if only CP-odd anomalous couplings are present.

3 Constraints on dimension-6 operators from TGCs

3.1 Effective Lagrangian

With the LHC discovery of the Higgs scalar and the study of its properties, experiments have finally addressed all aspects of the SM and more information on the EW sector has been gained. In particular, a linearly-realized EW symmetry breaking (EWSB) sector, described by an $SU(2)_L$ doublet H that obtains VEV, is clearly favored. Given the experimental data it is fair to assume that H is the only source of EW symmetry breaking. Moreover, no other states beyond those predicted by the SM have been found in the first LHC run. Thus, it is reasonable to assume that fundamental interactions at the weak scale can be described by the SM Lagrangian supplemented by higher-dimensional operators representing the effects of heavy new physics states.

We consider the effective Lagrangian of the form

$$\mathcal{L}_{\text{eff}} = \mathcal{L}_{\text{SM}} + \mathcal{L}^{D=5} + \mathcal{L}^{D=6} + \dots \tag{7}$$

The first term is the SM Lagrangian. The following ones contain $SU(3)_C \times SU(2)_L \times U(1)_Y$ invariant operators of dimension $D > 4$ constructed out of the SM gauge, fermion and Higgs fields that modify the predictions of the SM. In the effective Lagrangian philosophy, one assumes that the lowest dimension operators have the largest impact on observables. The only operators at $D = 5$ that one can construct are of the form $(LH)^2$; these give masses to neutrinos and are irrelevant for the present discussion. At $D = 6$ there are 3 CP-even and 2 CP-odd

operators that affect the self-couplings of EW gauge bosons. In a convenient basis⁵ they can be written as⁶

$$\begin{aligned}\mathcal{L}_{\text{TGC}}^{D=6} &= \frac{c_{WB}g_Lg_Y}{m_W^2}B_{\mu\nu}W_{\mu\nu}^iH^\dagger\sigma^iH + \frac{ic_Wg_L}{2m_W^2}\left(H^\dagger\sigma^i\overleftrightarrow{D}^\mu H\right)(D^\nu W_{\mu\nu})^i + \frac{c_{3W}g_L^3}{m_W^2}\epsilon^{ijk}W_{\mu\nu}^iW_{\nu\rho}^jW_{\rho\mu}^k \\ &+ \tilde{c}_{WB}\frac{g_Lg_Y}{m_W^2}\tilde{B}_{\mu\nu}W_{\mu\nu}^iH^\dagger\sigma^iH + \frac{\tilde{c}_{3W}g_L^3}{m_W^2}\epsilon^{ijk}W_{\mu\nu}^iW_{\nu\rho}^j\tilde{W}_{\rho\mu}^k.\end{aligned}\quad (8)$$

The coefficients c_i are formally of order m_W^2/M^2 , where M is the mass scale of new physics, and need to satisfy $c_i \ll 1$ for the effective theory approach to be valid. The anomalous TGCs in Eq.(3) are expressed by the coefficients of these 5 operators as

$$\begin{aligned}\delta\kappa_\gamma &= 4c_{WB}, \\ \delta\kappa_Z &= -4\frac{g_Y^2}{g_L^2}c_{WB} - \frac{g_L^2 + g_Y^2}{2g_L^2}c_W, \\ \delta g_Z &= -\frac{g_L^2 + g_Y^2}{2g_L^2}c_W, \\ \lambda_\gamma = \lambda_Z &= -6g_L^2c_{3W}, \\ \tilde{\kappa}_\gamma &= 4\tilde{c}_{WB}, \\ \tilde{\kappa}_Z &= -4\frac{g_Y^2}{g_L^2}\tilde{c}_{WB}, \\ \tilde{\lambda}_\gamma = \tilde{\lambda}_Z &= -6g_L^2\tilde{c}_{3W},\end{aligned}\quad (9)$$

while g_4^Z and g_5^Z are not generated by dimension-6 operators. Notice that in minimally coupled theories only \mathcal{O}_W can be generated perturbatively at loop-level, the other operators being necessarily loop-induced [47, 94, 226].

Three of the operators in Eq.(8) contribute not only to TGCs but also affect the Higgs boson couplings. One obtains

$$\begin{aligned}\Delta\mathcal{L}_{\text{Higgs}} &= c_{WB}\frac{h}{v}\frac{4g_Y^2}{g_L^2 + g_Y^2}\left[2Z_{\mu\nu}Z_{\mu\nu} - \frac{g_L^2 - g_Y^2}{g_Lg_Y}\gamma_{\mu\nu}Z_{\mu\nu} - \gamma_{\mu\nu}\gamma_{\mu\nu}\right] \\ &+ c_W\frac{h}{v}\left[(\partial_\nu W_{\mu\nu}^+W_\mu^- + \text{h.c.}) + \partial_\nu Z_{\mu\nu}Z_\mu + \frac{g_Y}{g_L}\partial_\nu\gamma_{\mu\nu}Z_\mu\right] \\ &+ \tilde{c}_{WB}\frac{h}{v}\frac{4g_Y^2}{g_L^2 + g_Y^2}\left[2Z_{\mu\nu}\tilde{Z}_{\mu\nu} - \frac{g_L^2 - g_Y^2}{g_Lg_Y}\gamma_{\mu\nu}\tilde{Z}_{\mu\nu} - \gamma_{\mu\nu}\tilde{\gamma}_{\mu\nu}\right].\end{aligned}\quad (10)$$

However, since other dimension-6 operators also contribute to the same Higgs couplings, processes like $h \rightarrow \gamma\gamma$, $h \rightarrow Z\gamma$ and the total width of $h \rightarrow VV^*$ ($V = W, Z$) cannot constrain the parameters of Eq. (10) in a model independent way [94, 224, 206]. For example, the operators

⁵Several other bases are commonly used in the literature. In the *GIMR basis* [222, 223], instead of the operator \mathcal{O}_W in Eq. (8), one has a combination of $\mathcal{O}_D \equiv J_h^W \cdot J_f^W$, $\mathcal{O}_{4f} \equiv J_f^W \cdot J_f^W$, $\mathcal{O}'_{D^2} \equiv |H^\dagger D^\mu H|^2$ (the J_i^W are $SU(2)_L$ currents) that contribute to TGCs [94]. In the *SILH basis* [47, 30], instead of the operator \mathcal{O}_{WB} in Eq. (8), one has a combination of $\mathcal{O}_{HW} \equiv D_\mu H^\dagger \sigma^i (D_\nu H) W_{\mu\nu}^i$, $\mathcal{O}_{HB} \equiv D_\mu H^\dagger D_\nu H B_{\mu\nu}$, \mathcal{O}_W and the operators $\mathcal{O}_{BB} \equiv |H|^2 B_{\mu\nu} B_{\mu\nu}$, $\mathcal{O}_{WW} \equiv |H|^2 W_{\mu\nu}^i W_{\mu\nu}^i$ and $\mathcal{O}_B \equiv H^\dagger \overleftrightarrow{D}_\mu H D_\nu B_{\mu\nu}$. Of these, only two combinations of \mathcal{O}_{HW} , \mathcal{O}_{HB} , \mathcal{O}_W contribute to TGCs [47, 224, 206]. All these bases are equivalent up to total derivatives, and only two independent combinations contribute to TGCs, whatever the basis.

⁶For a translation between Higgs operators in the SILH basis and TGCs see Ref. [225].

$-\frac{c_{BB}g_Y^2}{m_W^2}|H|^2B_{\mu\nu}B_{\mu\nu}$ and $-\frac{c_{WW}g_L^2}{m_W^2}|H|^2W_{\mu\nu}^iW_{\mu\nu}^i$ in the dimension-6 Lagrangian also contribute to the CP-even Higgs coupling to photons, and therefore the LHC measurement of the $h \rightarrow \gamma\gamma$ rate constrains the combination $c_{WB} + c_{WW} + c_{BB}$, and not c_{WB} alone. Model independent constraints on the operators of Eq. (10) could come from measurements of the differential distribution $h \rightarrow V\bar{f}f$ or $V^* \rightarrow Vh$ [227, 228], but these observables do not provide at present any meaningful constraints. One concludes that the TGC constraints are *complementary* to the Higgs constraints [94, 206].

Finally, we note that the \mathcal{O}_{WB} and \mathcal{O}_W operators contribute to the S parameter, $\Delta S = \frac{32\pi}{g_L^2}(c_W + 8c_{WB})$. However, ΔS depends also on another dimension-6 operator $i\frac{c_{BgY}}{2m_W^2}H^\dagger\overleftrightarrow{D}_\mu HD_\nu B_{\mu\nu}$. So, again, there is no model independent bound on the magnitude of anomalous TGCs from EW precision tests.

3.2 Fit to LEP WW data

We now present the simultaneous fit of the coefficients c_i of the dimension-6 operators in Eq. (8) to the LEP WW data. We follow a similar procedure as described in Section 2, with one important modification. In the effective theory approach it is not consistent to retain the quadratic correction on c_i to the observables, unless dimension-8 operators are also included in the analysis. Indeed, the coefficients c_i are formally $\mathcal{O}(m_W^2/M^2)$ where M is the mass scale of new physics. Thus, c_i^2 is $\mathcal{O}(m_W^4/M^4)$, just like the coefficients of dimension-8 operators. For this reason, we only include linear terms in c_i in our expression for $\delta\sigma_{LO}^I$ in Eq. (4). As before, we ignore other deformations of the SM that are more strongly constrained by EW precision tests on the Z-pole. In particular, we assume that the new physics contributions to the kinetic mixing between the $U(1)_Y$ and $SU(2)_L$ gauge bosons, which in our parametrization is proportional to $c_W + c_B + 8c_{WB}$, is negligible as required by Z-pole constraints on the S parameter. With this procedure we obtain

$$c_{WB} = -0.01 \pm 0.03, \quad c_W = 1.18 \pm 0.56, \quad c_{3W} = -0.30 \pm 0.16, \quad (11)$$

with the correlation matrix

$$\rho = \begin{pmatrix} 1 & -0.72 & -0.78 \\ -0.72 & 1 & 0.99 \\ -0.78 & 0.99 & 1 \end{pmatrix}. \quad (12)$$

The huge errors for c_W and c_{3W} are due to a near-degeneracy along the direction $c_{3W} \approx -0.3c_W + 0.05$ with $c_{WB} \approx 0$. Note that because of that the central values of c_W and c_{3W} do not have any physical meaning: for $c_i \sim 1$ the contribution of higher-than-6 dimensional operators cannot be neglected. In fact, including the corrections quadratic in c_i to $\delta\sigma_{LO}^I$ into the fit would completely change the central values and the errors. This degeneracy arises because the new physics contributions to the $ee \rightarrow WW$ cross section mostly affect just one class of polarization cross sections where left-handed electrons produce one helicity-1 and one helicity-0 W boson. These polarization cross sections happen to depend the combination $c_{3W} + 0.3c_W$, with a weak dependence on \sqrt{s} , and the flat direction occurs where the new physics deformation of these cross sections is minimized. Actually, there is also a large contribution to the polarization cross sections where two helicity-0 W bosons are produced. These depend on c_W but not on c_{3W} , which naively should break the degeneracy. However, in this case the linear effects of c_W on $e_L e_L \rightarrow WW$ and $e_R e_R \rightarrow WW$ cross sections are of opposite sign and approximately

cancel between each other. The flat direction persists also in the 2D fit when c_{WB} is constrained to vanish. Nevertheless, the fit we provide can be useful for constraining new physics that predicts some relations between the parameters of the effective theory that do not coincide with the near-degenerate direction in the c_W - c_{3W} subspace. As an example, in the case when $c_{3W} = 0$ we obtain

$$c_{WB} = 0.03 \pm 0.02, \quad c_W = 0.18 \pm 0.07, \quad \rho = \begin{pmatrix} 1 & 0.79 \\ 0.79 & 1 \end{pmatrix}. \quad (13)$$

This 2D fit only weakly depends on whether or not we include the corrections quadratic in c_i to $\delta\sigma_{LO}^I$.

Conclusions

We presented a new analysis of TGCs using LEP data on WW production cross section. Our results go beyond the previous fits in two ways: *i*) in the one-by-one constraints on TGCs, we derived limits on C- and P-violating couplings, and *ii*) we performed a general analysis of TGCs in the framework of the effective theory with dimension-6 operators beyond the SM. For the latter, we presented simultaneous constraints on the three CP-conserving dimension-6 operators contributing to TGCs, including their correlations. This is relevant as typical new physics models generate more than one operator. We also identified a flat direction in the effective theory fit, due to an accidental approximate degeneracy of the dimension-6 operator contribution to the $ee \rightarrow WW$ cross section. This flat direction should be lifted by including the constraints from single W production at LEP, and di-boson production at the LHC. This will be attempted in future publications.

Acknowledgments

AF was supported by the ERC advanced grant Higgs@LHC. FR acknowledges support from the Swiss National Science Foundation, under the Ambizione grant PZ00P2 136932.

Natural Models

Contribution 12

Model Independent Analyses of Vector-Like Quarks

D. Barducci, L. Basso, A. Belyaev, M. Buchkremer, G. Cacciapaglia, A. Deandrea, T. Flacke, J.H. Kim, S.J. Lee, S.H. Lim, F. Mahmoudi, L. Panizzi, and J. Ruiz-Álvarez

Abstract

We propose three simplified models based on a singlet and two doublet Vector-like Quarks, which describe all the relevant phenomenology for the LHC, single and pair production and decays into third generation and light quarks, in terms of 3 independent parameters. Such models can be used to reinterpret present searches, define new searches that can potentially close in unexplored parameter regions, and also perform systematic studies of the flavor bounds.

1 INTRODUCTION: SIMPLIFIED MODELS

Heavy partners of the top quark are predicted by many New Physics scenarios, including Little Higgs Models, Extra Dimensions, and Composite Higgs Models [229, 230, 172, 231, 158, 232]. Such new partners can be scalars as in supersymmetric models or vector-like fermions, and are generally introduced in order to cancel the contributions of the quadratic divergences to the Higgs mass renormalization. The observation of new heavy quarks thus plays an important role in the investigation of the Higgs sector, and in understanding the generation of quark masses.

Although vector-like quarks are usually assumed to mix with the third generation only following hierarchy or naturalness arguments (for recent works, see for instance Refs. [233, 234, 235, 236]), the top partners can mix in a sizable way with lighter quarks while remaining compatible with the current experimental constraints [237, 238]. Recent New Physics scenarios now take into account this possibility and must be considered with attention. Indeed, the top partners interactions with the electroweak and Higgs bosons are generically allowed through arbitrary Yukawa couplings, implying that the branching ratios into light quarks can be possibly competitive with the top quark. Another possibility that has been recently investigated is to couple the vector-like quarks to heavier states, like for instance a composite vector, thus decaying directly into three quarks [239].

In these proceedings, we will limit ourselves to the latter case of mixing via Yukawa couplings: in this case, the new quarks can only decay into a standard quark plus a boson, W^\pm , Z or Higgs. The relative branching ratios are purely determined by the weak quantum numbers of the multiplet the new quark belongs to [240]. Experimental collaborations are now considering the interplay between the various decays in their searches: a combination of the various channels can be found on the public result pages of both ATLAS [241, 242, 243, 244] and CMS [245, 246, 247, 248] collaborations, with final states in the third generation. Couplings to light generation have also been considered in single production [249], and in some few cases in the decays (see for instance Ref. [241] for the case of a b-partner). Here we want to provide a simple and model independent framework where all the experimental effort can be reinterpreted,

and also provide new channels to analyze. To do so, we adopt the simplified model approach, and propose to study a single representation that couples to standard quarks via Yukawa interactions. A simple Lagrangian can be written down, following Refs. [250, 251, 238]. The lagrangian can be largely simplified by the observation that the mixing to the light quarks is dominantly chiral: the new vector-like quarks couple to left-handed quarks for singlets and triplets of SU(2), and to right-handed quarks for doublets. During the Les Houches workshop, it was decided to focus on 3 benchmark scenarios: one with a singlet top partner T , one with a doublet with standard hypercharge (T, B) , and one with exotic hypercharge $Y_{\text{doublet}} = 7/6$, consisting of (X, T) where X has the exotic charge $+5/3$. These three cases well approximate the phenomenology of realistic models, even in the case where more states are present with near-degenerate masses (see Appendix of Ref. [238]). Also, 3 parameters are enough to encode all the model dependence relevant for the LHC:

- M , the vector-like mass of the multiplet, which is equal to the mass of the new quarks up to small corrections due to the mixing to the standard quarks;
- g_* , which represent a common coupling strength to light quarks in units of standard couplings, and which is only relevant when discussing single production;
- R_L , which describes the rate of decays to light quarks with respect to the third generation, so that $R_L = 0$ corresponds to coupling to top and bottom only, while $R_L = \infty$ coupling to light quarks only.

As an example, the Lagrangian for the singlet case T is given by

$$\begin{aligned} \mathcal{L}_T = g_* \left\{ \sqrt{\frac{R_L}{1+R_L}} \frac{g}{\sqrt{2}} [\bar{T}_L W_\mu^+ \gamma^\mu d_L] + \sqrt{\frac{1}{1+R_L}} \frac{g}{\sqrt{2}} [\bar{T}_L W_\mu^+ \gamma^\mu b_L] + \right. \\ \left. \sqrt{\frac{R_L}{1+R_L}} \frac{g}{2 \cos \theta_W} [\bar{T}_L Z_\mu \gamma^\mu u_L] + \sqrt{\frac{1}{1+R_L}} \frac{g}{2 \cos \theta_W} [\bar{T}_L Z_\mu \gamma^\mu t_L] + \right. \\ \left. - \sqrt{\frac{R_L}{1+R_L}} \frac{gM}{2m_W} [\bar{T}_R H u_L] - \sqrt{\frac{1}{1+R_L}} \frac{gM}{2m_W} [\bar{T}_R H t_L + \frac{m_t}{M} \bar{T}_L H t_R] \right\} + h.c. \end{aligned} \quad (1)$$

where the subscripts L and R label the chiralities of the fermions. The last term proportional to the top mass m_t encodes a correction to the Higgs coupling which is suppressed by the top mass over the vector-like mass M , and it is only relevant for low masses. Analogously, we write down the Lagrangian for the doublet (X, T) :

$$\begin{aligned} \mathcal{L}_{(X,T)} = g_* \left\{ \sqrt{\frac{R_L}{1+R_L}} \frac{g}{\sqrt{2}} [\bar{X}_R W_\mu^+ \gamma^\mu u_R] + \sqrt{\frac{1}{1+R_L}} \frac{g}{\sqrt{2}} [\bar{X}_R W_\mu^+ \gamma^\mu t_R] + \right. \\ \left. \sqrt{\frac{R_L}{1+R_L}} \frac{g}{2 \cos \theta_W} [\bar{T}_R Z_\mu \gamma^\mu u_R] + \sqrt{\frac{1}{1+R_L}} \frac{g}{2 \cos \theta_W} [\bar{T}_R Z_\mu \gamma^\mu t_R] + \right. \\ \left. - \sqrt{\frac{R_L}{1+R_L}} \frac{gM}{2m_W} [\bar{T}_L H u_R] - \sqrt{\frac{1}{1+R_L}} \frac{gM}{2m_W} [\bar{T}_L H t_R + \frac{m_t}{M} \bar{T}_R H t_L] \right\} + h.c. \end{aligned} \quad (2)$$

In the latter note the absence of the coupling of T with the W because the mixing is dominantly right-handed (a left-handed term exists, however it is suppressed by the light quark mass). The Lagrangian for the doublet (T, B) can be constructed as above. Note that in the Lagrangians above, we coupled the new quarks to the first generation: the reason for this choice is that a coupling to both first and second generation would lead to strong flavor bounds, thus we chose the first generation to enhance the single-production cross sections.

The Lagrangians for the three simplified models have been implemented in FeynRules [252, 253], and the validated model files can be found on the official website ¹. The model files also

¹<http://feynrules.irmp.ucl.ac.be/wiki/VLQ>

include gauge couplings between two vector-like quarks and electroweak gauge bosons, which may be relevant for some electroweak pair production processes. The three free parameters are set to the benchmark values: $g_* = 0.1$, which is in rough agreement with bounds on first generation couplings, $M = 1$ TeV and $R_L = 0.5$.

The main goal of this working group on vector-like quarks is to use these simplified models as test scenarios at the LHC for both present searches and new ones. As the case of couplings to third generation have been already extensively studied by the experimental collaborations, we will focus on single production channels and the couplings to light quarks. Single production, in fact, is the only channel that allows a direct test of the coupling strength g_* , i.e. of the level of mixing between the vector-like quarks and the standard model ones. During the workshop at Les Houches, samples of data have been produced and tested using MadGraph version 5 [126], and for the LHC at 8 TeV of center of mass energy.

One interesting point that has been explored is the relevance of final states with 3 or more leptons. In fact, the increase in the lepton multiplicity when choosing the signature from the vector-like quark will eventually improve signal to background ratio, even though it would also lead to a decrease in the signal rates. The question is which lepton multiplicity is optimal for the best signal significance against the respective backgrounds. It was shown in Ref. [254] that in case of Minimal Universal Extra Dimensions (MUED) the tri-lepton signature plays a leading role for the LHC sensitivity to the MUED scale. At the same time, for a generic vector-like quark model, it is not obvious since the lepton multiplicity drops faster than in the MUED case due to real Z and W -bosons which appear in the decay chains. Eventually their decay branching ratios are dominated by hadronic channels. A preliminary analysis performed under the assumption of decays to third generation only ², i.e. $R_L = 0$, confirms that tri-lepton signatures play the leading role for the LHC sensitivity to pair production. This statement is also confirmed by recent CMS studies [245] on inclusive searches for a vector-like T quark at 8 TeV LHC. The current combined limit on the T mass varies between 687 and 782 GeV depending on the different channels contribution, and it is primarily driven by the tri-lepton signature which is far better than the single-lepton channel and visibly better than di-lepton channel. Therefore the tri-lepton channel is expected to play also the leading role for 13 TeV LHC projection. We also studied the impact of tri- and four-lepton signatures to the case of significant mixing to light quarks, i.e. $R_L > 0$, as reported in Section 2.

Multi lepton signatures can also play a role in single production: in this case, however, due to the smaller number of gauge bosons in the final state, the cross sections for the leptonic signatures are rather small. Thus, fully hadronic signatures have the advantage of larger effective cross sections and a careful reconstruction of the final state kinematics may allow to beat the large backgrounds, as described in Section 3. On the other hand, from the results in Section 4, tri-lepton final states may have a better chance at higher energies. Finally, the presence of the Higgs in the final state coming from decays of the vector-like quarks [255, 251] offers new interesting search channels, as studied in Section 5.

The simple parametrisation we propose here can also be used for a systematic study of the flavor bounds on the mixing to light and heavy generations. This step is in fact crucial in order to have an independent estimate of the maximum allowed mixing, i.e. maximum possible g_* , and therefore the impact of single production to the future search strategies. In fact, single production decreases with increasing vector-like mass in a slower fashion than pair production, therefore at higher masses single production may become more important than QCD pair pro-

²Work in progress by A. Belyaev, D. Barducci and L. Panizzi.

duction. Efforts in the direction of a systematic study of flavor bounds have been initiated after this Les Houches workshop.

2 PAIR PRODUCTION: TRI- AND FOUR-LEPTON SIGNATURES³

Selecting events with one charged lepton, same-sign and opposite-sign di-leptons have been shown to provide efficient channels for vector-like quark searches (see, e.g., the CMS searches [256, 245]). Despite a reduced production rate, three and four lepton signatures may also be used to uncover such new heavy states. Events with multileptons, jets and missing energy have been considered in the framework of pair-produced heavy quarks coupling to the top quark, but not yet to the lighter generations. In this section, we report on tentative new strategies for future top partner searches at the TeV scale, with three and four charged leptons in the final state, and considering general assumptions on their mixings with all three Standard Model quark families.

For convenience, we exemplify our analysis with the T singlet and (X, T) doublet scenarios. As a representative parameter point for our analysis, we considered $g^* = 0.1$ and $M = 500$ GeV for the mass of the heavy quarks. The R_L parameter is set to 0.5, allowing for generic mixings with the first, second and third SM quark families. The vector-like quarks can therefore decay both into a third generation quark, top or bottom, and a light jet. This benchmark scenario allows for non-exclusive decay modes, so that channels with mixed decays, where one heavy quark decays to a top and the other to a light jet, contribute to several signal regions. Interestingly, the possibility for top partners coupling simultaneously to the light and the third quark generations opens the production modes

$$pp \rightarrow Q\bar{Q} \rightarrow Vt + V'j \text{ with } Q = X, T \text{ and } V^{(\prime)} = W, Z, H, \quad (3)$$

which are not allowed for the exclusive mixing scenarios $R_L \rightarrow 0$ and $R_L \rightarrow \infty$, and lead to novel signatures with boosted objects, one top quark and at least two jets with large transverse momentum, one being a b -quark. Such topologies are always present for $R_L > 0$, and allow for final states with three and four leptons. As an illustration, we depict in Fig. 1 the multilepton signatures

$$pp \rightarrow T\bar{T} \rightarrow ZtZ\bar{q} \rightarrow l^+l^-l^+\nu b\bar{q}'\bar{q}', \quad (4)$$

$$pp \rightarrow X\bar{X} \rightarrow W^+tW^-\bar{q} \rightarrow l^+\nu l^-\nu l^-\nu b\bar{q}, \quad (5)$$

$$pp \rightarrow T\bar{T} \rightarrow ZtZ\bar{q} \rightarrow l^+l^-bq'\bar{q}'l^+l^-\bar{q}, \quad (6)$$

as representative decay channels for pair-produced top partners. For the simplified scenarios considered here, one of the two decay channels $ZtZj$ and $WtWj$ is always present. Assuming non-exclusive coupling to the first or the third generation, i.e., considering $R_L = 0.5$, the total contribution of the $top + jets$ final states in $pp \rightarrow Q\bar{Q}$ pair-production sums up to a total branching ratio of $2R_L/(1 + R_L)^2 = 44.4\%$ with respect to the full signal.

The final states of interest for our analysis are

$$pp \rightarrow l^\pm l^\pm l^\mp + n \text{ jets} + \text{MET}, \quad (7)$$

$$pp \rightarrow l^+ l^- l^+ l^- + n \text{ jets} + \text{MET}, \quad (8)$$

where the number of jets depends on the underlying process. Multilepton signatures are well known to avail themselves of low background contamination. The Standard Model processes

³Contributing authors: G. Cacciapaglia, M. Buchkremer

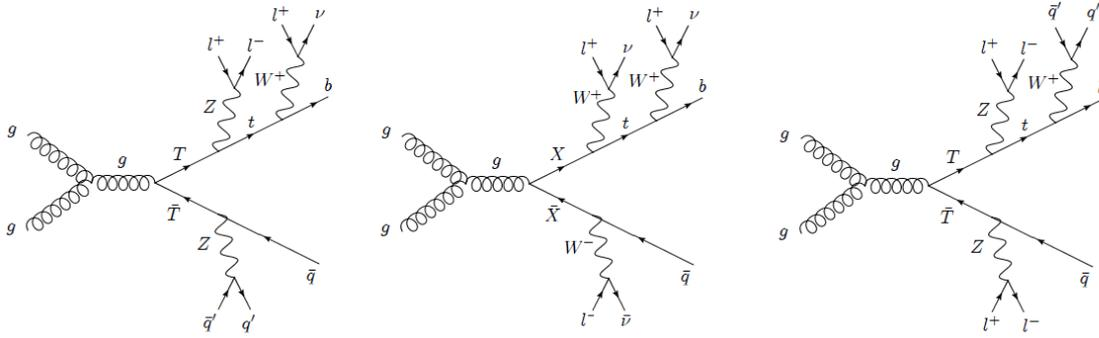


Figure 1: Representative $T\bar{T}$ and $X\bar{X}$ pair-production channels to three-lepton (left, middle) and four-lepton (right) final states in non-exclusive mixing scenarios (e.g., with $R_L > 0$).

leading to possibly significant background to trilepton events involve $t\bar{t}$ production in association with W and Z bosons, diboson, and triboson decays. As for four lepton candidate events, the backgrounds involving two pairs of leptons can be produced in hard interactions, including ZZ and $Zt\bar{t}$ production in association with jets. The prompt decays to three (four) charged leptons from WZ (ZZ) production with (without) transverse missing energy may also generate a significant source of misidentification if both bosons decay leptonically. Given its large production cross section, $t\bar{t} + jets$ provides another potential background to trilepton signals if the two underlying W bosons decay leptonically and one bottom quark gives a third isolated lepton. Yet, the latter (reducible) background has not been included in our analysis as we cannot estimate it at the parton-level. Similarly, possible contributions from non-prompt or fake lepton candidates have been neglected. These background sources are expected to be severely suppressed when imposing appropriate cuts on the number of jets, total hadronic transverse energy H_T and missing transverse energy MET.

Minimal requirements on relevant variables such as, e.g., the missing transverse momentum of the signal or the number of jets, have been set so to avoid the main background contributions. The most problematic process for multilepton signals with three and four lepton candidates consists in the irreducible $Zt\bar{t} + jets$, whose events can involve one Z boson, two W bosons, two bottom quarks and large transverse energy. In Table 1, we summarise the production cross-sections for the signals and for the various backgrounds in the multilepton channels. All the background samples (i.e., $t\bar{t}$, ZZ , WZ , $Wt\bar{t}$ and $Zt\bar{t}$) used in this report have been generated at leading order with MadGraph5 [126], using the CTEQ6L1 parton distribution functions. Although we did not include them in the present analysis, the K-factors for pair-produced VLQ are known to lie in the range 1.5 – 1.8 for Vector-Like quark masses between 500 GeV and 1 TeV [257]. Parton showering and hadronization have been carried out with PYTHIA6 [258]. Event analysis has been performed with MadAnalysis5 [259]. Detector simulation is left for a more realistic analysis.

The MadGraph default cuts are used at the generation level, and we select events with electrons and muons having $p_T^l \geq 10$ GeV, within $|\eta|_l < 2.5$ ($l = e, \mu$). All jets are required to have transverse momentum larger than 20 GeV and pseudorapidity $|\eta| < 5$. The standard identification criteria for jet-lepton separation are applied. It is required that all final particles are isolated within a cone of $\Delta R = 0.4$. As for isolating the multilepton signal, we imposed the

Process	$\sigma \times BR(l^\pm l^\pm l^\mp)$ (fb)	$\sigma \times BR(l^+ l^- l^+ l^-)$ (fb)
T singlet signal ($M = 500$ GeV)	31.85 (55.10)	4.26 (7.36)
(X, T) doublet signal ($M = 500$ GeV)	112.06 (195.50)	11.89 (18.33)
ZZ background	25.62	57.97
WZ background	1092	–
$Wt\bar{t}$ background	17.93	–
$Zt\bar{t}$ background	19.70	3.434

Table 1: Leading order cross-sections computed with MadGraph5 at $\sqrt{s} = 14$ TeV for the three- and the four-lepton signal and background event samples, with no added jets. The NLO+NLL predictions for the signal are given in parentheses [257].

following requirements, in order:

- *Cut 1:* a minimum of three charged leptons must be identified with each $p_T > 10$ GeV, including at least one with $p_T > 20$ GeV.
- *Cut 2:* the signal events are selected so that they contain at least two jet constituents, including one b -tagged jet.
- *Cut 3:* all the events with total hadronic transverse energy H_T smaller than 300 GeV are rejected.

The optimisation of the cuts, so as to maximise the signal-over-background significance, is left for future work. Asking further for missing transverse energy $\text{MET} \geq 20$ GeV allows for a significant suppression of the QCD multi-jet background. Altogether, the above basic requirements significantly reduce the diboson backgrounds, while the contributions originating from $Zt\bar{t} + jets$, $WZ + jets$ and $ZZ + jets$ remain significant. We observe that the distributions for the signal and the background jet multiplicities, shown in Fig. 2, display similar shapes and are both peaked at $N_j = 5$ and $N_b = 2$. The p_T and η distributions of the leading jets and leptons for the multilepton event samples are also displayed against backgrounds.

Although a more aggressive cut on the total transverse energy, $H_T > 500$ GeV, significantly reduces the background for the considered benchmark, applying a more stringent selection on the transverse momenta of either the leading jets or the leptons also enhances sizably the signal significance. We also checked that requiring a forward-jet tag with a transverse momentum as large as 80 GeV suppresses most of the background arising from $Wt\bar{t} + jets$, while additionally asking $p_T > 70$ GeV for the second hardest jet removes most of the $Zt\bar{t} + jets$ contribution. A similar selection efficiency can be obtained by imposing $p_T > 100$ GeV and $p_T > 40$ GeV for the first and second hardest leptons, respectively. Alternatively, requiring the presence of *exactly* one b quark with $p_T > 20$ GeV and $|\eta| < 2.4$ allows to extract most of the signal, provided that no other b -jet is tagged. Setting cuts on p_T^b only mildly improves the selection efficiency. Other directions for refinement could involve mass reconstruction in specific decay modes, or using boosted techniques to increase the sensitivity.

Despite the fact that the total number of tri- and four-lepton events is expected to decrease significantly for larger masses, these signatures provide encouraging alternatives to search for pair-produced Vector-Like quarks in the forthcoming searches. This is true, in particular, for top partners having sizable mixings with both the light and the third SM quark generations, that are allowed to decay simultaneously to top quarks and light jets with high transverse momenta.

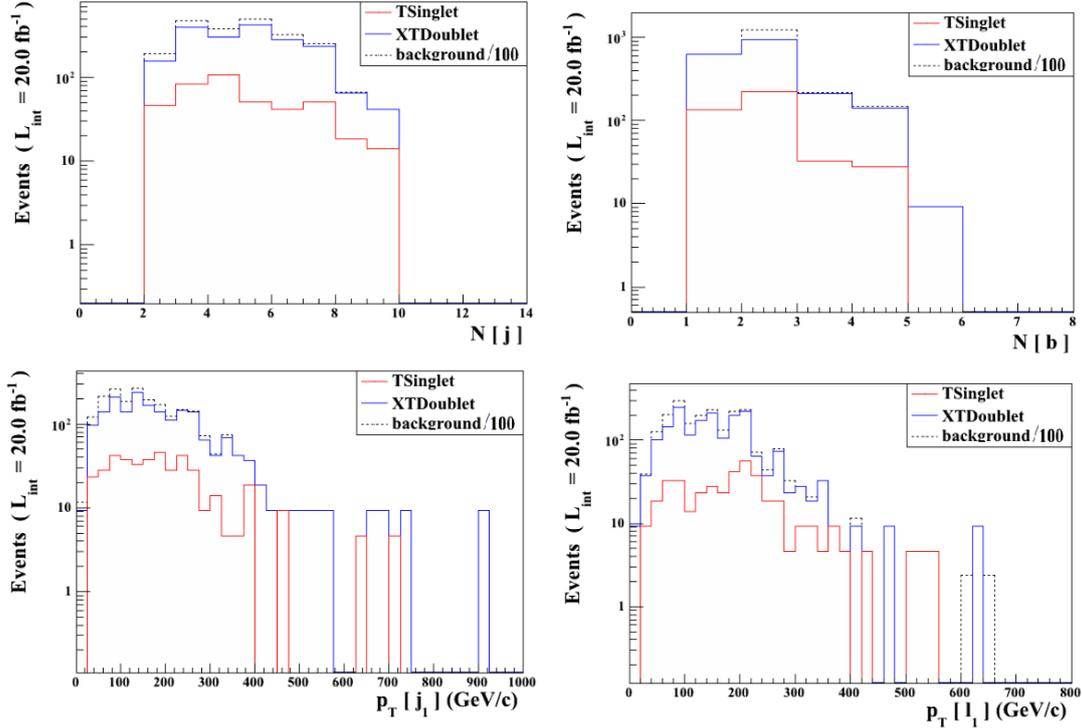


Figure 2: Leading order kinematical distributions for the light jets multiplicity (top left), the light jets transverse momentum (bottom left), the b -jets multiplicity (top right) and the b -jets transverse momentum (bottom right), in the three- and four-lepton channels, for an integrated luminosity of 20 fb^{-1} at the LHC 14 TeV. The total expected numbers of event is plotted for the T singlet (red) and (X, T) doublet (blue) signal models, versus the backgrounds (black), after imposing the standard cuts.

3 SINGLE PRODUCTION: FULLY HADRONIC SIGNATURE⁴

Single production of vector-like quarks can give information about the size of the mixing with the standard quarks, but also on the nature of the new particle itself. As an example, in this contribution we will consider the case of the doublet (X, T) , even though similar considerations can be done for the standard doublet (T, B) . Due to the suppression of the coupling to the W , the top partner T can be produced via coupling to the third generation only in association with a top quark, due to the absence of tops in the colliding protons. If an even small coupling to the first generation is allowed, then a new channel is open

$$pp \rightarrow Tj \rightarrow Htj \rightarrow b\bar{b}bjj. \quad (9)$$

The production here takes place via the coupling with a Z boson and an up quark. The decay, on the other hand, can be dominated by the third generation: here we will focus in particular on the decay to a Higgs, which fares about 50%, because we are interested in fully hadronic final states. Final states with leptons can be obtained when the T decays to a Z boson, however the event rate pays for the small leptonic Z fraction (the leptonic channel will be studied in the next section). The aim of our preliminary study is to show that it is in principle possible to reconstruct the T in a fully hadronic final state, and distinguish it from the dominant backgrounds.

⁴Contributing authors: G. Cacciapaglia, A. Deandrea, J.L. Ruiz-Álvarez

Process	XS (pb)	Ex. Events
QCD (bbjjj)	500	10000000
W+jets	37509	750180000
Z+jets	3503.71	70074200
$t\bar{t}$	234	4680000
t	114.85	2297000
Diboson	96.82	1936400

Table 2: Cross sections and number of events for backgrounds.

The final state we are interested in consists of 5 jets with high p_T , three of which being b-jets, coming from the T decays, and a more forward jet at production. In this analysis we considered the backgrounds listed in Table 2, where cross sections and number of events at 8 TeV for 20 fb^{-1} are also listed. All the events have been produced using MadGraph5 [126], and Pythia 6 [258] for the hadronization of the samples at parton-level. Proper matching between the hard radiation generated by MadGraph and the soft ISR/FSR radiation added by Pythia have been implemented. For the QCD sample, jets were produced with a $p_T > 30$ GeV and within $|\eta| < 5$. All the other background samples have jets with $p_T > 10$ GeV, while no pseudo-rapidity cut have been imposed. In samples containing at least one Z (di-boson processes ZZ and WZ , and Z +jets) the mass of the di-lepton pair was required to be $M_{ll} > 50$ GeV. Finally, the signal sample has been produced with $p_T > 10$ GeV on jets. For the signal with $M_T = 734$ GeV around 700 events were expected at 8 TeV with 20 fb^{-1} , where the couplings have been chosen to reproduce the benchmark point in Ref. [238]. For this mass point the signal has a cross section around 200 fb.

An important feature of the fully hadronic channel is the possibility of having a bump-hunt strategy: in fact, a full reconstruction of all the decay products coming from the top partner is possible. Our goal is therefore to find a bump in the invariant mass distribution for the five jets coming from T . The same distribution on the backgrounds should be flat-falling, while the cuts may affect this expected shape. The main difficulty with this strategy is the dependence on the good identification of the jets that reconstruct the T decay.

As a positive point, various characteristics of the signal can be exploited in order to differentiate it from the backgrounds. We propose in this short study two variables of interest. First, the production process of the top partner generates also a light quark that adds an extra jet in the event. In Figure 3 the pseudorapidity η distribution for this additional jet is shown at parton level, showing that it is mainly a forward jet as expected. It should be useful therefore to require that each event has at least one jet with $|\eta| > 2.5$. Second, as the top partner has a large mass, signal events should have a substantial deposit of energy from all the decay products in the detector. This can be studied with the total hadronic energy of the event, defined as $H_T = \sum |p_T^j|$. In Figure 3 the distribution for this variable is shown for the signal and different backgrounds. From the H_T plot, it is possible to say that cutting around 600 GeV will help to extract the signal.

Finally, in order to reduce the combinatorics when reconstructing the T it should be useful to require two b tags, either for the full identification of the Higgs and for the identification of the top and one of the jets coming from the Higgs. Even though requiring $H \rightarrow b\bar{b}$ closes up some decay channels of the Higgs, this choice will surely lead to a better reconstruction of the mass peak, and additionally will lead to kill a lot of the background coming from QCD processes. In

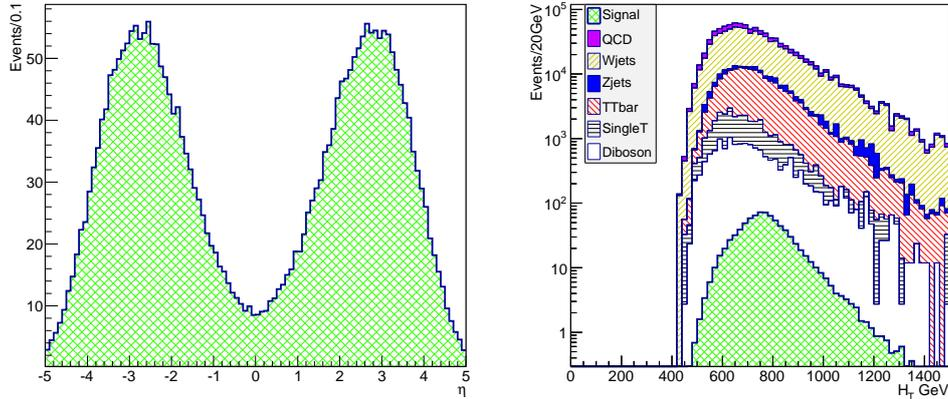


Figure 3: *LEFT: pseudorapidity η of the associated light jet at parton level. RIGHT: total hadronic energy for backgrounds (stacked) and signal (overimposed).*

Figure 4 the mass peak of the T is shown using two b tags and selecting other three jets to be compatible with the top and Higgs as decay products coming from the top partner.

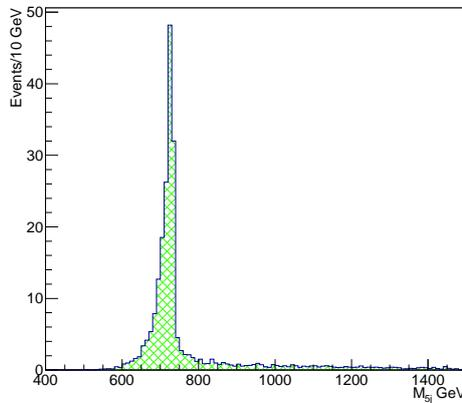


Figure 4: *Reconstructed T mass for the signal sample.*

4 SINGLE PRODUCTION: TRI-LEPTON SIGNATURE⁵

As previously mentioned, an interesting scenario is the case of the singlet vector-like top partner coupling both to first and third generation quarks. In the case of single production, the T' is produced in association with a light jet, and it can decay into a Z boson and a top quark. A very rich final state can hence be studied. In this subsection, we concentrated on the largest lepton

⁵Contributing author: L. Basso

multiplicity, namely a trilepton signature, as follows:

$$pp \rightarrow jT' \rightarrow jZt \rightarrow j(\ell^\pm \ell^\mp) b\ell^\pm \nu. \quad (10)$$

Backgrounds to this signature are mainly the reducible $WZjj$, $t\bar{t}$, and $t\bar{t}\ell\nu$, and the irreducible tZj . The difference between the two backgrounds encompassing top quarks arise from the source of the third lepton: in the $t\bar{t}$ case, a third lepton comes from a semi-leptonic B -hadron decay in the b -jet, whilst in the $t\bar{t}\ell\nu$ case, a prompt lepton is considered (from $t\bar{t}W$). Regarding $t\bar{t}$, the main suppression comes from requiring that the leptons are isolated, as the one stemming from the b -jet passes this selection only in about few percent of the cases. Further, it is strongly reduced by the reconstruction of the leptonic vector bosons (W and Z) as in the signal (despite leptonic W bosons being present, the combinatorics in reconstructing first the Z boson heavily affect it). We therefore expect it to be comparable to all others, despite the large $t\bar{t}$ production cross section of 25 pb (when both top quarks decay semi-leptonically).

We start by pinning down the properties of the signal at parton level. The cut flow for this analysis is as follows: first we apply typical detector acceptances as follows: $p_T^\ell > 20$ GeV, $p_T^j > 40$ GeV, $|\eta_{j(\ell)}| < 2.5$, where $\ell = e, \mu$ and η_j is restricted only to the tracker to allow for b -tagging. Further, all final state particles are required to be isolated in a cone of $\Delta R_{jj} = \Delta R_{\ell j} = 0.5$ and $\Delta R_{\ell\ell} = 0.2$, for jets and leptons, respectively. The analysis is carried out in the MadAnalysis package [259]. Then, the pair of leptons that best reconstructs the Z boson is chosen, with the third lepton assigned to the W boson, and further combined with the b -quark to reconstruct the top quark. We see in Figure 5 that this algorithm works very well. A window around the Z mass, $|M(\ell\ell) - 91.8 \text{ GeV}| \leq 20 \text{ GeV}$, is selected. Regarding the W boson, an asymmetric window $20 \text{ GeV} \leq M_T(\ell\nu) \leq 100 \text{ GeV}$ is selected. Finally, around the top quark, another asymmetric window $100 \text{ GeV} \leq M_T(b\ell\nu) \leq 190 \text{ GeV}$ is considered. The optimisation of these windows in order to maximise the signal-over-background sensitivity is left for future work.

Cross sections for the process of eq. (10) for $\sqrt{s} = 8 \text{ TeV}$ are too small to leave one with a sufficient amount of events: with the same benchmark [238] considered in the previous section, we obtain $\sigma(400 \text{ GeV}) = 2.5 \text{ fb}$ and $\sigma(600 \text{ GeV}) = 1.4 \text{ fb}$. We therefore study the sensitivity at 14 TeV and $\mathcal{L} = 20 \text{ fb}^{-1}$ including also the backgrounds described earlier on. At 14 TeV, cross sections for $pp \rightarrow tZj \rightarrow 3\ell + X$ ($\ell = e, \mu$) are as follows:

$T' (400 \text{ GeV}) :$	$\sigma = 4.0 \text{ fb},$	$tZj :$	$\sigma = 15.5 \text{ fb},$
$T' (600 \text{ GeV}) :$	$\sigma = 2.6 \text{ fb},$	$WZjj :$	$\sigma = 246.7 \text{ fb},$ (with generation cuts)
$T' (800 \text{ GeV}) :$	$\sigma = 1.6 \text{ fb},$	$t\bar{t}\ell\nu :$	$\sigma = 5.7 \text{ fb},$
		$t\bar{t} :$	$\sigma = 25.0 \text{ pb},$ ($\sigma_{2\ell}$)

For a more realistic analysis, we performed our study at hadron level, after showering (but without account for detector simulation, hence in a “perfect detector” scenario). All signal and background samples have been produced with CalcHEP 3.4 [189] (a part for the $t\bar{t}$ one done with MadGraph 5 [126]), and then showered with Pythia 6.4 [258]. Jet reconstruction has been performed with FastJet [170], employing the anti- k_T algorithm with radius $R = 0.5$. Further, b -tagging efficiency is set to 70% and light flavour mistagging to 10%. In our event selection, we require exactly 3 leptons, at least 2 jets of which exactly one is a b -jet, to further reduce $t\bar{t}$ backgrounds and the irreducible tZj , where j is mainly a b -jet. Numbers of events for $\mathcal{L} = 20 \text{ fb}^{-1}$ and relative efficiencies are given in Table 3, for our backgrounds and 3 benchmark masses for the signal.

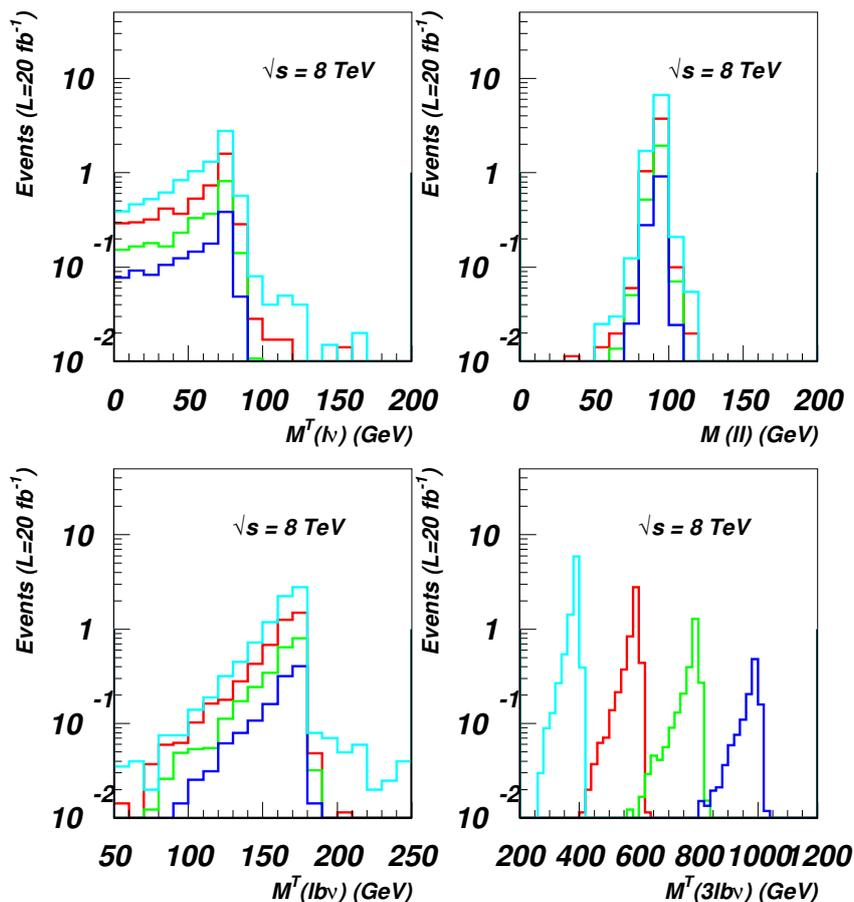


Figure 5: Plots for signal: (top-left) W -boson reconstruction: transverse mass of 1 lepton; (top-right) Z -boson reconstruction: invariant mass of pair of lepton closest in value to M_Z ; (bottom-left) top reconstruction: transverse mass of W -boson and b -quark; (bottom-right) T' reconstruction: transverse mass of b -quark and all 3 leptons.

After the last cut (i.e., the top reconstruction), the signal is clearly visible in the transverse mass of the b -jet and the 3 leptons, see Figure 6. It is clear that the largest background is the irreducible SM tZj , while the larger $WZjj$ is effectively suppressed by the b -tagging. Also $t\bar{t}$ is effectively reduced, and it has not a tail as the others. Notice that they all peak at roughly 300 GeV. 20 fb^{-1} seems to be a sufficient integrated luminosity to probe this channel for T' masses up to $\mathcal{O}(600)$ GeV, although a more realistic detector simulation is required to confirm its feasibility.

5 HIGGS SEARCHES FOR VECTOR-LIKE QUARK PARTNERS⁶

Vector-like (VL) quark partner searches in Higgs final states have been performed in the context of top partner searches [245], which assumes that dominant production channel for the top

⁶Contributing authors: T. Flacke, J.H. Kim, S.J. Lee and S.H. Lim

#	400 GeV	$\varepsilon(\%)$	600 GeV	$\varepsilon(\%)$	800 GeV	$\varepsilon(\%)$
0	79.4	—	51.4	—	31.5	—
1	48.4	61.0	34.6	67.4	20.8	66.0
2	6.7	13.7	4.3	15.4	3.3	15.8
3	5.2	78.4	4.0	74.1	2.3	70.2
4	4.5	86.1	3.5	89.3	2.1	89.5

#	tZj	$\varepsilon(\%)$	$WZjj$	$\varepsilon(\%)$	$t\bar{t}l\nu$	$\varepsilon(\%)$	$t\bar{t}$	$\varepsilon(\%)$
0	309.2	—	4934.0	—	114.3	—	$5 \cdot 10^5$	—
1	194.5	62.9	2078.8	42.1	35.9	31.4	937.7	0.2
2	23.4	12.0	57.3	2.8	4.6	12.8	69.4	7.4
3	19.9	84.8	47.5	83.0	1.2	25.8	35.9	51.7
4	17.3	87.2	14.1	29.6	0.5	40.8	19.2	53.3

Table 3: Events and efficiencies for 20 fb^{-1} after the application of cuts (efficiency always with respect to previous item) for (top) signal and (bottom) backgrounds. #0: no cuts, #1: only leptonic cuts, #2: only hadronic cuts and b -tagging, #3: W and Z reconstruction, #4: top reconstruction.

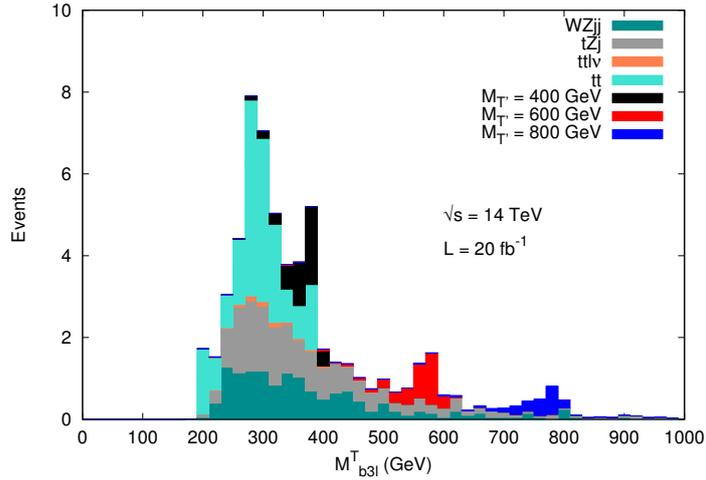


Figure 6: T' reconstruction: transverse mass of b -quark and all 3 leptons.

partner is through QCD pair production. The LHC bound for a top partner with 100% branching fraction (BR) into top plus Higgs is found to be $M > 706 \text{ GeV}$ [245]. On the contrary, a similar search for a VL bottom quark partner [246] does not yield bounds if 100% BR into bottom plus Higgs is assumed, and bounds for light quark family partners have mostly been obtained for partner decays into gauge bosons and jets [260].⁷ Only Ref. [262] established bounds on VL light quark partners in the Higgs channel from current LHC data, where the standard model Higgs searches from $H \rightarrow \gamma\gamma$ channel have been used. In this analysis, we generalize the study of Ref. [262], which was performed in the context of minimal composite Higgs models [153], into simplified models [238].

⁷For prospects of VL quark searches in Higgs channels *cf. e.g.* Refs. [261, 229, 251].

5.1 Vector-Like quark searches in Higgs final states – Models

In the following, we discuss searches for vector-like quark partners in Higgs final states. As we want to be more general than the simplified scenarios described in the Introduction, we will use in this study the Lagrangian proposed in Ref. [238], which describes single production and decay of a vector-like up-type quark partner ⁸:

$$\begin{aligned} \mathcal{L}_{T\text{single}} &= \kappa_W V_{L/R}^{4i} \frac{g}{\sqrt{2}} [\bar{T}_{L/R} W_\mu^+ \gamma^\mu d_{L/R}^i] + \kappa_Z V_{L/R}^{4i} \frac{g}{2c_W} [\bar{T}_{L/R} Z_\mu \gamma^\mu u_{L/R}^i] \\ &- \kappa_H V_{L/R}^{4i} \frac{M}{v} [\bar{T}_{R/L} h u_{L/R}^i] + h.c., \end{aligned} \quad (11)$$

where i is a family index. For simplicity, we focus on partners of purely the up-, charm-, or top-quark in what follows, *i.e.* we choose to keep partners of only one family in the following analysis. The Lagrangian in Eq. (11) can be identified with \mathcal{L}_T in the introduction by renaming $V_L^{4u} = \sqrt{\frac{R_L}{1+R_L}}$ and $V_L^{4t} = \sqrt{\frac{1}{1+R_L}}$, and setting $V_R^{4i} = 0$ and $\kappa_W = \kappa_Z = \kappa_H = g_*$ (thus neglecting the m_t/M term): large differences compared to this case can be achieved in models with large mixing between VL quarks. The “mixing” couplings described by the Lagrangian (11) arise when expressing the gauge and Higgs interactions of the SM-like quarks and the up-type partner in the mass eigenbasis. Mixing of SM-like quarks and the quark partner in the left-handed quark sector is strongly constrained from electroweak precision tests (*cf.* *e.g.* Refs. [263, 264]), while in the right-handed sector substantial mixing is possible [265]. To capture phenomenologically viable models, we study two sample scenarios.

In Model I, we assume $V_R^{4i} \gg V_L^{4i}$ and $\kappa_H \gg \kappa_{W,Z}$.⁹ The full effective Lagrangian of the model is given by

$$\mathcal{L}_{\text{eff}} = \mathcal{L}_{\text{SM}} + \bar{T} \left(i\partial_\mu + e\frac{2}{3}A_\mu - g\frac{2}{3}\frac{s_w^2}{c_w}Z_\mu + g_3G_\mu \right) \gamma^\mu T - M\bar{T}T - \left[\lambda_{\text{mix}}^{\text{eff},i} h \bar{T}_L u_R^i + \text{h.c.} \right]. \quad (12)$$

Matching the last term to the simplified model parameters in Eq. (11) yields $\lambda_{\text{mix}}^{\text{eff},i} = \kappa_H V_R^{4i} M/v$. The effective coupling $\lambda_{\text{mix}}^{\text{eff},i}$ can be sizable without being in conflict with electroweak precision constraints. This has important consequences for the T production channels discussed in the next section. Concerning the decay, $T \rightarrow hu^i$ is the only allowed decay channel, such that this sample model can only be tested in Higgs final states at the LHC.

For Model II, we assume $V_R^{4i} \simeq V_L^{4i}$.¹⁰ The effective Lagrangian of this model is given by

$$\begin{aligned} \mathcal{L}_{\text{eff}} &= \mathcal{L}_{\text{SM}} + \bar{T} \left(i\partial_\mu + e\frac{2}{3}A_\mu - g\frac{2}{3}\frac{s_w^2}{c_w}Z_\mu + g_3G_\mu \right) \gamma^\mu T - M\bar{T}T \\ &- \left[\lambda_{\text{mix}}^{\text{eff},i} \frac{m_Z}{M_1} \bar{T}_L Z_\mu \gamma^\mu u_L^i + \sqrt{2} \lambda_{\text{mix}}^{\text{eff},i} \frac{m_W}{M_1} \bar{T}_L W_\mu \gamma^\mu d_L^i + \lambda_{\text{mix}}^{\text{eff}} h \bar{T}_L u_R^i + \text{h.c.} \right], \end{aligned} \quad (13)$$

where matching with the simplified model Lagrangian Eq. (11) yields $\lambda_{\text{mix}}^{\text{eff},i} = \kappa_H V_R^{4i} M/v = \kappa_W V_L^{4i} M/v = \kappa_Z V_L^{4i} M/v$. In this sample model, electroweak precision constraints require the

⁸We work in unitary gauge. And we focus on up-type partners here. Concerning the discussion of Higgs interactions in this section, down-type partners can be treated completely analogously.

⁹An explicit realization of this parameter choice has been discussed in Ref. [262] in terms of a partially composite right-handed quark model.

¹⁰This model setup arises for example in the fully composite quark model discussed in Ref. [262].

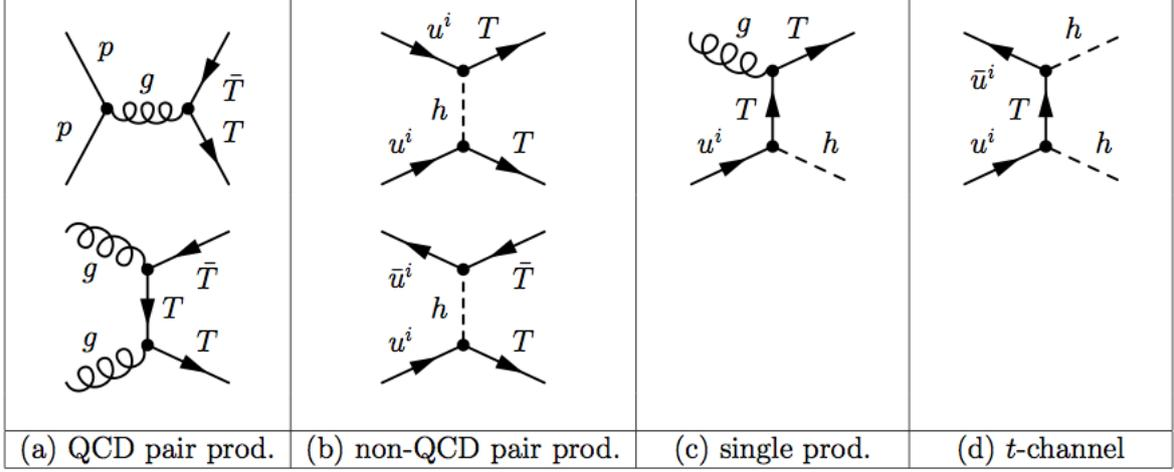


Figure 7: Main channels leading to BSM Higgs final states from Model I and II. The label p in the first diagram in (a) stands for any parton of the proton: g , q and \bar{q} .

couplings $\lambda_{\text{mix}}^{\text{eff},i}$ to be small. Therefore, single-production of the T is suppressed. The branching fractions of the T decays into W , Z , or Higgs and a SM-like quark are approximately 50%, 25% and 25% [262].

5.2 BSM Production channels with Higgs final states

The dominant channels which lead to BSM final state Higgses from our sample models I and II are shown in Fig. 7. For small $\lambda_{\text{mix}}^{\text{eff},i}$ (which is required in Model II but not in Model I), BSM production of Higgses arises mainly through QCD production of a T pair shown in panel (a) and their decay into a Higgs and an SM-like quark. The remaining channels (non-QCD T pair production in panel (b), single T production in panel (c), and di-Higgs production in panel (d)) only play a role when $\lambda_{\text{mix}}^{\text{eff},i}$ is not suppressed. For vector-quark partners which mainly interact with the up-quark, these channels considerably enhance the T pair production cross section and also yield sizable single T production and BSM di-Higgs production, while for second or third family quark partners, these channels are PDF suppressed. Figures 8-10 show the respective cross-sections for T pair-, and single production and direct BSM di-Higgs production as a function of the partner quark mass M for LHC at $\sqrt{s} = 8$ TeV and 14 TeV for a reference value of $\lambda_{\text{mix}}^{\text{eff},i} = 1$, which corresponds to $\kappa_H V_R^{4i} = v/M$ in terms of the simplified model parameters. We also included the production cross-sections for down-type partner quarks which can be implemented analogously to the up-type partners.

The processes shown in Fig. 7 yield T pairs (for both, Model I and II), as well as Th , or a Higgs pair for Model I. In the case of Model I, the T decays into hu^i . The main BSM signature of this model is therefore a di-Higgs with zero, one, or two high- p_T u^i . For Model II, QCD T pair production dominates, and the T decays into W , Z or h with an associated quark (top/bottom or jet, depending on which V_R^{4i} dominates). Therefore for Model II, final states with gauge bosons are available¹¹ while final states with a Higgsboson are reduced due the BRs.

¹¹For a top-partner, the strongest bound from such signatures is $M > 696$ GeV [245]. For a bottom-partner the strongest constraint is $M > 700$ GeV [246]. For light quark partners, no bounds are available yet.

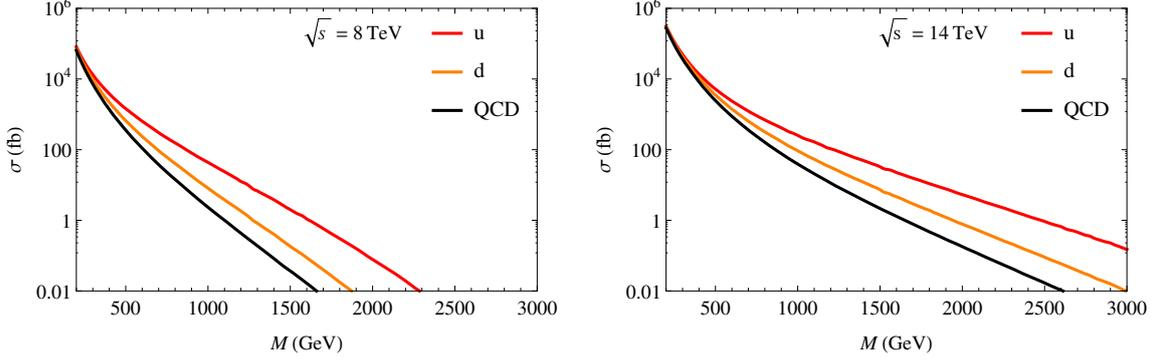


Figure 8: Production cross section for a pair of vector-like quark partners in Model I as a function of the partners' mass M for LHC at 8TeV (left) and 14TeV (right). The first two lines from the top correspond to the pair production cross section with $\kappa_H V_R^{4i} = v/M$ for partners of the up (red) and down (orange), while the third line (black) denotes the QCD pair production cross section. The non-QCD pair production cross sections for partners of the s , c and b quarks are PDF suppressed. Thus, the pair production cross section for these quark partners is to a good approximation given by the QCD pair production cross section.

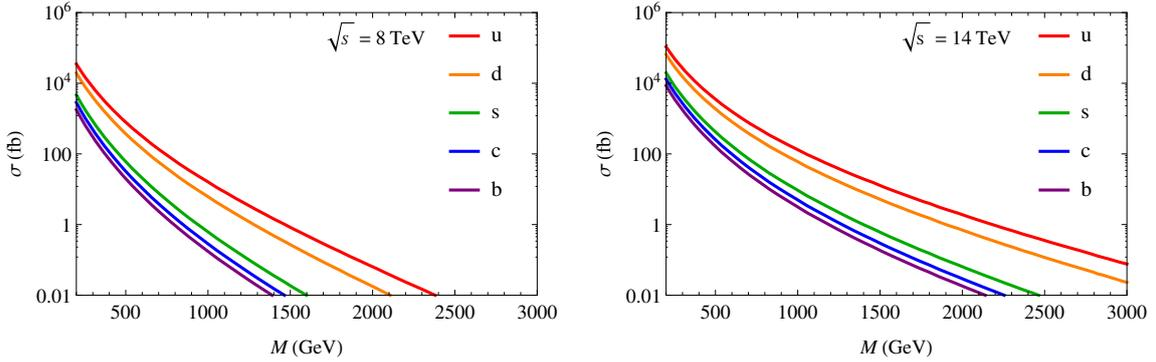


Figure 9: Production cross section for a single T as a function of its mass M for LHC at 8TeV (left) and 14TeV (right). Lines denote (from right to left): Single production cross section with $\kappa_H V_R^{4i} = v/M$ for partners of the u , d , s , c , b quark.

5.3 Results for vector-like partners of light quarks

The di-Higgs signature provides a very promising search channel for Model I and (to a lesser extend) for Model II, but ATLAS and CMS did not release results in these channels yet. In the remainder of this section we therefore focus on obtaining bounds on Models I and II from the currently available Standard Model Higgs searches. To distinguish Higgses from SM and the above discussed BSM production channels, notice that Higgses arising from heavy T decays result in a high p_T Higgs and a high p_T quark which are untypical for SM Higgs production. Measurements of p_T distributions in Higgs decays can therefore yield a good discriminator.

In Ref. [266], the ATLAS collaboration presented results on differential cross sections of the Higgs in the $h \rightarrow \gamma\gamma$ channel. In particular, Ref. [266] studies the $p_T^{\gamma\gamma}$, N_{jets} , and the highest p_T^{jet} distributions which are in good agreement with the SM predictions. We simulate the BSM contribution to these distributions which arise in Model I and II from the processes shown

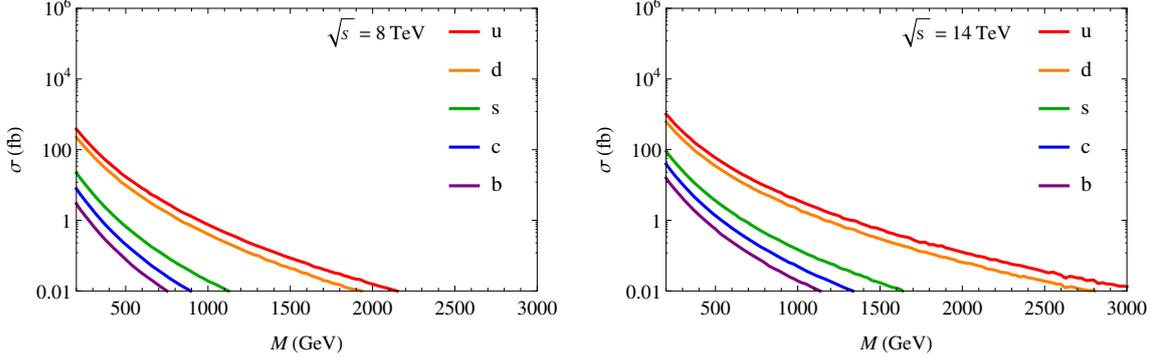


Figure 10: Production cross section for two Higgses via t -channel exchange of a T quark for LHC at 8 TeV (left) and 14 TeV (right). Lines denote (from right to left): Cross section with $\kappa_H V_R^{4i} = v/M$ for the exchange of u, d, s, c, b quark partners.

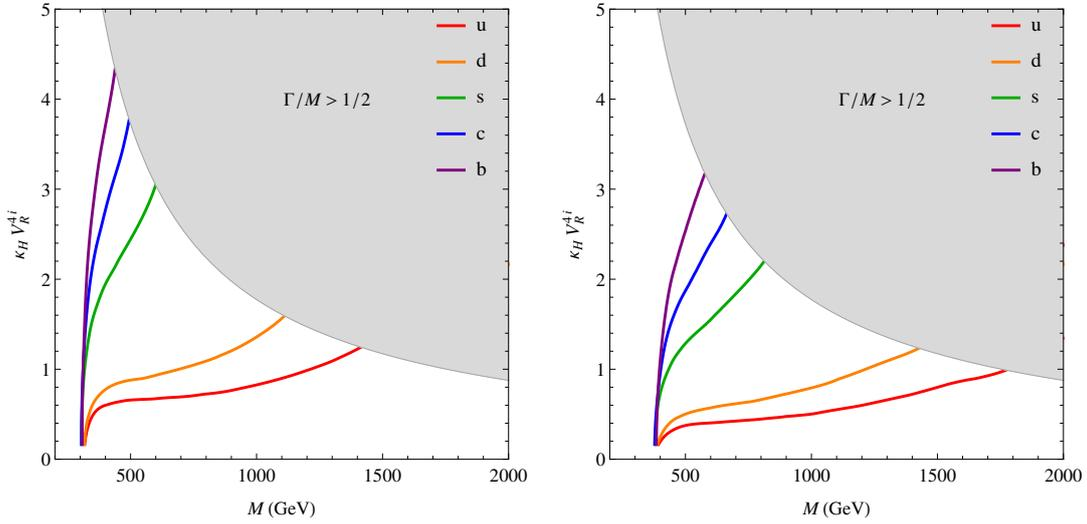


Figure 11: The exclusion plots for partners of the u, d, s, c and b quark (curves from right to left) within sample Model I. Left: 95% CL exclusion limits including the signal bins of Ref. [266]. Right: Would-be 95% CL exclusion limits when both signal and overflow bin data of Ref. [266] is included in the analysis. The parameter region to the top-left region from the respective curve is excluded at 95% CL. For reference, the gray region in each of the plots shows $\Gamma/M > 1/2$ and the coupling above which the narrow-width-approximation does not apply anymore. Ref. [262] did not search through this region.

in Fig. 7. Bounds on the vector-quark partner parameter space are obtained by comparing the BSM contributions in the respective $p_T^{\gamma\gamma}$, N_{jets} , and highest p_T^{jet} bins to the measured bounds determined in Ref. [266]. The details of the simulation and data evaluation can be found in Ref. [262].

Figure 11 shows the resulting bounds on the vector-quark partner of a u, b, s, c and b quark. On the left, we show the 95% CL bounds which arise when only including the signal bins of Ref. [266].¹² On the right, we show the bounds which would be obtained when including the overflow bins into the analysis. The signal and overflow bins are treated on a different footing

¹²Ref. [266] chose as their highest signal bins for their p_T distributions $100 \text{ GeV} < p_T^{\gamma\gamma} < 200 \text{ GeV}$ and

in Ref. [266], and the left figure therefore represents the (conservative) constraints obtained from our analysis. The right plot indicates how much these bounds could be increased by a dedicated search for high $p_T^{\gamma\gamma}$ (which yields the dominant improvement) and high p_T^{j1} events. For reference, in both plots, the grey-shaded region corresponds to the parameter space in which the T width is larger than $M/2$ such that the narrow width approximation does not apply. Our analysis is not relying on the narrow width approximation. This information is mainly provided because it is relevant for future searches which aim to reconstruct the invariant mass of the T .

From Fig. 11 we obtain a quark flavor and κ_H - independent bound of $M > 310$ GeV at 95% CL from the signal bin analysis ($M > 385$ GeV when including the overflow bins). These bounds arise solely from QCD pair produced T 's (*c.f.* Fig. 8) which subsequently decay into a Higgs and a quark. The flavor and κ_H dependent increase of the bound arises due to the increase of the T pair-, and single production (*c.f.* Figs. 8 and 9) while the increase of the direct di-Higgs production (*c.f.* Fig. 10) plays a minor role. For Model I, in which the vector-like quark partner only decays into a Higgs and a quark, the constraints presented above are the only currently available bounds for light quark partners. Only for top quark partners a stronger bound of $M > 706$ GeV is available from a dedicated CMS search for top partners in Ref.[245].

The analogous analysis for Model II yields a flavor and κ_H independent bound of $M > 212$ GeV at 95% CL from the signal bin analysis ($M > 240$ GeV when including the overflow bins). The constraint is weaker than for Model I because only $\sim 25\%$ of the T decays yield a final state Higgs. Furthermore, there is no κ_H or flavor dependent increased bound because in Model II QCD production of T pairs dominates. For top- and bottom partners within Model II, stronger bounds from searches for pair produced quark partners with an electroweak gauge boson and a b quark in the final state exist ($M > 696$ GeV for a t -partner [245] and $M > 700$ GeV for a b -partner [246]), while for u, d, s and c partners, the constraint presented above represents the strongest bound within the Model II setup.

CONCLUSIONS

The search for vector-like partners of the top quark is entering a crucial era, as the bounds from the searches at the LHC are approaching the TeV scale. For this reason, it is useful to take a model-independent look at the searches and allow for all possible channels and couplings. In this report, we propose a simple parametrisation of the lagrangian with 3 parameters, which can approximate with good accuracy the phenomenology of many realistic models. A crucial novelty is the fact that we allow for couplings to light quarks, and not only third generation. The coupling to light quarks generates new signatures, some of which can contribute to searches designed for decays into the third generation. An example of this is given by final states with three or four leptons. Sizable couplings to the light quarks also allows for larger single-production processes in association with a light jet, and interesting final states can be obtained when the vector-like quark further decays into a top. Two exploratory studies of this case have been presented: in the channel $pp \rightarrow Tj \rightarrow Htj$, the final state can be reconstructed in the fully hadronic decays of the Higgs and top and a bump-hunt strategy in the 5-jet invariant mass may allow for a distinction of the signal over backgrounds; another promising channel is generated by $pp \rightarrow Tj \rightarrow Ztj$, where both the Z and top decays leptonically. In the latter case, the suppression due to the leptonic branching ratios requires the larger energy of the LHC in order

100 GeV $< p_T^{j1} < 140$ GeV. Events with higher p_T are collected in $p_T^{\gamma\gamma}$ and p_T^{j1} overflow bins.

to have a detectable number of events. Finally, we presented a complete overview of the final states with a Higgs boson, both in the case of a generic model with couplings to light quarks, and in a specific scenario inspired by composite Higgs models. The studies presented in this report finally show that, although the massive effort by the experimental collaborations ATLAS and CMS have provided us with plenty of channels to constraint models with vector-like quarks, the most general scenario still offers new unexplored and promising channels at the LHC.

ACKNOWLEDGEMENTS

LB and JRA would like to thank Eric Conte and Jeremy Andrea for their support with Mad-analysis and insightful comments. LB has received partial support from the Theorie-LHC France initiative of the CNRS/IN2P3 and by the French ANR 12 JS05 002 01 BATS@LHC, and from the Deutsche Forschungsgemeinschaft through the Research Training Group grant GRK 1102 *Physics at Hadron Accelerators* and by the Bundesministerium für Bildung und Forschung within the Förderschwerpunkt. GC and AD acknowledge the Labex-LIO (Lyon Institute of Origins) under grant ANR-10-LABX-66 and the Theorie-LHC France initiative of the CNRS/IN2P3 for partial support. AD is partially supported by Institut Universitaire de France.

Contribution 13

Cornering Compressed Supersymmetric Spectra with Monotops

B. Fuks, P. Richardson, A. Wilcock

Abstract

We investigate the sensitivity of the Large Hadron Collider to compressed supersymmetric scenarios in which one of the possible experimental signals consists of a single top quark produced in association with missing transverse energy, also referred to as monoton. We perform our study using Monte Carlo simulations of 10 fb^{-1} of collisions expected to occur at a center-of-mass energy of 14 TeV. Focusing on leptonically decaying monoton states, we present an analysis strategy sensitive to regions of supersymmetric parameter space featuring small sparticle mass splittings and illustrate its strengths in the context of a particular set of benchmark points.

1 INTRODUCTION

While the Standard Model (SM) of particle physics has proven enormously successful in predicting most high-energy physics data, it exhibits a set of conceptual problems and is therefore believed to be the low-energy limit of a more fundamental theory. This has led to the development of a plethora of new physics models, the most popular and well studied of which being weak scale supersymmetry (SUSY) [267, 268]. The absence of any new physics hints at the Large Hadron Collider (LHC) means that bounds on the superpartner masses are being pushed to higher scales. Most of these constraints can however be evaded for specific benchmark scenarios where the low-energy part of the SUSY mass spectrum is compressed. In compressed scenarios, superparticles decay into missing energy carried by the lightest sparticle and soft leptons and jets. Consequently, the transverse momenta of the decay products fall below the typical trigger thresholds of the LHC experiments and the smaller expected amount of missing transverse energy makes kinematical quantities traditionally employed to reduce the SM background less effective. These observations have motivated several studies trying to constrain compressed models by non-standard means, such as benefiting from monojet or monophoton signatures [269, 270, 271, 272, 273, 274].

In our approach, we focus on the production of monoton systems that are defined as states comprised of a single top quark and missing transverse energy and that are expected to be easily observable at the LHC for a large range of new physics masses and coupling strengths [275, 276, 277, 278]. In the framework of simplified compressed SUSY scenarios where the electroweak superpartners are neglected (with the exception of the lightest neutralino), a monoton signature is expected to arise from the production of the three-body final state of a gluino, top squark and top quark. In this case, both superpartners give rise to a small amount of missing energy produced together with soft objects. Restricting ourselves to the case

Process	Simulation details	$\sigma^{\text{total}}[\text{pb}]$	$N_{\text{event}}^{\text{surviving}}$
$W(\rightarrow l\nu) + \text{light-jets}$	W -boson production simulated at NLO and matched to LO production of the W -boson with 1 or 2 extra jets using SHERPA 2.0 [279].	67453	≈ 0
$\gamma^*/Z(\rightarrow \bar{l}l/\nu\bar{\nu}) + \text{jets}$	As above and requiring $m_{ll}, m_{\nu\nu} > 10\text{GeV}$.	38990	≈ 0
$t\bar{t}$	Parton-level hard events simulated at NLO using the POWHEGBOX [280] and matched to Herwig++ for parton showering and hadronization.	781	1387
Single top [t -channel]	As above [281].	244.3	1.2
Single top [s -channel]	As above [282].	10.4	0.1
tW production	As above, suppressing doubly-resonant diagrams following the prescription of Ref. [283]	77.1	73
$Wb\bar{b}$ with $W \rightarrow l\nu$	Parton-level hard events, with $W \rightarrow l\nu$, simulated at LO with MADGRAPH 5 and matched to Herwig++ for parton showering and hadronization.	122.1	≈ 0
Diboson	Simulated at NLO using the built-in POWHEG implementation in Herwig++ [284].	157.7	≈ 0
$(m_{\tilde{t}_1}, m_{\tilde{\chi}_1^0}) = (200, 190)\text{GeV}$	Details given in text.	0.8	272

Table 1: Cross sections and simulation details for the background processes and an example signal scenario. In all cases, $l = e, \mu, \tau$ and ν denotes any neutrino. Also shown are the number of events, N_{events} , surviving all selection criteria described in Section 3. Results correspond to 10 fb^{-1} of LHC collisions at a center-of-mass energy of 14 TeV.

of a leptonically decaying top quark, we illustrate how to benefit from the presence of the latter to get sensitivity to the initially produced sparticles, and adopting a typical monotop selection strategy, we show that 10 fb^{-1} of LHC collisions at a center-of-mass energy of 14 TeV should be sufficient for observing hints of new physics in the context of compressed SUSY scenarios.

The outline of this contribution is as follows: In Section 2, we describe the technical setup for the Monte Carlo simulations of both the new physics signal and the relevant sources of SM background. Our analysis strategy allowing for extracting a monotop signal from the background is detailed in Section 3 and the results are presented in Section 4. Our conclusions are given in Section 5.

2 SIMULATION

Event generation for the hard scattering signal process, including the subsequent decay of the top quark $t \rightarrow bW \rightarrow bl\nu_l$ where $l = e, \mu, \tau$ has been simulated using the MADGRAPH 5 [126] program with the parton density function (PDF) set CTEQ6L1 [285]. Additionally, the decays of the \tilde{t}_1 and \tilde{g} through the modes $\tilde{t}_1 \rightarrow c\tilde{\chi}_1^0$ and $\tilde{g} \rightarrow q\bar{q}\tilde{\chi}_1^0$ have been simulated with Herwig++ 2.7 [162, 286]. Finally, parton-level hard event samples have been matched with the parton shower and hadronization infrastructure provided by Herwig++ . In this study we consider scenarios with maximal stop mixing and with purely bino $\tilde{\chi}_1^0$. The corresponding signal cross section for an example compressed spectra scenario with $m_{\tilde{t}_1} = m_{\tilde{g}} = 200\text{GeV}$ and $m_{\tilde{\chi}_1^0} =$

190GeV can be found in Table 1.

The signature of a leptonically decaying monotop state consists of a hard lepton, a jet originating from the fragmentation of a b -quark and missing transverse energy. As such, the main sources of background arise from $t\bar{t}$ events where one of the two top quarks decays leptonically and from events related to the production of a single-top quark in association with a W -boson, where either the top quark or the W -boson decays leptonically. Other contributing background processes consist of the other single-top production modes, W -boson plus jets production, γ^*/Z -boson plus jets production and diboson production. The respective total cross sections of these background processes are presented in Table 1 along with details of the Monte Carlo programs used in their simulation. In all cases, the CTEQ6L1 [285] and CTEQ6M [285] PDF sets were used in the simulation of processes generated at leading order (LO) and next-to-leading order (NLO) respectively. While QCD multijet production processes should also be taken into account, a correct estimation of their contribution relies more on data-driven approaches than Monte Carlo simulations. Therefore, we have chosen to neglect it and ensure good control of this source of background through appropriate event selection criteria, as detailed in Section 3. Moreover, we neglect all possible sources of instrumental background, this task going beyond the scope of this work.

3 EVENT SELECTION

The object reconstruction used in this study is based on the typical approach of the ATLAS experiment in studies of single-top production, see for example Ref. [287], while the event selection criteria has been chosen to reflect the particle content of final states originating from the signal process. As such, we demand the presence of exactly one lepton candidate in each event, with electron (muon) candidates required to have a transverse momentum $p_T^l > 20$ GeV and a pseudorapidity $|\eta| < 2.47$ (2.5). Lepton candidates are constrained to be isolated by restricting the sum of the transverse momenta of all charged particles in a cone of $\Delta R < 0.2$ ¹ around the particle to be less than 10% of its transverse momentum.

Jets have been reconstructed from all visible final-state particles fulfilling $|\eta| < 4.9$ using the FASTJET [170] implementation of the anti- k_T algorithm with a radius parameter of $R = 0.4$ [171]. Moreover, the transverse momentum of the reconstructed jet candidates has been required to satisfy $p_T > 10$ GeV and jets which overlap with candidate electrons within a distance of $\Delta R < 0.2$ have been discarded. Having done so, only jets with $p_T > 20$ GeV and $|\eta| < 2.5$ are retained and any lepton candidate within a distance $\Delta R < 0.4$ of the closest remaining jet has been discarded. We further identify jets as originating from a b -quark if they lie within $\Delta R < 0.3$ of a b -hadron and impose a p_T -dependent b -tagging probability as described in Ref. [288], which corresponds to an average efficiency of 70% for $t\bar{t}$ events. We then select events by requiring the presence of exactly one b -jet with $p_T^b > 30$ GeV and $|\eta| < 2.5$. Finally, to reflect the expectation that the decay products of the \hat{t}_1 and \hat{g} are largely invisible, any event containing an extra jet with transverse momentum $p_T > \min(p_T^b, 40\text{GeV})$ has been discarded.

The following selection criteria have then been imposed in order to increase the sensitivity, s , of the analysis to the signal process, where we define $s = S/\sqrt{S+B}$ in which S and B are the number of signal and background events passing all selection criteria, respectively. The

¹We define $\Delta R = \sqrt{\Delta\phi^2 + \Delta\eta^2}$ where $\Delta\phi$ and $\Delta\eta$ denote the differences in the azimuthal angle with respect to the beam direction and in pseudorapidity of the charged particle and the lepton, respectively.

missing transverse momentum in the event, p_T^{miss} , has been determined from the vector sum of the transverse momenta of all visible final-state particles. The magnitude of this quantity, E_T^{miss} , is required to satisfy $E_T^{\text{miss}} > 150\text{GeV}$. The choice of such a loose E_T^{miss} selection criterion is motivated by the observation that while a higher requirement would improve background rejection it would also significantly reduce the signal acceptance, leading to an overall reduction in the sensitivity. This low E_T^{miss} limit is moreover feasible in the context of event triggers for the LHC experiments by requiring the presence of a relatively hard, isolated lepton in the selected events, which opens up the possibility of using leptonic triggers. We have verified that the transverse momentum requirement on the candidate lepton could be increased to $p_T^l > 30\text{GeV}$, which allows for an improvement of the trigger efficiencies, without a significant degradation of the signal.

While the selection criterion on E_T^{miss} must be low to avoid the rejection of signal events, the sensitivity of the analysis can be further improved by constraining the orientation of p_T^{miss} with respect to the identified lepton. As such, we impose a minimum value of the W -boson transverse mass, defined by

$$m_T^W = \sqrt{2p_T^l E_T^{\text{miss}} (1 - \cos(\Delta\phi_{l,p_T^{\text{miss}}}))}, \quad (1)$$

where $\Delta\phi_{l,p_T^{\text{miss}}}$ is the difference in azimuthal angle between the lepton and p_T^{miss} . When the missing transverse momentum in the event originates solely from the leptonic decay of a W -boson, the distribution is peaked at a lower value of m_T^W than when its source is both a W -boson decay and a pair of invisible particle as in the signal case. Therefore, we require events to satisfy $m_T^W > 120\text{GeV}$, which also ensures that the non-simulated QCD multijet background contribution is under control [289, 290].

In order to reduce the number of background events in which the identified lepton and b -jet do not originate from a single top quark, the restriction on the invariant mass of the lepton plus b -jet system, $m_{bl} < 150\text{GeV}$, has been imposed. Finally, a minimum value of the invariant mass of the lepton, b -jet and missing transverse momentum system, $m(E_T^{\text{miss}}, l, b)$, has been enforced, $m(E_T^{\text{miss}}, l, b) > 1.0\text{TeV}$. This serves to further reduce the number of $t\bar{t}$ and tW events passing all the selection criteria.

4 RESULTS

The numbers of events surviving all selection criteria described in Section 3 are listed separately in Table 1 for the different background contributions and the example compressed spectra scenario of Section 2. The effect of our analysis strategy is further illustrated in Figure 1 which shows the m_T^W distributions after all selection requirements, excepted $m_T^W > 120\text{GeV}$, for the remaining background sources ($t\bar{t}$ and single-top) and the considered signal scenario. In the case of the background, a peak, related to events in which both the lepton and missing transverse momentum originate from the decay of a single W -boson, is visible in the region $m_T^W \simeq 80\text{GeV}$. In contrast, the signal distribution exhibits a suppression in the region $m_T^W \lesssim 120\text{GeV}$, which motivates our choice of selection criterion for this observable. Relatively large background contributions from $t\bar{t}$ and, to a lesser extent, tW production are however still foreseen after the requirement $m_T^W > 120\text{GeV}$ has been imposed. Despite this, the sensitivity of the LHC to this point reaches $s = 6.1$ after all selections, although a more precise quantitative statement requires further studies involving detector effects or the instrumental background. This however goes beyond the scope of this prospective work which only aims to demonstrate the feasibility

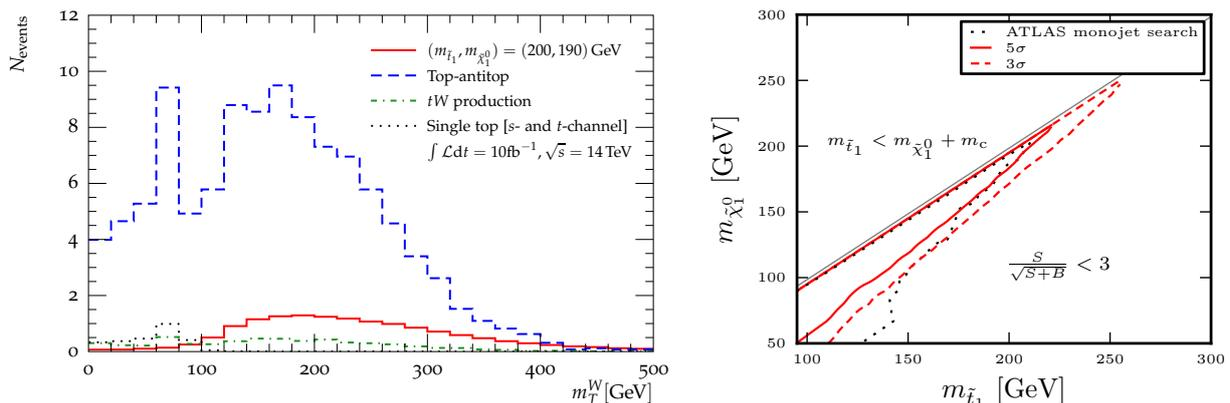


Figure 1: Left: W -boson transverse mass distribution m_T^W , as defined in Eq. (1), for surviving background contributions and the example signal scenario of Section 2 after all selection criteria have been applied, excepted $m_T^W > 120$ GeV. Right: LHC sensitivity to SUSY monotop signals in the $(m_{\tilde{t}_1}, m_{\tilde{\chi}_1^0})$ plane with $m_{\tilde{t}_1} = m_{\tilde{g}}$. We superimpose a previous exclusion bound set by an ATLAS analysis searching for stops decaying into a charm quark and the lightest neutralino using monojet events.

of searching for monotop SUSY signals at the LHC in the case of compressed superparticle mass spectra.

To more extensively study the LHC sensitivity to different compressed spectra SUSY scenarios, a scan of the $(m_{\tilde{t}_1}, m_{\tilde{\chi}_1^0})$ plane with $m_{\tilde{t}_1} = m_{\tilde{g}}$ has been performed. We have derived in this way contours corresponding to 5 σ and 3 σ observation boundaries, that we respectively show by solid and dashed red lines in Figure 1. A more careful optimization of the event selection criteria could however possibly extend the reach of our search strategy. We superimpose on our results exclusion bounds at the 95% confidence level, indicated by a black dotted line, set by the ATLAS collaboration on the basis of 20.3 fb $^{-1}$ of collision data at a center-of-mass energy of 8 TeV [291]. They arise from a monojet search for the pair production of top squarks that each decay into a charm quark and the lightest neutralino.² It is likely that searches for monotop compressed SUSY signals could provide an independent check of the exclusion bounds obtained from a more standard monojet analysis. Moreover, as both channels are statistically uncorrelated, an improvement of the bounds could result from combining the two results.

5 CONCLUSION

In this study, we have investigated the feasibility of using monotop searches to get a handle on SUSY scenarios featuring a compressed spectrum. We have considered the process $pp \rightarrow \tilde{g} \tilde{t}_1 \bar{t}_1$, where the top quark decays leptonically and the sparticles decay via $\tilde{t}_1 \rightarrow c \tilde{\chi}_1^0$ and $\tilde{g} \rightarrow q \bar{q} \tilde{\chi}_1^0$. We consider small mass splittings between the \tilde{t}_1 , \tilde{g} and $\tilde{\chi}_1^0$, meaning jets produced in the superparticle decays are soft and the corresponding observable signal is a single top quark with missing transverse momentum, referred to as monotop. Using Monte Carlo simulations of 10 fb $^{-1}$ of LHC collisions at a center-of-mass energy of 14 TeV, we have shown that signals of this type will in principle be reachable at the LHC for mass spectra scenarios close to the $m_{\tilde{t}_1} =$

²The analysis of Ref. [291] also presents an exclusion boundary derived using charm-flavour identification techniques. This extends the limits away from the $m_{\tilde{t}_1} = m_{\tilde{\chi}_1^0} + m_c$ boundary into a region of the parameter space not probed by our analysis. For this reason, it has not been shown on Figure 1.

$m_c + m_{\tilde{\chi}_1^0}$ boundary in the case where $m_{\tilde{t}_1} = m_{\tilde{g}}$. This result motivates further investigation of SUSY monotop signals, both into the optimization of the event selection criteria and the case of hadronic top quark decay, as well as consideration of detector effects and instrumental background or alternative compressed spectrum setups.

ACKNOWLEDGEMENTS

The authors would like to thank the Les Houches school for physics for their hospitality during the workshop where some of the work was performed, as well as the workshop organizers. AW and PR acknowledge the support of the European Union via MCNet, PITN-GA-2012-315877. AW also acknowledges support from the Science and Technology Facilities Council. The work of BF has been partially supported by the Theory-LHC France initiative of the CNRS/IN2P3 and by the French ANR 12 JS05 002 01 BATS@LHC.

Contribution 14

Constraining Natural Supersymmetry from the LHC Stop and Sbottom Search Results at 8 TeV

J. Bernon, G. Chalons, E. Conte, B. Dumont, B. Fuks, A. Gaz, S. Kraml, S. Kulkarni, L. Mitzka, S. Pataraia, W. Porod, S. Sekmen, D. Sengupta, N. Strobbe, W. Waltenberger, F. Würthwein, C. Wymant

Abstract

Both the ATLAS and CMS collaborations have been searching for light stops and sbottoms in a variety of different channels. The mass limits published by the experimental collaborations however typically assume 100% branching ratio for a given decay mode. A coherent picture of the status of light third-generation squarks, in particular in combination with light higgsinos (aka natural supersymmetry) is however still missing. We report on the progress in developing such a coherent picture by means of a scan over physical parameters, namely stop and sbottom masses and mixing angles, and higgsino masses. We present results obtained with SMODELS in the Simplified Models approach and describe the status of the implementation and validation of various stop and sbottom analyses from ATLAS and CMS in the MADANALYSIS 5 framework. Finally, we describe the extensions done in MADANALYSIS 5 to adapt it for this project.

1 INTRODUCTION

In order to solve the gauge hierarchy problem of the Standard Model (SM), supersymmetric (SUSY) particles that have sizable couplings to the Higgs sector should have masses not too far above the electroweak (EW) scale. This concerns in particular the squarks of the third generation, stops and sbottoms, which should be lighter than about a TeV in order not to create a severe naturalness problem. Moreover, the higgsino mass parameter μ should be small, because its intimate relation with the EW scale: $-M_Z^2/2 = |\mu|^2 + m_{H_u}^2$. Since the standard searches for gluinos and light-flavor squarks at the LHC have so far produced only null results and precision measurements in flavor physics are frustratingly consistent with SM predictions, the scenario with light stops and sbottoms and light higgsinos, but multi-TeV first and second generation squarks – commonly dubbed “natural supersymmetry” (NSUSY) – is increasingly becoming the new paradigm of SUSY phenomenology.

The ATLAS and CMS collaborations have been searching for light stops and sbottoms in a variety of channels [292, 293]. This has led to mass limits of the order of 500–700 GeV. These limits however depend on various assumptions. In particular, 100% branching fraction for a given decay mode is typically assumed. In realistic scenarios, stops and sbottoms can however have a variety of decays, in particular into charginos and neutralinos, with the branching ratios depending not only on the mass pattern (kinematics) but also on the mixing angles

in the stop/sbottom and the chargino/neutralino sectors. It is thus interesting to assess in detail how the current ATLAS and CMS searches, performed during the first phase of LHC running, constrain NSUSY in general. This assessment is the aim of this project.

2 NATURAL SUSY PARAMETER SCAN

In order to achieve a good survey of the relevant parameter space, we choose to work with physical stop and sbottom masses and mixing angles $(m_{\tilde{t}_1}, m_{\tilde{t}_2}, m_{\tilde{b}_1}, m_{\tilde{b}_2}, \theta_{\tilde{t}}, \theta_{\tilde{b}})$. The reason for this is the strong dependence on the A_t parameter and the large radiative corrections in the stop/sbottom sector, which make it difficult to reach all corners of physical parameter space when working with soft-breaking terms. In the chargino/neutralino sector it is more convenient to compute the masses and mixings from the Lagrangian parameters M_1, M_2, μ and $\tan \beta$.

For our first scan, we fix slepton and first and second generation squark masses at 5 TeV, the gluino mass at 2 TeV, and $M_1 = M_2 = 1$ TeV. We then vary

$$\begin{aligned}
m_{\tilde{t}_1} &= 150, 200, 300, 400, \dots, 1000 \text{ GeV}; \\
m_{\tilde{b}_1} &= 150, 200, 300, 400, \dots, 1000 \text{ GeV}; \\
\mu &= 100, 200, 300, 400, 500 \text{ GeV}; \\
\theta_{\tilde{t}} &= 0, 45, 90 \text{ deg}; \\
\theta_{\tilde{b}} &= 0, 45, 90 \text{ deg}; \\
\tan \beta &= 10, 50.
\end{aligned} \tag{1}$$

Further scans also consider $\theta_{\tilde{t}, \tilde{b}} = 135^\circ$ and 180° , and lower gluino masses of 750 and 1000 GeV. The computation of the chargino and neutralino masses and of all decay branching ratios is done with SPHENO [294, 295]. The \tilde{t}_2 is assumed to be heavy and irrelevant for LHC phenomenology at 8 TeV. We do not worry about the value of the light Higgs mass because $m_h \simeq 126$ GeV can always be achieved by adjusting $m_{\tilde{t}_2}$ and A_t . Note that in order to have a neutralino as the lightest SUSY particle (LSP), the ranges in Eq. (1) are effectively limited to $m_{\tilde{t}_1}, m_{\tilde{b}_1} > \mu$.

The stop and sbottom masses and mixing angles are however not completely independent: because of the $SU(2)_L$ symmetry the \tilde{t}_L and \tilde{b}_L masses depend on the same mass parameter $M_{\tilde{Q}_3}$. This implies the sum rule

$$m_W^2 \cos 2\beta = m_{\tilde{t}_1}^2 \cos^2 \theta_{\tilde{t}} + m_{\tilde{t}_2}^2 \sin^2 \theta_{\tilde{t}} - m_{\tilde{b}_1}^2 \cos^2 \theta_{\tilde{b}} - m_{\tilde{b}_2}^2 \sin^2 \theta_{\tilde{b}} - m_t^2 + m_b^2 \tag{2}$$

at tree level. This means we have to be careful when $\theta_{\tilde{t}} = 0$ or 90° in our scan. In case of $\theta_{\tilde{t}} = 0$, one has a pure \tilde{t}_L in the game and thus also a nearby \tilde{b}_L . We compute the mass of \tilde{b}_L using the tree-level mass relation above. In case that this mass is below the $m_{\tilde{b}_1}$ chosen for this scan point, we flip the ordering of the sbottom masses and change the mixing matrix accordingly. Moreover, when $\theta_{\tilde{t}} = 90^\circ$, we consider only $\theta_{\tilde{b}} = 90^\circ$. In total the first scan set, Eq. (1), thus contains 3696 points.

The choice of small μ together with large $M_{1,2}$ leads to a higgsino LSP. Moreover, the other higgsinos, $\tilde{\chi}_2^0$ and $\tilde{\chi}_1^\pm$, are almost mass-degenerate with the $\tilde{\chi}_1^0$. For $\mu \geq 200$ GeV, the $\tilde{\chi}_2^0 - \tilde{\chi}_1^0$ mass difference is around 10 GeV while the $\tilde{\chi}_1^\pm - \tilde{\chi}_1^0$ mass difference is about 3–4 GeV. The masses for $\tan \beta = 10$ are given in Table 1. For $\tan \beta = 50$ one obtains very similar numbers, differing only by about 1 GeV.

Since the $\tilde{\chi}_1^0$, $\tilde{\chi}_2^0$ and $\tilde{\chi}_1^\pm$ are basically pure higgsinos, leaving aside kinematic effects, the stop (sbottom) branching ratios depend only on the stop (sbottom) mixing angle and $\tan \beta$.

Table 1: Lightest neutralino and chargino masses (in GeV) as a function of μ (in GeV), for $\tan\beta = 10$.

μ	100	200	300	400	500
$m_{\tilde{\chi}_1^0}$	94.9	194.2	293.4	392.3	490.8
$m_{\tilde{\chi}_2^0}$	98.2	202.6	302.4	402.3	502.1
$m_{\tilde{\chi}_1^\pm}$	102.9	197.6	296.8	395.8	494.6

Table 2: Stop and sbottom branching ratios for $m_{\tilde{t}_1, \tilde{b}_1} = 600$ GeV, $\mu = 200$ GeV and $\tan\beta = 10$.

$\theta_{\tilde{t}_1}$ [deg]	0	45	90	$\theta_{\tilde{b}_1}$ [deg]	0	45	90
$\text{BR}(\tilde{t}_1 \rightarrow t\tilde{\chi}_{1,2}^0)$	0.96	0.59	0.44	$\text{BR}(\tilde{b}_1 \rightarrow b\tilde{\chi}_{1,2}^0)$	0.04	0.08	0.56
$\text{BR}(\tilde{t}_1 \rightarrow b\tilde{\chi}_1^+)$	0.04	0.41	0.56	$\text{BR}(\tilde{b}_1 \rightarrow t\tilde{\chi}_1^-)$	0.96	0.92	0.44

Table 3: Stop and sbottom branching ratios for $m_{\tilde{t}_1, \tilde{b}_1} = 600$ GeV, $\mu = 200$ GeV and $\tan\beta = 50$.

$\theta_{\tilde{t}_1}$ [deg]	0	45	90	$\theta_{\tilde{b}_1}$ [deg]	0	45	90
$\text{BR}(\tilde{t}_1 \rightarrow t\tilde{\chi}_{1,2}^0)$	0.57	0.49	0.44	$\text{BR}(\tilde{b}_1 \rightarrow b\tilde{\chi}_{1,2}^0)$	0.43	0.55	0.56
$\text{BR}(\tilde{t}_1 \rightarrow b\tilde{\chi}_1^+)$	0.43	0.51	0.56	$\text{BR}(\tilde{b}_1 \rightarrow t\tilde{\chi}_1^-)$	0.57	0.45	0.44

Illustrative examples are given in Tables 2 and 3. It is worth noting that the $\tilde{t}_1 \rightarrow b\tilde{\chi}_1^+$ decay is never completely dominant unless $m_{\tilde{t}_1} - m_{\tilde{\chi}_1^0} < m_t$. Likewise, $\tilde{b}_1 \rightarrow b\tilde{\chi}_{1,2}^0$ is never completely dominant unless the decay into $t\tilde{\chi}_1^-$ is kinematically suppressed. Note, however, that the numbers in Tables 2 and 3 can change drastically if $\tilde{t}_1 \rightarrow \tilde{b}_1 W$ or $\tilde{b}_1 \rightarrow \tilde{t}_1 W$ decays are kinematically allowed.

3 SIMPLIFIED MODELS RESULTS

In order to get a first overview of how the current searches perform in case of a higgsino LSP, we pass the scenarios created in our scan (for the 2 TeV gluino case) through SMODELS [296]. SMODELS decomposes each scenario into its Simplified Model Spectra (SMS) topologies and compares the $\sigma \times \text{BR}$ of each topology to the 95% confidence level (CL) upper limits given by the experimental collaborations. The procedure and the analyses considered are explained in detail in Ref. [296]. Note that because of the small mass difference of $\Delta m < 5$ GeV, the $\tilde{\chi}_1^\pm$ decays into the LSP are treated as invisible in SMODELS; the $\tilde{\chi}_2^0$ decays on the other hand are assumed to be visible ($\Delta m > 5$ GeV). The exception is the $\mu = 100$ GeV case, where the $\tilde{\chi}_1^\pm - \tilde{\chi}_2^0$ mass pattern is inverted.

Figure 1 shows the excluded and not excluded points in the $\tilde{\chi}_1^0$ versus \tilde{t}_1 and \tilde{b}_1 mass planes (left and right panels, respectively). In the $\tilde{\chi}_1^0$ versus \tilde{t}_1 case, the results are separated for different mixing angles by introducing a small artificial offset in the stop mass in the figure. We see that for $m_{\tilde{\chi}_1^0} \simeq 100$ GeV, stop masses up to 400 GeV are excluded, irrespective of the mixing angle, bottom mass, or $\tan\beta$. For 500 GeV stop quarks, there are already some

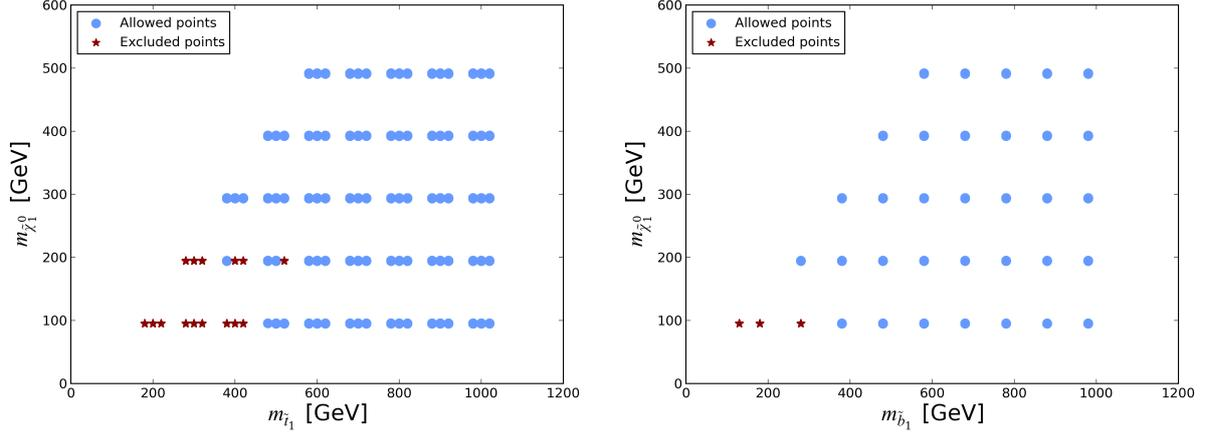


Figure 1: Simplified Models results, obtained with SMOBELS, for the scan with $m_{\tilde{g}} = 2$ TeV described in Section 2. Excluded mass combinations are marked by a red star, while combinations that are not excluded for at least one combination of the scanned parameters are marked by a blue point. In the $\tilde{\chi}_1^0$ versus \tilde{t}_1 mass plane (left panel), the results are presented for 3 stop mixing angles, with a small offset introduced in the stop mass to make the points visible. For each $(\tilde{t}_1, \tilde{\chi}_1^0)$ mass combination, the connected points thus represent, from left to right, a pure \tilde{t}_L , a mixed \tilde{t}_{LR} and a pure \tilde{t}_R ($\theta_{\tilde{t}} = 0, 45, 90$ deg). The results in the \tilde{b}_1 versus $\tilde{\chi}_1^0$ mass plane (right panel) depend less on the bottom mixing angle, thus $\theta_{\tilde{b}}$ is marginalized over.

parameter combinations such that the point cannot be strictly excluded. At $m_{\tilde{\chi}_1^0} \simeq 200$ GeV, right-handed and mixed stop quarks of 400 GeV mass are excluded, while a pure \tilde{t}_L is not. Moving on to a stop mass of 500 GeV, only the \tilde{t}_R is strictly excluded, while a \tilde{t}_L or a mixed stop quark evades the limits.

This can be understood as follows. For the scan considered, the only relevant SMS topologies for which experimental limits are available consist in the production of a top-antitop and bottom-antibottom pair of quarks in association with missing energy ($t\bar{t} + \text{MET}$ and $b\bar{b} + \text{MET}$). At $\mu = 100$ GeV, these topologies arise from $\tilde{t}_1 \rightarrow t\tilde{\chi}_{1,2}^0$ and $\tilde{b}_1 \rightarrow b\tilde{\chi}_{1,2}^0$ decays, respectively. At $\mu \geq 200$ GeV, $t\bar{t} + \text{MET}$ arises from $\tilde{t}_1 \rightarrow t\tilde{\chi}_1^0$ and $\tilde{b}_1 \rightarrow t\tilde{\chi}_1^-$ decays, while $b\bar{b} + \text{MET}$ arises from $\tilde{t}_1 \rightarrow b\tilde{\chi}_1^+$ and $\tilde{b}_1 \rightarrow b\tilde{\chi}_1^0$ decays (*cf.* the higgsino mass splittings shown in Table 1)¹. Let us now take the scenario $\mu = 200$ GeV and $m_{\tilde{t}_1} = 500$ GeV as a concrete example. At $\theta_{\tilde{t}} = 90$ deg ($\tilde{t}_1 = \tilde{t}_R$), the point is [marginally] excluded by the ATLAS search in the $b\bar{b} + \text{MET}$ channel [297]. For a mixed stop, the $\text{BR}(\tilde{t}_1 \rightarrow b\tilde{\chi}_1^-)$ is somewhat reduced and the scenario escapes this exclusion. At $\theta_{\tilde{t}} = 0$ deg ($\tilde{t}_1 = \tilde{t}_L$), the point is excluded by the CMS leptonic stop search ($t\bar{t} + \text{MET}$ topology) [298] for $\tan\beta = 10$, but not for $\tan\beta = 50$. The reason is that at high $\tan\beta$ the branching ratio into $t + \tilde{\chi}_1^0$ is reduced; moreover, only the decay into the $\tilde{\chi}_1^0$ is accounted for in the $t\bar{t} + \text{MET}$ signature. Concretely, we have $\text{BR}(\tilde{t}_1 \rightarrow t\tilde{\chi}_1^0) \simeq 26\%$, so only 6.6% of the $\tilde{t}_1\tilde{t}_1^*$ events can lead to $t\bar{t} + \text{MET}$, which is not enough for an exclusion. At the same time $\text{BR}(\tilde{t}_1 \rightarrow b\tilde{\chi}_1^+) \simeq 40\%$ is also insufficient for an exclusion through the $b\bar{b} + \text{MET}$ topology.

For a better sensitivity, it would be necessary to consider mixed events with one \tilde{t}_1 decaying into $t\tilde{\chi}_1^0$ and the other one into $b\tilde{\chi}_1^+$, and/or combine the results from different channels.

¹Note however that these are subject to theoretical uncertainties of the order of 1% in the calculation of the mass spectrum.

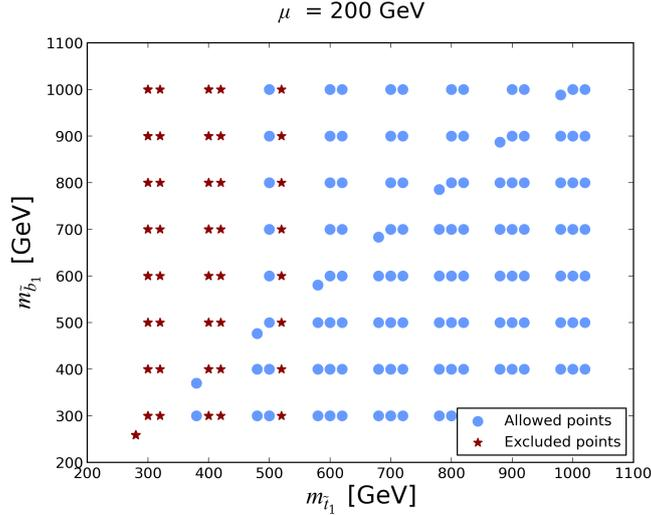


Figure 2: Same as Figure 1 (left) but in the \tilde{t}_1 versus \tilde{b}_1 mass plane for fixed $\mu = 200$ GeV. See text for details.

Results for $t\bar{b} + \text{MET}$ topologies are however not available, and for a combination of results we would need the likelihood of the exclusion limits instead of just the the 95% CL values (and even then the statistically correct treatment is not obvious).

In Figure 2 the same results are presented in the \tilde{t}_1 versus \tilde{b}_1 mass plane for a fixed neutralino mass of about 200 GeV. Again, three different points for a given $(\tilde{t}_1, \tilde{b}_1)$ mass combination represent three different stop mixing angles ($\theta_{\tilde{t}} = 0, 45, 90$ deg). Note that for $\theta_{\tilde{t}} = 0$ deg, the sbottom mass cannot be chosen freely but is related to the stop mass as explained in Section 2, Eq. (2). This restricts the $\theta_{\tilde{t}} = 0$ case to $m_{\tilde{b}_1} \leq m_{\tilde{t}_1}$ and also causes the small offset of $m_{\tilde{b}_1}$ for the left-hand points in the figure. The figure confirms the conclusions from Figure 1. We see that stop masses around 300 GeV are always excluded, while stop masses of 600 GeV and above are not excluded for any sbottom mass or stop mixing angle. In the best case scenario $\theta_{\tilde{t}} = 90$ deg stop masses up to 500 GeV can be excluded irrespective of the sbottom mass. The reach is less good for a mixed stop ($\theta_{\tilde{t}} = 45$ deg), again irrespective of the sbottom mass. Interestingly, the case $\theta_{\tilde{t}} = 0$, where $m_{\tilde{b}_1} \leq m_{\tilde{t}_1}$ and hence both stop and sbottom events should contribute, is less well constrained than the other scenarios. The reason is to large extent the strong $\tan \beta$ dependence in this case.

4 ANALYSIS IMPLEMENTATION IN MADANALYSIS 5

In order to go beyond Simplified Models, we decided to implement the relevant ATLAS and CMS searches in MADANALYSIS 5 [259, 299, 300], interfaced with DELPHES 3. Within this framework, we produce and read the event files, implement all experimental selection requirements (commonly dubbed *cuts*), and produce histograms and cut flows. The aim is to produce a database of re-implemented and validated analyses that can readily be used for re-interpretation studies. Table 4 shows a list of relevant analyses which should be implemented within this project.

Direct searches for electroweak-inos may also be relevant, but will be considered only at a later stage. The work of implementing one-by-one the analyses listed in Table 4 started only recently, because first several technical developments were necessary in MADANALYSIS 5, as

Table 4: Analyses to be implemented within this project.

Analysis	Reference
0 lepton	
$E_T^{\text{miss}}, 2 b$ jets	ATLAS-SUSY-2013-05 [297]
$E_T^{\text{miss}}, \geq 3 b$ jets	ATLAS-CONF-2013-061 [301]
$H_T, E_T^{\text{miss}}, \geq 1 b$ jets	CMS-SUS-12-024 [302]
$E_T^{\text{miss}}, n b$ jets with α_T	CMS-SUS-12-028 [303]
H_T, H_T^{miss}	CMS-SUS-13-012 [304]
1 lepton	
\tilde{t} search with $E_T^{\text{miss}}, \geq 2 b$ jets	ATLAS-CONF-2013-037 [305]
$E_T^{\text{miss}}, \geq 3 b$ jets	ATLAS-CONF-2013-061 [301]
$E_T^{\text{miss}}, \geq 2 b$ jets	CMS-SUS-13-007 [306]
\tilde{t} search with $E_T^{\text{miss}}, \geq 2 b$ jets	CMS-SUS-13-011 [298]
2 leptons	
\tilde{t} search with $E_T^{\text{miss}},$ jets	ATLAS-CONF-2013-048 [307]
SS 2ℓ	CMS-SUS-13-013 [308]
OS 2ℓ	CMS-SUS-13-016 [309]

will be described in Section 5. Before reporting in detail on the implementation and validation of the experimental searches, a few comments are in order.

For each analysis, validation of the implementation done within MADANALYSIS 5 is a crucial step. For that purpose, we consider the same benchmark points as in the experimental paper or in the analysis note and we generate associated samples of events in a manner as close as possible to what has been done by ATLAS or CMS. We then try to reproduce all publicly available results for these benchmark points: histograms of kinematic variables, number of events after given cuts defining a signal region, and, if available, cut flows.

Unfortunately, the information publicly available in the experimental papers and in the analyses notes often does not suffice for an unambiguous validation. First of all, the definition of the benchmark points, in particular when they correspond to Simplified Model scenarios, is often incomplete because the mixing angles in the relevant squark and electroweak-ino sectors are omitted. In some cases, the relevant branching ratios are also not clearly defined. A simple way to overcome such problems would be that the experimental collaborations follow more closely the recommendations of Ref. [310] and systematically provide the employed supersymmetric spectra under the Supersymmetry Les Houches Accord (SLHA) format [79, 78], *e.g.* on the Twiki pages or on HepData [311] or INSPIRE [312]. ATLAS currently provides SLHA files on HepData for a number of SUSY analyses, which is extremely useful; we hope that this will be generalized to all ATLAS and CMS SUSY analyses in the future.

Generating events in the same way as done by ATLAS or CMS is an additional source of uncertainty, since the matching procedure between the parton shower and matrix element description is not publicly available. Furthermore, rather softs objects are almost always difficult

to treat correctly, given the [lack of] publicly available information on trigger and identification efficiencies.

Finally, the description of the analyses (*i.e.* the description of the selection criteria, event cleaning, signal isolation cuts, efficiencies, *etc.*) is sometimes not clear and/or incomplete and makes it necessary to contact the authors of the analysis for clarification of crucial elements. This can make the implementation and validation of some analyses a tedious process, which is only successful if enough inside information can be obtained from the experimental collaboration.

4.1 CMS-SUS-13-011: search for stop quarks in the single-lepton final state

The CMS search for stops in the single lepton and missing energy, $\ell + E_T^{\text{miss}}$, final state with full luminosity at a center-of-mass energy $\sqrt{s} = 8$ TeV [298], has been taken as a “template analysis” to develop a common language and framework for the analysis implementation. It also allowed us to test the new developments in MADANALYSIS 5 (see Section 5) which were necessary for carrying out this project.

The analysis targets two possible decay modes of the stop quark: $\tilde{t}_1 \rightarrow t\tilde{\chi}_1^0$ and $\tilde{t}_1 \rightarrow b\tilde{\chi}_1^+$, where one of the W -bosons produced in the decay of the top quark or the chargino decays leptonically and the other one hadronically. In the cut-based version of the analysis², two sets of signal regions (SRs) with different cuts, dedicated to one of the two decay modes, are defined. These two sets are further divided into “low ΔM ” and “high ΔM ” categories, targeting small and large mass differences with the LSP, respectively. Finally, each of these four categories are further sub-divided using four different E_T^{miss} requirements. In total, 16 different, potentially overlapping SRs are defined. Two cuts are based on rather complex and specific kinematic variables designed to reduce the dilepton $t\bar{t}$ background: a χ^2 resulting from the full reconstruction of the hadronic top quark and M_{T2}^W – a variant of the M_{T2} observable. The implementation of the χ^2 quantity in our code was straightforward thanks to the C++ ROOT code provided on the CMS Twiki page, whilst as shown in Section 5.2, the M_{T2}^W variable has been implemented from the algorithm presented in Ref. [313]. Overall, this analysis is very well documented. A missing piece of information, however, is details on the lepton and b -jet efficiencies.

The validation of the reimplementing of the analysis can be done using the eleven benchmark points presented in the experimental paper: four for the “T2tt” simplified model (in which the stop always decays as $\tilde{t}_1 \rightarrow t\tilde{\chi}_1^0$), and seven for the “T2bW” simplified model (in which the stop always decays as $\tilde{t}_1 \rightarrow b\tilde{\chi}_1^+$), with different assumptions on the various masses. The distributions of the kinematic variables used in the analysis are given in Figure 2 of Ref. [298] after the preselection cuts, with at least one benchmark point for illustration. Also provided are the corresponding histograms after the $M_T > 120$ GeV cut, as supplementary material on the CMS Twiki page. We use this information, together with the final number of events in the individual SRs (*i.e.* after all selection cuts) for given benchmark points provided in Tables 4 and 6 of Ref. [298] for the validation of our reimplementing within MADANALYSIS 5.

The validation material both before and after cuts defining the SRs is truly valuable information since one can separately check on the one hand the implementation of the kinematic variables and the preselection/cleaning cuts, and on the other hand the series of cuts defining the SRs. Furthermore, the large number of benchmark points allows us to check in detail the

²The search also contains an analysis based on boosted decision tree multivariate discriminants; such analyses generically cannot be externally reproduced and are therefore ignored in this work.

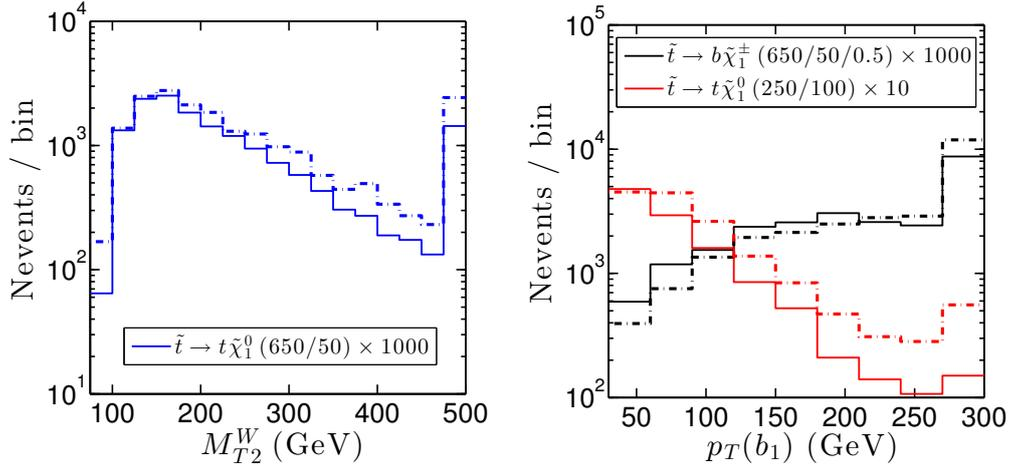


Figure 3: Distributions of the kinematic variable M_{T2}^W and the p_T of the leading b -tagged jet after preselection cuts of the analysis CMS-SUS-13-011. The solid lines correspond to the CMS results, given in Figure 2 of Ref. [298], while the dashed lines are obtained from our re-interpretation within MADANALYSIS 5.

quality of the reimplemention in complementary regions of phase space.

The validation process was based on (partonic) event samples, in LHE format, provided by the CMS collaboration. The provision of such event files greatly reduced the uncertainties in the first stage of validation since it avoided possible differences in the configuration of the used Monte Carlo tools. In the case of the CMS-SUS-13-011 analysis, the setup of MADGRAPH 5 [126], the event generator employed for generating the hard scattering matrix elements, is crucial, in particular with respect to the merging of samples with different (parton-level) jet multiplicities as performed by the CMS collaboration. The LHE files were passed through PYTHIA 6 [258] for parton showering and hadronization, then processed by our modified version of DELPHES3 (see Section 5.3) for simulation of the detector effects. The number of events after cuts and histograms produced by MADANALYSIS 5 were then normalized to the correct luminosity after including cross sections at next-to-leading order and next-to-leading logarithmic (NLO+NLL) accuracy, as tabulated by the LHC SUSY Cross Section Working Group [314]. Section 5.1 contains some snippets of our implementation of this search, to illustrate the new MADANALYSIS 5 syntax for signal regions and cuts.

Some examples of histograms reproduced for the validation are shown in Figure 3. The shapes of the distributions shown – as well as all other distributions that we obtained but do not show here – follow closely the ones from CMS, which indicates the correct implementation of the analysis and all the kinematic variables. (Note that discrepancies in bins where the number of events is relatively small, as seen on a logarithmic scale, suffers from larger statistical uncertainties and hence should not be over-interpreted.) The expected yields for several benchmark points in two example SRs are given in Tables 5 and 6. While the agreement is good for benchmark points with $m_{\tilde{t}_1} \geq 600$ GeV, large discrepancies appear when the stop is lighter and when the mass splittings are reduced. We are currently investigating the origin of these discrepancies. Two possible effects are under scrutiny: first, after generating the samples of events with MADGRAPH 5, CMS is applying a correction because of the incorrect Monte Carlo modeling of the initial-state radiation as explained in Appendix B of Ref. [298]. The effect can be as large as 20%, depending on the p_T of the system recoiling against the initial-state radiation jets. Second,

Table 5: Final number of events for the SR $\tilde{t} \rightarrow b\tilde{\chi}_1^\pm$, low ΔM , $E_T^{\text{miss}} > 250$ GeV of the analysis CMS-SUS-13-011. For each benchmark point, the first number indicates the stop mass, the second the LSP mass and the third one is x , defined as $m_{\tilde{\chi}_1^+} = x \cdot m_{\tilde{t}_1} + (1-x)m_{\tilde{\chi}_1^0}$.

$\tilde{t} \rightarrow b\tilde{\chi}_1^\pm$, low ΔM , $E_T^{\text{miss}} > 250$ GeV		
benchmark point	CMS result	MADANALYSIS 5 result
$\tilde{t} \rightarrow b\tilde{\chi}_1^\pm$ (650/50/0.5)	8.4 ± 0.4	8.0
$\tilde{t} \rightarrow b\tilde{\chi}_1^\pm$ (650/50/0.75)	11 ± 0.5	10.4
$\tilde{t} \rightarrow b\tilde{\chi}_1^\pm$ (600/100/0.5)	7.9 ± 0.5	7.8
$\tilde{t} \rightarrow b\tilde{\chi}_1^\pm$ (450/50/0.25)	8.7 ± 1.4	15.2
$\tilde{t} \rightarrow b\tilde{\chi}_1^\pm$ (250/50/0.5)	21 ± 3.4	34.2
$\tilde{t} \rightarrow b\tilde{\chi}_1^\pm$ (250/50/0.75)	56 ± 6.4	87.1

Table 6: Final number of events for the SR $\tilde{t} \rightarrow t\tilde{\chi}_1^0$, low ΔM , $E_T^{\text{miss}} > 250$ GeV of the analysis CMS-SUS-13-011. For each benchmark point, the first number indicates the stop mass, the second the LSP mass.

$\tilde{t} \rightarrow t\tilde{\chi}_1^0$, low ΔM , $E_T^{\text{miss}} > 250$ GeV		
benchmark point	CMS result	MADANALYSIS 5 result
$\tilde{t} \rightarrow t\tilde{\chi}_1^0$ (650/50)	6.2 ± 0.1	7.2
$\tilde{t} \rightarrow t\tilde{\chi}_1^0$ (250/50)	12 ± 1.2	16.9

the selection and isolation efficiencies we are currently using for the leptons may be inaccurate, as not enough information is provided by CMS³.

4.2 ATLAS-CONF-2013-048: search for stop quarks in the dilepton final state

The ATLAS search for stops in the dilepton and missing transverse energy, $2\ell + E_T^{\text{miss}}$, final state with full luminosity at $\sqrt{s} = 8$ TeV [307] has also been implemented within MADANALYSIS 5. Four SRs are defined with increasing requirements on M_{T2} and the hadronic activity in the final state. All SRs target the pair production of stop quarks, followed by a $\tilde{t}_1 \rightarrow b\tilde{\chi}_1^+$ decay. The different cuts on M_{T2} and on the hadronic activity are designed to provide sensitivity to both small and large mass differences between the stop quark and the chargino, as well as between the chargino and the LSP. The four SRs are then divided according to the flavor of the two leptons: Same Flavor (SF, $ee + \mu\mu$) and Different Flavor (DF, $e\mu$).

Two benchmark points have been employed in this analysis, $(m_{\tilde{t}_1}, m_{\tilde{\chi}_1^+}, m_{\tilde{\chi}_1^0}) = (150, 120, 1)$ GeV and $(400, 250, 1)$ GeV. The gauge-eigenstate composition (*i.e.* the mixing) of the superpartners, which affects the kinematics, is not specified in the paper. We take the stop to be left-handed,

³Efficiencies as function of p_T are provided for other CMS analyses, like for instance in Ref. [308]. However, as details in lepton selection differ between these analyses, it is not possible to use the information provided in one CMS note to validate another analysis. A more consistent approach in providing such detailed information for all analyses would be desirable.

the lightest chargino to be wino-like, and the LSP to be bino-like. The validation material consists of histograms showing the transverse hadronic activity in the event, $p_{Tb}^{\ell\ell}$, and the kinematic variable M_{T2} in the different SRs (Figures 1–5 of Ref. [307]). Apart from M_{T2} , the distributions are all presented after all cuts. Moreover, Appendix A of the conference note provides a cut flow for the benchmark point $(m_{\tilde{t}_1}, m_{\tilde{\chi}_1^\pm}, m_{\tilde{\chi}_1^0}) = (400, 250, 1)$ GeV. This cut flow is indeed valuable for the validation process, which is however still in an early stage.

4.3 ATLAS-SUSY-2013-05: Search for direct third-generation squark pair production in final states with missing transverse momentum and two b -jets

In this ATLAS analysis [297], \tilde{b}_1 and \tilde{t}_1 quarks are searched for in final states with large missing transverse momentum and two jets identified as b -jets. The results are presented for an integrated luminosity of 20.1 fb^{-1} of data and two possible sets of SUSY mass spectra are investigated. In the first one, the lightest sbottom, \tilde{b}_1 , is the only colored sparticle being produced and is assumed to decay exclusively via the $\tilde{b}_1 \rightarrow b\tilde{\chi}_1^0$ decay mode. In the second set of spectra, the lightest stop quark, \tilde{t}_1 , is this time the only colored sparticle that can be produced and it decays via the $\tilde{t}_1 \rightarrow b\tilde{\chi}_1^\pm$ channel, with undetectable products of the subsequent decay of the chargino $\tilde{\chi}_1^\pm$ due to the small mass splitting between the $\tilde{\chi}_1^\pm$ and the $\tilde{\chi}_1^0$ states. Two sets of SRs, denoted by SRA and SRB, are defined to provide sensitivity to the kinematic topologies associated with the two sets of SUSY mass spectra. SRA targets signal events with large mass splittings between the squark and the neutralino, while SRB is designed to enhance the sensitivity when the squark–neutralino mass difference is small; for the benchmarks points considered here, $\Delta m = m_{\tilde{\chi}_1^\pm} - m_{\tilde{\chi}_1^0} = 5 \text{ GeV}$.

Let us first describe the selection cuts common to both regions. Events are selected by requiring a large amount of missing transverse energy, $E_T^{\text{miss}} > 150 \text{ GeV}$, and any event containing an identified muon or electron is vetoed. For the SR selections, all jets with a pseudorapidity $|\eta| < 2.8$ are ordered according to their p_T , and two out of the n identified jets are required to be b -tagged. The following variables are then defined:

- $\Delta\phi_{\text{min}}$ is defined as the minimum azimuthal distance, $\Delta\phi$, between any of the three leading jets and the $\mathbf{p}_T^{\text{miss}}$ vector. Multijet background events are typically characterized by small values of $\Delta\phi_{\text{min}}$;
- m_{eff} is defined as the scalar sum of the p_T of the k leading jets and the E_T^{miss} , $k = 2$ for SRA and $k = 3$ for SRB;
- $H_{T,3}$ is defined as the scalar sum of the p_T of the n jets, without including the three leading jets;
- m_{bb} is defined as the invariant mass of the system of the two b -tagged jets;
- m_{CT} is the contranverse mass [315], a kinematic variable that can be used to measure the masses of pair-produced semi-invisibly decaying heavy particles. In this analysis, the two b -jets originating from the squark decays are the visible particles and the invisible particles are either the two $\tilde{\chi}_1^0$ particles or the decay products of the charginos, depending on the considered benchmark scenario. A correction to m_{CT} for the transverse boost due to initial state radiation is also applied [316]. The m_{CT} variable was implemented in our analysis using the publicly available library provided by the authors of Ref. [316]⁴.

In the SRA, the first two leading jets must be b -tagged and are identified as the sbottom or

⁴The library can be downloaded from <http://projects.hepforge.org/mctlib>.

stop decay products. The event is vetoed if any additional central jet ($|\eta| < 2.8$) with $p_T > 50$ GeV is found. To reject the multijet background large $\Delta\phi_{\min}$ and $E_T^{\text{miss}}/m_{\text{eff}}$ are required. To reduce the SM backgrounds a cut on $m_{bb} > 200$ GeV is applied. As a final selection, five different thresholds on m_{CT} ranging from 150 GeV to 350 GeV are demanded.

In SRB, the sensitivity to small squark-neutralino mass difference is increased by selecting events whose leading jet have a very large p_T , which is likely to have been produced from initial state radiation, recoiling against the squark-pair system. High thresholds on the leading jet and on the missing transverse momentum, which are required to be almost back-to-back in ϕ , are imposed. The leading jet is required to be non- b -tagged and two additional jets are required to be b -tagged. Just like for SRA, large values of $\Delta\phi_{\min}$ and $E_T^{\text{miss}}/m_{\text{eff}}$ are required, thereby suppressing the multijet background. The selection for SRB is finally completed by demanding that the additional hadronic activity is bounded from above, $H_{T,3} < 50$ GeV.

As validation material, several kinematic variable spectra are available in Ref. [297]. For SRA, both the m_{CT} and m_{bb} distributions are presented for two benchmark points, $(m_{\tilde{b}_1}, m_{\tilde{\chi}_1^0}) = (500, 1)$ GeV and $(m_{\tilde{t}_1}, m_{\tilde{\chi}_1^0}) = (500, 100)$ GeV with $\Delta m = 5$ GeV. After the SRA selection with $m_{CT} > 250$ GeV, 3% of the simulated events are retained for the signal point corresponding to $(m_{\tilde{b}_1}, m_{\tilde{\chi}_1^0}) = (500, 1)$ GeV.

For SRB, the missing transverse-momentum distribution is shown with all other selection criteria applied. Moreover, the distribution of $H_{T,3}$ is provided with all cuts but the $H_{T,3}$ requirement. The results are again shown for two benchmark points: $(m_{\tilde{b}_1}, m_{\tilde{\chi}_1^0}) = (300, 200)$ GeV and $(m_{\tilde{t}_1}, m_{\tilde{\chi}_1^0}) = (250, 150)$ GeV with $\Delta m = 5$ GeV.

To validate our implementation of this analysis we simulated 10^5 events for each benchmark point using MADGRAPH 5 interfaced to PYTHIA 6, with the CTEQ6L1 [285] set of parton distribution functions. The signal cross sections were normalized to the 8 TeV predictions computed at the NLO+NLL accuracy in the strong coupling constant [314]. At the time of writing, the validation is still in progress. This task is made difficult by the fact that only the final distributions, once almost all the cuts have been applied, are provided; since no cut-flows are available, tracking the validation procedure step-by-step is not possible. A complete description of the configuration employed in the event simulation together with a cut-flow would make the validation considerably easier.

5 NEW DEVELOPMENTS IN MADANALYSIS 5 and DELPHES

5.1 Region selection manager: dealing with multiple signal regions

In many experimental analyses performed at the LHC, including all of the new physics searches considered in this work, a branching set of selection criteria (“cuts”) is used to define several different sub-analyses (“regions”) within the same analysis. Versions of MADANALYSIS 5 older than v.1.1.10, however, were not expected to deal with this situation: the program was mainly dedicated to the design of prospective analyses, for which more than one sub-analysis is typically unnecessary. In other coding frameworks, multiple regions can be implemented but only with a nesting of conditions checking the cuts, which grows exponentially more complicated with the number of cuts. The scope of this project therefore motivated us to develop the MADANALYSIS 5 package to facilitate the handling of analyses with multiple regions.

Analyses in the MADANALYSIS 5 framework are divided into three functions:

- Initialize, which is dedicated to the initialization of the signal regions, histograms and

- cuts;
- Execute, which consists of the analysis to be applied to each event; and
- Finalize, which controls the production of histograms and cut-flow charts, or in other words, the results of the analysis.

The function `Finalize` has been internally automated within `MADANALYSIS 5`, so that the user can skip its implementation if desired; the two other methods however should be written by the user to suit his/her physics needs.

For the rest of this section we will illustrate the handling of multiple regions in the new `MADANALYSIS 5` framework by showing extracts of our implementation of the search `CMS-SUS-13-011` (see Section 4.1). This search defines 16 different SRs, and hence our `Initialize` function contains the initialization/declaration of 16 regions, all using the same syntax. For illustration, two of the 16 SRs are declared as

```
Manager()->AddRegionSelection("Stop->t+neutralino,LowDeltaM,MET>150");
Manager()->AddRegionSelection("Stop->t+neutralino,LowDeltaM,MET>200");
```

The declaration of each region relies on the `AddRegionSelection` method of the analysis manager class, of which `Manager()` is an instance. It takes as its argument a string which uniquely defines the SR under consideration.

Selection cuts must also be declared in `Initialize`. They fall into two categories: those which are common to all regions, and those which are not (*i.e.* those which apply only to some of the regions, thus serving to define the different regions). Two examples of the declaration of common cuts are:

```
Manager()->AddCut("1+ candidate lepton");
Manager()->AddCut("1 signal lepton");
```

The `AddCut` method of the analysis manager class has been used, which takes as argument a string which uniquely defines the cut. The declaration of cuts shared by some (but not all) regions makes use of the same `AddCut` function but requires a second argument: either a string or an array of strings, consisting of the names of all the regions to which the cut under consideration applies. For instance, we have

```
string SRForMet150Cut[] = {"Stop->b+chargino,LowDeltaM,MET>150",
    "Stop->b+chargino,HighDeltaM,MET>150",
    "Stop->t+neutralino,LowDeltaM,MET>150",
    "Stop->t+neutralino,HighDeltaM,MET>150"};
Manager()->AddCut("MET > 150 GeV",SRForMet150Cut);
```

for a cut on the missing transverse energy that applies to four of the SRs of the `CMS-SUS-13-011` analysis.

Histograms are initialized using the `AddHisto` method. As for the `AddCut` method, a string argument is required to act as a unique identifier for the object (histogram or cut), and a further optional argument consisting of a string or array of strings can be used to associate the object to desired regions.

We now move to the description of the `Execute` function that contains the analysis itself. It mainly relies on standard methods described in the manual of `MADANALYSIS 5` [259], which

are used to declare particle objects and compute observables related either to specific particles or to the event as a whole. We therefore restrict ourselves here to a description of the new manner in which cuts are applied and histograms filled, using the analysis manager class developed in this work. Having declared and filled a vector `SignalLeptons` with objects satisfying the signal lepton definition used in CMS-SUS-13-011, we impose a selection cut demanding exactly one signal lepton by including, in the `Execute` method of the analysis, the lines

```
unsigned int nsl = SignalLeptons.size();
if( !Manager()->ApplyCut((nsl==1), "1 signal lepton"))
    return;
```

Calling the `ApplyCut` using the syntax `if(!Manager()->ApplyCut(...)) return;` ensures that we stop analysing any given event as early as possible if all regions fail the cuts.

In the new framework, histogramming becomes as easy as applying a cut. For example in this search we are interested in the transverse-momentum spectrum of the leading lepton, and thus our code contains

```
Manager()->FillHisto("pT(1)", SignalLeptons[0]->momentum().Pt());
```

This fills the histogram which was previously declared with the name `"pT(1)"` in the `Initialize` method. The filling or not of histograms, according to whether cuts have been passed, is handled automatically.

For both selection cuts and histograms, all the kinematical observables described in Ref. [259] can be employed, as well as the new `isolCones()` method attached to the `RecLeptonFormat` class. This returns a vector of `IsolationConeType` objects describing the transverse activity in a cone of radius ΔR centered on the lepton. The properties of such objects can be accessed through

- `deltaR()`: returns the size of the cone,
- `sumPT()`: returns the scalar sum of the transverse momenta of the tracks lying in a cone of radius ΔR centered on the lepton,
- `sumET()`: returns the scalar sum of the transverse energy deposits in a cone of radius ΔR centered on the lepton.

These features can be used together with the modifications of DELPHES 3 described in Section 5.3.

5.2 Special kinematic variables

It is helpful if special kinematic variables, which appear repeatedly in the experimental analyses, are directly available for the user. For this reason we have added two such variables, namely M_{T2} [317] and M_{T2}^W [313], in the `PHYSICS` class of `MADANALYSIS 5`.

The M_{T2} variable has been implemented following the algorithm of Ref. [318]. It can be computed with the function

```
PHYSICS->Transverse->MT2(p1,p2,met,mass)
```

in the `Execute` function of a given analysis. In this notation we assume the pair production of a new state decaying into an invisible particle, whose mass is represented by the variable `mass`,

and a visible particle. The final state thus contains two visible particles referred to by the p1 and p2 objects and some missing transverse energy represented by the object met.

The M_{T2}^W variable has been implemented following the algorithm presented in Ref. [313]. The observable can be computed using

```
PHYSICS->Transverse->MT2W(jets,lep,met)
```

in the Execute function of an analysis. Here, the variable jets is a vector containing all jets of the event under consideration, lep a single lepton candidate and met the missing transverse energy of the event. Only the three leading jets are considered for the computation of the M_{T2}^W variable and, if available, the b -tagging information is used.

Further kinematical variables will be added as the need arises.

5.3 Modifications in DELPHES3

DELPHES [319] is a C++ framework which allows one to simulate a generic detector used in collider experiments. DELPHES does not simulate fully the particle-matter interactions but uses detector response parameterizations and reconstructs the main physics objects. The speed of the simulation is therefore enhanced and the accuracy level is suitable for phenomenological investigations.

From the computing side, DELPHES is a very modular framework where developers are invited to tune the default parameterization and add their own contributions. This modularity is based on a simulation process split into modules (derived from the TTask ROOT class). The configuration file using the TCL script language allows to easily add or to remove some modules. The content of the produced ROOT files can be configured in the same way. According to the goals of the present physics project, a tuning of the DELPHES3 release has been performed in order to supply all required information for recasting. The main changes are the following:

- In the initial DELPHES3 simulation processing, an isolation criterion is applied to both leptons and photons. Only particles satisfying the criterion are saved in the ROOT file. In our case, this isolation criterion is a part of the analysis selection. That is why a new DELPHES module called CalculationIsolation has been implemented to compute some isolation variables: the scalar sum of the track transverse momenta, the scalar sum of the calorimeter tower transverse energies and the number of tracks in the isolation cone. These variables are calculated for different isolation cone sizes, $\Delta R = 0.5, 0.4, 0.3$ and 0.2 . The initial DELPHES module filtering the lepton and photon candidates according to their isolation is skipped in order to keep all the candidates in the ROOT files. The isolation selection cut is thus postponed to the analysis step. This development has been achieved together with the isolCones() method of the RecLeptonFormat class of MADANALYSIS 5 (Section 5.1).
- As isolated leptons and isolated photons are not defined during the DELPHES simulation, the module UniqueObjectFinder which gives a unique identification to reconstructed objects is by-passed.
- Adding isolation variables to the data format increases the size of produced ROOT files. A cleaning of the collections is in order to reduce the file size. Collections such as calorimeter towers and particle-flow objects are not stored. The remaining heavy collection is the collection of generated particles at the hard scattering process level and after parton

showering and hadronization. This information is however useful to perform some cross-checks by matching reconstructed objects with generated particles. A skim is applied in order to keep only particles produced at the hard-scattering process level, final state leptons and b -quarks after showering. The size of the produced ROOT file is in this way divided by ten with respect to that obtained with the default configuration file.

- The parameterization related to the b -jet tagging efficiency and the rate of b -jet misidentification has been tuned in order to better mimic the performance of the CMS detector [320, 321].

Note that the latest release of DELPHES can also simulate the presence of pile-up events and the corresponding degradation of the detector reconstruction performance. This functionality is however not used in this project due to the lack of validation results.

6 MONTE CARLO EVENT GENERATION

Using the SUSY spectra created by SPHENO 3, we produce events at the parton-level for sbottom and stop pair production with up to two additional partons with MADGRAPH 5 [126]. Our simulation setup differs from the default loaded when starting MADGRAPH 5. First, we take into account initial b -quarks and antiquarks. We then work with the `mssm-full` model [322] of MADGRAPH 5 and the CTEQ6L1 set of parton densities. We then apply the loose generator cuts given in Table 7. As we produce up to two extra partons in the final state, we will need to

Table 7: Loose cuts applied during the event generation.

Minimal distance between two (parton-level) jets	0.001
Minimal distance between two (parton-level) b -jets	0.001
Minimal distance between a (parton-level) b -jet and a (parton-level) light jet	0.001

merge the different multiplicities and match them to the parton shower. This is performed with PYTHIA 6 [258] and following the MLM standard procedure [323], although the exact values for the merging parameters need to be determined process by process.

A correct choice for the merging parameters is crucial as it yields a consistent and smooth splitting of the phase space into regions dominated by matrix-element-based predictions and regions where parton showering correctly describes QCD radiation. The smoothness of the transition between these regions, or equivalently a check of the merging setup, can be investigated via differential jet rate distributions, a class of variables consisting of the distributions of the scale at which a specific event switches from a N -jet configuration to a $N + 1$ -jet configuration. In order to determine the setup for the processes under consideration, we performed a scan over the two main parameters to determine the `xqcut` and `qcut` parameters of MADGRAPH 5 and PYTHIA 6, respectively. We scanned `xqcut` from 10 to 70 GeV, and varied `qcut` in the range [`xqcut` + 5 GeV, $2 \cdot \text{xqcut}$]. For each combination we generated 60000 events, processed them up to the parton shower and computed the DJR spectra. A wide range of `xqcut` and `qcut` combinations were observed to be acceptable, with only a slight mass dependence. We illustrate this validation for stop pair production with $N = 0$ (left panel) and $N = 1$ in Figure 4 (right panel). The final values are `xqcut`=50 GeV and `qcut`=90 GeV, for pair production of fully left-handed stop quarks of mass $m_{\tilde{t}_1} = 600$ GeV. These values were found to be appropriate for

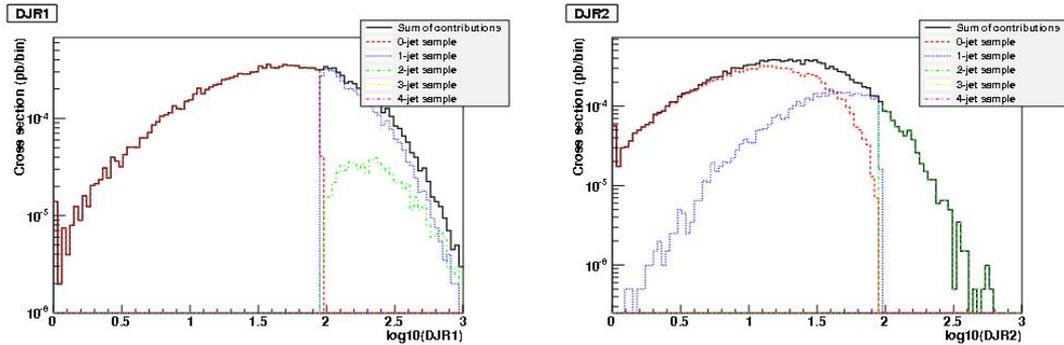


Figure 4: Differential jet rate spectra for stop pair production with $m_{\tilde{t}_1} = 600$ GeV. On the left the DJR distribution for $1 \rightarrow 0$ transition is shown, while on the right we show the $2 \rightarrow 1$ DJR spectra.

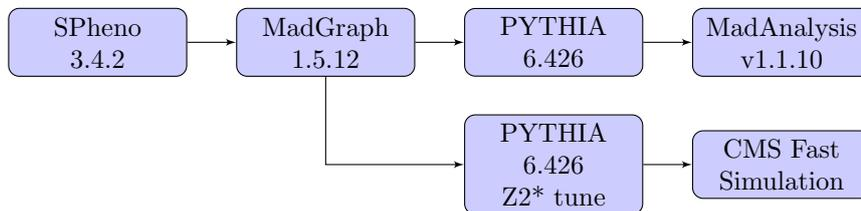


Figure 5: Schematic depiction of the programs used in the production chain.

stop and sbottom masses ranging up to 1 TeV, and were cross-checked by varying the gluino mass between 500 GeV and 2 TeV, and by changing the stop and sbottom mixing matrices.

With this choice of parameters, we produced 50000 events for each process and parameter space point. The computational resources required for this were accessed via the GlideinWMS [324] on the Open Science Grid [325]. We decayed the sparticles in the events according to the branching ratios given in the SLHA file from SPHENO and applied parton showering and hadronization with PYTHIA 6. The resulting event samples can then be parsed through the re-implemented analyses described in Section 4 after including a simulation of the detector response (see Section 5.3).

The (hard-scattering-level) LHE files stemming from MADGRAPH 5 will be also handed over to CMS for further processing. The sparticles therein will first be decayed using PYTHIA 6, according the SLHA decay table for that particular parameter point. Once this is done, they will go through the usual CMS procedure for producing SUSY scans. The parton shower and hadronization will be done with PYTHIA 6, using the Z2* tune, after which the events will be processed with the official CMS Fast Simulation software. Once completed, the scan will be made available to the SUSY analysis groups, who can then run their analysis on the sample, and provide efficiencies and upper limits for the considered parameter points. A flowchart of the production chain is depicted in Figure 5.

7 CONCLUSIONS

Our project is targeted at

- 1) assessing in detail the status of “natural supersymmetry” after the 8 TeV LHC run, and

- 2) developing a general analysis framework, within MADANALYSIS 5, which can serve as a platform for re-implementing ATLAS and CMS search results for new physics.

In the present contribution, we reported on the progress of this project. We presented a scan over physical parameters, namely stop and sbottom masses and mixing angles, and higgsino masses, which lays the basis of any later re-interpretation of the experimental results. The SLHA files from this scan are readily available and may also be used by ATLAS and/or CMS for interpreting their results.

Analyzing these SLHA spectra with SMOBELS in the Simplified Models approach, we found that the exclusion limits indeed seem to depend quite sensitively on the precise scenario at hand – even if it contains only a light \tilde{t}_1 , light higgsinos ($\tilde{\chi}_1^0$, $\tilde{\chi}_2^0$ and $\tilde{\chi}_1^\pm$), and possibly a light \tilde{b}_1 .

The implementation of the relevant ATLAS and CMS searches for stops and sbottoms in the MADANALYSIS 5 framework first required several extensions of MADANALYSIS 5 as well as some modifications of DELPHES 3, in order to adapt them for this project. A large part of the work thus concerned developing the necessary tools. This part is now concluded.

The process of implementation and validation is still ongoing. It is impeded by the fact that the information publicly available in the experimental papers and/or analyses notes and/or on Twiki pages is usually not sufficient for an unambiguous validation. It would be of immense advantage for efforts like the one which we are undertaking here, if the experimental collaborations followed more closely the *Les Houches Recommendations for the Presentation of LHC Results* [310]. In particular it would be extremely helpful if well-defined benchmark points, efficiencies and cut-flows were made available in a more systematic manner.

Two other program packages for confronting new physics scenarios with LHC Data were published recently. They are largely complementary to the ones we have been discussing in this contribution. The first one, CHECKMATE [326], is based on fast simulation and determines whether a model is excluded or not at 95% confidence level by comparing to several recent experimental analyses; the analyses currently implemented in CHECKMATE are mostly from ATLAS and have only little overlap with the ones we are interested in in this project. The second program is FASTLIM [327] and reconstructs the visible cross sections [of SUSY events] from pre-calculated efficiency tables and cross section tables for simplified event topologies. FASTLIM has only ATLAS analyses implemented, including however in particular those targeted at stop and bottom searches. It will be interesting to compare the different approaches – a comparison between SMOBELS and FASTLIM is on the way.

ACKNOWLEDGEMENTS

We gratefully acknowledge the use of the computational power provided by the Open Science Grid [325] that were accessed via GlideinWMS [324].

This work was financed in part by the Theory-LHC-France initiative of the CNRS/IN2P3, the PEPS-PTI project “LHC-itools” and by the EGIDE/DAAD project nr. PROCOPE 54366394. EC and BF acknowledge partial support from the French ANR 12 JS05 002 01 BATS@LHC. LM and WP are supported by the BMBF, project nr. 05H12WWE. LM acknowledges moreover support from the Elitenetzwerk Bayern. NS is supported by a Ph.D. fellowship of the Research Foundation - Flanders (FWO).

Contribution 15

Reviving Minimal Left-Right Supersymmetry in the Light of LHC Data

A. Alloul, L. Basso, B. Fuks, M. E. Krauss, W. Porod

Abstract

In the context of left-right supersymmetric theories we present a reinterpretation of three experimental searches dedicated to signatures induced by a W' -boson, of which one is sensitive to the presence of right-handed neutrinos. We emphasize that according to the way the experimental results are provided, this task can be either easily feasible or could be rather complex, if not impossible in the general way. We consequently provide recommendations to improve the situation in the future.

1 INTRODUCTION

Large classes of theories have been proposed over the last decades to extend the Standard Model (SM) and provide tentative answers to one or several of its conceptual questions. Among those, weak scale supersymmetry is one of the most studied options, both at the theoretical and experimental levels. However, no hint for any superpartner has been found so far, both through direct searches at colliders and via indirect probes at low-energy experiments. Most results have been derived under either the framework of the so-called Minimal Supersymmetric Standard Model (MSSM) or by assuming simplified models inspired by the latter. Often these minimal assumptions are too limiting. There exist alternative, non-minimal realizations of supersymmetry that evade the current bounds and at the same time have novel features possibly not covered by current searches.

In this report, we consider one of these non-minimal supersymmetric theories that exhibit a left-right (LR) symmetry [328, 329, 330, 331], and focus on the consequences of the presence of an additional charged gauge boson, commonly denoted by W' (or, as we will use from now on, W_R), arising from the extended gauge structure. In contrast to the non-supersymmetric case, the new boson can decay into lighter supersymmetric particles, which implies that the branching ratios into commonly searched for signatures, and thus the derived bounds on the W_R -boson mass and couplings, could be reduced. To illustrate this statement, we recast three recent CMS searches in a left-right supersymmetric framework. We start by revisiting two classical W_R analyses where the new charged gauge boson is expected to decay either into a pair of jets [332] or into a two-body system comprised of a top and of a bottom quark [333]. In the first analysis, the experimental results have been derived in the very specific theoretical framework constructed in Refs. [334, 335, 336, 337] while in the second analysis, an effective Lagrangian encompassing a W' -boson coupling uniquely to quarks has been employed. Next, we focus on regions of the parameter space where right-handed neutrinos can be copiously produced at the Large Hadron Collider (LHC), and reinterpret the results of a recent search for

right-handed neutrinos based on a simplified setup where they always decay into a lepton plus dijet final state [338].

The rest of this contribution is organized as follows: in Section 2, we briefly describe our theoretical framework and provide information on our choices of benchmark scenarios and on the simulation chain that has been employed to generate signal events. Our results related to the reinterpretation of the three above-mentioned analyses are then shown in Section 3, where we also emphasize that the way in which the results are presented is not often appropriate for recasting. We therefore take the opportunity to provide recommendations aiming to facilitate the communication between theorists and experimentalists in the future. Our conclusions are presented in Section 4

2 THE MODEL

2.1 Model description

There exist many versions of left-right symmetric supersymmetric theories [328, 329, 330, 331], each based on the $SU(3)_c \times SU(2)_L \times SU(2)_R \times U(1)_{B-L}$ gauge group. Aside the gauge structure, all these models include four vector superfields, directly related to the gauge structure, and (s)quark and (s)lepton degrees of freedom organized in left- and right-handed doublets of both $SU(2)$ symmetries. They differentiate in the Higgs sector, that is generally very rich in order to allow for a successful symmetry breaking scheme without spoiling current data. In the scenario we have adopted, it comprises two $SU(2)_L \times SU(2)_R$ bidoublets Φ_1 and Φ_2 not sensitive to the $B-L$ symmetry, two $SU(2)_L$ ($SU(2)_R$) triplets Δ_{1L} (Δ_{1R}) and Δ_{2L} (Δ_{2R}) with $B-L$ charges of -2 and $+2$, respectively, and one gauge singlet S .

Focusing on the model-dependent part of the superspace action, the superpotential is given by

$$\begin{aligned}
W = & Q_L y_Q^1 \Phi_1 Q_R + Q_L y_Q^2 \Phi_2 Q_R + L_L y_L^1 \Phi_1 L_R + L_L y_L^2 \Phi_2 L_R + L_L y_L^3 \Delta_{2L} L_L + L_R y_L^4 \Delta_{1R} L_R \\
& + (\mu_L + \lambda_L S) \Delta_{1L} \cdot \Delta_{2L} + (\mu_R + \lambda_R S) \Delta_{1R} \cdot \Delta_{2R} + (\mu_1 + \lambda_1 S) \Phi_1 \cdot \Phi_1 \\
& + (\mu_2 + \lambda_2 S) \Phi_2 \cdot \Phi_2 + (\mu_{12} + \lambda_{12} S) \Phi_1 \cdot \Phi_2 + \frac{1}{3} \lambda_s S^3 + \mu_s S^2 + \xi_s S,
\end{aligned} \tag{1}$$

where we refer to Ref. [339] for details on the underlying (understood) index structure as well as for a more extensive description of the model. In this expression, Q_L (L_L) and Q_R (L_R) are the left- and right-handed doublets of quark (lepton) superfields and the interaction strengths have been embedded into 3×3 Yukawa matrices (y_Q^i and y_L^j , $i = 1, 2, j = 1, \dots, 4$), a single linear ξ term, a set of supersymmetric mass (μ) terms and trilinear Higgs(ino) self-interactions (λ). From the superpotential, we can derive the form of the soft supersymmetry-breaking Lagrangian which contains, in addition to scalar and gaugino mass terms, trilinear scalar interactions of sfermions and Higgs bosons (T_Q and T_L) and linear (ξ), bilinear (B) and trilinear (T) Higgs self-interactions.

2.2 Benchmark scenarios and technical setup

In order to design theoretically motivated benchmark scenarios, we have implemented the left-right supersymmetric model of the previous subsection into SARAH [340, 341], which allows one to automatically calculate all the model mass matrices, vertices and tadpole equations and pass the information to SPHENO [295] for spectrum calculation at the one-loop level. Several

analytical cross checks with the model implementation in FEYNRULES [252, 253] have been performed. The model information has then been translated into the UFO format [203] and linked to MADGRAPH 5 [126] for simulating LHC collisions and reinterpreting the three CMS analyses of Section 3. The model implementations have been further validated via a confrontation of numerical results as computed by both MADGRAPH and CALCHEP [189].

We have employed the tadpole equations to calculate the soft masses of the Higgs bidoublets and triplets in terms of the vacuum expectation values (vevs). We have then scanned over the remaining parameter space on the basis of a setup analogous to the one of Ref. [339], to which we refer for more information. All bilinear superpotential terms μ_i and the corresponding soft breaking parameters (B_i) have hence been set to zero, together with the λ_1 , λ_2 , ξ_s and ξ parameters. The vev of the gauge singlet Higgs field has been imposed to be $v_s = 10 \text{ TeV}$ ¹, while most of the other vevs have been taken to be vanishing, with the exception of those of the neutral scalar component of the Δ_R superfields, controlling the W' -boson mass, and those of the scalar component of the $(\Phi_1)^1_1$ and $(\Phi_2)^2_2$ superfields related to the weak boson masses. Moreover, we have imposed that both $SU(2)_L$ and $SU(2)_R$ gauge coupling strengths are equal at the weak scale, that the spectrum exhibits a Standard Model-like Higgs boson with a mass in the 122 – 128 GeV range, and that a lower bound of 220 GeV on the mass of the doubly-charged Higgs boson is satisfied [342]².

3 RECASTING LHC RESULTS

3.1 W_R decays into SM-particles

The search for new heavy charged gauge bosons comprises several search channels. The seemingly most stringent bounds are set by investigating the signature of a charged lepton and missing energy, assuming that the new gauge boson decays into a lepton and a low-mass neutrino which escapes detection, see *e.g.* Ref. [343]. In a left-right symmetric scenario the results associated with this search however do not apply. When neutrino data is explained by some sort of seesaw mechanism, the decay of the W_R into a lepton and a low-mass neutrino is generally suppressed by the small neutrino mixing, while the naive $W_R \rightarrow \ell \nu_R$ mode does not lead to missing energy since the right-handed neutrino decays.

On the other hand, searches with hadronic two-body final states do apply to left-right models since the coupling strength of the W_R -boson to a pair of quarks is equal to that of the SM W -boson, given that $g_R = g_L$ holds. The tightest current bounds are provided by the CMS searches into a) a top-bottom pair of quarks [333], and b) a dijet final state [332]. In order to have a meaningful comparison, we apply the same strategy of calculating the cross section (*i.e.* parton distribution functions (PDFs), K -factors and selection requirements) as was used by the experimental collaborations when deriving the bounds. However, concerning the bounds for the $t\bar{b}$ final state of Ref. [333], the choice of the PDF set has been used inconsistently: in [333] leading order (LO) matrix elements have been convoluted with next-to-leading order (NLO) PDFs and the resulting cross section has then been multiplied by an additional K -factor. The correct procedure, however, is to use both (matrix elements and PDFs) at NLO, or both at LO

¹Variations from this choice can be obtained via the λ parameters.

²The lowest bounds on a doubly-charged Higgs boson is 198 GeV when it decays with a branching fraction of 100 % into two tau leptons. Since in general all three lepton flavours are possible as a decay product and the bounds on the other final states are more severe, we restrict ourselves to the case where $m_{H^{\pm\pm}} > 220 \text{ GeV}$ and $\text{BR}(H^{\pm\pm} \rightarrow \tau\tau) > 0.8$.

and to apply in the latter case a K -factor such that $\sigma_{LO} \cdot K = \sigma_{NLO}$. In Fig. 1 we display both the cross section evaluated as it should be, using the LO PDF sets CTEQ6L1 [285] and a K -factor $K = 1.2$, and as done in Ref. [333] with the NLO set of parton densities CTEQ6M and a K -factor also set to $K = 1.2$. One observes that the difference in cross section between both approaches is of about 10 %. Moreover, the bound on the W_R -boson mass in our model from tb searches is around $M_{W_R} > 1970$ GeV, which is about 50 GeV lower than the bounds on a W' -boson decaying into standard modes only. For completeness we remark that in Ref. [333] the results are given for three generations of leptons.

The reason for the experimental choice is to have a better handle on the PDF systematics. Our investigation showed that this procedure, albeit theoretically inconsistent, however only marginally affects the results. We suggest to experimentalists to use a consistent framework, either with NLO matrix elements when available, or with a more suitable definition of the K -factor as in their setup to avoid NLO over counting. Aside for this technical point, we confirm the suitability of employing simplified models in these simple searches, since they capture the essence of the models within few percent.

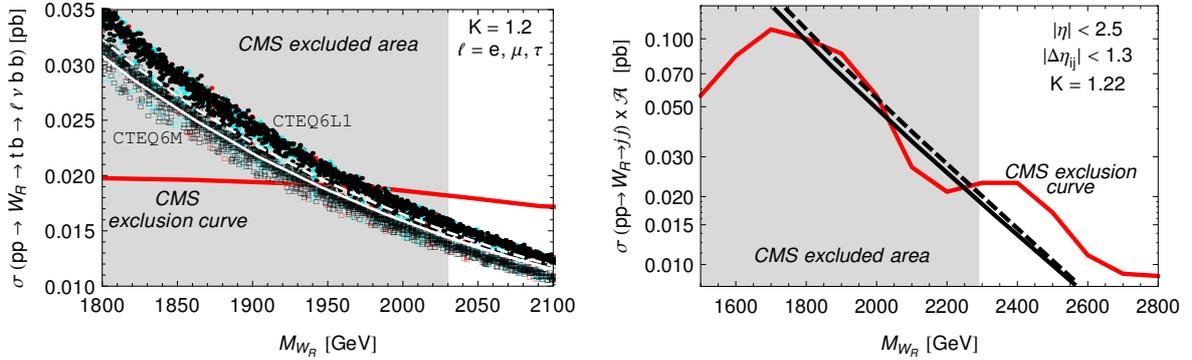


Figure 1: (Left) Bounds from W_R -boson searches in the tb mode: the red line shows the CMS upper limit on the cross section $pp \rightarrow W_R \rightarrow tb \rightarrow \ell \nu bb$, where $\ell = e, \mu, \tau$. Red benchmark points present a valid spectrum but with $198 < m_{H_1^{\pm\pm}}/\text{GeV} < 220$ or $\text{BR}(H_1^{\pm\pm} \rightarrow \tau\tau) < 0.8$. Cyan points exhibit a more sensible doubly-charged Higgs boson ($m_{H_1^{\pm\pm}} > 220$ GeV and $\text{BR}(H_1^{\pm\pm} \rightarrow \tau\tau) > 0.8$). Black points are a subset of the former that is relevant for section 3.2, *i.e.* when $m_{H_1^{\pm\pm}} < m_{\nu_{R,i}}$. The shown cross sections visualized by dots (squares) have been obtained using the PDF set CTEQ6L1 (CTEQ6M), as explained in the text. The parameters have been varied within the ranges $3.8 \leq v_R/\text{TeV} \leq 4.6$, $-1 \leq \lambda_{s/L/R} \leq 1$, $-0.1 \leq \lambda_{12} \leq 0.1$, $200 \leq M_{2L/2R}/\text{GeV} \leq 900$, $0 < M_1/\text{GeV} \leq 500$, $4 \leq \tan \beta \leq 15$. We also show in white the cross sections of two specific parameter points with reduced branching ratios of the W_R -boson to SM particles, evaluated with CTEQ6L1. The values have been set to $\lambda_s = 0.8$, $\lambda_L = \lambda_R = -1$, $\lambda_{12} = 0.025$, $M_1 = M_{2R} = 250$ GeV, $M_{2L} = 500$ GeV, $\tan \beta = 30$ (solid line) and $\lambda_s = 0.3$, $\lambda_L = \lambda_R = -0.4$, $\lambda_{12} = 0.04$, $M_1 = 200$ GeV, $M_{2R} = M_{2L} = 550$ GeV, $\tan \beta = 10$ (dashed line).

(Right) Bounds from W_R -boson searches in the dijet mode: shown is the cross section exclusion line from CMS (red) at 8 TeV center-of-mass energy and 19.6 fb^{-1} [332]. The black solid and dashed lines depict the calculated cross section for two parameter choices as in the left figure.

Moving to the dijet search, we give again the results obtained after applying the same selection requirements as in Ref. [332], namely imposing that the pseudorapidity of the jets

satisfies $|\eta| < 2.5$, and that the relative difference in pseudorapidity between the jets j_i and j_j fulfills $|\Delta\eta_{ij}| < 1.3$. The subsequent acceptance resulting from these selections is $\mathcal{A} \approx 0.5$. In Fig. 1 we compare the cross sections for two parameter choices with the CMS bounds in this dijet analysis. We chose the PDF set CTEQ6L1 and a K -factor of 1.22 as in Ref. [332]. We see that the W_R -boson mass is constrained to lie above 2250 GeV, with the exception of a small window between 1800 and 2030 GeV. Combining this with the results on the tb -channel, this window gets reduced to the range 1970–2030 GeV.

By virtue of several difficulties we encountered when intending to confront our results to the experimental bounds, we would like to encourage our experimental colleagues to present their results in a more transparent way when comparing measured cross sections to theory expectations. This encompasses in our understanding a profound explanation of the understood theory assumptions and/or simplifications, the details of modelling the signal as well as the provision of a table of the excluded cross sections as has been done by the authors of Ref. [332]. All details of how signals should be produced in order to be suitable for comparing to the exclusions should also be given (*e.g.* PDF set, final state, selection requirements, K -factor, model assumptions, and so on) to allow for reproducibility and cross checks.

3.2 Interplay with right-handed neutrinos

It is usually assumed in left-right symmetric models that the right-handed neutrinos can only decay via the W_R -boson, which can be either on- or off-shell. This is used by experimental collaborations to set strict bounds on a combination of masses of ν_R and W_R , see, *e.g.*, Ref. [338].

However, this simplified assumption can sometimes be too restrictive, in particular in our model. The right-handed neutrino acquires its mass via the coupling y_L^4 to the $SU(2)_R$ triplet Δ_{1R} . This implies that $y_L^4 \sim \mathcal{O}(0.1)$ for a right-handed neutrino mass m_{ν_R} lying in the range 100 GeV–1 TeV and that the vev v_R is of $\mathcal{O}(1 \text{ TeV})$. In addition, one of the six physical singly-charged Higgs bosons present in our model (H_1^\pm) can be rather light with a mass of $\mathcal{O}(200 \text{ GeV})$. The coupling of this state to the right-handed neutrino ν_R is y_L^4 times the entry of the charged-Higgs mixing matrix connecting H_1^\pm to Δ_{1R} . Hence, the two-body decay $\nu_R \rightarrow H_1^\pm \ell$ will usually dominate over the three-body decays mediated by an off-shell W_R -boson. This can be seen in Fig. 2 where we show the branching ratios $BR(\nu_R \rightarrow H_1^\pm \ell)$, $BR(\nu_R \rightarrow \ell jj)$ and $BR(\nu_R \rightarrow \ell tb)$, the latter two mediated by an off-shell W_R -boson. As soon as $m_{\nu_R} > m_{H_1^\pm}$, $\nu_R \rightarrow H_1^\pm \ell$ becomes the dominant decay mode and the branching ratio for the $\nu_R \rightarrow W_R \ell \rightarrow \ell jj$ channel, which is considered by the experimental analyses, gets significantly reduced. Finally, H_1^\pm decays almost exclusively into a $t\bar{b} + \bar{t}b$ final state.

Experimental results that are possible to recast are available only for $m_{\nu_R} = \frac{1}{2}M_{W_R}$ [338]. We depict in Fig. 3 the results for our model and compare them with these bounds for two cases: (a) the right-handed neutrino $\nu_{R,\mu}$ has half of the W_R -boson mass and (b) all three heavy neutrinos are degenerate in mass. In the setup used in Ref. [338] the lower bounds on the mass of the W_R -boson M_{W_R} are about 2.45 TeV and 2.75 TeV, respectively. Taking into account the additional decay modes we find that these bounds can be reduced by about 600 GeV each. Note that, although we can not compare to bounds for more general mass patterns, it is clear that in the case of even lighter right-handed neutrinos, the bounds are even more relaxed since the three-body decay gets more suppressed with respect to the open two-body decay, as can be seen in Fig. 2. Unfortunately currently there is no data available to study this case in detail.

As in the previous subsection, we would like to address a message to experimentalists.

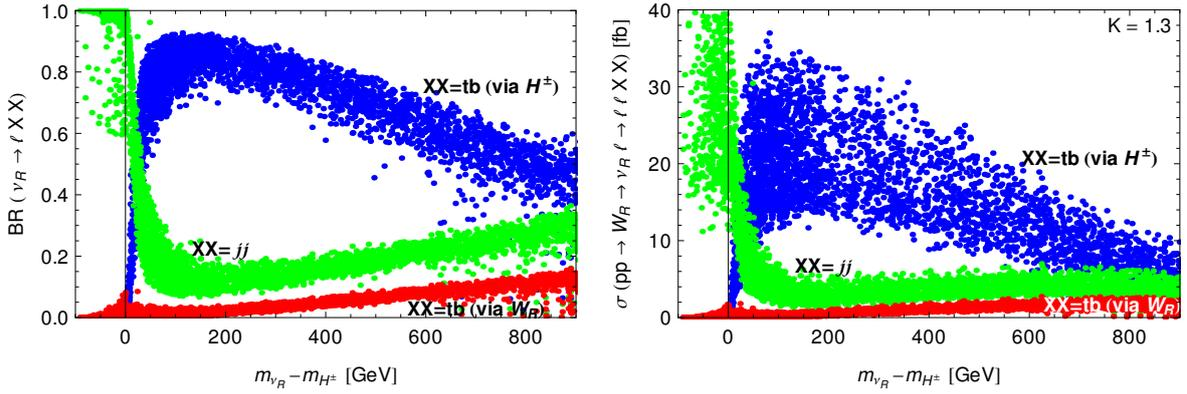


Figure 2: Branching ratios of the right-handed neutrino as a function of the mass difference to the lightest charged Higgs state (left) and the corresponding cross section of the respective neutrino state produced by a W_R -resonance (right), using the PDF set CTEQ6L1 as in Ref. [338] and a K -factor of 1.3. Blue points depict cases where the right-handed neutrino ν_R decays to a ℓH_1^\pm state, with the charged Higgs boson H_1^\pm further decaying to a tb final state, whereas green (red) points represent cases where it decays into a ℓjj (tb) state mediated by an intermediate off-shell W_R -boson. The parameters have been varied within the ranges $3.8 \leq v_R/\text{TeV} \leq 4.3$, $-1 \leq \lambda_{s/L/R} \leq 1$, $-0.1 \leq \lambda_{12} \leq 0.1$, $200 \leq M_{2L/2R}/\text{GeV} \leq 900$, $0 < M_1/\text{GeV} \leq 500$, $4 \leq \tan\beta \leq 15$. The mass of the charged Higgs boson H_1^\pm lies in the range of $180 < m_{H_1^\pm}/\text{GeV} < 320$. Let us note that the branching fractions shown do not always add to 1 for some parameter points due to three-body decays into $\ell \tilde{\chi}^\pm \tilde{\chi}^0$ states that are kinematically accessible.

The simple exclusions as presented in Ref. [338] are not useful, because we cannot recast them for new models or modified assumptions (other than for $m_{\nu_R} = \frac{1}{2}M_{W_R}$) in the absence of expected and observed cross sections and relative efficiencies. In this case, a table of excluded cross sections in the $M_{W_R} - m_{\nu_R}$ plane would be of great help.

4 CONCLUSIONS

We have studied a supersymmetric variant of a left-right-symmetric model focusing in particular on the bounds on the mass of the additional charged vector-boson W_R . We have shown that the bounds obtained by experimental collaborations get reduced as new decay channels are open. Our findings are that this effect is strongest in scenarios where the W_R can decay into right-handed neutrinos as the latter have an additional decay channel into a ℓH^\pm state. In this case, the bounds on the mass of the W_R -boson M_{W_R} get reduced by about 600 GeV. Finally, we have remarked how in our view the communication between experiment and theory could be improved by a more detailed way of presenting the analysis results.

ACKNOWLEDGEMENTS

We thank the organisers for setting up this nice event (including the great food and amazing sceneries of the French alps) and for the nice working atmosphere. MEK thanks Florian Staub for many useful discussions about the model implementation. We further thank John Paul Chou, Bryan M. Dahmes, Robert M. Harris, Freya Blekman, and Maxim Perfilov for helpful clarifications concerning the experimental analyses. The work of AA, LB and BF has received partial

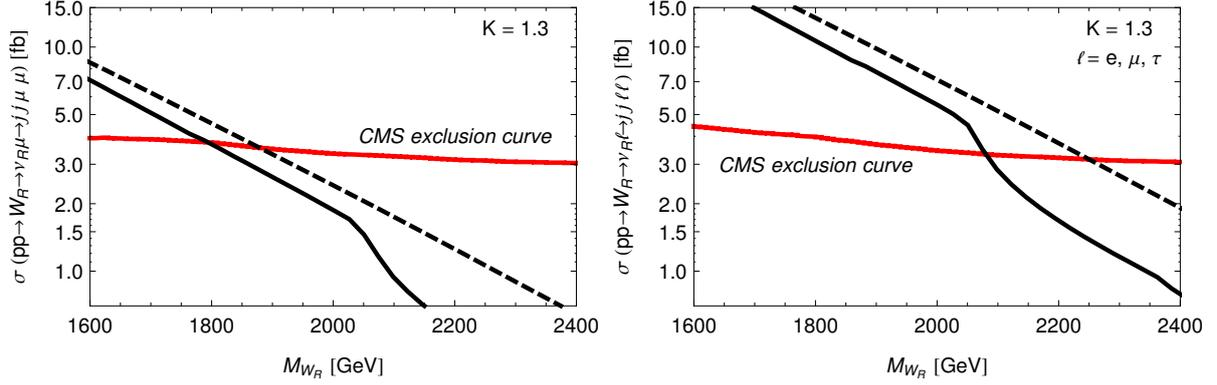


Figure 3: Bounds on the cross section $\sigma(pp \rightarrow W_R \rightarrow \nu_R \ell \rightarrow jj\ell\ell)$ at $\sqrt{s} = 8$ TeV for $m_{\nu_R} = \frac{1}{2}M_{W_R}$ considering $\sigma \cdot BR(jj\mu\mu)$ only (left) and for the case that all three right-handed neutrinos are degenerate in mass (right). Our curves have been obtained from the results given in Ref. [338]. The same two parameter points as in Fig. 2, but with adjusted masses for the right-handed neutrinos, are shown, and the vev v_R has been varied from 3 TeV to 6 TeV. The black solid and dashed lines depict the calculated cross sections for the two parameter choices as in Fig. 1, and we note that for the parameter choice depicted by the solid black line, the two-body decay into a chargino and a slepton opens at $m_{\nu_R} \approx 1$ TeV.

support from the Theorie-LHC France initiative of the CNRS/IN2P3 and by the French ANR 12 JS05 002 01 BATS@LHC. LB is also supported by the Deutsche Forschungsgemeinschaft through the Research Training Group grant GRK 1102 *Physics at Hadron Accelerators* and by the Bundesministerium für Bildung und Forschung within the Förderschwerpunkt *Elementary Particle Physics*. MEK and WP are supported by the DFG research training group 1147 and by the DFG project no. PO-1337/3-1. WP is also supported by DAAD project PROCOPE 54366394.

Contribution 16

Benchmark Models for Spin-1 Resonances in Composite Higgs Theories

R. Contino, D. Greco, C. Grojean, D. Liu, D. Pappadopulo, A. Thamm, R. Torre, A. Wulzer

Abstract

Heavy spin-1 resonances are a generic prediction of theories where electroweak symmetry breaking is triggered by new strongly-interacting dynamics at the TeV scale. In this contribution we study the phenomenology of spin-1 resonances in composite Higgs theories based on the coset $SO(5)/SO(4)$. We introduce a simple model to describe their dynamics and give its implementation in the parton-level generator MadGraph5. The model captures the basic features of the resonances' phenomenology in terms of a minimal set of parameters, and can be used as a benchmark in the search for heavy spin-1 states at the LHC and future colliders.

1 Introduction

One of the robust predictions of theories with strong electroweak symmetry breaking (EWSB) is the existence of spin-1 resonances excited from the vacuum by the conserved currents of the strong dynamics. They form multiplets of the unbroken global symmetry, which includes an $SO(4) \sim SU(2)_L \times SU(2)_R$ in the case of composite Higgs theories [146]. The phenomenology of these resonances can be rather different from the one of heavy Z' states in weakly coupled extensions of the Standard Model (SM). They interact strongly with longitudinally-polarized W and Z bosons and the Higgs boson, and thus tend to be broader than weakly-coupled vectors. The strength of their couplings to SM fermions depends on whether these latter participate to the strong dynamics or are purely elementary states. A simple possibility is that SM fermions couple in the EWSB dynamics according to their masses, so that the lightest ones are the most weakly coupled. This idea has an elegant implementation in the framework of partial compositeness [344, 231] and can give a qualitative explanation of the hierarchies in the Yukawa matrices of the SM fermions [345, 346] in terms of RG flows [347, 153].

In this work we study the phenomenology of spin-1 resonances in composite Higgs theories by means of a simplified description based on an effective Lagrangian. This is aimed at capturing the main features relevant for the production of the resonances at high-energy colliders and their effects in low-energy experiments, avoiding the complication of a full model. Although simplified, our construction will be sophisticated enough to properly include those aspects which are distinctive predictions of the class of theories under consideration, such as for example the pseudo Nambu-Goldstone (NG) nature of the Higgs boson. We will focus on minimal $SO(5)/SO(4)$ composite Higgs theories and consider resonances transforming as $(3, 1)$ and $(1, 3)$ of $SO(4)$, respectively denoted as ρ_L and ρ_R in the following. We assume that SM fermions are fully elementary and couple to the heavy resonances only through the mixing of the

latter with elementary gauge fields. This implies small universal couplings of ρ_L, ρ_R to fermions of order $\sim g_{SM}^2/g_\rho$, where g_ρ sets the interaction strength of the resonances to other composite states, including longitudinally-polarized W and Z bosons and the Higgs boson. This construction can be generalized to include direct couplings of the heaviest SM fermions, in particular of the top and bottom quarks, to composite states as implied by partial compositeness. Starting from the Lagrangian defining our model, we discuss the rotation to the mass-eigenstate basis and derive the physical spectrum and interactions. We provide a calculator of physical quantities (masses and couplings) and an implementation of the model in the parton-level generator MadGraph5 [126] for the simulation of MonteCarlo events. These tools can be downloaded from the HEPMDB website at the URL <http://hepmdb.soton.ac.uk/hepmdb:0214.0154> and are the main result of this work.

Aim of this work is to provide a benchmark model to be used in searches for heavy spin-1 states at the LHC and at future colliders. A simple kinematic model based on the width and the production cross section times the decay branching ratio ($\sigma \times BR$) is sufficient to guide searches for narrow resonances in individual channels and to set limits, see the recent discussion in Ref. [348]. However, combining the results obtained in different final states as well as interpreting the limits on $\sigma \times BR$ in explicit models of physics beyond the SM requires an underlying dynamical description, such as the one given by a simplified Lagrangian. Here we provide such a dynamical description for spin-1 resonances appearing in a motivated and sufficiently large class of composite Higgs theories. Our construction fully takes into account the non-linear effects due to multiple insertions of the Higgs vev and does not rely on an expansion in v/f , where v is the electroweak scale and f is the decay constant of the NG boson Higgs. In the limit $v/f \ll 1$ our Lagrangian can be matched onto the more general one of Ref. [348], which covers a more ample spectrum of possibilities in terms of a larger number of free parameters. In this sense, the main virtue of our model is that of describing the phenomenology of spin-1 resonances in composite Higgs theories in terms of a minimal set of fundamental quantities: one mass and one coupling strength for each resonance. Expressing the experimental results in such restricted parameter space is thus extremely simple and gives an immediate understanding of the reach of current searches in the framework of strongly interacting models for EWSB.

In the next section we define our model and discuss the rotation to the mass eigenstate basis. The collider phenomenology of the spin-1 resonances is briefly analyzed in Section 3 by focussing on the LHC. Section 4 explains in detail how to run the calculator and the MadGraph5 model implementing the spin-1 resonances. We conclude in Section 5 and collect some useful analytic formulas in the Appendix.

2 The Model

We describe our spin-1 resonances using vector fields and write the effective Lagrangian by adopting the CCWZ formalism [349, 350], following the notation and conventions of Ref. [202].

The Lagrangian reads: ¹

$$\begin{aligned} \mathcal{L} = & -\frac{1}{4g_{el}^2} W_{\mu\nu}^a W^{a\mu\nu} - \frac{1}{4g_{el}^2} B_{\mu\nu} B^{\mu\nu} + \bar{\psi} \gamma^\mu \left(i\partial_\mu - \frac{\sigma^a}{2} W_\mu^a P_L - Y B_\mu \right) \psi + \frac{f^2}{4} (d_\mu^{\hat{a}})^2 \\ & - \frac{1}{4g_{\rho_L}^2} \rho_{\mu\nu}^{a_L} \rho^{a_L\mu\nu} - \frac{1}{4g_{\rho_R}^2} \rho_{\mu\nu}^{a_R} \rho^{a_R\mu\nu} + \frac{m_{\rho_L}^2}{2g_{\rho_L}^2} (\rho_\mu^{a_L} - E_\mu^{a_L})^2 + \frac{m_{\rho_R}^2}{2g_{\rho_R}^2} (\rho_\mu^{a_R} - E_\mu^{a_R})^2. \end{aligned} \quad (1)$$

The CCWZ covariant variables $d_\mu^{\hat{a}}, E_\mu^{a_L, a_R}$ ($\hat{a} = 1, \dots, 4$, $a_L, a_R = 1, 2, 3$) are functions of the four $SO(5)/SO(4)$ Nambu-Goldstone bosons $\pi^{\hat{a}}$ and are defined by

$$-iU^\dagger D_\mu U = d_\mu + E_\mu, \quad (2)$$

where $U = \exp(i\sqrt{2}\pi/f)$, $\pi = \pi^{\hat{a}} T^{\hat{a}}$ and $T^{\hat{a}, a_L, a_R}$ are $SO(5)$ generators. The Lagrangian (1) describes an elementary sector of $SU(2)_L \times U(1)_Y$ gauge fields (W_μ, B_μ) and fermions (ψ), as well as a composite sector comprising the NG bosons and the resonances ρ_L, ρ_R . While the elementary sector has a local $SU(2)_L \times U(1)_Y$ gauge invariance (with the fermions falling into the SM representations), the composite sector has a global $SO(5)$ symmetry spontaneously broken to $SO(4)$. The resonances ρ_L and ρ_R transform respectively like a $(3, 1)$ and $(1, 3)$ of $SO(4) \sim SU(2)_L \times SU(2)_R$. The elementary W_μ, B_μ fields weakly gauge a subgroup $SU(2)_L \times U(1)_Y$ of the global $SO(5)$ misaligned by an angle θ with respect to the unbroken $SO(4)$. ² Such misalignment eventually implies the breaking of the low-energy electroweak symmetry, hence the angle θ can be seen as an EWSB order parameter. More details about the symmetry construction and the CCWZ formalism for $SO(5)/SO(4)$ can be found in Ref. [202]. The Lagrangian (1) provides a minimal description of the spin-1 resonances. Additional operators involving $\rho_{L,R}$ can be in general included and play a relevant role at energies of order of the resonances' mass, see for example Ref. [202]. In the following we will omit them for simplicity.

The only source of interactions in Eq. (1) among the composite $\rho_{L,R}$ and the elementary fields is the $\rho_L - W$ and $\rho_R - B$ mass mixings that follow from the last two terms in the second line of Eq. (1) (ρ mass terms). This can be seen explicitly by expanding d_μ and E_μ at quadratic order in the fields ($i, j = 1, 2, 3$):

$$\begin{aligned} d_\mu^{\hat{a}} &= A_\mu^{\hat{a}} + \sqrt{2} \frac{\partial_\mu \pi^{\hat{a}}}{f} + \frac{\sqrt{2}}{2f} \delta^{\hat{a}j} \left(\epsilon^{iaj} \pi^i (A_\mu^{a_L} + A_\mu^{a_R}) + \pi^4 (A_\mu^{j_L} - A_\mu^{j_R}) \right) - \frac{\sqrt{2}}{2f} \delta^{\hat{a}4} \left(\pi^i A_\mu^{i_L} - \pi^i A_\mu^{i_R} \right), \\ E_\mu^{a_L} &= A_\mu^{a_L} + \frac{1}{2f^2} \left(\epsilon^{aLij} \pi^i \partial_\mu \pi^j + \delta^{aLi} (\pi^i \partial_\mu \pi^4 - \pi^4 \partial_\mu \pi^i) \right) + \frac{\sqrt{2}}{2f} \left(\epsilon^{aLij} \pi^i A_\mu^j + \delta^{aLi} (\pi^i A_\mu^4 - \pi^4 A_\mu^i) \right), \\ E_\mu^{a_R} &= A_\mu^{a_R} + \frac{1}{2f^2} \left(\epsilon^{aRij} \pi^i \partial_\mu \pi^j - \delta^{aRi} (\pi^i \partial_\mu \pi^4 - \pi^4 \partial_\mu \pi^i) \right) + \frac{\sqrt{2}}{2f} \left(\epsilon^{aRij} \pi^i A_\mu^j - \delta^{aRi} (\pi^i A_\mu^4 - \pi^4 A_\mu^i) \right), \end{aligned} \quad (3)$$

¹We normalize hypercharge as $Y = Q - T_{3L}$ and define the projector over left-handed fermions as $P_L = (1 - \gamma_5)/2$.

²The derivative in Eq. (2) is thus covariant under the local $SU(2)_L \times U(1)_Y$, $D_\mu = \partial_\mu + iT^a W_\mu^a + iY B_\mu$.

where

$$\begin{aligned}
A_\mu^{\hat{i}} &= \frac{\sin \theta}{\sqrt{2}} (W_\mu^i - \delta^{i3} B_\mu), & A_\mu^{\hat{4}} &= 0, \\
A_\mu^{aL} &= \left(\frac{1 + \cos \theta}{2} \right) W_\mu^a + \delta^{a3} \left(\frac{1 - \cos \theta}{2} \right) B_\mu, \\
A_\mu^{aR} &= \left(\frac{1 - \cos \theta}{2} \right) W_\mu^a + \delta^{a3} \left(\frac{1 + \cos \theta}{2} \right) B_\mu.
\end{aligned} \tag{4}$$

Therefore, the global mass matrix of spin-1 fields (W, B, ρ_L, ρ_R) is non-diagonal and must be diagonalized by a proper field rotation.

Before discussing the rotation to the mass-eigenstate basis, let us first count how many parameters appear in our Lagrangian: there are five couplings $(g_{el}, g'_{el}, g_{\rho_L}, g_{\rho_R}, f)$, two mass scales (m_{ρ_L}, m_{ρ_R}) , and the misalignment angle θ , for a total of 8 parameters. Notice that we have listed the NG decay constant f as a coupling, since it controls the strength of the NG boson interactions. The misalignment angle is determined by the radiatively-induced Higgs potential, and can be conveniently traded for the variable $\xi \equiv \sin^2 \theta$. All the Lagrangian (input) parameters can be re-expressed in terms of physical quantities in the mass eigenbasis. Three of them must be fixed to reproduce the basic electroweak observables, which we conveniently choose to be G_F , α_{em} and m_Z . Of the remaining five input parameters, ξ controls the modifications of the Higgs couplings from their SM values and is thus an observable, while the other four can be traded for the following physical quantities: the masses of the neutral heavy resonances $m_{\rho_1^0}, m_{\rho_2^0}$ and their couplings to the charged leptons, $g_{\rho_1 ll}, g_{\rho_2 ll}$.

In order to fix three of the input parameters in terms of G_F , α_{em} and m_Z we need the expressions of the latter in terms of the former. It turns out that G_F and α_{em} are very simple to compute and read:

$$G_F = \frac{1}{\sqrt{2} f^2 \xi}, \tag{5}$$

$$\frac{1}{4\pi \alpha_{em}} = \frac{1}{g_{el}^2} + \frac{1}{g_{\rho_L}^2} + \frac{1}{g_{el}^{\prime 2}} + \frac{1}{g_{\rho_R}^2} = \frac{1}{g^2} + \frac{1}{g'^2}, \tag{6}$$

where we have conveniently defined the intermediate parameters

$$\frac{1}{g^2} \equiv \frac{1}{g_{el}^2} + \frac{1}{g_{\rho_L}^2}, \quad \frac{1}{g'^2} \equiv \frac{1}{g_{el}^{\prime 2}} + \frac{1}{g_{\rho_R}^2}. \tag{7}$$

Notice that α_{em} does not get corrections after EWSB at any order in ξ . The formula for G_F can be most easily derived by integrating out first the composite ρ 's using their equations of motion at leading order in the derivative expansion, $\rho_\mu = E_\mu + O(p^3)$. From Eq. (1) one can then see that the low-energy Lagrangian for the elementary fields contains two extra operators, $(E_{\mu\nu}^L)^2$ and $(E_{\mu\nu}^R)^2$, which however do not contribute to G_F . This means that the expression of G_F in terms of the elementary parameters does not receive any tree-level contribution from the composite ρ 's, hence the simple formula (5). Finally, the formula of m_Z is in general quite complicated and we do not report it here. By making use of such expression and of Eqs. (5), (6), for given values of the other input parameters $(g_{\rho_L}, g_{\rho_R}, m_{\rho_L}$ and $m_{\rho_R})$ we can fix that of g_{el}, g'_{el} and f so as to reproduce the experimental values of G_F, α_{em} and m_Z .

We now discuss the rotation to the mass eigenstate basis. The mass matrix consists of a 3×3 charged block and a 4×4 neutral block, their expressions are reported in Eqs. (A.1)-(A.3) of the Appendix. Although it can be diagonalized analytically, the expressions of its eigenvectors and eigenstates are extremely complicated in the general case. It is thus more convenient to perform a numerical diagonalization unless specific limits are considered in which expressions simplify. We provide a Mathematica code which makes such numerical diagonalization for given values of the input parameters $\{m_{\rho_L}, m_{\rho_R}, g_{\rho_L}, g_{\rho_R}, \xi\}$ and returns the values of all the relevant physical couplings and masses. The program is illustrated in detail in section 4. A limit in which it is useful to perform the diagonalization analytically is that of small ξ , which is also phenomenologically favored by the constraints coming from the electroweak precision tests. The corresponding eigenvalues (physical masses) in this case are, at linear order in ξ :

$$\begin{aligned}
m_W^2 &= f^2 \xi \frac{g^2}{4}, \\
m_Z^2 &= f^2 \xi \frac{(g'^2 + g^2)}{4}, \\
m_{\rho_1^\pm}^2 &= m_{\rho_L}^2 \frac{g_{\rho_L}^2}{g_{\rho_L}^2 - g^2} \left[1 - \frac{\xi}{2} \frac{g^2}{g_{\rho_L}^2} \left(1 - \frac{g^2 f^2}{2m_{\rho_L}^2} \right) \right], \\
m_{\rho_2^\pm}^2 &= m_{\rho_R}^2, \\
m_{\rho_1^0}^2 &= m_{\rho_L}^2 \frac{g_{\rho_L}^2}{g_{\rho_L}^2 - g^2} \left[1 - \frac{\xi}{2} \frac{g^2}{g_{\rho_L}^2} \left(1 - \frac{g^2 f^2}{2m_{\rho_L}^2} \right) \right], \\
m_{\rho_2^0}^2 &= m_{\rho_R}^2 \frac{g_{\rho_R}^2}{g_{\rho_R}^2 - g'^2} \left[1 - \frac{\xi}{2} \frac{g'^2}{g_{\rho_R}^2} \left(1 - \frac{g'^2 f^2}{2m_{\rho_R}^2} \right) \right],
\end{aligned} \tag{8}$$

We have defined the mass eigenstates so that for ξ small ρ_1 and ρ_2 are mostly made of respectively ρ_L and ρ_R . If we use Eq. (5) and define (to all orders in ξ) the electroweak scale as $v = \sqrt{\xi} f$, then m_W and m_Z in Eq. (8) have formally the same expression as in the SM.³ The masses of the resonances instead arise at zeroth order in ξ and get corrections after EWSB. In the case of ρ_1 , the $O(\xi)$ corrections to the charged and neutral masses are equal, since they do not depend on g'_{el} , which is the only parameter in the bosonic sector to break the custodial symmetry. Another accidental property of the charged sector is that if $m_{\rho_L} = m_{\rho_R}$ then one of the mass eigenstates, i.e. $m_{\rho_2^\pm}$ in our notation, remains unperturbed at all orders in ξ . That is, the formula for $m_{\rho_2^\pm}$ reported in Eq. (8) becomes exact in this limit. This can be easily understood by noticing that for $m_{\rho_L} = m_{\rho_R} = m_\rho$ the charged mass matrix contains a 2×2 sub-block proportional to the identity and, as a consequence, its characteristic polynomial $\det(M^2 - \lambda 1)$ is proportional to $(\lambda - m_\rho)$.

Once the form of the rotation to the mass eigenbasis is derived, either numerically or analytically, it is straightforward to obtain the physical interactions between the heavy resonances and the SM fields. In the following we will focus on trilinear couplings, neglecting for simplicity quartic interactions. The terms in the Lagrangian with cubic interactions involving one

³With this choice the $O(\xi^2)$ corrections appear in m_W and m_Z but not in v . One could equivalently define v through the formula $m_W = gv/2$, so that G_F in Eq. (5) deviates from its SM expression at $O(\xi^2)$ once rewritten in terms of v .

heavy resonance are: ⁴

$$\begin{aligned}
\mathcal{L}_\rho = & ig_{\rho^+ WZ} [(\partial_\mu \rho_\nu^+ - \partial_\nu \rho_\mu^+) W^{\mu-} Z^\nu - (\partial_\mu W_\nu^- - \partial_\nu W_\mu^-) \rho^{\mu+} Z^\nu \\
& + (\partial_\mu Z_\nu - \partial_\nu Z_\mu) \rho^{\mu+} W^{\nu-} + h.c.] \\
& + ig_{\rho^0 WW} [(\partial_\mu W_\nu^+ - \partial_\nu W_\mu^+) W^{\mu-} \rho^{0\nu} + \frac{1}{2}(\partial_\mu \rho_\nu^0 - \partial_\nu \rho_\mu^0) W^{\mu+} W^{\nu-} + h.c.] \\
& + g_{\rho^+ Wh} (h \rho_\mu^+ W^{\mu-} + h.c.) + g_{\rho^0 Zh} h \rho_\mu^0 Z^\mu \\
& + \frac{1}{\sqrt{2}} g_{\rho^+ ud} (\rho_\mu^+ \bar{\psi}_u \gamma^\mu P_L \psi_d + h.c.) \\
& + \rho_\mu^0 \bar{\psi}_u \gamma^\mu \left[\frac{1}{2} (g_{\rho^0 ffL} - g_{\rho^0 ffY}) P_L + g_{\rho^0 ffY} Q[\psi_u] \right] \psi_u \\
& + \rho_\mu^0 \bar{\psi}_d \gamma^\mu \left[-\frac{1}{2} (g_{\rho^0 ffL} - g_{\rho^0 ffY}) P_L + g_{\rho^0 ffY} Q[\psi_d] \right] \psi_d,
\end{aligned} \tag{9}$$

where ρ indicates either of ρ_1 and ρ_2 , and ψ_u (ψ_d) stands for any of the SM up-type quarks and neutrinos (down-type quarks and charged leptons). The expressions of the couplings appearing in Eq. (9) are reported in the Appendix at linear order in ξ .

The Lorentz structure of the vertices among three vector fields is the same as the one of triple gauge vertices in the SM. This is because the kinetic terms for both composite and elementary fields in Eq. (1) imply interactions of the SM form, and rotating to the mass eigenbasis does not obviously change the Lorentz structure. The value of the $VV\rho$ and $Vh\rho$ couplings ($V = W, Z$) can be extracted by using the Equivalence Theorem for $m_\rho \gg m_V$. In this limit the leading contribution to the interaction comes from the longitudinal polarizations of the SM vector fields, and the overall strength equals that of the coupling of one ρ to two NG bosons, $\rho\pi\pi$, up to small corrections of $O(m_V^2/m_\rho^2)$. As it can be directly seen from Eq. (1), the $\rho\pi\pi$ coupling is proportional to $g_\rho a_\rho^2$, where $a_\rho \equiv m_\rho/(g_\rho f)$ is a quantity expected to be of order 1 according to naive dimensional analysis (NDA). Finally, the interactions of the heavy resonances to the SM fermions follow entirely from the universal composite-elementary mixing, that is, from the elementary component of the heavy spin-1 mass eigenstate (the fermions are assumed to be fully elementary). As a consequence, the three couplings $g_{\rho^+ ud}$, $g_{\rho^0 ffL}$, $g_{\rho^0 ffY}$ are of order $\sim g^2/g_\rho$ and do not depend on the fermion species, i.e. they are universal. From the above discussion it follows that, in the limit $g_\rho \gg g$, the heavy resonances are most strongly coupled to composite states, i.e. the longitudinal polarizations of W , Z and the Higgs boson, while their coupling strength to the SM fermions is extremely weak.

⁴All interaction terms between SM fermions and spin-1 resonances in this Lagrangian are flavor diagonal. This follows from assuming that fermions are fully elementary: in absence of elementary-composite fermion mixings one can always make fields rotations to diagonalize the fermionic kinetic terms in flavor space. Of course the assumption is very crude, since in this way fermions are massless. By allowing for some degree of compositeness and non-vanishing elementary-composite couplings λ , the Lagrangian (9) is valid at $O(\lambda^0)$ in the weak interaction eigenbasis for the fermions. In this basis the fermion masses are not diagonal in flavor space. After rotating the fermion fields to diagonalize their mass matrices, a V_{CKM} matrix appears in the vertex $\rho^+ \bar{\psi}_u \psi_d$, while the interactions of ρ^0 remain diagonal.

3 Production and decay of spin-1 resonances at the LHC

Despite their suppressed couplings to the SM fermions, the main production mechanism of the heavy resonances at the LHC is Drell–Yan processes. Under the validity of the Narrow Width Approximation (NWA), each production rate can be factorized into an on-shell cross section times a decay branching fraction. The on-shell cross sections are controlled by the universal couplings g_{ρ^+ud} , g_{ρ^0ffL} , g_{ρ^0ffY} and can be written as ⁵

$$\begin{aligned}\sigma(pp \rightarrow \rho^+ + X) &= g_{\rho^+ud}^2 \cdot \sigma_{u\bar{d}}, \\ \sigma(pp \rightarrow \rho^- + X) &= g_{\rho^+ud}^2 \cdot \sigma_{d\bar{u}}, \\ \sigma(pp \rightarrow \rho^0 + X) &= g_{\rho^0uu}^2 \cdot \sigma_{u\bar{u}} + g_{\rho^0dd}^2 \cdot \sigma_{d\bar{d}},\end{aligned}\tag{10}$$

where ρ stands for either ρ_1 or ρ_2 , g_{ρ^0uu} and g_{ρ^0dd} are the coupling strengths of respectively up- and down-type fermions to the resonance,

$$\begin{aligned}g_{\rho^0uu} &\equiv \left[\left(\frac{1}{2} (g_{\rho^0ffL} - g_{\rho^0ffY}) + \frac{2}{3} g_{\rho^0ffY} \right)^2 + \left(\frac{2}{3} g_{\rho^0ffY} \right)^2 \right]^{1/2}, \\ g_{\rho^0dd} &\equiv \left[\left(-\frac{1}{2} (g_{\rho^0ffL} - g_{\rho^0ffY}) - \frac{1}{3} g_{\rho^0ffY} \right)^2 + \left(-\frac{1}{3} g_{\rho^0ffY} \right)^2 \right]^{1/2},\end{aligned}\tag{11}$$

and we defined ($\psi_u = u, c, \psi_d = d, s$)

$$\begin{aligned}\sigma_{u\bar{d}} &= \sum_{\psi_u, \psi_d} \sigma(pp \rightarrow \psi_u \bar{\psi}_d \rightarrow \rho^+ + X) \Big|_{g_{\rho^+ud}=1}, \\ \sigma_{d\bar{u}} &= \sum_{\psi_u, \psi_d} \sigma(pp \rightarrow \psi_d \bar{\psi}_u \rightarrow \rho^- + X) \Big|_{g_{\rho^+ud}=1}, \\ \sigma_{u\bar{u}} &= \sum_{\psi_u} \sigma(pp \rightarrow \psi_u \bar{\psi}_u \rightarrow \rho^0 + X) \Big|_{g_{\rho^0uu}=1}, \\ \sigma_{d\bar{d}} &= \sum_{\psi_d} \sigma(pp \rightarrow \psi_d \bar{\psi}_d \rightarrow \rho^0 + X) \Big|_{g_{\rho^0dd}=1}.\end{aligned}\tag{12}$$

The total production rates (10) are thus simply given in terms of the ‘‘fundamental’’ cross sections of Eq.(12) –which include the contributions of all the initial partons and can be computed once for all– appropriately rescaled by g_{ρ^+ud} , g_{ρ^0uu} and g_{ρ^0dd} . Figure 1 shows the fundamental cross sections as functions of the physical mass of the resonance for a collider center-of-mass energy $\sqrt{s} = 8 \text{ TeV}$ and $\sqrt{s} = 14 \text{ TeV}$.

In order to illustrate the typical size of the production cross sections and decay rates, we will show results as functions of one mass and one coupling strength, fixing the other parameters. ⁶ We will consider the following two sets of benchmark values:

$$\begin{aligned}\text{(I)} \quad m_{\rho_L} &= 0.5 m_{\rho_R}, \quad g_{\rho_L} = g_{\rho_R} \equiv g_\rho, \quad \xi = 0.1 \\ \text{(II)} \quad m_{\rho_L} &= 2.0 m_{\rho_R}, \quad g_{\rho_L} = g_{\rho_R} \equiv g_\rho, \quad \xi = 0.1.\end{aligned}\tag{13}$$

⁵Another convenient way to parametrize the production cross sections is in terms of partial widths and parton luminosities, see Ref. [348].

⁶All the plots shown in this section have been obtained by making use of our Madgraph5 model. Although several sanity checks have been performed to test it, a full validation of the model has not been done and is left for a future work.

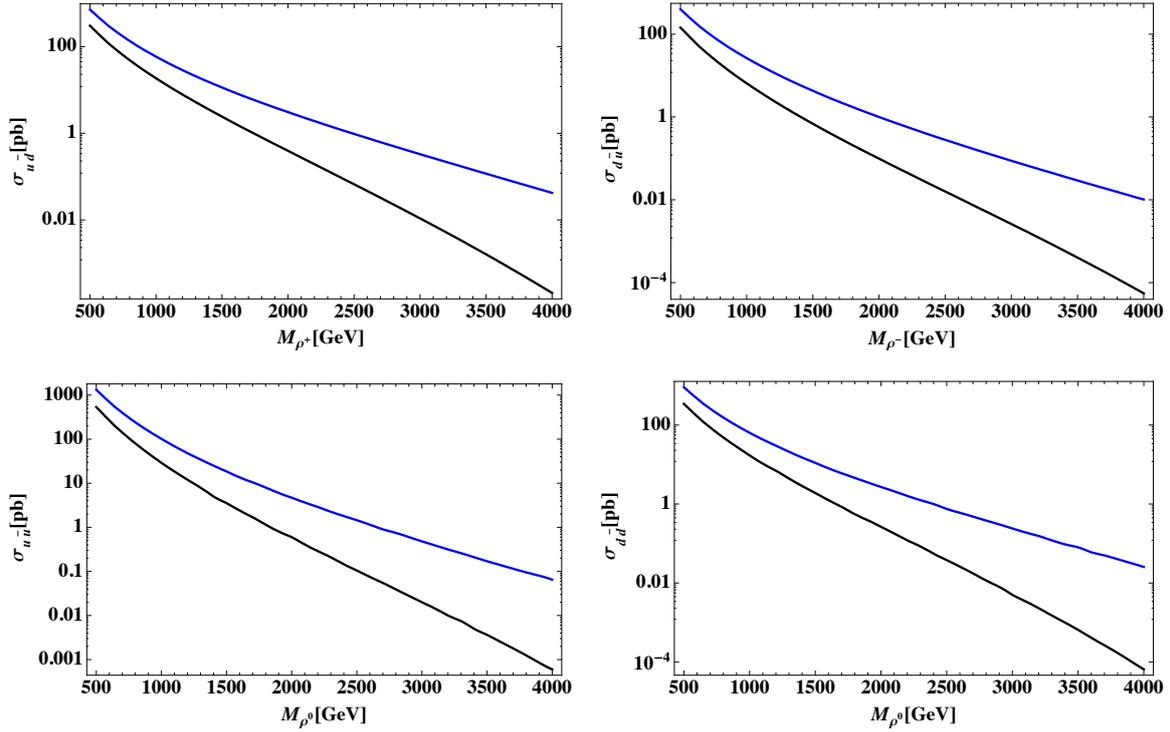


Figure 1: Fundamental cross sections of Eq. (12) as functions of the physical mass of the resonance. Black (blue) curves are obtained for a collider center-of-mass energy $\sqrt{s} = 8$ TeV ($\sqrt{s} = 14$ TeV).

In case (I) the lightest charged and neutral resonances are ρ_1^\pm and ρ_1^0 . They are mostly made of ρ_L and both couple to SM fermions with strength $\sim g_{el}^2/g_\rho$. In fact, their couplings and masses are equal up to $O(\xi)$ terms, see Eq. A.10, because the breaking of the custodial symmetry due to the hypercharge coupling g'_{el} enters only through EWSB effects. In case (II), on the other hand, the lightest resonances are ρ_2^\pm and ρ_2^0 , mostly made of ρ_R . While ρ_2^0 couples to SM fermions with strength $\sim g_{el}^2/g_\rho$, the coupling of ρ_2^\pm to fermions is further suppressed by a factor ξ , see Eq. A.11. Prior to EWSB, indeed, the lightest charged resonance is purely ρ_R and thus does not couple to SM fermions as it does not mix with any elementary vector field. In fact, this holds true even after EWSB if $m_{\rho_L} = m_{\rho_R}$. As previously explained, in this case the mass eigenstate ρ^\pm remains unperturbed at all orders in ξ , and does not couple to elementary fields. In all cases in which its coupling to fermions is sufficiently suppressed, the production of this charged resonance at the LHC proceeds mainly via vector boson fusion (VBF), $pp \rightarrow W^\pm Z jj \rightarrow \rho^\pm jj$, or through cascade decays of the heaviest ones.

Figure 2 shows the contours of constant cross section for the production of the lightest resonance in the plane (m_{ρ_L}, g_ρ) for the benchmark choice (I) of Eq. (13). For simplicity we have neglected the contribution from VBF and possible cascade decays. As expected, the cross section increases for smaller values of g_ρ , since in that limit the couplings to SM fermions get larger as a consequence of the larger elementary-composite mixing. In case (II) the shapes of the contours are similar, but the overall size of the cross section is smaller by a factor $\sim (g'/g)^2$ and $\sim \xi (g'/g)^2$ respectively for the neutral and the charged state.

Concerning the decay of the resonances, for $g_\rho \gg g$ the dominant branching fractions are those to VV and Vh final states, where $V = W, Z$. The decay rates to fermions, in the

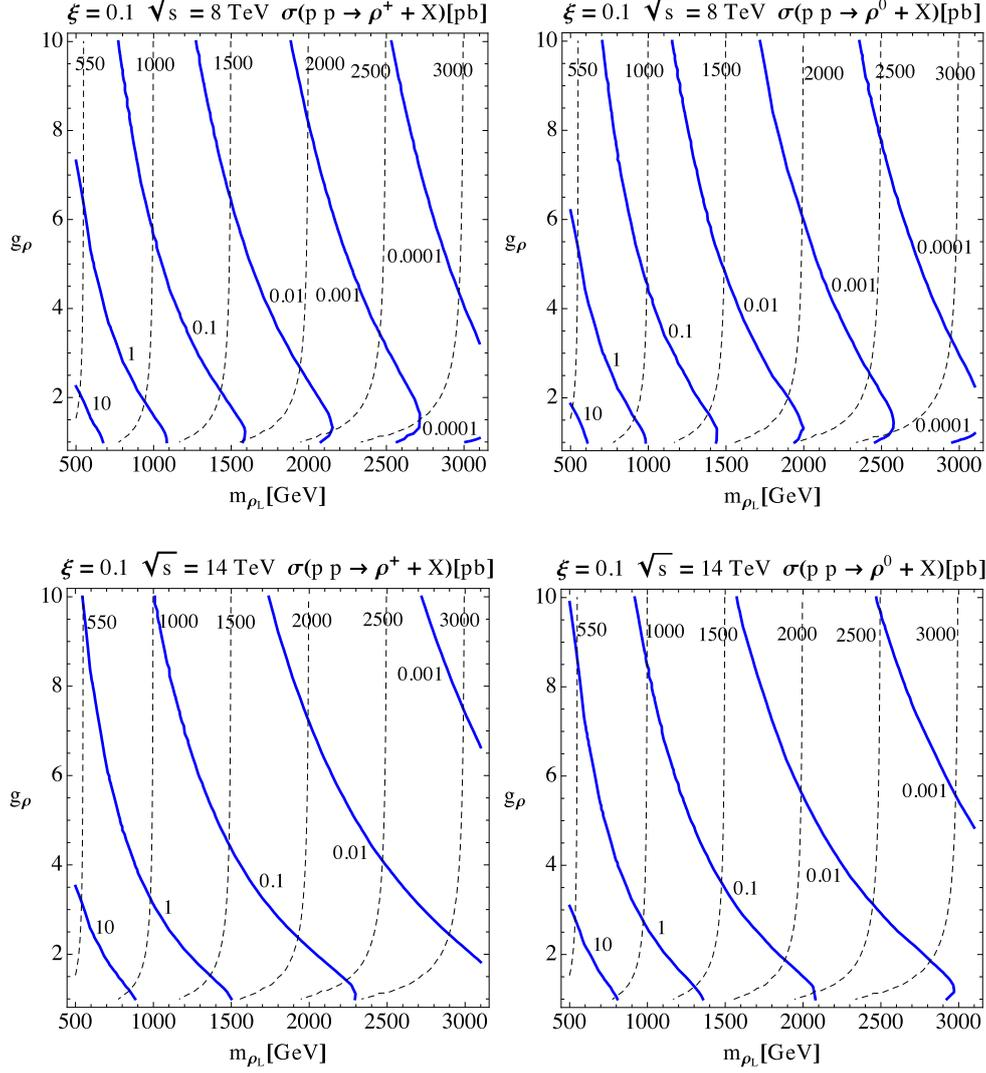


Figure 2: Contours of constant cross section (blue lines, labels in picobarn) in the plane (m_{ρ_L}, g_ρ) for the production of the lightest charged and neutral resonances at the LHC, in the benchmark case (I) of Eq. (13). The dashed curves denote the contours of constant mass of the lightest resonance (in GeV units). The plots in the upper row are done for $\sqrt{s} = 8$ TeV, those in the lower row assume $\sqrt{s} = 14$ TeV. The contribution from vector boson fusion and possible cascade decays has been neglected for simplicity.

same limit, are strongly suppressed. This is illustrated in Fig. 3, where we have plotted the branching ratios of the lightest neutral and charged resonance as functions of g_ρ for case (I) with $m_{\rho_L} = g_{\rho_L} f$ (hence $a_{\rho_L} \equiv m_{\rho_L}/(f g_{\rho_L}) = 1$), and for case (II) with $m_{\rho_R} = g_{\rho_R} f$ (hence $a_{\rho_R} \equiv m_{\rho_R}/(f g_{\rho_R}) = 1$). Notice that the branching fractions to WZ and Wh , as well as those to WW and Zh , are equal to very good approximation. This is implied by the Equivalence Theorem, which works well since $m_{\rho_{L,R}} \gg m_{W,Z}$ for the chosen values of parameters. As expected, the branching ratios of the charged resonance to fermions are much smaller in case (II) than in case (I), as a consequence of the suppressed couplings. In case (I) the approximate custodial symmetry implies that $BR(t\bar{t}) \simeq BR(b\bar{b}) \simeq 3 BR(l^+l^-)$. The equality of the $t\bar{t}$ and l^+l^- decay fractions in case (II) is instead a numerical accident.

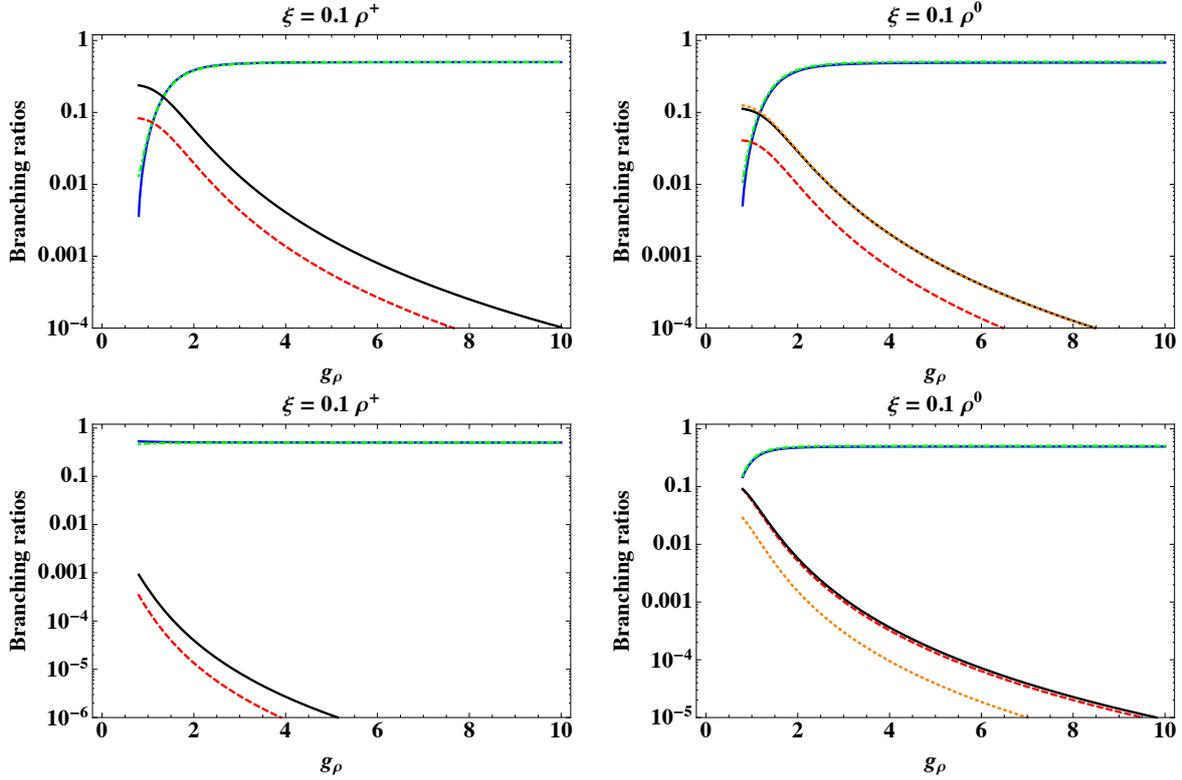


Figure 3: Decay branching ratios of the lightest charged (left plots) and neutral (right plots) resonance as functions of g_ρ . Upper plots are done for the benchmark case (I) of Eq. (13), the lower ones refer to case (II). The various curves correspond to the following decay channels: WZ (solid blue), Wh (dot-dashed green), $l\nu$ (dashed red), $t\bar{b}$ (solid black) in left plots; WW (solid blue), Zh (dot-dashed green), l^+l^- (dashed red), $t\bar{t}$ (solid black), $b\bar{b}$ (dotted orange) in right plots.

Figure 4 shows the total decay width of the lightest charged and neutral resonance for case (I) (left plot) and case (II) (right plot) of Eq. (13), respectively in units of m_{ρ_L} and m_{ρ_R} . In general, for large values of g_ρ the total width is dominated by the decay modes VV , Vh and scales as g_ρ^2 . Since the relative importance of these final states is fixed by the Equivalence Theorem, this explains why all total widths become equal for large g_ρ . For very small g_ρ , on the other hand, the decay modes to fermions dominate and the width increases if g_ρ decreases. This is in fact not true for the special case of the charged lightest resonance in case (II), where the couplings to fermions are extremely small and the bosonic final states always dominate. Notice also that while the total decay widths of ρ^0 and ρ^\pm are different at small g_ρ in case (II), they are always equal to very good approximation in case (I). In fact, the two curves lie on top of each other in Fig. 4 and cannot be distinguished. This equality is again a consequence of the approximate custodial symmetry which is present for small ξ . In all cases, the NWA is sufficiently accurate for $g_\rho \lesssim 4 - 5$. This remains true also for different values of ξ and a_{ρ_L} , a_{ρ_R} provided the latter two parameters are of $O(1)$ as expected from NDA.

All the cross sections and partial decay widths described in this section can be computed analytically by using the Mathematica calculator provided with our package. It is useful to stress that the results presented in this section are based on the validity of the Narrow Width Approximation. This latter assumes that the production rate can be factorized into an on-shell cross

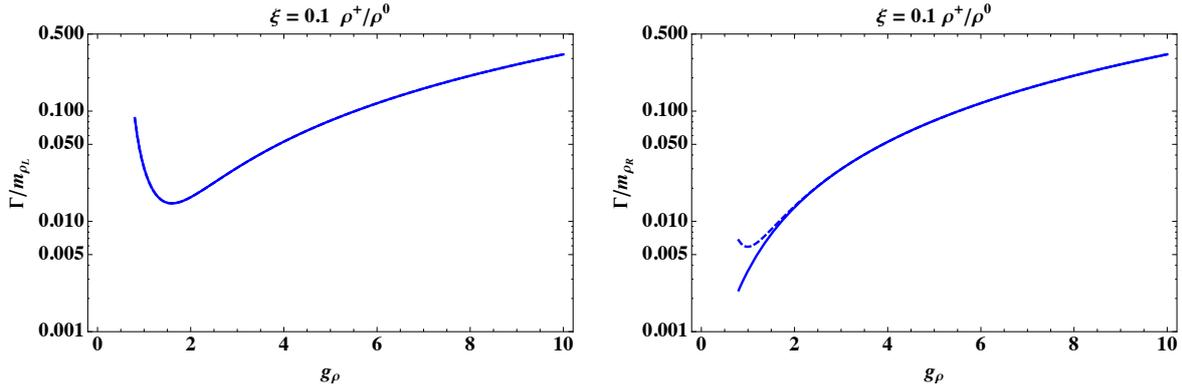


Figure 4: Total decay width the lightest charged (solid curve) and neutral (dashed curve) resonance for case (I) (left plot) and case (II) (right plot) of Eq. (13), respectively in units of m_{ρ_L} and m_{ρ_R} . In the left plot the solid and dashed curves lie on top of each other and cannot be distinguished.

section times a decay branching ratio, and neglects the interference with the SM background. Experimental analyses performed by following this approach must be carried out consistently with its underlying assumptions, e.g. the limits on the production rate of the new particles should be set by focusing on the on-shell signal region. When this is possible, it allows for a fast, analytical scan over the parameter space of the model. On the contrary, in the case of a broad resonance, or when the fast variation of the parton distribution functions makes the NWA no longer reliable due to a relevant off-shell tail at low-invariant masses, the factorized approach cannot be used. In this case, a robust shape analysis must rely on a full MonteCarlo simulation, thus becoming more model dependent and much more demanding (for a detailed discussion of these aspects see Ref.[348]).

4 How to run the Mathematica calculator and the MadGraph5 model

In this section we illustrate how to run the Mathematica calculator and the MadGraph5 model implementing the spin-1 resonances. All the software can be downloaded in a single package from the HEPMDB website at the following URL: <http://hepmdb.soton.ac.uk/hepmdb:0214.0154>. De-compressing the downloaded archive creates a directory called `rho_model` where all the main files are. These include the file `frhoWSimp.nb`, which is the Mathematica calculator, the directory `rho` containing the MadGraph5 model, and other scripts that can be used to set up the event generation.

4.1 The Mathematica calculator

The Mathematica calculator can be used to compute numerically the physical couplings and masses by specifying the input parameters. It also implements the analytical formulas for the computation of the cross sections and partial decay rates discussed in the previous section. The program is divided into four sections.

Section 1 is where all basic routines are defined and should be thus executed first. The user does not need to open it.

Section 2 is where the numerical calculation of the physical couplings and masses can be performed by means of the routine

ComputeOutputParameters[InputData, fileinput.dat, fileoutput.dat, mode]

InputData is a list of input points, each point representing a list of input parameters. By appropriately setting the variable “mode”, the user can choose among three operational modes: in the first (“mode=LR”), both a ρ_L and a ρ_R are considered and the format of each input point must be $\{\xi, m_{\rho_L}, g_{\rho_L}, m_{\rho_R}, g_{\rho_R}\}$; in the second (“mode=L”), only a ρ_L is considered and the format of an input point is $\{\xi, m_{\rho_L}, g_{\rho_L}\}$; in the third (“mode=R”), only a ρ_R is considered and the input point must be specified in the format $\{\xi, m_{\rho_R}, g_{\rho_R}\}$. For each of the input points the routine computes the physical masses and couplings and writes them in the file fileoutput.dat in the following format:

$$n_p, m_W, \xi, m_{\rho_1^+}, m_{\rho_1^0}, g_{\rho_1^+ WZ}, g_{\rho_1^0 WW}, g_{\rho_1^+ Wh}, g_{\rho_1^0 Zh}, g_{\rho_1^+ ud}, g_{\rho_1^0 ffL}, g_{\rho_1^0 ffY}, \\ m_{\rho_2^+}, m_{\rho_2^0}, g_{\rho_2^+ WZ}, g_{\rho_2^0 WW}, g_{\rho_2^+ Wh}, g_{\rho_2^0 Zh}, g_{\rho_2^+ ud}, g_{\rho_2^0 ffL}, g_{\rho_2^0 ffY}$$

where n_p is the number of the point. In the modes “L” and “R”, where only one ρ is included, the couplings of the second resonance ρ_2 are set to zero, and its mass is set to a default value.⁷ The value of the input parameters is recorded instead in the file fileinput.dat for convenience.

Section 3 contains the routines for the calculation of the production cross sections and decay branching ratios.

Finally, Section 4 contains the FeynRules [252, 253] code which can be used to generate a UFO library [203] to be linked with the MadGraph5 event generator. The user does not need to execute this section unless he/she wants to modify the MadGraph5 model, which is already provided in the directory rho.

4.2 The MadGraph5 model

The main directory contains a few additional files which are useful to set up the automatic generation of events with MadGraph5. The python script wmg5.py, in particular, should be executed first by using the syntax:

```
python wmg5.py -dataset=fileoutput.dat -runmode=1 -runtimes=n
               -scriptname=generateevents
```

It reads the physical parameters from the file fileoutput.dat and creates the new script generateevents which can be executed by MadGraph5 to run the events for each of the input points. The option runmode can be used to specify the run mode in MadGraph5 (set runmode=1 to run at parton level), while runtimes sets the number of event generations to be run for each input point (this is useful if one wants to execute multiple event generations by using the multi_run command in MadGraph5).

Once the python script has been executed and the script generateevents has been created, there are a few more steps to follow to generate the events. Let us indicate with MG5dir the main directory where MadGraph5 has been installed, and with Userdir the user directory where events will be generated. One should then:

1. Copy the directory rho to MG5dir/models.

⁷In this way it never contributes to physical processes generated by Madgraph5. Notice that $m_\rho \rightarrow \infty$ is a non-decoupling limit in our model, since the couplings to the NG bosons blow up. Therefore, one cannot decouple one of the resonances by giving it a large mass. Rather, one should set all its physical couplings to zero.

2. Edit the script `generateprocess` specifying: *i*) the process to generate and *ii*) the name of the directory `outdir` (a subdirectory of `Userdir`) to be used to store the files defining the process. Then copy the script to `Userdir` and run:

```
MG5dir/bin/mg5 generateprocess
```

from a terminal.

3. Edit the cards `param_card.dat`, `pythia_card.dat` and `run_card.dat` (a version of each card with default settings is provided in the main directory with the other scripts, for convenience of the user) and then copy them to `Userdir/outdir/Cards`.
4. Copy the script `generateevents` to `Userdir/outdir` and start the generation of events by executing the command:

```
Userdir/outdir/bin/madevent generateevents
```

from a terminal.

Through this procedure the user can generate events for each of the input points (i.e. for each choice of input masses and couplings) in an automatic way. By creating suitable grids of points it is thus easy to scan over the model's parameter space.

5 Conclusions

In this work we have studied the phenomenology of spin-1 resonances arising in $SO(5)/SO(4)$ composite Higgs models. We have focused on resonances transforming as $(3, 1)$ and $(1, 3)$ of $SO(4)$ and introduced a simple Lagrangian which contains a minimal set of parameters: one mass and one coupling strength for each resonance. We have discussed the rotation to the mass eigenstate basis and provided a numerical calculator of physical masses and couplings. We also derived approximate analytic formulas for the masses and couplings at linear order in $\xi = \sin^2\theta$, where θ is the vacuum misalignment angle. The model has been implemented in `MadGraph5` and can be used as a benchmark in the search for heavy spin-1 states at the LHC and future colliders.

Acknowledgments

We are grateful to the Galileo Galilei Institute for Theoretical Physics in Florence for hospitality during part of this project. C.G. is supported by the Spanish Ministry MICINN under contract FPA2010-17747 and by the European Commission under the ERC Advanced Grant 226371 `MassTeV` and the contract PCIG14-GA-2013-631962. D.P. has been supported by the NSF Grant PHY-0855653. D.L. is supported by the China Scholarship Foundation. A.T. and D.G. acknowledge support from the Swiss National Science Foundation under contract no. 200020-138131. The work of R.C, R.T. and A.W. was partly supported by the ERC Advanced Grant no. 267985 `DaMeSyFla`. R.T. also acknowledges support by the Research Executive Agency (REA) of the European Union under the Grant Agreement number PITN-GA- 2010-264564 `LHCPhenoNet`. A.W. acknowledges the MIUR-FIRB grant `RBF12H1MW`.

Appendix

A Analytical formulas

We collect here the analytical formulas discussed in the text.

The mass terms can be written as

$$\mathcal{L}_{mass} = X^+ M_{\pm}^2 X^- + \frac{1}{2} X^0 M_0^2 X^0, \quad (\text{A.1})$$

where $X^{\pm} = (X^1 \pm iX^2)/\sqrt{2}$, $X^{1,2} = \{W^{1,2}, \rho_L^{1,2}, \rho_R^{1,2}\}$ and $X^0 = \{W^3, \rho_L^3, B, \rho_R^3\}$. The charged and neutral mass matrices are:

$$M_{\pm}^2 = \begin{pmatrix} A & -\frac{(1+c_{\theta})g_{el}m_{\rho_L}^2}{2g_{\rho_L}} & -\frac{(1-c_{\theta})g_{el}m_{\rho_R}^2}{2g_{\rho_R}} \\ -\frac{(1+c_{\theta})g_{el}m_{\rho_L}^2}{2g_{\rho_L}} & m_{\rho_L}^2 & 0 \\ -\frac{(1-c_{\theta})g_{el}m_{\rho_R}^2}{2g_{\rho_R}} & 0 & m_{\rho_R}^2 \end{pmatrix} \quad (\text{A.2})$$

$$M_0^2 = \begin{pmatrix} A & -\frac{(1+c_{\theta})g_{el}m_{\rho_L}^2}{2g_{\rho_L}} & B & -\frac{(1-c_{\theta})g_{el}m_{\rho_R}^2}{2g_{\rho_R}} \\ -\frac{(1+c_{\theta})g_{el}m_{\rho_L}^2}{2g_{\rho_L}} & m_{\rho_L}^2 & -\frac{(1-c_{\theta})m_{\rho_L}^2 g'_{el}}{2g_{\rho_L}} & 0 \\ B & -\frac{(1-c_{\theta})m_{\rho_L}^2 g'_{el}}{2g_{\rho_L}} & C & -\frac{(1+c_{\theta})m_{\rho_R}^2 g'_{el}}{2g_{\rho_R}} \\ -\frac{(1-c_{\theta})g_{el}m_{\rho_R}^2}{2g_{\rho_R}} & 0 & -\frac{(1+c_{\theta})m_{\rho_R}^2 g'_{el}}{2g_{\rho_R}} & m_{\rho_R}^2 \end{pmatrix}, \quad (\text{A.3})$$

where $c_{\theta} \equiv \cos \theta$ and we have conveniently defined

$$\begin{aligned} A &= \frac{g_{el}^2}{4g_{\rho_L}^2 g_{\rho_R}^2} \left[(g_{\rho_R}^2 m_{\rho_L}^2 + g_{\rho_L}^2 m_{\rho_R}^2) \cos^2 \theta + 2 (g_{\rho_R}^2 m_{\rho_L}^2 - g_{\rho_L}^2 m_{\rho_R}^2) \cos \theta \right. \\ &\quad \left. + f^2 \sin^2 \theta (g_{\rho_L}^2 g_{\rho_R}^2 + g_{\rho_R}^2 m_{\rho_L}^2 + g_{\rho_L}^2 m_{\rho_R}^2) \right], \\ B &= \frac{g_{el} g'_{el} \sin^2 \theta}{4g_{\rho_L}^2 g_{\rho_R}^2} (m_{\rho_L}^2 g_{\rho_R}^2 + g_{\rho_L}^2 m_{\rho_R}^2 - f^2 g_{\rho_L}^2 g_{\rho_R}^2), \\ C &= \frac{g_{el}^2}{4g_{\rho_L}^2 g_{\rho_R}^2} \left[(g_{\rho_R}^2 m_{\rho_L}^2 + g_{\rho_L}^2 m_{\rho_R}^2) \cos^2 \theta + (2g_{\rho_L}^2 m_{\rho_R}^2 - 2g_{\rho_R}^2 m_{\rho_L}^2) \cos \theta \right. \\ &\quad \left. + f^2 \sin^2 \theta (g_{\rho_L}^2 g_{\rho_R}^2 + g_{\rho_R}^2 m_{\rho_L}^2 + g_{\rho_L}^2 m_{\rho_R}^2) \right]. \end{aligned} \quad (\text{A.4})$$

As explained in Section 2, it is useful to diagonalize the mass matrix analytically by expanding for ξ small. In the following we collect the expressions of the cubic vertices with zero and one ρ . Notice that our sign convention for these vertices differs from that of Ref. [202] while it coincides with the one implemented in Madgraph5 for the SM vertices. One can easily pass from one convention to the other by redefining the sign of the input couplings: $g_{el} \rightarrow -g_{el}$, $g'_{el} \rightarrow -g'_{el}$, $g_{\rho_{L,R}} \rightarrow -g_{\rho_{L,R}}$. Obviously this redefinition does not affect physical observables.

Let us start by discussing the vertices among three SM fields. By $U(1)_{em}$ gauge invariance, all the couplings appearing in vertices with a photon (WWA and $\bar{\psi}\psi A$) are equal (up to

the particle's charge) to the electromagnetic coupling $\sqrt{4\pi\alpha_{em}}$ given in Eq. (6). This holds to all orders in ξ . There are no non-minimal couplings involving the photon, since there are no non-minimal operators which can generate them in the initial Lagrangian (1). The triple gauge interaction WWZ has the same structure as in the SM and its coupling reads, at linear order in ξ :

$$g_{WWZ} = \frac{g^2}{\sqrt{g^2 + g'^2}}, \quad (\text{A.5})$$

where g, g' have been defined in Eq. (7). Notice that the $O(\xi)$ terms are vanishing, and EWSB corrections only arise at $O(\xi^2)$. We parametrize the couplings of the SM fermions to SM vector bosons as follows

$$\frac{1}{\sqrt{2}}g_{Wud}W_\mu^+\bar{\psi}_u\gamma^\mu P_L\psi_d + h.c. + Z_\mu\bar{\psi}\gamma^\mu(P_L(g_{ZffL} - g_{ZffY})T_L[\psi] + g_{ZffY}Q[\psi])\psi, \quad (\text{A.6})$$

where $T_L[\psi_u] = +1/2, T_L[\psi_d] = -1/2$ and ψ can be any of the ψ_u and ψ_d fermions in the case of the Z interaction. We find, at linear order in ξ

$$\begin{aligned} g_{Wud} &= g + \xi \frac{g^3(m_{\rho_L}^2 - f^2g^2)}{4g_{\rho_L}^2 m_{\rho_L}^2}, \\ g_{ZffL} &= \frac{g^2}{\sqrt{g^2 + g'^2}} - \xi \frac{\sqrt{g^2 + g'^2}(f^2g^4 - g^2m_{\rho_L}^2)}{4g_{\rho_L}^2 m_{\rho_L}^2}, \\ g_{ZffY} &= -\frac{g'^2}{\sqrt{g^2 + g'^2}} + \xi \frac{\sqrt{g^2 + g'^2}(f^2g'^4 - g'^2m_{\rho_R}^2)}{4g_{\rho_R}^2 m_{\rho_R}^2}. \end{aligned} \quad (\text{A.7})$$

The expressions for the $VV\rho$ and $Vh\rho$ couplings defined in Eq. (9) are, at leading order in ξ :

$$\begin{aligned} g_{\rho_1^0 WW} &= m_W^2 \left(-\frac{1}{f^2(g_{el}^2 + g_{\rho_L}^2)^{1/2}} + \frac{g_{el}^2 g_{\rho_L}^2}{m_{\rho_L}^2 (g_{el}^2 + g_{\rho_L}^2)^{3/2}} \right), \\ g_{\rho_1^+ WZ} &= \frac{m_Z}{m_W} g_{\rho_1^0 WW}, \\ g_{\rho_2^0 WW} &= m_W^2 \left(-\frac{1}{f^2(g_{el}^{\prime 2} + g_{\rho_R}^2)^{1/2}} + \frac{g_{\rho_R}^2 g_{el}^{\prime 2}}{m_{\rho_R}^2 (g_{el}^{\prime 2} + g_{\rho_R}^2)^{3/2}} \right), \\ g_{\rho_2^+ WZ} &= -\frac{m_W m_Z}{f^2 g_{\rho_R}}, \end{aligned} \quad (\text{A.8})$$

and

$$\begin{aligned}
g_{\rho_1^+ Wh} &= m_W \left(\frac{m_{\rho_L}^2 \sqrt{g_{el}^2 + g_{\rho_L}^2}}{f^2 g_{\rho_L}^2} - \frac{g_{el}^2}{\sqrt{g_{el}^2 + g_{\rho_L}^2}} \right), \\
g_{\rho_1^0 Zh} &= \frac{m_Z}{m_W} g_{\rho_1^+ Wh}, \\
g_{\rho_2^+ Wh} &= -\frac{m_{\rho_R}^2}{f^2 g_{\rho_R}} m_W, \\
g_{\rho_2^0 Zh} &= m_Z \left(\frac{g_{el}^2}{\sqrt{g_{el}^2 + g_{\rho_R}^2}} - \frac{m_{\rho_R}^2 \sqrt{g_{el}^2 + g_{\rho_R}^2}}{f^2 g_{\rho_R}^2} \right).
\end{aligned} \tag{A.9}$$

Here m_W and m_Z stand for the $O(\xi)$ expressions reported in Eq. (8). Notice that each of the couplings in Eqs. (A.8), (A.9), with the exception of $g_{\rho_2^+ WZ}$ and $g_{\rho_2^+ Wh}$, gets two $O(\xi)$ contributions, which have opposite relative sign: one comes from the ρ mass terms, the other from the kinetic term of the NG bosons. Some choices of input parameters lead to a cancellation between these two contributions resulting in an $O(\xi)$ term accidentally smaller than $O(\xi^2)$ terms. In these cases the formulas of Eqs. (A.8), (A.9) become numerically inaccurate.

Finally, at linear order in ξ , the couplings of the resonances to SM fermions appearing in Eq. (9) are given by:

$$\begin{aligned}
g_{\rho_1^+ ud} &= -\frac{g_{el}^2}{\sqrt{g_{el}^2 + g_{\rho_L}^2}} + \xi \frac{g_{el}^2 g_{\rho_L}^2 (m_{\rho_L}^2 (g_{el}^2 + g_{\rho_L}^2) - f^2 g_{el}^2 g_{\rho_L}^2)}{4m_{\rho_L}^2 (g_{el}^2 + g_{\rho_L}^2)^{5/2}}, \\
g_{\rho_1^0 ffL} &= g_{\rho_1^+ ud}, \\
g_{\rho_1^0 ffY} &= \xi \frac{g_{el}^2}{4m_{\rho_L}^2 (g_{el}^2 + g_{\rho_L}^2)^{3/2} (g_{\rho_R}^2 m_{\rho_L}^2 (g_{el}^2 + g_{\rho_L}^2) - g_{\rho_L}^2 m_{\rho_R}^2 (g_{el}^2 + g_{\rho_R}^2))} \\
&\quad \times \left[f^2 g_{el}^2 g_{\rho_L}^2 g_{\rho_R}^2 (g_{el}^2 m_{\rho_L}^2 + g_{\rho_L}^2 (m_{\rho_L}^2 - m_{\rho_R}^2)) \right. \\
&\quad \left. + m_{\rho_L}^2 (g_{el}^2 + g_{\rho_L}^2) (g_{\rho_L}^2 m_{\rho_R}^2 (g_{\rho_R}^2 - g_{el}^2) - g_{\rho_R}^2 m_{\rho_L}^2 (g_{el}^2 + g_{\rho_L}^2)) \right],
\end{aligned} \tag{A.10}$$

and

$$\begin{aligned}
g_{\rho_2^+ ud} &= \xi \frac{g_{el}^2 g_{\rho_L}^2 (m_{\rho_R}^2 - m_{\rho_L}^2)}{4g_{\rho_R} m_{\rho_L}^2 (g_{el}^2 + g_{\rho_L}^2) - 4g_{\rho_L}^2 g_{\rho_R} m_{\rho_R}^2}, \\
g_{\rho_2^0 ffL} &= -\xi \frac{g_{el}^2}{4m_{\rho_R}^2 (g_{el}^2 + g_{\rho_R}^2)^{3/2} (g_{\rho_L}^2 m_{\rho_R}^2 (g_{el}^2 + g_{\rho_R}^2) - g_{\rho_R}^2 m_{\rho_L}^2 (g_{el}^2 + g_{\rho_L}^2))} \\
&\quad \times \left[f^2 g_{\rho_L}^2 g_{\rho_R}^4 m_{\rho_L}^2 g_{el}^2 + g_{\rho_L}^2 m_{\rho_R}^4 (g_{el}^2 + g_{\rho_R}^2)^2 \right. \\
&\quad \left. - g_{\rho_R}^2 m_{\rho_R}^2 (g_{el}^2 + g_{\rho_R}^2) (f^2 g_{\rho_L}^2 g_{el}^2 + m_{\rho_L}^2 (g_{\rho_L}^2 - g_{el}^2)) \right], \\
g_{\rho_2^0 ffY} &= -\frac{g_{el}^2}{\sqrt{g_{el}^2 + g_{\rho_R}^2}} + \xi \frac{g_{\rho_R}^2 g_{el}^2 (m_{\rho_R}^2 (g_{el}^2 + g_{\rho_R}^2) - f^2 g_{\rho_R}^2 g_{el}^2)}{4m_{\rho_R}^2 (g_{el}^2 + g_{\rho_R}^2)^{5/2}}.
\end{aligned} \tag{A.11}$$

Flavour

Contribution 17

Indirect Constraints on Non-Minimal Flavour Violating Supersymmetry

K. De Causmaecker, B. Fuks, B. Herrmann, F. Mahmoudi, B. O'Leary, W. Porod, S. Sekmen, N. Strobbe

Abstract

We present an analysis of non-minimal flavour violating effects arising in general versions of the Minimal Supersymmetric Standard Model. Considering several flavour and electroweak observables and the recent discovery of a Higgs boson, we perform a scan of the model parameter space and then design a set of experimentally non-excluded reference scenarios for which we study the dependence of the considered observables on squark flavour violation.

Among all candidate theories extending the Standard Model (SM), supersymmetry remains, after more than 30 years, one of the most studied and popular choices. As a consequence, the quest for the supersymmetric partners of the SM particles is one of the key topics of the current high-energy physics experimental program. As up to now no sign of supersymmetry has been found, in particular at the Large Hadron Collider (LHC), either the superpartners are constrained to be heavy or the spectrum must present very specific properties allowing the superpartners to evade detection [292, 293]. However these statements are valid for interpretations within the context of simplified model spectra (SMSs), or the most constrained version of the Minimal Supersymmetric Standard Model (MSSM), where over a hundred free model parameters are reduced to a set of four parameters and a sign. General realizations of the MSSM could therefore turn out to be less constrained by data. In this work we consider a version of the MSSM with general flavour-violating squark mixings. This feature is expected to lead to interesting phenomenological consequences, both with respect to indirect constraints on new physics derived from low-energy, flavour and electroweak precision observables, and in the context of the LHC [351, 352, 353, 354, 355, 356, 357, 358, 359, 360, 361, 362, 363]. In the framework of a global effort to unveil flavour effects in supersymmetry in light of the present high-energy physics data, we investigate non-minimal flavour-violation (NMFV) in the squark sector for several flavour physics observables, for the anomalous magnetic moment of the muon and for the mass of the recently observed Higgs boson.

In the following, we briefly detail the properties of the form of the NMFV MSSM under consideration and present our strategy to design theoretically motivated reference scenarios not yet experimentally excluded, relevant to be considered in the context of LHC data. We then define two reference scenarios, for which we study in detail the dependence of the various considered observables on the NMFV parameters. Conclusions are given at the end of this contribution.

In the super-CKM basis, the mass matrices of the up- and down-type squarks are repre-

sented by

$$M_{\tilde{q}}^2 = \left(\begin{array}{ccc|ccc} M_{L,q_1}^2 & \Delta_{LL}^{q_1 q_2} & \Delta_{LL}^{q_1 q_3} & m_{q_1} X_{q_1} & \Delta_{LR}^{q_1 q_2} & \Delta_{LR}^{q_1 q_3} \\ \Delta_{LL}^{q_1 q_2*} & M_{L,q_2}^2 & \Delta_{LL}^{q_2 q_3} & \Delta_{RL}^{q_1 q_2*} & m_{q_2} X_{q_2} & \Delta_{LR}^{q_2 q_3} \\ \Delta_{LL}^{q_1 q_3*} & \Delta_{LL}^{q_2 q_3*} & M_{L,q_3}^2 & \Delta_{RL}^{q_1 q_3*} & \Delta_{RL}^{q_2 q_3*} & m_{q_3} X_{q_3} \\ \hline m_{q_1} X_{q_1}^* & \Delta_{RL}^{q_1 q_2} & \Delta_{RL}^{q_1 q_3} & M_{R,q_1}^2 & \Delta_{RR}^{q_1 q_2} & \Delta_{RR}^{q_1 q_3} \\ \Delta_{LR}^{q_1 q_2*} & m_{q_2} X_{q_2}^* & \Delta_{RL}^{q_2 q_3} & \Delta_{RR}^{q_1 q_2*} & M_{R,q_2}^2 & \Delta_{RR}^{q_2 q_3} \\ \Delta_{LR}^{q_1 q_3*} & \Delta_{LR}^{q_2 q_3*} & m_{q_3} X_{q_3}^* & \Delta_{RR}^{q_1 q_3*} & \Delta_{RR}^{q_2 q_3*} & M_{R,q_3}^2 \end{array} \right) \quad \text{with} \quad (q = u, d), \quad (1)$$

where the diagonal entries of each block are related to the parameters of the supersymmetry-breaking and SM sectors,

$$M_{L,q_i}^2 = \tilde{M}_{L,\tilde{q}_i}^2 + m_{q_i}^2 + m_Z^2 (I_q - e_q s_w^2) \cos 2\beta, \quad M_{R,q_i}^2 = \tilde{M}_{R,\tilde{q}_i}^2 + m_{q_i}^2 + e_q m_Z^2 s_w^2 \cos 2\beta, \\ X_{u_i} = A_{u_i}^* - \mu \cot \beta, \quad X_{d_i} = A_{d_i}^* - \mu \tan \beta. \quad (2)$$

In these expressions, m_Z and s_w denote the Z -boson mass and the sine of the electroweak mixing angle, respectively, and e_q and I_q are the electric charge and isospin quantum numbers of the (s)quarks. The up-type and down-type quark masses are represented by m_{u_i} and m_{d_i} with i being a flavour index and the matrices $\tilde{M}_{L,\tilde{q}}^2$ and $\tilde{M}_{R,\tilde{q}}^2$ are related to the usual soft squark mass matrices $\hat{m}_{\tilde{q}}^2$, $\hat{m}_{\tilde{u}}^2$ and $\hat{m}_{\tilde{d}}^2$ through

$$\tilde{M}_{L,\tilde{u}}^2 = V_{CKM} \hat{m}_{\tilde{q}}^2 V_{CKM}^\dagger, \quad \tilde{M}_{L,\tilde{d}}^2 = \hat{m}_{\tilde{q}}^2, \quad \tilde{M}_{R,\tilde{u}}^2 = \hat{m}_{\tilde{u}}^2, \quad \tilde{M}_{R,\tilde{d}}^2 = \hat{m}_{\tilde{d}}^2. \quad (3)$$

Turning to the Higgs sector parameters, μ stands for the off-diagonal Higgs mixing parameter, $\tan \beta$ for the ratio of the vacuum expectation values of the neutral components of the two Higgs doublets, and A_{q_i} for the trilinear couplings of the Higgs fields to squarks. As in earlier works, the non-diagonal entries of the mass matrices are normalized relatively to the diagonal ones,

$$\Delta_{ab}^{q_i q_j} = \lambda_{ab}^{q_i q_j} \tilde{M}_{a,\tilde{q}_i} \tilde{M}_{b,\tilde{q}_j}, \quad (4)$$

such that non-minimal flavour violation is parameterized by the dimensionless quantities $\lambda_{ab}^{q_i q_j}$. Since the matrices $\tilde{M}_{L,\tilde{u}}^2$ and $\tilde{M}_{L,\tilde{d}}^2$ are related by $SU(2)_L$ gauge invariance, the $\lambda_{LL}^{u_i u_j}$ parameters can be obtained from the knowledge of the $\lambda_{LL}^{d_i d_j}$ ones, so that we choose the latter as independent parameters. Moreover, motivated by measurements in the kaon sector, we ignore mixing of the first generation squarks [364] and further assume, for simplicity,

$$\lambda_L \equiv \lambda_{LL}^{sb}, \quad \lambda_R \equiv \lambda_{RR}^{sb} = \lambda_{RR}^{ct}, \quad \lambda_{LR} \equiv \lambda_{LR}^{ct} = \lambda_{RL}^{ct} = \lambda_{LR}^{sb} = \lambda_{RL}^{sb}. \quad (5)$$

This leaves us with three free parameters λ_L , λ_R , λ_{LR} describing squark flavour violation.

In addition to these parameters, the gaugino sector is further determined by the bino mass parameter M_1 , which we relate to the wino and gluino tree-level masses M_2 and M_3 through the relation $M_1 = M_2/2 = M_3/6$ inspired by Grand-Unified theories. Furthermore, all diagonal sfermion soft-mass parameters are set to the common scale M_{SUSY} , the trilinear couplings involving any third-generation sfermions are taken equal $A_t = A_b = A_\tau$, while all other trilinear scalar couplings are set to zero. Our model parametrization is finally completed by including the pole mass of the pseudoscalar Higgs boson m_{A^0} . We define all parameters at the electroweak scale and perform a grid scan over the following ranges in parameter space:

Observable	Experimental result	Reference
$\text{BR}(B \rightarrow X_s \gamma)$	$(3.43 \pm 0.21^{\text{stat}} \pm 0.07^{\text{sys}} \pm 0.24^{\text{th}}) \times 10^{-4}$	[365, 366, 367]
$\text{BR}(B_s \rightarrow \mu\mu)$	$(2.9 \pm 0.7^{\text{exp}} \pm 0.29^{\text{th}}) \times 10^{-9}$	[368, 369, 370, 371]
$\text{BR}(B \rightarrow K^* \mu\mu)_{q^2 \in [1,6] \text{ GeV}^2}$	$1.7 \pm 0.3^{\text{exp}} \pm 1.7^{\text{th}} \times 10^{-7}$	[372, 373, 374]
$\text{AFB}(B \rightarrow K^* \mu\mu)_{q^2 \in [1,6] \text{ GeV}^2}$	$(-0.17^{+0.06^{\text{exp}}+0.037^{\text{th}}}_{-0.06^{\text{exp}}-0.034^{\text{th}}}) \times 10^{-7}$	[372, 373, 374]
$\text{BR}(B \rightarrow X_s \mu\mu)_{q^2 \in [1,6] \text{ GeV}^2}$	$(1.60 \pm 0.68^{\text{exp}} \pm 0.16^{\text{th}}) \times 10^{-6}$	[375, 376, 377, 378]
$\text{BR}(B \rightarrow X_s \mu\mu)_{q^2 > 14.4 \text{ GeV}^2}$	$(4.18 \pm 1.35^{\text{exp}} \pm 0.44^{\text{th}}) \times 10^{-7}$	[375, 376, 377, 378]
$\text{BR}(B_u \rightarrow \tau\nu)$	$(1.05 \pm 0.25^{\text{exp}} \pm 0.29^{\text{th}}) \times 10^{-4}$	[379, 380, 381]
ΔM_{B_s}	$(17.719 \pm 0.043^{\text{exp}} \pm 3.3^{\text{th}}) \text{ps}^{-1}$	[365, 382]
Δa_μ	$(26.1 \pm 12.8) \times 10^{-10} [e^+ e^-]$	[383]
m_h	$125.5 \pm 2.5 \text{ GeV}$	[89, 134]

Table 1: Experimental constraints imposed in our parameter scan over the MSSM.

- $\tan \beta = [10, 40]$,
- $M_1 = [100, 350, 600, 850, 1100, 1350, 1600] \text{ GeV}$,
- $A_{t,b,\tau} = [-10000, \dots, 10000] \text{ GeV}$ in steps of 1000 GeV,
- $\mu = [100, 350, 600, 850] \text{ GeV}$,
- $m_{A_0} = [100, 350, 600, 850, 1100, 1350, 1600] \text{ GeV}$,
- $M_{\text{SUSY}} = [100, 350, 600, 850, 1100, 1350, 1600, 2000, 2500, 3000, 3500] \text{ GeV}$,
- $\lambda_L = [-0.8, \dots, 0.8]$ in steps of 0.1,
- $\lambda_{LR} = [-0.0025, \dots, 0.0025]$ in steps of 0.0005,
- $\lambda_R = [-0.8, \dots, 0.8]$ in steps of 0.1.

For each point in the parameter space, we calculate the theory predictions for all the flavour observables listed in Table 1. We then compute a likelihood for each observable based on its measurement, and then an overall likelihood for each point given as the product of the likelihoods for each observable, which allows us to select reference scenarios. Concerning the theoretical predictions of the observables under consideration, the branching ratio of the rare B decays $\text{BR}(B \rightarrow X_s \gamma)$, $\text{BR}(B \rightarrow K^* \mu\mu)$, $\text{BR}(B \rightarrow X_s \mu\mu)$, $\text{BR}(B_u \rightarrow \tau\nu)$ and the forward-backward asymmetry in the B meson three-body decay $\text{AFB}(B \rightarrow K^* \mu\mu)$ are calculated using the SuperISO package [380, 381], while the computation of the SM-like Higgs boson mass m_h , the supersymmetric contributions to the anomalous magnetic moment of the muon Δa_μ , the mass difference between the two neutral B_s^0 mesons and the branching ratio of $B_s \rightarrow \mu\mu$ rely on the SPheno program [294, 295]¹.

In the B physics sector, the observables that mostly constrain the choice of experimentally allowed scenarios are the branching ratio $\text{BR}(B \rightarrow X_s \gamma)$, which is particularly sensitive to left-left mixing, the B -meson oscillation parameter ΔM_{B_s} involving the products of left-left

¹The Higgs boson mass shows a rather important variation with the λ -parameters, in particular in the left-right sector for large values of $\tan \beta$. However, the associated two-loop calculations implemented in SPheno partly rely on flavour-conserving expressions which would have to be extended in case of flavour violation. Therefore the Higgs masses obtained have to be taken with a grain of salt and are not shown.

	M_1	M_{SUSY}	$A_{t,b,\tau}$	μ	$\tan \beta$	m_{A^0}	λ_L	λ_R	λ_{LR}
I	350	1100	2000	600	40	1600	0.1	0.4	0
II	350	1600	2000	100	10	600	0.3	0.8	0

Table 2: Two reference scenarios which are favoured by the experimental constraints of Table 1.

and right-right mixing parameters, the branching fraction $\text{BR}(B_s \rightarrow \mu\mu)$, largely depending on the parameters of the Higgs sector $\tan \beta$ and m_{A^0} , as well as the branching ratio $\text{BR}(B_u \rightarrow \tau\nu)$ which is sensitive to $\tan \beta$ and the mass of the charged Higgs boson. Additionally, the measurement of the anomalous magnetic moment of the muon leads to a preference for light sleptons, whereas achieving a correct mass for the Higgs boson requires a large left-right mixing in the stop sector and/or heavy stop masses and is in principle also sensitive to flavour mixing in the squark sector [384, 359, 385]. Moreover, the complicated structure of the scalar potential possibly allows for charge- and color-breaking minima [386]. We have verified with the program Vevacious [387] that the selected benchmark scenarios were stable or sufficiently long-lived against tunneling to vacua with combinations of non-zero s strange, s bottom, s charm and stop vacuum expectation values.

Based on the above-mentioned scan, we have identified two reference scenarios (given in Table 2) which are the most favoured by the current experimental constraints and which capture quite generic and interesting features of squark flavour mixing. The main differences between the two points reside in the value of the scalar mass scale M_{SUSY} and the Higgs-sector parameters μ , m_{A^0} and $\tan \beta$. Moreover, scenario II exhibits stronger generation mixings in both the left-left and right-right sectors. We have studied the dependence of the observables summarized in Table 1 on the three NMFV parameters and shown a selection of the most relevant results in Figs. 1 and 2. As expected, the $B \rightarrow X_s \gamma$ decay is in both cases very sensitive to mixing in the left-left sector, but almost independent of any mixing in the right-right and left-right sectors. For scenario I, the $B_s^0 \rightarrow \mu^+ \mu^-$ decay shows a strong dependence on both λ_L (in contrast to scenario II for which the influence of λ_L is less pronounced) and λ_{LR} , whilst the dependence on λ_R is found to be milder. Finally, any mixing induces large modification of the B -meson oscillation parameter ΔM_{B_s} , with interference effects involving λ_{LR} being in particular observed for scenario I.

In the first scenario, the ΔM_{B_s} observable constrains the parameters λ_L and λ_R the most, reducing the allowed interval to $\lambda_L \in [-0.09, 0.25]$ (and the $B \rightarrow X_s \gamma$ constraints is slightly less stringent) and $\lambda_R \in [-0.01, 0.68]$. The combination of constraints from the $B \rightarrow X_s \gamma$ and $B_s^0 \rightarrow \mu^+ \mu^-$ branching ratios restricts the λ_{LR} parameter to lie in the ranges $[-14.0, -12.8] \cdot 10^{-4}$ and $[-7.6, 9] \cdot 10^{-4}$. In the second scenario, the ΔM_{B_s} observable is again the most constraining one, the three parameters being bound to satisfy $\lambda_L \in [-0.03, 0.11]$ and $[0.23, 0.37]$ (and the constraints derived from the $B \rightarrow X_s \gamma$ measurement are less important here due to the lower value of $\tan \beta$ and the heavier squark masses), $\lambda_R \in [-0.10, 0.37]$ and $[0.67, 0.88]$, and $\lambda_{LR} \in [-0.9, 1.50] \cdot 10^{-4}$. Finally, the forward-backward asymmetry observed in $B \rightarrow K^* \mu^+ \mu^-$ decays mostly constrains, for both scenarios, flavour mixing in the left-left sector, but its influence is less stringent than that of the $B \rightarrow X_s \gamma$ branching ratio or ΔM_{B_s} .

In summary, we have shown that, despite all existing precise experimental measurements at low-energy, there is still room in the MSSM for sizable flavour-violating entries in the squark mass matrices concerning the mixing of second and third generations of squarks. We have

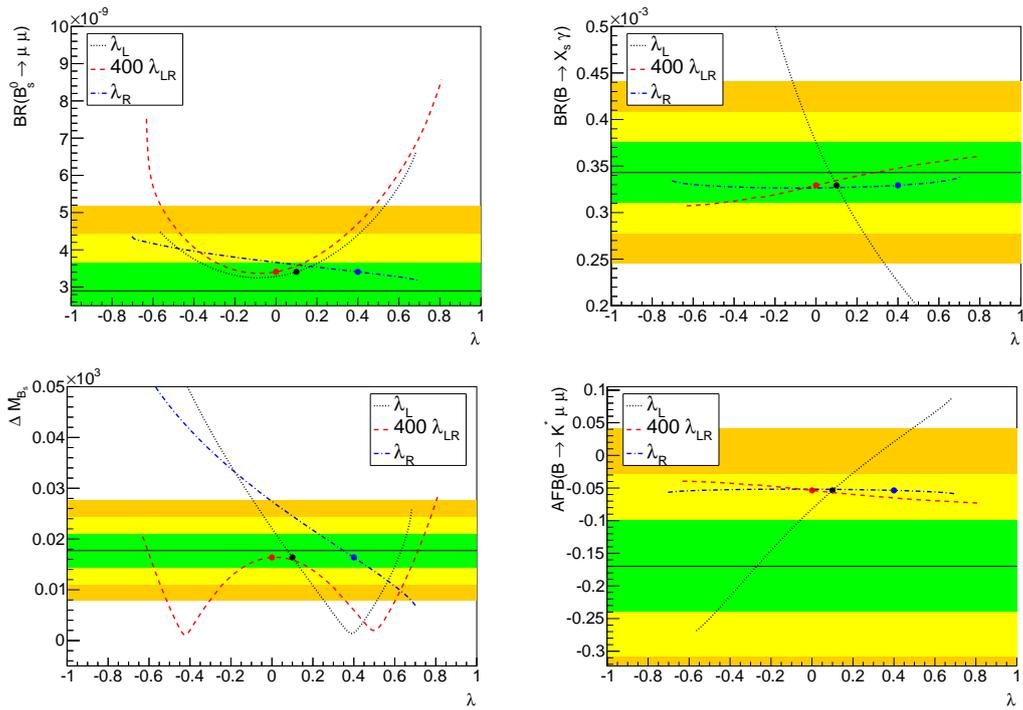


Figure 1: Dependence of selected observables on the NMFV-parameters λ_L , λ_{LR} , and λ_R around reference scenario I. The markers correspond to the scenario as defined in Table 2. The black horizontal lines indicate the experimental central value of Table 1. The green, yellow, and orange bands correspond to the limits at 1σ , 2σ , and 3σ confidence level, respectively.

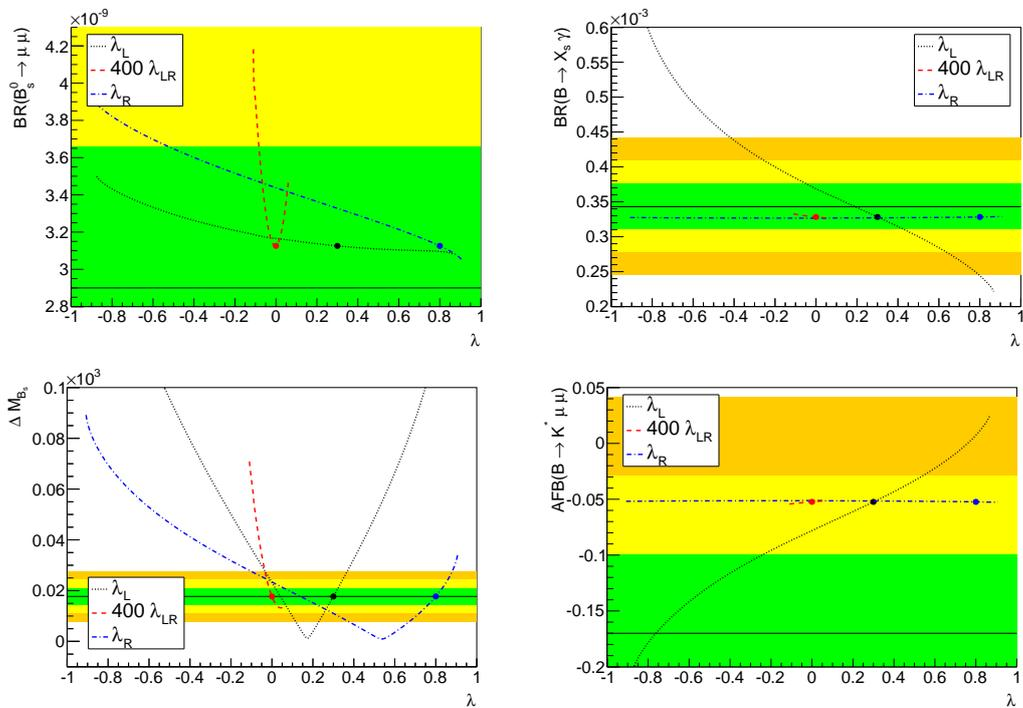


Figure 2: Same as Fig. 1 for variations of λ_L , λ_{LR} , and λ_R around reference scenario II.

defined and studied two scenarios favoured by current data that we aim to confront, in a future publication, with the LHC results. These scenarios are indeed characterized by new decay modes of squarks and gluinos [356, 355, 359, 358, 361, 385], which modify the standard decay patterns employed in the derivation of squark and gluino mass limits at the LHC. As a consequence, the reinterpretation of the experimental limits after accounting for flavour mixing in the squark sector might significantly reduce the bounds on the superpartners.

ACKNOWLEDGEMENTS

B.O'L. and W.P. are supported by DFG research training group GRK 1147, DFG project PO 1337-2/1 and by DAAD, project PROCOPE 54366394. B.H. is supported by France Campus, project PHC PROCOPE no. 26794YC. The work of B.F. has been partially supported by the Theory-LHC France-initiative of the CNRS/IN2P3 and by the French ANR 12 JS05 002 01 BATS@LHC. K.D.C. and N.S. are supported by an "FWO-Vlaanderen" aspirant fellowship and K.D.C. also by the Belgian Federal Science Policy Office through the Interuniversity Attraction Pole P7/37. K.D.C. acknowledges the support of the Strategic Research Program "High Energy Physics" and the Research Council of the Vrije Universiteit Brussel, the hospitality of the CERN TH group, and the support from the ERC grant 291377, "LHCtheory: Theoretical predictions and analyses of LHC physics: advancing the precision frontier".

Contribution 18

Effects of CP Violation in MSSM Scenarios

A. Arbey, J. Ellis, R. M. Godbole, F. Mahmoudi

Abstract

We consider the MSSM with CP violation in view of the LHC Higgs searches and the results of searches for dark matter, in both constrained and unconstrained MSSM scenarios, taking into account the effects of electric dipole moment constraints for the scenarios under consideration.

1 FRAMEWORK

Constrained MSSM scenarios such as the CMSSM or NUHM, with their limited number of parameters, offer simple frameworks to study the implications of the latest results from collider and dark matter searches (see, for example, [388] for the most recent global analysis of these constraints in the CMSSM and NUHM). These scenarios assume R-parity conservation and CP invariance, but they can be easily extended to incorporate CP-violating phases. On the other hand, the phenomenological MSSM (pMSSM) does not rely on any universality assumptions, and with its 19 parameters (assuming CP invariance and R conservation) provide a more general set-up. Thorough studies have been performed to reinterpret the LHC results in this context (see, for example, [389, 390, 391, 392, 393]). A preliminary exploration of these issues including CP violating phases in the framework of a MCMC analysis, before the LHC data became available also exists [394].

We consider here the implications of the latest collider data and dark matter searches, including the possibility of CP violation in both constrained MSSM scenarios and the pMSSM, which has six additional parameters corresponding to the CP-violating phases of the gaugino masses $M_{1,2,3}$ and of the trilinear couplings $A_{t,b,\tau}$. To study these scenarios, we generate spectra and compute the Higgs decay widths and Electric Dipole Moments (EDMs) using CPsuperH [395, 396, 397]. Flavour physics observables are also computed with CPsuperH and cross-checked with a development version of SuperIso [380, 381]. The dark matter relic density is computed with SuperIso Relic [398] for the pMSSM, and MicrOMEGAs [399, 400] is used for the relic density in constrained scenarios and for dark matter direct detection cross-sections.

For the constrained scenarios, we consider two CP-conserving benchmark scenarios that correspond to the CMSSM and NUHM1 best fit points obtained in the analysis of [388]:

Description	m_0 (GeV)	$m_{1/2}$ (GeV)	A_0 (GeV)	$\tan \beta$	$\text{sgn}(\mu)$	M_H^2 (GeV ²)
CMSSM	5650	2100	780	51	+	–
NUHM-1	1380	3420	3140	39	+	1.33×10^7

These points satisfy simultaneously constraints from the LHC Higgs and SUSY searches, flavour physics and dark matter relic density. Starting from these CP-conserving points, we perform a

Higgs observable	Constraint
M_H	$125 \pm 4 \text{ GeV}$
$\mu_{\gamma\gamma}$	1.20 ± 0.30
μ_{ZZ}	1.10 ± 0.22
μ_{WW}	0.77 ± 0.21
$\mu_{\tau\tau}$	0.78 ± 0.27
μ_{bb}	1.12 ± 0.45

EDM	Upper limit (e.cm)
Thallium	9×10^{-25}
Mercury	3.1×10^{-29}
Neutron	3×10^{-26}
Muon	1.9×10^{-19}

Table 1: Higgs and EDM constraints used in this study.

flat scan over the six CP-violating phases at the low-energy scale between -180° and 180° , in order to study the influence of CP violation on the different observables.

For the pMSSM study, we have set up the scan machinery in two ways: a random flat scan over the $19 + 6$ parameters, as well as an optimised scan using the geometric approach presented in [401]. Due to the large number of parameters, the flat scan is not very efficient since most of the points with large CP phases are excluded by EDM constraints, but it has the advantage of a flat distribution in the CP angles. The geometric scan, on the other hand, is much more efficient, and the neutron, thallium and mercury EDM are used in addition to the lightest Higgs mass to determine the optimised directions in the model parameter space.

We consider the set of constraints as described in [402], in addition to the EDM constraints. In particular, we require that the lightest neutralino is the lightest supersymmetric particle (LSP) and constitutes dark matter. We require that one of the three Higgs states lies in the mass range 121-129 GeV. If the h_2 or h_3 is at about 125 GeV, we impose LEP and LHC Higgs search constraints. We also consider the constraints on the signal strengths for h_1 . The Higgs signal strengths μ_{XX} are defined for each channel as the ratio of the Higgs production cross-section times branching ratio relative to the Standard Model values. Furthermore, we impose flavour constraints and use the upper limit on the relic density constraint. We compare the results with the case without phases in order to investigate the impact of the CP phases. Table 1 summarizes the Higgs and EDM constraints that are applied to the MSSM points.

2 HIGGS SECTOR

In the CMSSM and NUHM1 scenarios, the Higgs discovered at the LHC is identified with the lightest MSSM Higgs boson, and also in the presence of CP-violating phases. In Fig. 1, we present the distributions of the masses of the three Higgs bosons for the benchmark scenarios after varying the six phases, before applying the EDM constraints. For comparison, in Fig. 2 the distributions are shown after applying the EDM constraints. The figures reveal that the heavy Higgs masses are nearly unaffected by CP violation, whereas the lightest Higgs mass can be modified by a few GeV. Once the EDM constraints are applied, only the scenarios with very small EDMs survive, resulting in distributions with peaks at the positions of the CP-conserving points. After applying the EDM constraints, the statistics reduces substantially, whilst still allowing for a modification of the Higgs mass by up to 2-3 GeV. We have also studied the Higgs couplings for the benchmark points, and found that all the signal strengths of Table 1 remain close to unity, and varying the CP phases leads to less than 2% modifications.

The Higgs sector of the pMSSM with CP violation can differ more strongly from the CP-conserving case, with substantial mixing between the CP-even and CP-odd states. However,

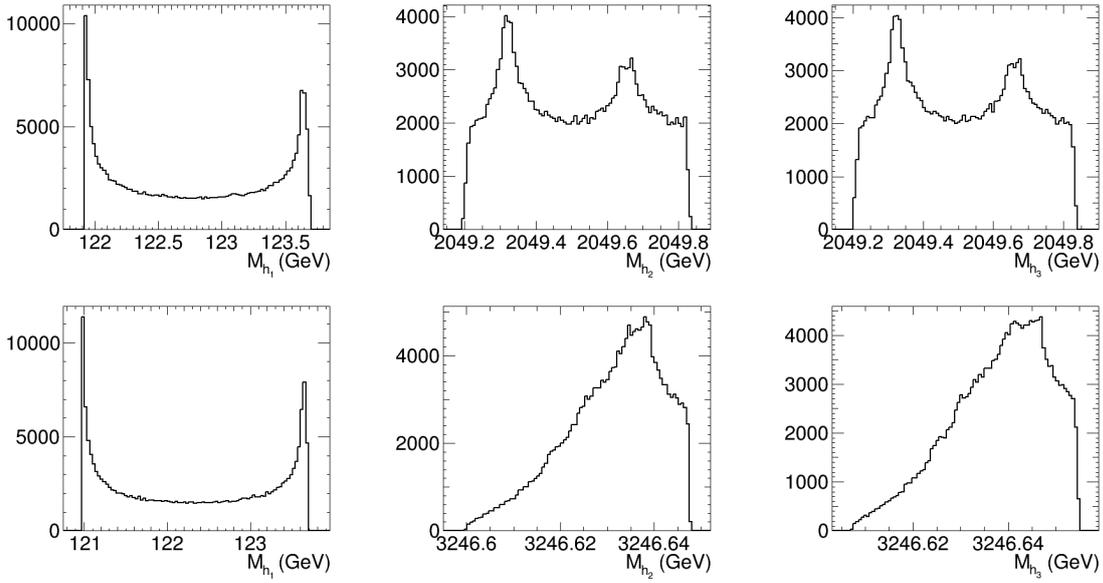


Figure 1: Distributions of the h_1 (left), h_2 (center) and h_3 (right) Higgs masses for the CMSSM (top), and NUHM1 (bottom) in the best-fit benchmark scenarios *before* applying the EDM constraints.

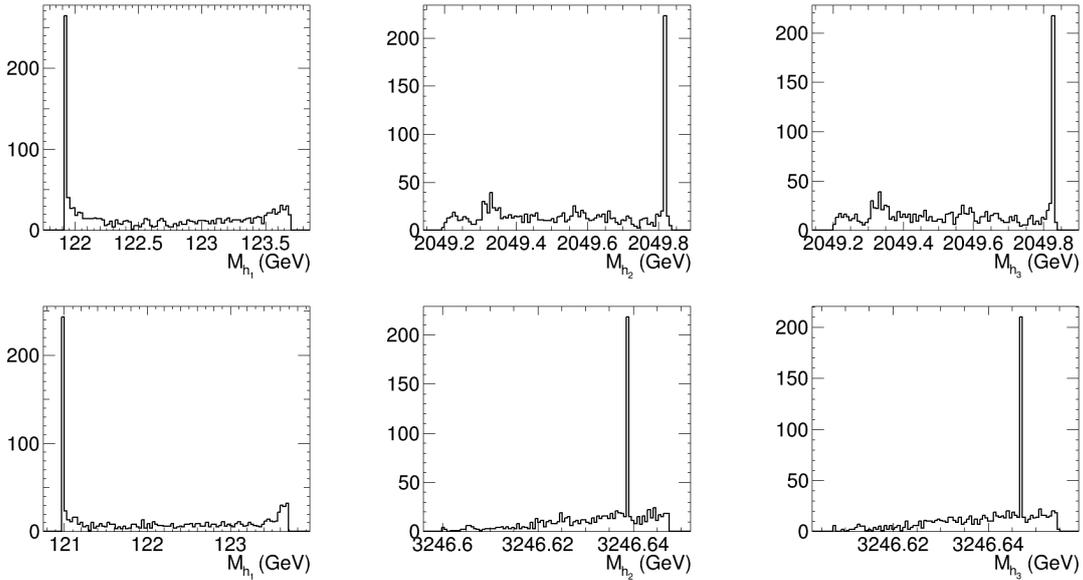


Figure 2: Distributions of the h_1 (left), h_2 (center) and h_3 (right) Higgs masses for the CMSSM (top) and NUHM1 (bottom) best-fit benchmark scenarios *after* applying the EDM constraints.

the recently-discovered Higgs boson has a large decay rate to two vector bosons, which implies that it is mainly CP-even. If this Higgs is identified with the lightest CPV-pMSSM Higgs boson h_1 , in most of the cases h_2 is CP-even and h_3 CP-odd, which corresponds to a set-up similar to that of the CP-conserving pMSSM.

In Fig. 3 we show all the points that satisfy the EDM constraints and for which either h_2 or h_3 has a mass close to 125 GeV. Once the constraints on the Higgs signal strengths are applied,

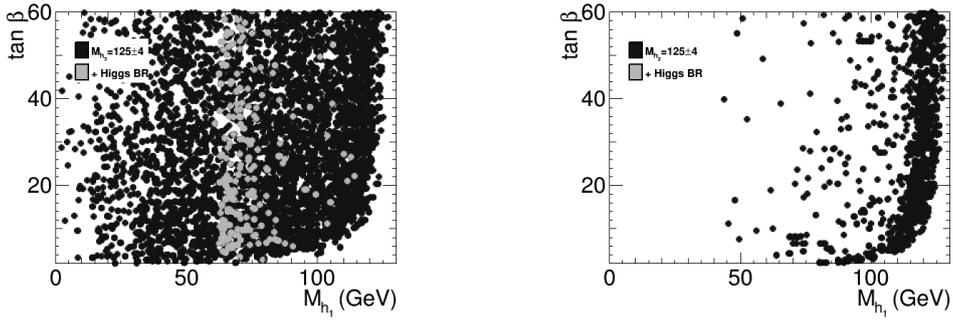


Figure 3: CPV-pMSSM model points satisfying the EDM constraints in the plane $(M_{h_1}, \tan \beta)$, in the case where either the h_2 (left) or the h_3 (right) is identified with the Higgs state discovered at the LHC.

only a small region remains in the case of h_2 at 125 GeV, while no possibility is found for the case where h_3 is at 125 GeV. However, if we consider in addition flavour physics constraints, no solution is found any more also for former case. This result is similar to that obtained in the CP-conserving pMSSM [403, 404]. Hence, the Higgs boson observed at the LHC has to be identified with h_1 in the CPV-pMSSM, which we will assume in the following.

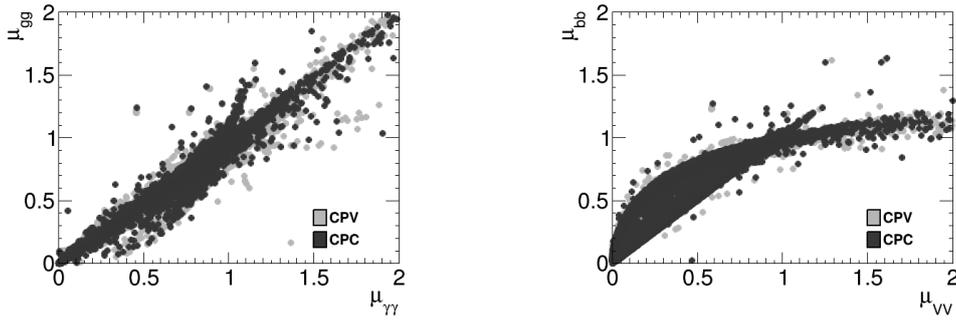


Figure 4: The strength of the coupling of the lightest Higgs boson to two gluons as a function of the coupling strength to photon pairs (left), and the strength of the coupling to $b\bar{b}$ pairs as a function of the coupling strength to two vector bosons (right).

In Fig. 4 we present the correlations between the signal strengths in the $\gamma\gamma$, gg and $b\bar{b}$, VV channels, comparing the CP-conserving and CP-violating cases. The results are very similar in both cases, with the CP-violating case offering a possibility of small deviations in comparison to the CP-conserving case. This shows that it will be difficult to discriminate between the two cases via more precise measurements of the Higgs signal strengths.

However, we have seen that CP violation can modify the Higgs mass by a few GeV, as well as the signal strengths by a few percent. In addition to the Higgs observables, the flavour sector and EDM observables provide direct probes of the CP properties. The interplay between the different sectors can therefore help determining the MSSM parameters and the CP properties of the model. Another sector of interest is the neutralino dark matter sector, that we consider in the next Section.

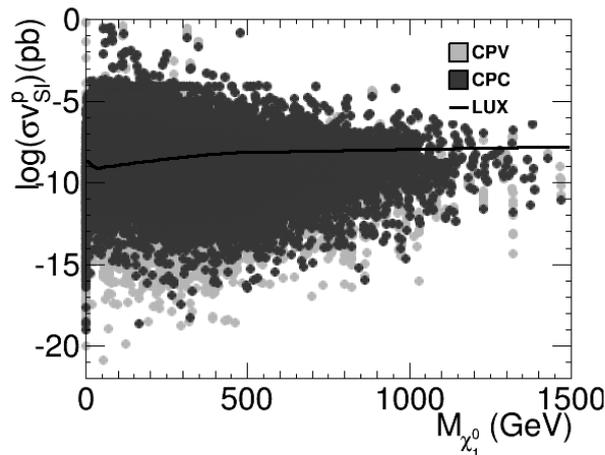


Figure 5: Spin-independent dark matter scattering cross-section on a proton as a function of the lightest neutralino mass.

3 DARK MATTER DIRECT DETECTION

Dark matter searches provide important constraints, even if they suffer in general from astrophysical and cosmological uncertainties. In the following, we apply different constraints on the MSSM scenarios into consideration. First, we impose the relic density constraint, but only as an upper bound, in order to account for the possibility of cosmological modifications of the properties of the early Universe [405, 406]. Older analyses of the effects of CP violating phases in Supersymmetric theories, on the relic density of neutralino dark matter exist in literature [407, 408]. Here we analyze the issue in light of the latest data on various fronts. We do not apply constraints from indirect dark matter detection searches, as they are subject to large astrophysical uncertainties. However, we consider the results of direct dark matter detection searches, which are sensitive primarily to the local density of dark matter.

The LUX collaboration has recently released strong upper limits on direct dark matter detection [409], in particular on the spin-independent scattering cross-section of a WIMP with the proton, that we consider in the following. The impact of the direct dark matter detection results from the LUX experiment on the CP-conserving and CP-violating pMSSM is presented in Fig. 5. The figure reveals that the inclusion of CP phases can lead to smaller scattering cross-sections, therefore allowing the neutralino to evade more easily the direct detection limits.

The constrained MSSM benchmark scenarios, being simpler, give more possibilities to test CP violation with direct dark matter detection. In Figs. 6 and 7, we show the distributions of the spin-independent neutralino-proton scattering cross-section in the constrained MSSM benchmark scenarios, before and after applying the EDM constraints. As can be seen, the scattering cross-sections are close to the LUX limit. After including the CP phases, the scattering cross-sections may decrease by a factor up to 5. Applying the EDM constraints, while strongly decreasing the statistics, does not change this feature. Therefore, dark matter direct detection can probe CP violation. If neutralino dark matter is discovered in direct searches, a better determination of the local density of dark matter could help in understanding the CP properties of the MSSM.

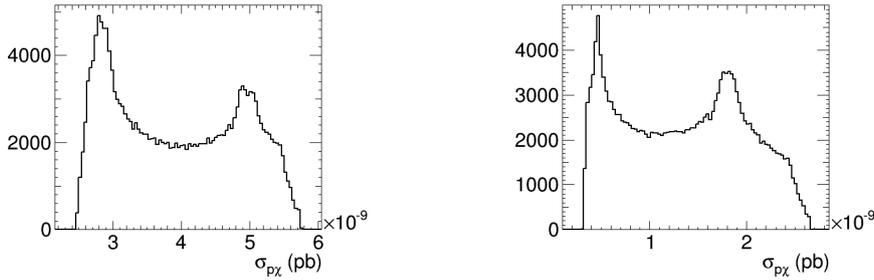


Figure 6: Distributions of the spin-independent dark matter scattering cross-section on the proton in the CMSSM (left) and NUHM1 (right) benchmark scenarios *before* applying the EDM constraints.

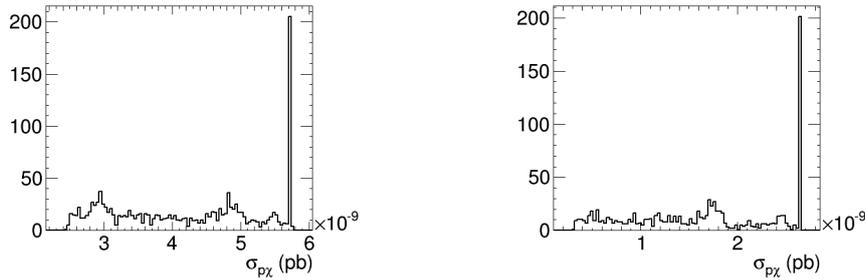


Figure 7: Distributions of the spin-independent dark matter scattering cross-section on the proton in the CMSSM (left) and NUHM1 (right) benchmark scenarios *after* applying the EDM constraints.

CONCLUSIONS

We have studied the effects of CP violation in the MSSM, in particular in view of the EDM constraints, Higgs observables and direct dark matter detection. The EDM constraints are well-known probes of CP violation, as well as flavour observables such as CP asymmetries in B meson decays. We have shown that the observed Higgs boson has to be identified with the lightest Higgs boson state h_1 , and that CP violation mostly changes the h_1 mass but does not affect much the Higgs signal strengths, rendering more difficult the possibility of discriminating between CP conserving and CP violating models in the Higgs sector.

We have also considered direct dark matter detection, and shown that CP violation can modify the neutralino-proton scattering cross-section by a factor up to 5. However, direct detection currently suffers from cosmological uncertainties that can limit the interpretations.

Finally, once all the present constraints are applied, and since all present observables are compatible with the CP-conserving results, discovering CP violation in this type of new physics scenario will be a difficult task, as they are already strongly constrained. However, the direct dark matter detection situation may improve in the near future.

ACKNOWLEDGEMENTS

The authors would like to thank the organizers of the Les Houches workshop where this work was initiated. The work of A.A. was supported by the Fédération de Recherche A.-M. Ampère de Lyon. The work of J.E. is supported in part by the London Centre for Terauniverse Studies (LCTS), using funding from the European Research Council via the Advanced Investigator

Grant 267352. RMG wishes to thank the Department of Science and Technology, Government of India, for support under the J.C. Bose Fellowship under grant no. SR/S2/JCB-64/2007.

Dark Matter

Contribution 19

Dark Matter Effective Field Theory at Colliders

A. Arbey, M. Battaglia, G. Bélanger, A. Goudelis, F. Mahmoudi, S. Pukhov

Abstract

The absence of signals for physics beyond the Standard Model at the LHC and the strong evidence for dark matter motivate the use of a fairly model-independent effective field theory approach to the study of dark matter physics. We present some preliminary results on constraints of the effective scalar operators coupling dark matter to quarks and gluons derived by combining results from monojet searches at the LHC, the recent upper limits on spin-independent WIMP-nucleon scattering cross section and the determination of the relic dark matter abundance in the Universe. We also comment on the potential of the next LHC runs as well as that of a future 100 TeV pp collider to further constrain the dark matter properties.

1 INTRODUCTION

The Large Hadron Collider has been extremely successful in pushing the mass scale of new physics towards the TeV scale. The discovery of a particle compatible with the Standard Model (SM) Higgs boson has given no hint of physics beyond the SM, while all direct searches for new physics have placed stringent bounds on the masses and couplings of new particles.

At the same time, there is strong evidence that physics beyond the SM (BSM) does exist, the most striking example being the existence of dark matter (DM). In the most commonly adopted freeze-out picture, the so-called “WIMP miracle” occurs: stable particle(s) with electroweak (EW) scale masses and couplings can actually account for the observed relic DM abundance in the universe. If the mass of the DM particle(s) lies indeed at the EW scale, it is highly likely that it can be produced at colliders, in particular at the LHC. This has motivated several experimental searches for final states with large missing transverse energy which would signal the production (and escape) of weakly interacting massive particles (WIMPs) from the detector.

A common problem of these searches stems from the fact that the interpretation of their results require rather strong assumptions on the nature of the underlying model, in particular when long decay chains are involved. In recent years, there has been an increasing interest in approaching DM physics using effective field theory (EFT) techniques, to overcome the limitations due to model-dependence. The basic underlying hypothesis of the EFT approach is that the sector mediating the interactions between dark matter particles and the SM is heavy and no light state is relevant for DM physics. Most analyses reported in the recent literature make the additional assumption that a single effective operator mediates the DM-SM interactions.

However, it should be kept in mind that the EFT approach is not completely free of assumptions. In fact, in many concrete models, the DM particles couple at tree-level to the Higgs and Z bosons, whereas even if all DM-SM mediators are heavy enough for an EFT approach

to be valid, upon integrating them out a *set* of effective operators is obtained, and not a single operator. These may interfere destructively or constructively changing the resulting DM-SM interaction. Last but not least, the standard EFT approach fails to capture specific features common to several DM models, such as the existence of resonances or co-annihilation processes which may be crucial in determining the DM relic density. Keeping these limitations in mind, we should also note that the EFT approach to dark matter has the advantage of encompassing different theoretical frameworks and, to some extent, manages to provide us with relatively generic information on DM.

In this work, we perform an investigation of the constraints on the dark matter EFT coming from the LHC, direct detection and the DM relic abundance. We examine the potential of the increases in LHC energy and luminosity to constrain the DM EFT for the case of scalar operators. In view of the discussions currently taking place in the HEP community on future collider projects, we comment on the possible impact of a future hadron collider reaching a centre-of-mass energy of 100 TeV.

2 THE DARK MATTER EFFECTIVE FIELD THEORY

In this preliminary study, we assume that the dark matter particle is not charged under the SM gauge group and the DM stability is ensured by some discrete \mathcal{Z}_2 -like symmetry under which the SM particles are even and the DM particles are odd, which amounts to the DM particles only appearing in pairs in the Lagrangian of the full (UV-complete) theory. This feature is assumed to be preserved upon integration of the heavy degrees of freedom, while now the DM interactions with the SM are suppressed by powers of some mass scale M_* , which should be understood as $M_* \sim M/\sqrt{g_1 g_2}$, with M being the mass of the heavy mediator and g_1, g_2 the mediator couplings to the SM and DM particle, respectively.

We focus on effective operators linking two DM particles to two quarks or two QCD field strengths, which are those most relevant for hadron colliders. In general, the DM particle can be either a real or complex scalar, a Dirac or Majorana fermion or a vector, when restricting ourselves to spin up to 1. Sets of effective operators coupling these classes of DM particles to the SM have been already defined under various assumptions [410, 411, 412, 413]. In this note, we focus our preliminary study on two of these operators assuming the DM particles are real scalar fields, namely

$$\begin{aligned} R_1 &= \frac{m_q}{2M_*^2} \chi \chi \bar{q} q \\ R_3 &= \frac{\alpha_s}{8M_*^2} \chi \chi G_{\mu\nu} G^{\mu\nu} \end{aligned} \quad (1)$$

where m_q is the mass of the quark q , χ is the dark matter particle, α_s is the strong coupling and G is the QCD field strength tensor ¹.

As mentioned above, the validity of the effective field theory approach must be verified. Whereas the description of DM interactions with the SM particles via effective operators can be justified in the case of direct detection for DM particle masses as low as $\mathcal{O}(\text{few GeV})$ and mediator masses as low as $\mathcal{O}(10^2 \text{ MeV})$, this is certainly not the case for the searches at the LHC. The EFT approach is at best valid for $M > 2M_{\text{WIMP}}$ and embedding the EFT in a weakly

¹Our operator naming scheme follows the notations of Ref. [412].

coupled theory would require $g_1 g_2 < (4\pi)^2$. This leads to the requirement $M_{\text{WIMP}} < 2\pi M_*$ for the EFT description to be valid. In fact, this bound may be overly optimistic for the validity of the effective field theory, since the actual momentum transfer involved in each process must also be considered [414, 415]. For simplicity, in this note we will adopt to the limit $M_{\text{WIMP}} < 2\pi M_*$ to define the region of validity of the EFT approach.

3 ANALYSIS AND FIRST RESULTS

We consider dark matter constraints in combination with monojet search results from ATLAS and CMS, for the two effective operators R_1 and R_3 defined above. For this study, we have set-up a software framework similar to that described in [402]. In particular, we have implemented the effective operator Lagrangians in FeynRules [253], which provides us with an automatic export of the model to the CalcHEP [416, 189] and Universal FeynRules Output (UFO) [203] file formats. The model files have then been imported in micrOMEGAs [417, 399, 400, 418] and Madgraph 5 [126]. The former program calculates the WIMP relic density and dark matter direct detection scattering cross-sections off matter, and the CalcHEP model file has been specifically modified to compute the scattering cross-section of WIMPs with gluons. These scattering cross-sections allow us to re-cast the LHC monojet searches in terms of DM direct detection constraints, and the results are compared to the recent LUX [409] and XENON [419, 420] 90% C.L. upper limits. We also consider the upper limit on the relic cold DM density $\Omega h^2 = 0.1199 \pm 0.0027$ [421], derived from latest PLANCK cosmic microwave background measurements.

WIMP masses are probed up to 2 TeV, and M_* is varied between 0 and 3 TeV. For each parameter point and each operator, the dark matter relic density and direct detection spin-independent scattering cross-sections are computed and the detectability through monojet searches at 8, 14 and 100 TeV centre-of-mass energies is evaluated as follows: We use the event reconstruction and selection criteria of the ATLAS [291] and CMS [422] preliminary monojet analyses performed on $\sim 20 \text{ fb}^{-1}$ of 8 TeV data. This analysis follows the procedure discussed in Ref. [423]. Monojet signal events have been generated for each parameter point using Madgraph 5 and Pythia 6 [258] with the CTEQ6L1 parton distribution functions (PDFs) [285]. Physics objects have been reconstructed using the Delphes 3.0.7 [424, 319] parametric detector simulation. The reconstruction and selection cuts of the original analyses have been applied, namely we required the events to have one jet with large transverse momentum, p_t , and missing transverse energy, MET, no electrons or muons fulfilling the fiducial p_t and $|\eta|$ experimental cuts and at most one additional jet with p_t in excess to 30 GeV. In the ATLAS analysis the leading jet p_t must exceed 280 GeV and the MET must be larger than 220 GeV. The CMS analysis requires instead a jet with $p_t > 110$ GeV and defines seven MET signal regions (MET > 250, 300, 350, 400, 450, 500, 550 GeV). We use the background estimates obtained by the experiments rescaled by the ratio of the products of production cross section times cut acceptance at the different energies of interest compared to 8 TeV and the ratio of the assumed luminosity to that used in the original 8 TeV analyses. The production cross section and acceptance of signal events have been computed using a similar procedure as that described above for the monojet signal. The 95% confidence level (C.L.) exclusion of each generated model point in presence of background only is determined using the CLs method [425]. These results are projected towards the reach of the HL-LHC project for 3 ab^{-1} at 14 TeV and a more “futuristic” 100 TeV pp collider delivering an integrated luminosity of 1 ab^{-1} [426]. In this preliminary analysis the experimental cuts are not optimised at the two energies and a further improvement

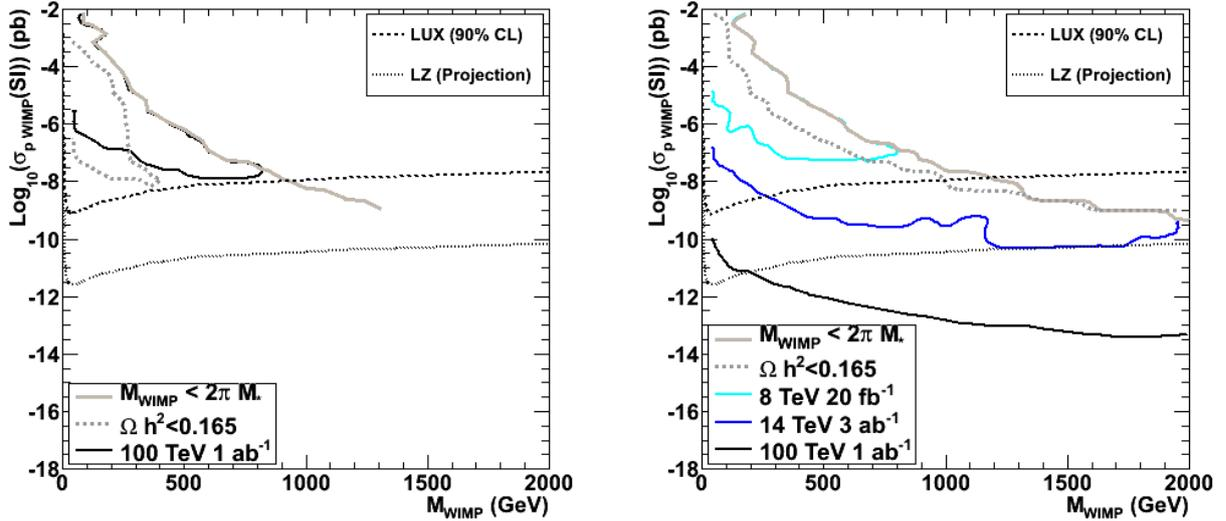


Figure 1: Constraints obtained for the R_1 (left panel) and R_3 (right panel) operators in the spin-independent scattering cross section vs. WIMP mass plane. The preliminary results for monojet searches at 8, 14 and 100 TeV are compared to the current LUX 90% C.L. upper limits and the expected reach of the future LZ experiment. The constraint derived from relic dark matter density and the limit of validity of the EFT approach are also shown.

of these exclusion contours can be therefore expected. The results from the monojet analyses are then interpreted in terms of exclusion contours in the spin-independent scattering cross section vs. WIMP mass plane as shown in Figure 1 where they are also compared to the EFT validity region defined by $M_{\text{WIMP}} < 2\pi M_*$ and the DM relic density constraint. We observe that the elusive R_1 could be probed only with energies of the order of 100 TeV and then down to scattering DM-nucleon cross section of the order of the current LUX and XENON bounds. On the contrary, monojet searches at HL-LHC at 14 TeV will push the sensitivity to the operator R_3 well below the current LUX and XENON cross section bounds to match the projected accuracy of LZ [427] and to WIMP masses of about 2 TeV. The availability of 100 TeV pp collision data will push this sensitivity further down into a completely un-chartered territory. We expect that the optimisation of the monojet event selection for 14 and 100 TeV will further extend this region of sensitivity.

CONCLUSIONS

In this preliminary investigation we have considered the impact of the latest results from the LHC monojet searches at 8 TeV as well as their projections at 14 and 100 TeV in the context of two effective models with real scalar WIMPs. We have seen that the R_1 operator is not constrained by the 8 TeV LHC searches and will be hardly probed by the LHC future run. It will be necessary to perform searches at future higher energy colliders to set constraints on this elusive model. On the contrary, the R_3 operator is already strongly probed by the current LHC result, and the experimental prospects to tighten these bounds in the 14 TeV and high luminosity LHC runs are favourable.

The study presented here represents the first step of a more general program of studies of

the effective approach supported by the development of a versatile software framework design which will make easy the extension of the study to other operators. Planned developments consist of the interpretation of the LHC monojet searches in a broader range of effective models, for real and complex scalar, Dirac and Majorana fermion, vector, spin 3/2 and tensor WIMPs. Moreover, in view of our introductory comments, we believe it is appropriate to move past the minimal picture where a single effective operator is assumed to be responsible for the DM couplings to the SM and examine the consequences of the inclusion of multiple operators and of direct couplings of dark matter particles to the Higgs and Z bosons in the analysis. These issues will be addressed in details as part of a future study.

ACKNOWLEDGEMENTS

The authors would like to thank the organisers of the Les Houches workshop where this work was initiated. The work of A.A. was supported by the Fédération de Recherche A.-M. Ampère de Lyon.

Contribution 20

The Interplay of the LHC and Direct Dark Matter Detection in Unravelling Natural Supersymmetry at the Focus Point

D. Barducci, S. Belyaev, A. Bharucha, W. Porod and V. Sanz

Abstract

In this paper we present our results on the interplay of the LHC at 13 TeV (LHC13TeV) and direct dark matter (DDM) experiments in probing the far focus point (FFP) region of natural supersymmetry, within the MSSM framework. This parameter space is characterised by low values of μ and a compressed spectrum for χ_1^0 , χ_2^0 and χ_1^\pm – the lightest MSSM particles – which can only be probed via mono-jet signatures. We therefore study such signatures in our analysis. The low signal-to-background ratio is a challenging but important characteristic of this search which, as we show, never exceeds 6%, such that the control of the systematic error is crucial. We take into account a) realistic systematic errors and b) fast detector simulation which are both essential in estimating the correct LHC sensitivity to the FFP region. We have found a high degree of the complementarity between the LHC13TeV and DDM search experiments: LHC13TeV@ 1.5 ab⁻¹ would be able to exclude FFP parameter space for $m_{\tilde{\chi}_1^0}$ with a mass *below* 120 (200) GeV for a 5% (3%) systematic error on the background while XENON1T would be able to probe FFP space with $m_{\tilde{\chi}_1^0}$ *above* 320 GeV. The sensitivity to the mass gap between 120 (200) GeV and 320 GeV is problematic even for the combination of the LHC13TeV and XENON1T experiment and requires further attention. Our findings on the collider searches are also applicable to a more general SUSY framework beyond the MSSM.

1 Introduction

The naturalness of supersymmetry (SUSY), which has already been discussed for close to two decades has become even more relevant today, at the time of the LHC running, when the scale of SUSY is finally being tested in the TeV region. Indeed, the lack of evidence for superparticles at the CERN LHC, along with the rather high value of the Higgs boson mass for SUSY, raised the questions of whether the remaining allowed parameter space suffers from a high degree of fine-tuning, and if there is any parameter space of Natural SUSY (NSUSY) left. We discuss this problem in the framework of the well-motivated minimal supersymmetric standard model (MSSM), however note that our findings on collider searches are applicable to a general SUSY framework.

In the first papers on this subject, the NSUSY space was connected to light gluino and stop masses [428], on which the limits have already reached the 1 TeV scale in the case where

the gluino and stops are not degenerate with the LSP (see for example Refs. [302, 303]). Note, though, that experimental limits relying on certain dominant decay channels (e.g. $\tilde{t} \rightarrow t\chi_1^0$) can be significantly relaxed in the scenario we consider below with Higgsino-like dark matter, where the branching ratios would depend on the left-right admixture of the lightest stop. At the same time it has been shown that fine-tuning can be low even if the masses of the supersymmetric scalars and gluino are large. This happens in so called "hyperbolic branch"(HB) [429] or "focus point" (FP) [430, 431, 432] region of parameter space, where the value of the μ -parameter is low.

The states directly related to naturalness (primarily the stop and higgsinos) are especially challenging, and model independent collider bounds are weak or non-existent. Light stops can be searched directly via missing energy signatures, or indirectly making use of the Higgs data [433, 434, 435, 436, 437, 438].

This study is devoted to NSUSY in the HB/FP region. In the constrained MSSM, for example, μ is driven to low values when m_0 parameter is being increased. In this region the magnitude of the μ parameter falls, and the higgsino components of the lighter neutralinos increase. It was recently argued [439] that electroweak fine tuning in SUSY can be grossly overestimated by neglecting additional non-independent terms which lead to large cancellations favouring HB/FP for NSUSY. In the case of large M_1 and M_2 gaugino masses, MSSM particles, namely χ_1^0 , χ_2^0 and χ_1^\pm become quasi-degenerate and acquire a significant higgsino component. This scenario also provides a naturally low dark matter (DM) relic density via gaugino annihilation and co-annihilation processes into Standard Model gauge and Higgs bosons. We therefore have relatively light higgsinos-electroweakinos compared to the other SUSY particles. This scenario is not just motivated by its simplicity, but also by the lack of evidence for SUSY to date, indicating that a weak scale SUSY spectrum is likely non-universal. Already one decade ago it was shown that HB/FP parameter space is challenging to probe at the LHC [440] even if the mass gap between gauginos is large enough to provide leptonic signatures. The most challenging case takes place when only χ_1^0 , χ_2^0 and χ_1^\pm are accessible at the LHC, and the mass gap between them is not enough to produce any leptonic signatures. We call this scenario Far Focus Point region (FFP). The only way to probe FFP is via a mono-jet signature, as suggested in [441]. This has been applied to studies on compressed SUSY spectra [271, 442, 443].

In this contribution we present our results on the interplay of LHC13TeV with direct dark matter search experiments in order to probe the FFP region of NSUSY. We focus on scenarios where the lightest states are nearly pure higgsinos, and plan to consider scenarios with higgsino-bino mixing in future work. We also take into account realistic systematic error and perform a fast detector simulation analysis for FFP, crucial in correctly estimating the correct LHC sensitivity to FFP.

2 Spectrum and decays

We consider scenarios where the lightest neutralinos and charginos are higgsino-like and where all sfermions have masses in the multi-TeV range.

In the limit $|\mu| \ll |M_1|, |M_2|$ one finds

$$m_{\tilde{\chi}_{1,2}^0} \simeq \mp \left[|\mu| \mp \frac{m_Z^2}{2} (1 \pm s_{2\beta}) \left(\frac{s_W^2}{M_1} + \frac{c_W^2}{M_2} \right) \right] \quad (1)$$

$$m_{\tilde{\chi}_1^\pm} \simeq |\mu| \left(1 + \frac{\alpha(m_Z)}{\pi} \left(2 + \ln \frac{m_Z^2}{\mu^2} \right) \right) - s_{2\beta} \frac{m_W^2}{M_2} \quad (2)$$

where we have defined $s_{2\beta} = \sin(2\beta) \text{sign}(\mu)$. We have included the EM corrections in case of $m_{\tilde{\chi}_1^\pm}$. In the case of $\mu > 0$, the eigenstates are

$$\tilde{\chi}_{1,2}^0 \simeq \frac{1}{\sqrt{2}} (\tilde{H}_d^0 \mp \tilde{H}_u^0) \quad (3)$$

$$\tilde{\chi}_1^\pm \simeq \tilde{H}_{u,d}^\pm \quad (4)$$

The mass separation is given by

$$\Delta m_o = m_{\tilde{\chi}_2^0} - m_{\tilde{\chi}_1^0} \simeq m_Z^2 \left(\frac{s_W^2}{M_1} + \frac{c_W^2}{M_2} \right) \quad (5)$$

$$\Delta m_\pm = m_{\tilde{\chi}_1^\pm} - m_{\tilde{\chi}_1^0} \simeq \frac{\Delta m}{2} + \mu \frac{\alpha(m_Z)}{\pi} \left(2 + \ln \frac{m_Z^2}{\mu^2} \right) \quad (6)$$

where we have neglected corrections of the order $1/\tan\beta$ and μ/M_i^2 .

In the case of pure higgsinos, the three body decays are dominated by virtual vector bosons. However, due to the small mass differences the decays into third generation fermions are suppressed. Note that in the scenario where M_1 is close to $|\mu|$ also the off-shell light Higgs boson h^0 can give sizeable contributions [444], in particular if $\tan\beta$ is large. Therefore the essential parameters for the scenario under study are μ and M_1 .

Three body decays in the limit of small mass separation are discussed in [445], where an effective theory study of the pseudo-Dirac Dark Matter scenario [446, 447, 448] such as the higgsino-like was done. In this limit, the decay width does not depend on the overall neutralino mass, just on the mass difference,

$$\Gamma(\tilde{\chi}_1^\pm, \tilde{\chi}_2^0 \rightarrow f f' \tilde{\chi}_1^0) = \frac{C^4}{120\pi^3} \frac{\Delta m^5}{\Lambda^4} \quad (7)$$

where $\Lambda \simeq m_{W,Z,h^0}$ and Δm is either $m_{\tilde{\chi}_2^0} - m_{\tilde{\chi}_1^0}$ or $m_{\tilde{\chi}_1^\pm} - m_{\tilde{\chi}_1^0}$.

For example, for off-shell Z exchange and decay into leptons, the coefficient C is as follows

$$C^4 = \frac{1}{4} \frac{g^4}{c_W^4} (s_w^2 - 1/2)^2 (N_{13}N_{23} - N_{14}N_{24})^2 \simeq \frac{1}{4} \frac{g^4}{c_W^4} (s_w^2 - 1/2)^2 \quad (8)$$

and similarly for the off-shell W -decay.

The proper decay length is very sensitive to the value of Δm , and values below the GeV could lead to a displaced vertex, or a collider-stable situation. Indeed, for the decay $\tilde{\chi}_2^0 \rightarrow f \bar{f} \tilde{\chi}_1^0$ with a Z -exchange, the proper decay length is given by

$$L = c\tau \simeq 0.01 \text{ cm} \left(\frac{\Delta m}{1 \text{ GeV}} \right)^{-5} \text{ (Z-exchange)} \quad (9)$$

which implies that for $\Delta m \lesssim 0.1 \text{ GeV}$, $\tilde{\chi}_2^0$ would be collider stable. Similarly, for $\Delta m \lesssim 1 \text{ GeV}$ one could look for displaced vertices of order $100 \mu\text{m}$. Note that the measured decay

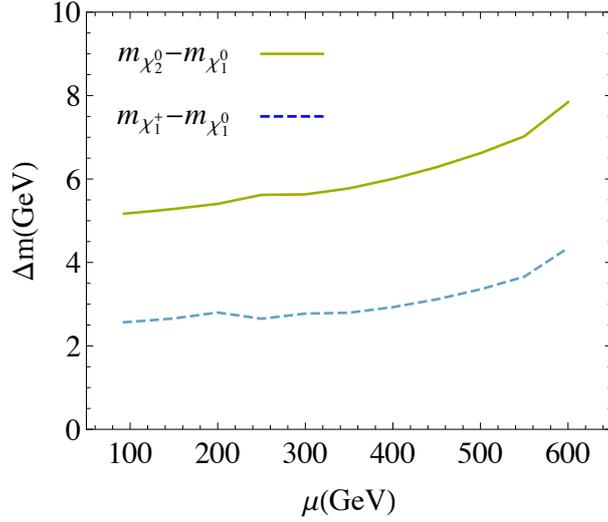


Figure 1: The mass splitting between χ_2^0/χ_1^\pm and χ_1^0 for the case $M_1=1$ TeV and $\tan\beta=5$ versus μ .

length would depend on the boost factor of the decaying neutralino, and in Ref. [445] a detailed discussion on how to introduce it is presented.

For W -exchange the situation is very similar,

$$\tilde{\chi}_1^\pm \rightarrow f f' \tilde{\chi}_1^0 \quad (10)$$

with W -exchange leading to

$$L = c\tau \simeq 0.006 \text{ cm} \left(\frac{\Delta m}{1 \text{ GeV}} \right)^{-5} \quad (\text{W-exchange}) \quad (11)$$

μ (GeV)	$m_{\chi_1^0}$ (GeV)	$m_{\chi_2^0}$ (GeV)	$m_{\chi_3^0}$ (GeV)	$m_{\chi_1^\pm}$ (GeV)
93	98.4	103.6	994.2	101.0
200	201.9	207.2	994.4	204.6
300	289.8	295.4	994.5	292.6
400	400.0	406.0	994.8	402.9
500	502.7	509.3	995.1	506.1

Table 1: Masses of the higgsino-like lightest gauginos as a function of μ for the scenario with $M_1 = 1$ TeV and $\tan\beta = 5$

In Table 1 and Fig. 1 we show the mass spectrum and the mass splitting for the higgsino-like lightest electroweakinos as a function of μ . These results are presented for $M_1 = 1$ TeV and $\tan\beta = 5$, however for such large values of M_1 and M_2 the mass spectrum, as well as mass splitting pattern varies slightly (below 1% level) for the whole range of $\tan\beta$ (5-50) under consideration.

In the following sections 3 and 4, where we have studied the dark matter and collider phenomenology respectively, M_2 and M_3 are kept fixed to 2 TeV and 1.5 TeV respectively, while we decouple the effect of squarks and sleptons in the electroweakino production and

decay by keeping their mass at $\simeq 2$ TeV. The dark matter results are presented for the cases $M_1 = \mu$, $M_1 = (\mu + 1 \text{ TeV})/2$ and $M_1 = 1 \text{ TeV}$ and for $\tan \beta = 5, 15, 25, 50$, whereas the collider results are presented for $M_1 = 1 \text{ TeV}$ and $\tan \beta = 5$.

3 Dark Matter

The newly released results from Planck [449] (see also WMAP [450]) mean that the uncertainty on the already very precise measurement of the dark matter (DM) relic density ($\Omega_{\text{DM}} h^2$), assuming Λ_{CDM} cosmology, has become even smaller, $\Omega_{\text{DM}}^{\text{Planck}} h^2 = 0.1198 \pm 0.0026$.

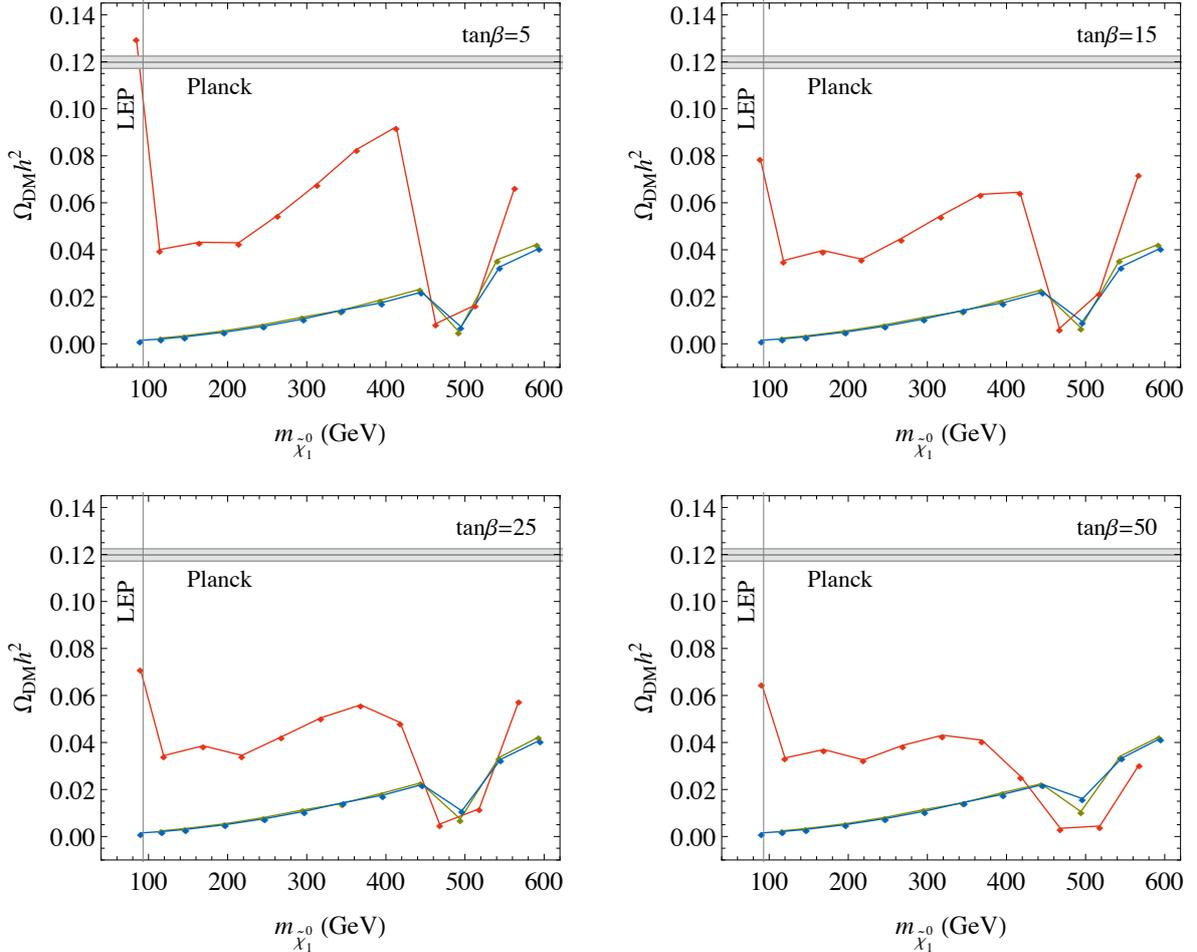


Figure 2: The predicted value of the dark matter relic density $\Omega_{\text{DM}} h^2$ is shown as a function of the mass of the lightest neutralino $m_{\chi_1^0}$ for four different values of $\tan \beta$ as indicated. The red, yellow and blue lines indicate $M_1 = \mu$, $M_1 = (\mu + 1 \text{ TeV})/2$ and $M_1 = 1 \text{ TeV}$ respectively. The relic density measured by the Planck satellite, $\Omega_{\text{DM}}^{\text{Planck}} h^2$, is also shown for comparison. The vertical line shows the LEP limit on $m_{\tilde{\chi}^+}$ [451].

The lightest supersymmetric particle (LSP), if stable, will contribute to this relic density. In the scenarios considered here, the LSP is the lightest neutralino, composed predominantly of the higgsino and, to varying degrees, of the bino. It is well known that a higgsino-like LSP produces an under-density of dark matter, i.e. the annihilation cross-section is too high to obtain the relic abundance observed by Planck. On the other hand, if the LSP is bino-like, annihilation

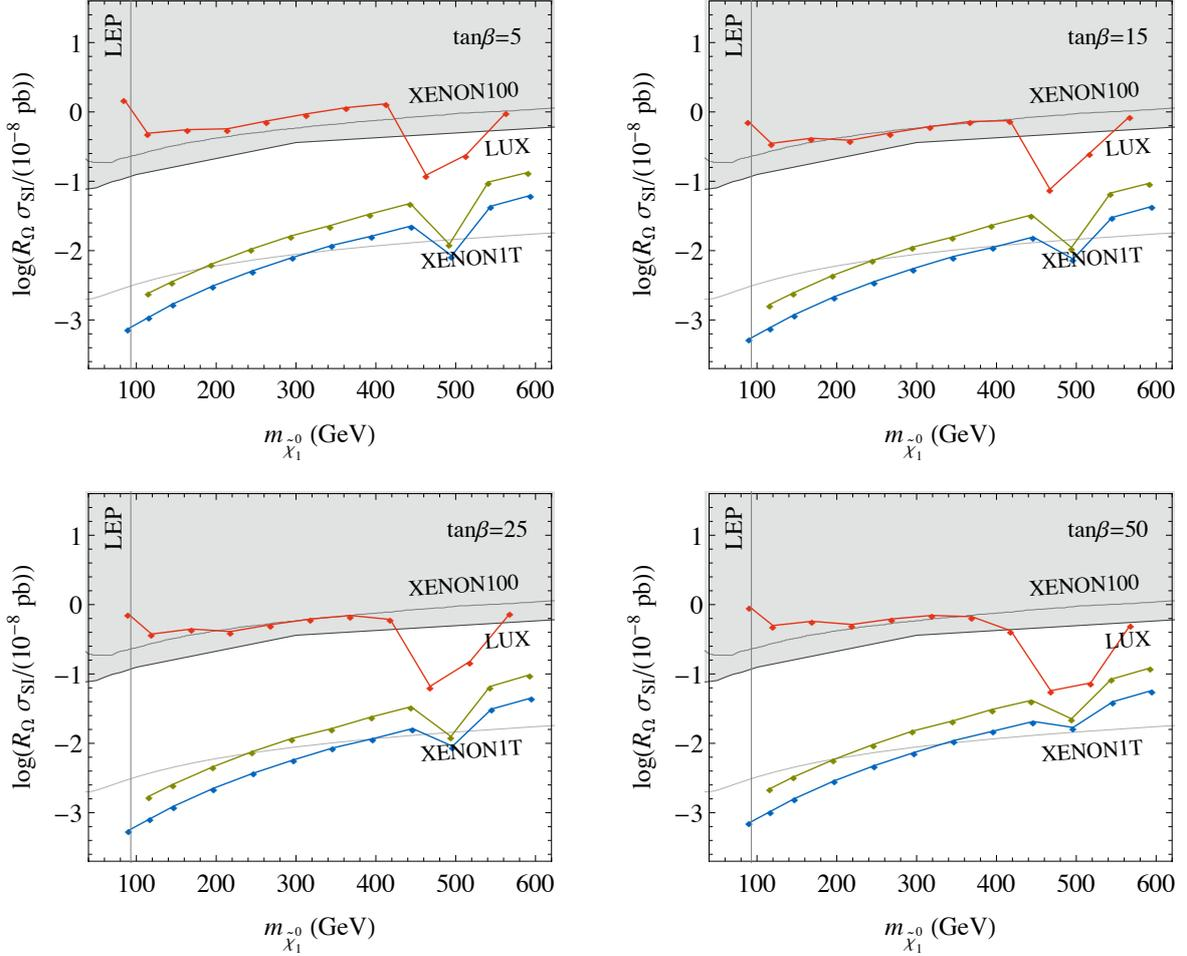


Figure 3: The predicted value of the spin-independent annihilation cross section for direct detection $R_\Omega \sigma_{\text{SI}}$ (pb), rescaled by $R_\Omega = \Omega_{\text{DM}}/\Omega_{\text{DM}}^{\text{Planck}}$, is shown as a function of the mass of the lightest neutralino $m_{\tilde{\chi}^0}$, where colours are as in Fig. 2. The exclusion limits from XENON100 and LUX, as well as the projected limit from XENON1T are also shown for comparison.

is suppressed, and an over-density is predicted. Therefore a mixed LSP can, at low LSP masses ~ 100 GeV, lead to a correct prediction of the relic abundance and this is known as the focus point (FP) region. Therefore we chose this $\mu \lesssim M_1$ scenario which results in the value of $\Omega_{\text{DM}} h^2$ being pausably not above the measured value from Planck which solves the typical problem of the over-closure of the universe for generic SUSY parameter space.

We then assume that the remaining relic abundance is accounted for by other means, for example:

- Adding a light multi-TeV moduli field where the higgsino LSP is non-thermally produced (e.g. Ref. [452])
- Mixed axion-higgsino dark matter (e.g. Ref. [453])

In order to assess the compatibility of the scenarios studied with existing results from dark matter experiments, we have calculated $\Omega_{\text{DM}} h^2$ and the spin-independent cross section for direct detection using `micrOmegas 2.4.1` [399, 454]. In Fig. 2 we show the results for $\Omega_{\text{DM}} h^2$ as a function of the mass of the LSP, i.e. the lightest neutralino, for four different values of

$\tan\beta$ as indicated. The red, blue and yellow lines indicate $M_1 = \mu$, $M_1 = (\mu + 1 \text{ TeV})/2$ and $M_1 = 1 \text{ TeV}$ respectively. From this plot we see, as expected, that in general $\Omega_{\text{DM}} h^2$ lies below $\Omega_{\text{DM}}^{\text{Planck}} h^2$, and decreases as the neutralino becomes increasingly higgsino-like. The reason causing the difference between the mixed gaugino/higgsino case and the nearly pure higgsino case is the Higgs contribution. The Higgs bosons can couple maximally to neutralinos if they are a nearly equal admixture of gauginos and higgsinos as is the case for $M_1 = \mu$ (red line). Moreover, the dip close to $m_{\tilde{\chi}_1^0} \simeq 500 \text{ GeV}$ is due to the pseudo-scalar Higgs boson A^0 which has a mass close to 1 TeV in our case. Again the effect is more pronounced in case of $M_1 = \mu$. In Fig. 3 we further show the spin-independent annihilation cross section for direct detection, again for four different values of $\tan\beta$ as indicated, and with colour-coding analogous to Fig. 2. For convenience, on these plots we additionally indicate the most recent limits from XENON100 [455] and LUX [409], as well as the projected limits from XENON1T after 2 years live-time and 1 ton fiducial mass (see e.g. Ref. [456]). Instead of σ_{SI} , we plot the rescaled $R_\Omega \sigma_{\text{SI}}$ (pb), where the scaling factor $R_\Omega = \Omega_{\text{DM}}/\Omega_{\text{DM}}^{\text{Planck}}$ allows easy comparison with these bounds, which in general assume the relic density to be the value measured by Planck. Fig. 3 illustrates that in the focus point region for low LSP masses, where the correct relic density is predicted and which is also easiest to see at colliders, is in fact excluded as the the spin-independent cross section for the direct detection experiments is too high. We would further like to highlight the interesting complementarity between the reach of the collider searches and the direct detection searches, particularly interesting for low dark matter masses.

4 Projections for the LHC run at 13 TeV

In this section we perform a study to obtain the projected sensitivity of the LHC run at 13 TeV to the electroweakino sector in Natural SUSY. Conservatively, we assume that the sfermions are heavy, and consider a scenario where the mass separations Δm and Δm_\pm is not large enough as to produce visible decay products.

This scenario with degenerate higgsinos, i.e. the NSUSY scenario, is the most difficult one to test since pair electroweakino production *per se* will be not detectable. One requires the help of initial- or final-state radiation (ISR, FSR), which could produce a high p_T jet [271] or photon [457, 458] recoiling against the neutralino system.¹ The diagrams for the mono-jet + \cancel{E}_T signature are shown in Fig. 4 where we have omitted contribution from heavy squarks. Therefore the signal subject of our study will be

$$pp \rightarrow \chi\chi j \quad \chi = \chi_{1,2}^0, \chi_1^\pm \quad (12)$$

In the following, the results are presented for $M_1 = 1 \text{ TeV}$ and $\tan\beta = 5$, and other parameters are as mentioned in section 2.

4.1 Analysis Setup

We performed a parton-level simulation using MadGraph [126] with the MSSM model from FeynRules [253]², and cross-checked with CalcHEP [189] with the MSSM model from the HEPMDB website³. Parton-level Standard Model background simulations have been also cross

¹ Note that mono-Z [459] or mono-W [460] signatures could also be used to constrain this scenario, although monojet is the most promising channel.

²<http://feynrules.irmp.ucl.ac.be/wiki/MSSM>

³<http://hepmdb.soton.ac.uk/hepmdb:0611.0028>

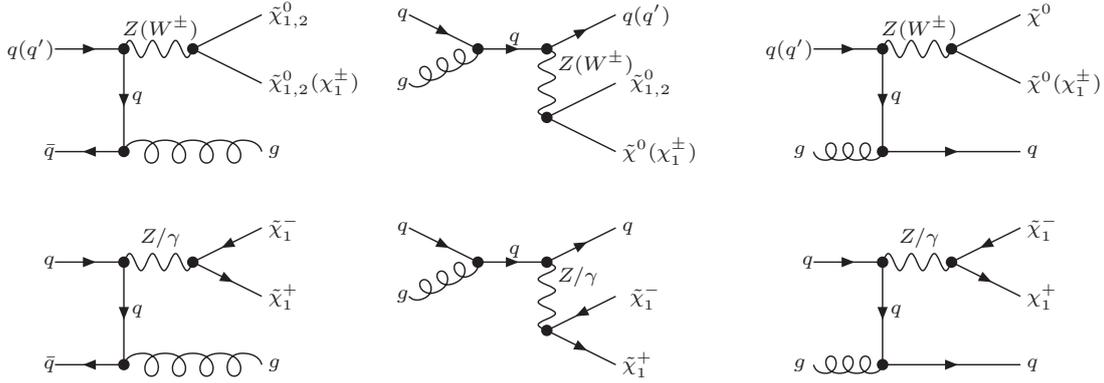


Figure 4: Representative diagrams for pair neutralino-chargino production in association with quark/gluon leading to mono-jet signature.

checked between two packages. Our choice of PDF sets is CTEQ6L1 [285] and we used the MadGraph dynamical choice of renormalization scale. Parton-level events went through hadronization and parton-showering using PYTHIA [258], followed by the the Delphes3 [319] package for fast detector simulation.

4.2 Signal versus background analysis and LHC prospects

It should be stressed that soft leptons and quarks coming from χ_2^0 and χ_1^\pm decays will not be visibly boosted by the ISR since the momenta of the boosted particles is proportional to their mass. The boost will mostly be taken by the neutralino, whose mass is already limited by LEP to be above 90 GeV in this scenario [461].

The main SM background to our high p_T jet + high \cancel{E}_T (monojet) signature is the irreducible $Z + jet \rightarrow \nu\bar{\nu} + jet$ (Zj). The relative size and shape difference of the signal versus the Zj background is presented in the left and right frames of Fig. 5 respectively for p_T^j distribution. In this figure we see that a sizeable cut on p_T needs to be applied. With a basic $P_T^j > 20$ GeV cut the Zj background is about 3 orders of magnitude higher than the signal for the lowest allowed mass of $m_{\chi_1^0} \simeq 100$ GeV.

An important feature of the signal versus background is that the *shape* of the background distribution is quite different from the signal: the background falls more rapidly with p_j^T , and the difference of slope with respect to the signal is bigger for higher neutralino masses. The different slope is mainly due to the mass difference between the neutralino from signal and neutrino from the background. One should also notice that the difference between shapes of signal and background p_j^T distributions vanishes for very large values of $p_j^T \gg m_{\chi_1^0}$, as one would expect.

After inspecting these distributions, one expects that the best sensitivity will be achieved for a high enough values of p_j^T cut and eventually correlated values of \cancel{E}_T cut. Ultimately, though, the sensitivity will be limited by the systematic uncertainty on the background prediction. From Fig. 5 (left) one can see that even for very large values of p_j^T cut the highest signal to background ratio (S/B) will be about 1/10, hence one needs to control the systematic error at the few percent level. Therefore, in our projections for 13 TeV LHC we carefully take the systematic error into account ⁴.

⁴Note that in a similar study [442], the authors relied on 1% systematic uncertainty which we believe is unre-

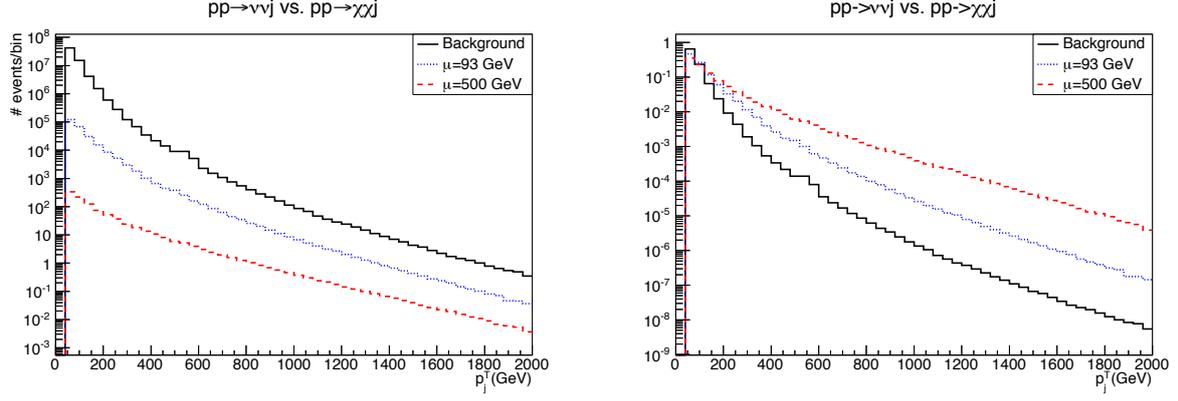


Figure 5: Signal (dotted blue and dashed red) and Zj background (solid black) parton-level p_j^T distributions for the 13 TeV LHC for the DHS scenario. Left: p_j^T distributions for 100 fb^{-1} integrated luminosity. Right: normalised signal and Zj background distributions.

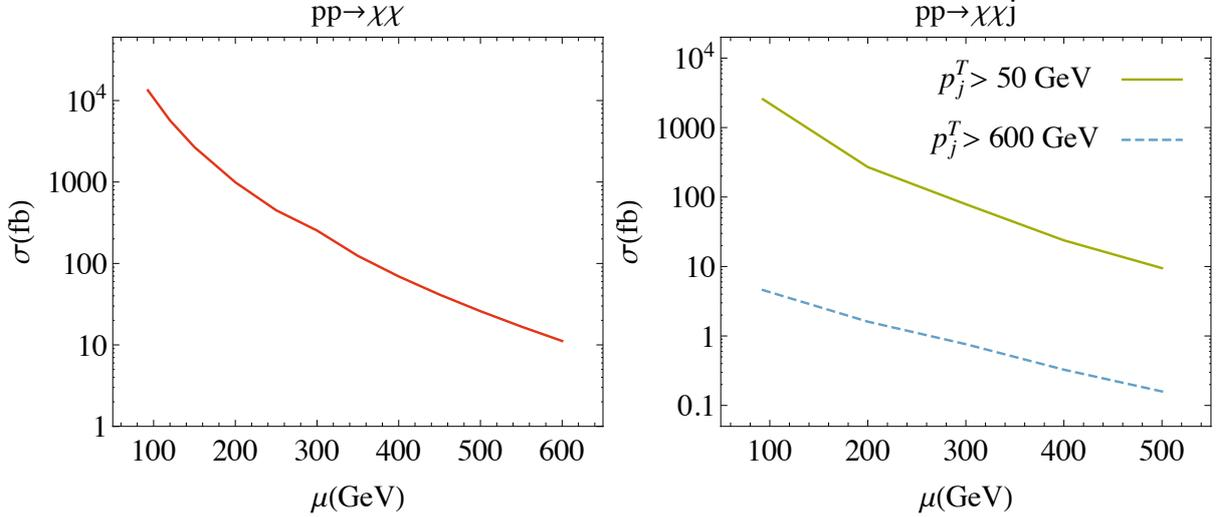


Figure 6: Cross section of the $pp \rightarrow \chi\chi$ (Left) and $pp \rightarrow \chi\chi j$ (Right) processes ($\chi = \chi_{1,2}^0, \chi_1^\pm$) at the 13 TeV LHC for two choices of cuts at parton level on the leading jet p_j^T .

To give the reader an idea on expected signal rates we present the total cross section of the $pp \rightarrow \chi\chi j$ process as a function of μ in Fig. 6 for two different values of p_j^T cut: 50 GeV (green curve) and 600 GeV (blue dashed curve). One can see that a high p_j^T cut such as 600 GeV or even higher would be required, which provides high enough S/B to comply with control over systematic uncertainties.

Besides taking into account crucial aspect of controlling on systematic uncertainties, the steps of going beyond parton-level simulation is essential. By performing a fast simulation, one can take into account multiple ISR effects, realistic detector energy resolution and particle acceptances. In particular, the perfect correlations between p_j^T and \cancel{E}_T which take place at parton level can be considerably spoilt at the level of the fast detector simulation, as we can see from Fig. 7. As we will see below, the lack of the perfect p_j^T vs \cancel{E}_T correlations leads to a visible difference of the S/B ratio and significance, and should be taken into account. Note that

alistic.

in Ref. [443] degenerate higgsinos were studied at parton-level, hence this analysis misses the effects we just mentioned– as the authors already pointed out.

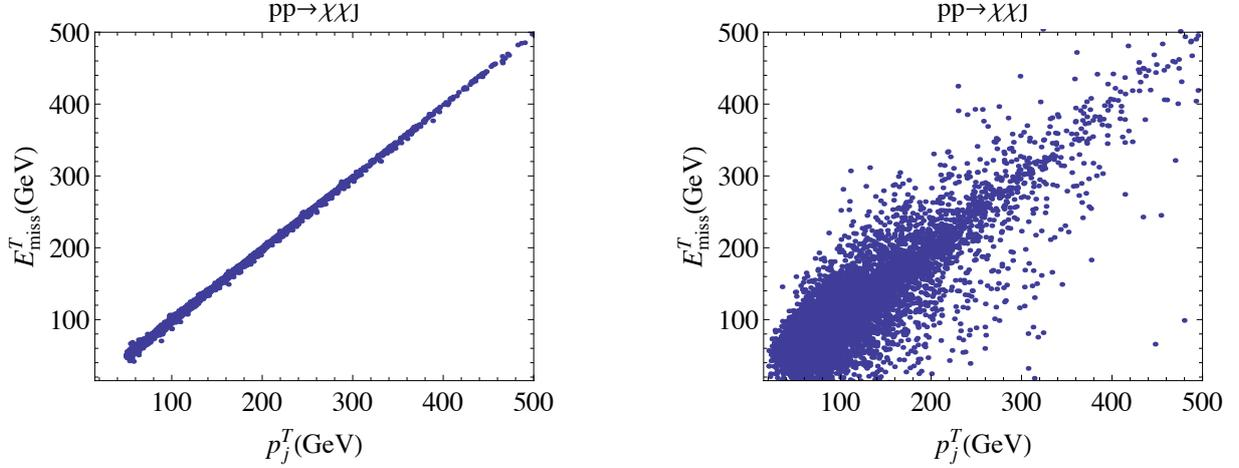


Figure 7: p^T of the leading jet versus \cancel{E}_T for the $pp \rightarrow \chi\chi j$ process ($\chi = \chi_{1,2}^0, \chi_1^\pm$) process in the NSUSY scenario at parton level (left) and detector simulation level (right).

Besides the leading Zj background, we also considered the irreducible $W + jet \rightarrow l\nu + jet$ (Wj) background which mimics the signal when the charged lepton goes below the lepton acceptance cuts. To suppress this background we have applied veto on the charged leptons with the following p^T cuts:

$$p_{e^\pm, \mu^\pm}^T > 10 \text{ GeV} \quad p_{\tau^\pm}^T > 20 \text{ GeV} \quad (13)$$

and standard acceptance pseudorapidity cuts

$$|\eta_{e^\pm, \mu^\pm}| < 2.5. \quad (14)$$

We also checked that the $t\bar{t}$ QCD background is subleading to the electroweak SM background, once final cuts on the p_j^T an \cancel{E}_T bigger than $\simeq 1$ TeV are applied.

	$Z(\nu\bar{\nu})j$	$W(\ell\nu)j$	$\mu = 93 \text{ GeV}$	$\mu = 500 \text{ GeV}$
$p_{jet}^T > 50 \text{ GeV}, \eta_{jet} < 4.5$	6.4 E+7	2.9 E+8	2.6 E+5	948
Veto $p_{e^\pm, \mu^\pm / \tau^\pm}^T > 10/20 \text{ GeV}$	6.2 E+7	1.2 E+8	2.5 E+5	921
$p_j^T > 500 \text{ GeV}$	2.5 E+4	2.0 E+4	1051	32
$p_j^T = \cancel{E}_T > 500 \text{ GeV}$	1.5 E+4	4.1 E+3	747	27
$p_j^T = \cancel{E}_T > 1000 \text{ GeV}$	315 (375)	65 (32)	21 (31)	2 (2)
$p_j^T = \cancel{E}_T > 1500 \text{ GeV}$	18 (20)	2 (1)	1 (2)	0 (0)
$p_j^T = \cancel{E}_T > 2000 \text{ GeV}$	1 (1)	0 (0)	0 (1)	0 (0)

Table 2: Number of events at the 13 TeV LHC with 100 fb^{-1} integrated luminosity for the backgrounds and for the signal, $\mu=93 \text{ GeV}$ and $\mu=500 \text{ GeV}$ after the respective cuts indicated in the left column. Numbers in round brackets correspond to the parton-level predictions. Numbers are rounded to the integer.

In Table 2 we present our results for the cut-flow for signal and background events for a centre-of-mass energy of 13 TeV and an integrated luminosity of 100 fb^{-1} .

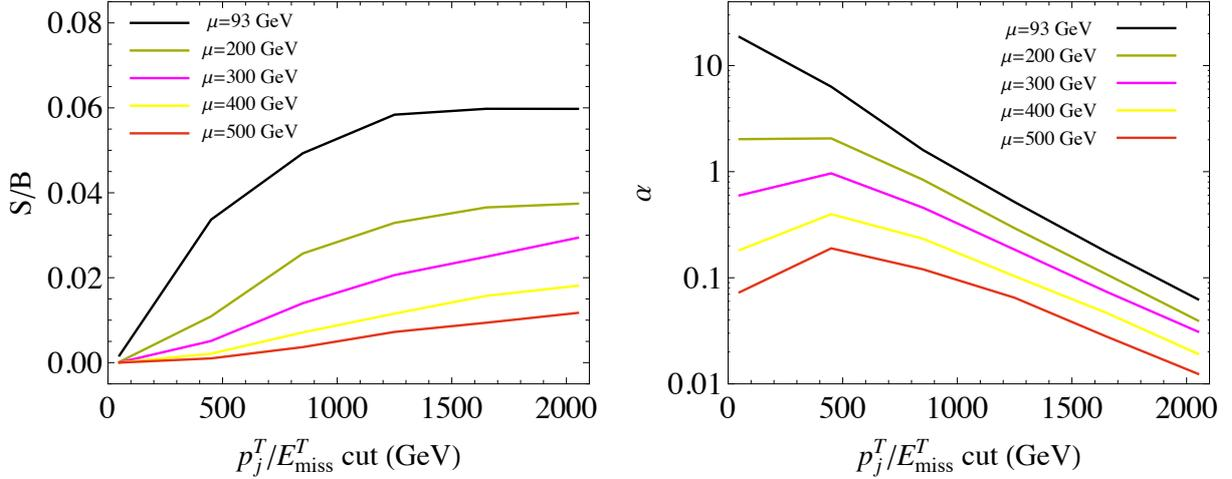


Figure 8: Signal over background ratio (left) and statistical significance (right) for the 13 TeV LHC with 100 fb^{-1} of integrated luminosity as a function of the $p_j^T = \cancel{E}_T$ cut at detector simulation level after the applications of the lepton veto. Colour code in the legend.

The effect of the p_j^T and \cancel{E}_T on the S/B and significance is presented in Fig. 8. The significance α is based only on statistical error and is calculated as

$$\alpha = 2(\sqrt{S+B} - \sqrt{B}) \quad (15)$$

From Fig. 8 one can clearly see the tension between the increase of S/B and decrease of statistical significance as a function of p_j^T . One can also note that S/B ratio is never better than 6%, which demands the respective systematic error to be well under control. In Fig. 9 we present our final results for the 13 TeV LHC sensitivity in Luminosity- $m_{\chi_1^0}$ plane for different S/B assumptions. Under each assumption, for each point in the parameter space, the cut on p_j^T/\cancel{E}_T has been chosen in order to have at least the chosen S/B ratio. Even for optimistic S/B=5% ratio, corresponding to the respective systematic error which is consistent with the recent CMS and ATLAS analyses for LHC8[422, 462], the LSP exclusion is limited to about 120 (130) GeV at 95%CL at 1.5 (3) ab^{-1} (left figure).

If there is a chance for systematics to go below the LHC8 mark the situation would be drastically better. For example, we show the results for S/B=3%, a case where the LHC would be able to probe the NSUSY scenario considerably better: $m_{\chi_1^0} > 200 \text{ GeV}$ would be excluded with 1.5 ab^{-1} integrated luminosity while even for $L=100 \text{ fb}^{-1}$ LHC would be able to exclude $m_{\chi_1^0} > 140 \text{ GeV}$. Unfortunately, control of S/B=1% assumed in previous works is not realistic.

Finally in the right figure we show the prospects of discovering such a scenario. In case of S/B ratio at the 5% level, we could be able to claim a discovery up to 110 GeV LSP with 3 ab^{-1} .

5 Complementarity of the LHC and Dark Matter Direct Detection search experiments

Let us now take a look at the combined sensitivity of the LHC and DDM experiments to the FFP parameter space presented in Fig. 10. One can see that sensitivity of the present DDM

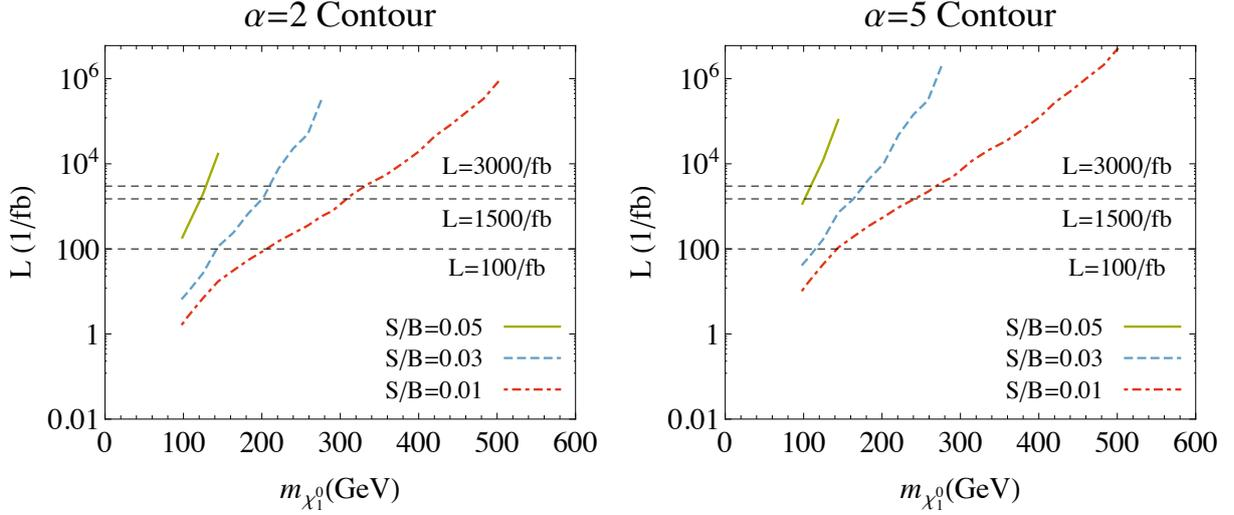


Figure 9: $\alpha=2$ and $\alpha=5$ contour plot in the $m_{\chi_1^0}, L$ plane for the 13 TeV LHC.

experiments such as XENON100 and LUX is clearly not enough to probe FFP parameter space with the naturally low DM relic density. Another point to stress is that cross section of LSP-nuclei scattering grows *faster* with the DM mass than the sensitivity of XENON1T does, which make XENON1T actually able to access the region of FFP parameter space starting from $m_{\tilde{\chi}_0} \gtrsim 320$ GeV. One should again note that in order to ease comparison with the DDM search experiment bounds, the cross-section calculated should be rescaled with the respective R_Ω factor as in section 3 to take into account the lower DM relic density in our scenario. At the same

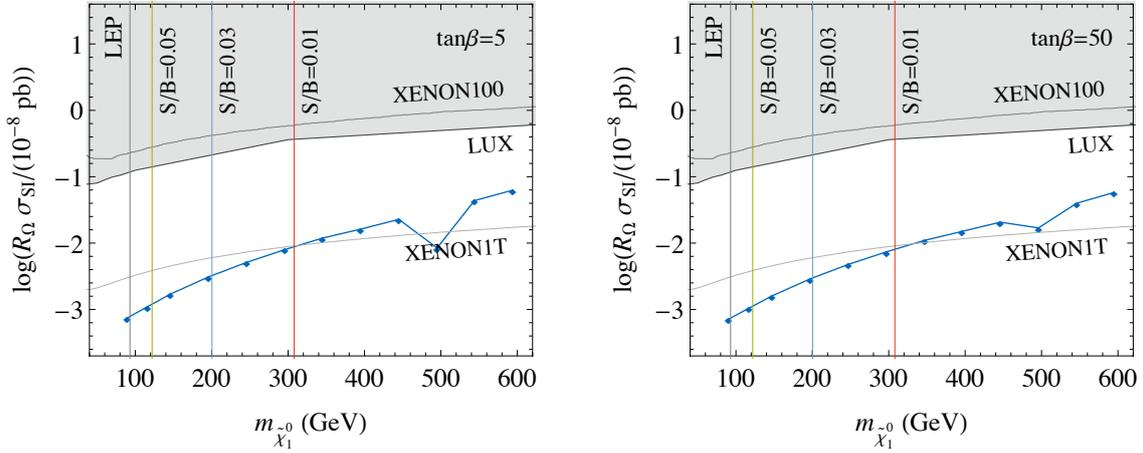


Figure 10: Current (XENON100, LUX) and future (XENON1T) cross section limits on SI DDM scattering off the nuclei as a function of the $m_{\chi_1^0}$. The cross-section is rescaled with $R_\Omega = \Omega_{\text{DM}}/\Omega_{\text{DM}}^{\text{Planck}}$ factor discussed in the text. Vertical lines represent the projected sensitivity of LHC13TeV to the FFP parameter space, for different assumptions on the control of the systematic error (S/B).

time, collider sensitivity is eventually independent of R_Ω . One can see that the LHC reach in probing the FFP parameter space via monojet signature from production of higgsinos is highly complementary to DDM search experiments. The vertical lines presents LHC reach for 1.5 ab^{-1} integrated luminosity and different assumptions on the systematic error (S/B). One can see that

for S/B control at 5% level, $m_{\tilde{\chi}_0}$ up to 120 GeV is covered, while making the very optimistic assumption that S/B \simeq 3%, the sensitivity of the LHC could extend up to $m_{\tilde{\chi}_0} \simeq$ 200 GeV. Just for reference, in order to check against results of previous studies, we present S/B=1% case (which is not realistic) for which LHC would cover FFP parameter space up to $m_{\tilde{\chi}_0} \simeq$ 300 GeV. One should note that LHC sensitivity to FFP region can be inferred from ATLAS[463] and CMS[464] results on monojet searches which can be translated into limits on the effective $q\bar{q}\tilde{\chi}_0\tilde{\chi}_0$ operators and then compared with the spin-dependent(SD) and spin-independent(SI) limits from DDM search experiments. The best current limit from DDM search experiments is the SI one from LUX experiment which is slightly better than the XENON100 one. It turns out that even rescaled XENON100 limit on the SI scattering of the neutralino off the nuclei is more than two orders of magnitude better than the analogous limits from ATLAS and CMS searches mentioned above.

6 Conclusions

In this study we explore the LHC13TeV sensitivity to the focus point region of the MSSM parameter space which is characterised by low values of μ parameter, a necessary condition for natural SUSY with low fine-tuning. In the case of the M_1 and M_2 parameters being large, three MSSM particles, namely χ_1^0 , χ_2^0 and χ_1^\pm become quasi-degenerate and acquire a significant higgsino component. This scenario also provides a naturally low dark matter relic density via gaugino annihilation and co-annihilation processes into Standard Model gauge and Higgs bosons. In the case where coloured SUSY particles are heavy and out-of-reach of the LHC, as in the FFP region, the only way to probe SUSY is via monojet signature.

We present here the first realistic results on the LHC13TeV projections to probe FFP parameter space taking into account a) realistic systematic errors and b) fast detector simulation. Both components are crucial in order to estimate the correct LHC sensitivity to FFP. It turns out that for a very optimistic estimate of the control on S/B at the 3% level, the LHC will be able to exclude (at 95%CL) FFP parameter space with neutralino masses below 140 GeV with with 100 fb^{-1} and below 200 GeV with 1.5 ab^{-1} integrated luminosity. The LHC sensitivity depends drastically on the systematic uncertainty level: for a 5% S/B ratio the limits drop down to $m_{\tilde{\chi}_1^0} = 120 \text{ GeV}$ (compared to 200 GeV at S/B=3%) with 1.5 ab^{-1} integrated luminosity.

We have found that while the LHC is sensitive to the low end of $\tilde{\chi}_1^0$ mass range, the DDM search experiments, especially the future XENON1T, become sensitive to the upper end of FFP $\tilde{\chi}_1^0$ mass range, starting from about 320 GeV. This high degree of complementarity of the LHC and DDM search experiments is crucial for pinning down the whole range of FFP parameter space. One should note that coverage of the mass gap between 200 GeV and 320 GeV is problematic even for the combination of the LHC13TeV and XENON1T experiment and requires further attention.

Acknowledgments

The authors acknowledge the use of the IRIDIS High Performance Computing Facility, and associated support services at the University of Southampton, in the completion of this work. DB and AB are financed in part through the NEXt Institute. WP acknowledges partial support from German Ministry of Education and Research (BMBF) under contract no. 05H12WWE.

Bibliography

- [1] A. Djouadi, J. Kalinowski, and M. Spira, *Comput.Phys.Commun.* **108** (1998) 56–74, [[hep-ph/9704448](#)]. 9, 13
- [2] A. Djouadi, M. Muhlleitner, and M. Spira, *Acta Phys.Polon.* **B38** (2007) 635–644, [[hep-ph/0609292](#)]. 9, 13
- [3] M. Spira, *Fortsch.Phys.* **46** (1998) 203–284, [[hep-ph/9705337](#)]. 9
- [4] A. Djouadi, *Phys.Rept.* **457** (2008) 1–216, [[hep-ph/0503172](#)]. 9, 37
- [5] A. Djouadi, *Phys.Rept.* **459** (2008) 1–241, [[hep-ph/0503173](#)]. 9, 37, 50
- [6] A. Djouadi, M. Spira, and P. M. Zerwas, *Z. Phys.* **C70** (1996) 427–434, [[hep-ph/9511344](#)]. 9
- [7] A. Djouadi, J. Kalinowski, and P. M. Zerwas, *Z. Phys.* **C70** (1996) 435–448, [[hep-ph/9511342](#)]. 9
- [8] M. S. Carena, M. Quiros, and C. E. M. Wagner, *Nucl. Phys.* **B461** (1996) 407–436, [[hep-ph/9508343](#)]. 9
- [9] H. E. Haber, R. Hempfling, and A. H. Hoang, *Z. Phys.* **C75** (1997) 539–554, [[hep-ph/9609331](#)]. 9
- [10] M. S. Carena *et. al.*, *Nucl. Phys.* **B580** (2000) 29–57, [[hep-ph/0001002](#)]. 9
- [11] G. Degrassi, S. Heinemeyer, W. Hollik, P. Slavich, and G. Weiglein, *Eur. Phys. J.* **C28** (2003) 133–143, [[hep-ph/0212020](#)]. 9
- [12] A. Djouadi, J. Kalinowski, and P. M. Zerwas, *Z. Phys.* **C57** (1993) 569–584. 9
- [13] A. Djouadi, P. Janot, J. Kalinowski, and P. M. Zerwas, *Phys. Lett.* **B376** (1996) 220–226, [[hep-ph/9603368](#)]. 9
- [14] A. Djouadi, J. Kalinowski, P. Ohmann, and P. M. Zerwas, *Z. Phys.* **C74** (1997) 93–111, [[hep-ph/9605339](#)]. 9
- [15] J. Butterworth, F. Maltoni, F. Moortgat, P. Richardson, S. Schumann, *et. al.*, [arXiv:1003.1643](#). 10
- [16] M. Spira, A. Djouadi, D. Graudenz, and P. Zerwas, *Nucl.Phys.* **B453** (1995) 17–82, [[hep-ph/9504378](#)]. 10, 11, 12, 15
- [17] R. Hempfling, *Phys.Rev.* **D49** (1994) 6168–6172. 10, 20
- [18] L. J. Hall, R. Rattazzi, and U. Sarid, *Phys.Rev.* **D50** (1994) 7048–7065, [[hep-ph/9306309](#)]. 10, 20
- [19] M. S. Carena, M. Olechowski, S. Pokorski, and C. Wagner, *Nucl.Phys.* **B426** (1994) 269–300, [[hep-ph/9402253](#)]. 10, 20
- [20] D. M. Pierce, J. A. Bagger, K. T. Matchev, and R.-j. Zhang, *Nucl.Phys.* **B491** (1997) 3–67, [[hep-ph/9606211](#)]. 10, 20
- [21] M. S. Carena, S. Mrenna, and C. Wagner, *Phys.Rev.* **D60** (1999) 075010, [[hep-ph/9808312](#)]. 10, 20
- [22] A. Czarnecki and K. Melnikov, *Nucl.Phys.* **B544** (1999) 520–531, [[hep-ph/9806244](#)]. 10
- [23] K. Chetyrkin, R. Harlander, T. Seidensticker, and M. Steinhauser, *Phys.Rev.* **D60** (1999) 114015, [[hep-ph/9906273](#)]. 10
- [24] I. R. Blokland, A. Czarnecki, M. Slusarczyk, and F. Tkachov, *Phys.Rev.Lett.* **93** (2004) 062001, [[hep-ph/0403221](#)]. 10

- [25] I. R. Blokland, A. Czarnecki, M. Slusarczyk, and F. Tkachov, *Phys.Rev.* **D71** (2005) 054004, [[hep-ph/0503039](#)]. 10
- [26] A. Czarnecki, J. G. Korner, and J. H. Piclum, *Phys.Rev.* **D81** (2010) 111503, [[1005.2625](#)]. 10
- [27] J. Gao, C. S. Li, and H. X. Zhu, *Phys.Rev.Lett.* **110** (2013) 042001, [[1210.2808](#)]. 10
- [28] M. Brucherseifer, F. Caola, and K. Melnikov, *JHEP* **1304** (2013) 059, [[1301.7133](#)]. 10
- [29] R. Harlander, M. Muhlleitner, J. Rathsman, M. Spira, and O. Stal, [1312.5571](#). 10
- [30] R. Contino, M. Ghezzi, C. Grojean, M. Muhlleitner, and M. Spira, *JHEP* **1307** (2013) 035, [[1303.3876](#)]. 11, 13, 16, 83
- [31] U. Aglietti, R. Bonciani, G. Degrassi, and A. Vicini, *Phys.Lett.* **B595** (2004) 432–441, [[hep-ph/0404071](#)]. 11
- [32] U. Aglietti, R. Bonciani, G. Degrassi, and A. Vicini, *Phys.Lett.* **B600** (2004) 57–64, [[hep-ph/0407162](#)]. 11
- [33] G. Degrassi and F. Maltoni, *Phys.Lett.* **B600** (2004) 255–260, [[hep-ph/0407249](#)]. 11
- [34] S. Actis, G. Passarino, C. Sturm, and S. Uccirati, *Phys. Lett.* **B670** (2008) 12–17, [[arXiv:0809.1301](#)]. 11
- [35] S. Actis, G. Passarino, C. Sturm, and S. Uccirati, *Nucl. Phys.* **B811** (2009) 182–273, [[arXiv:0809.3667](#)]. 11
- [36] T. Inami, T. Kubota, and Y. Okada, *Z.Phys.* **C18** (1983) 69. 11, 15
- [37] A. Djouadi, M. Spira, and P. Zerwas, *Phys.Lett.* **B264** (1991) 440–446. 11, 15
- [38] K. Chetyrkin, B. A. Kniehl, and M. Steinhauser, *Phys.Rev.Lett.* **79** (1997) 353–356, [[hep-ph/9705240](#)]. 11, 15
- [39] K. Chetyrkin, B. A. Kniehl, and M. Steinhauser, *Nucl.Phys.* **B510** (1998) 61–87, [[hep-ph/9708255](#)]. 11, 15
- [40] M. Kramer, E. Laenen, and M. Spira, *Nucl.Phys.* **B511** (1998) 523–549, [[hep-ph/9611272](#)]. 11, 15
- [41] Y. Schroder and M. Steinhauser, *JHEP* **0601** (2006) 051, [[hep-ph/0512058](#)]. 11, 15
- [42] K. Chetyrkin, J. H. Kuhn, and C. Sturm, *Nucl.Phys.* **B744** (2006) 121–135, [[hep-ph/0512060](#)]. 11, 15
- [43] P. Baikov and K. Chetyrkin, *Phys.Rev.Lett.* **97** (2006) 061803, [[hep-ph/0604194](#)]. 11, 15
- [44] ATLAS Collaboration, *Phys.Lett.* **B716** (2012) 1–29, [[1207.7214](#)]. 13, 18, 25, 30, 39, 48, 55, 59
- [45] CMS Collaboration, *Phys.Lett.* **B716** (2012) 30–61, [[1207.7235](#)]. 13, 18, 25, 30, 39, 48, 55, 59
- [46] R. Contino, M. Ghezzi, C. Grojean, M. Muhlleitner, and M. Spira, *to appear*. 13
- [47] G. Giudice, C. Grojean, A. Pomarol, and R. Rattazzi, *JHEP* **0706** (2007) 045, [[hep-ph/0703164](#)]. 13, 41, 68, 73, 83
- [48] J. R. Ellis, M. K. Gaillard, and D. V. Nanopoulos, *Nucl.Phys.* **B106** (1976) 292. 15
- [49] M. A. Shifman, A. Vainshtein, M. Voloshin, and V. I. Zakharov, *Sov.J.Nucl.Phys.* **30** (1979) 711–716. 15
- [50] B. A. Kniehl and M. Spira, *Z.Phys.* **C69** (1995) 77–88, [[hep-ph/9505225](#)]. 15
- [51] CMS Collaboration Collaboration, [1307.7135](#). 15

- [52] **ATLAS Collaboration** Collaboration, [1307.7292](#). **15**
- [53] S. Dawson, A. Gritsan, H. Logan, J. Qian, C. Tully, *et. al.*, [1310.8361](#). **15**
- [54] H. Baer, T. Barklow, K. Fujii, Y. Gao, A. Hoang, *et. al.*, [1306.6352](#). **16**
- [55] M. Bicer *et. al.*, **TLEP Design Study Working Group** Collaboration, *JHEP* **1401** (2014) 164, [[1308.6176](#)]. **16**
- [56] H. E. Haber and G. L. Kane, *Nucl.Phys.* **B250** (1985) 716. **16**
- [57] M. Muhlleitner and M. Spira, *Nucl.Phys.* **B790** (2008) 1–27, [[hep-ph/0612254](#)]. **16**
- [58] J. Baglio, T. Dao, R. Grober, M. Muhlleitner, H. Rzehak, *et. al.*, *EPJ Web Conf.* **49** (2013) 12001. **18**
- [59] J. Baglio, R. Grober, M. Muhlleitner, D. Nhung, H. Rzehak, *et. al.*, [1312.4788](#). **18, 19, 20**
- [60] P. Fayet, *Nucl.Phys.* **B90** (1975) 104–124. **18**
- [61] R. Barbieri, S. Ferrara, and C. A. Savoy, *Phys.Lett.* **B119** (1982) 343. **18**
- [62] M. Dine, W. Fischler, and M. Srednicki, *Phys.Lett.* **B104** (1981) 199. **18**
- [63] H. P. Nilles, M. Srednicki, and D. Wyler, *Phys.Lett.* **B120** (1983) 346. **18**
- [64] J. Frere, D. Jones, and S. Raby, *Nucl.Phys.* **B222** (1983) 11. **18**
- [65] J. Derendinger and C. A. Savoy, *Nucl.Phys.* **B237** (1984) 307. **18**
- [66] J. R. Ellis, J. Gunion, H. E. Haber, L. Roszkowski, and F. Zwirner, *Phys.Rev.* **D39** (1989) 844. **18**
- [67] M. Drees, *Int.J.Mod.Phys.* **A4** (1989) 3635. **18**
- [68] U. Ellwanger, M. Rausch de Traubenberg, and C. A. Savoy, *Phys.Lett.* **B315** (1993) 331–337, [[hep-ph/9307322](#)]. **18**
- [69] U. Ellwanger, M. Rausch de Traubenberg, and C. A. Savoy, *Z.Phys.* **C67** (1995) 665–670, [[hep-ph/9502206](#)]. **18**
- [70] U. Ellwanger, M. Rausch de Traubenberg, and C. A. Savoy, *Nucl.Phys.* **B492** (1997) 21–50, [[hep-ph/9611251](#)]. **18**
- [71] T. Elliott, S. King, and P. White, *Phys.Lett.* **B351** (1995) 213–219, [[hep-ph/9406303](#)]. **18**
- [72] S. King and P. White, *Phys.Rev.* **D52** (1995) 4183–4216, [[hep-ph/9505326](#)]. **18**
- [73] F. Franke and H. Fraas, *Int.J.Mod.Phys.* **A12** (1997) 479–534, [[hep-ph/9512366](#)]. **18**
- [74] M. Maniatis, *Int.J.Mod.Phys.* **A25** (2010) 3505–3602, [[0906.0777](#)]. **18**
- [75] U. Ellwanger, C. Hugonie, and A. M. Teixeira, *Phys.Rept.* **496** (2010) 1–77, [[0910.1785](#)]. **18**
- [76] R. Peccei and H. R. Quinn, *Phys.Rev.Lett.* **38** (1977) 1440–1443. **18**
- [77] R. Peccei and H. R. Quinn, *Phys.Rev.* **D16** (1977) 1791–1797. **18**
- [78] P. Z. Skands, B. Allanach, H. Baer, C. Balazs, G. Belanger, *et. al.*, *JHEP* **0407** (2004) 036, [[hep-ph/0311123](#)]. **19, 116**
- [79] B. Allanach, C. Balazs, G. Belanger, M. Bernhardt, F. Boudjema, *et. al.*, *Comput.Phys.Commun.* **180** (2009) 8–25, [[0801.0045](#)]. **19, 116**
- [80] K. Ender, T. Graf, M. Muhlleitner, and H. Rzehak, *Phys.Rev.* **D85** (2012) 075024, [[1111.4952](#)]. **19**
- [81] T. Graf, R. Grober, M. Muhlleitner, H. Rzehak, and K. Walz, *JHEP* **1210** (2012) 122, [[1206.6806](#)]. **19**

- [82] D. T. Nhung, M. Muhlleitner, J. Streicher, and K. Walz, *JHEP* **1311** (2013) 181, [[1306.3926](#)]. 19
- [83] M. S. Carena, D. Garcia, U. Nierste, and C. E. Wagner, *Nucl.Phys.* **B577** (2000) 88–120, [[hep-ph/9912516](#)]. 20
- [84] M. S. Carena, J. R. Ellis, S. Mrenna, A. Pilaftsis, and C. Wagner, *Nucl.Phys.* **B659** (2003) 145–178, [[hep-ph/0211467](#)]. 20
- [85] J. Guasch, P. Haffiger, and M. Spira, *Phys.Rev.* **D68** (2003) 115001, [[hep-ph/0305101](#)]. 20
- [86] D. Noth and M. Spira, *Phys.Rev.Lett.* **101** (2008) 181801, [[0808.0087](#)]. 20
- [87] D. Noth and M. Spira, *JHEP* **1106** (2011) 084, [[1001.1935](#)]. 20
- [88] L. Mihaila and C. Reisser, *JHEP* **1008** (2010) 021, [[1007.0693](#)]. 20
- [89] ATLAS Collaboration, Tech. Rep. ATLAS-CONF-2013-014, CERN, Geneva, Mar, 2013. 26, 155
- [90] ATLAS Collaboration, Tech. Rep. ATLAS-CONF-2013-034, CERN, Geneva, Mar, 2013. 26, 30, 48, 49, 50
- [91] CMS Collaboration, Tech. Rep. CMS-PAS-HIG-12-045, CERN, Geneva, 2012. 26
- [92] G. Moreau, *Phys.Rev.* **D87** (2013) 015027, [[1210.3977](#)]. 26
- [93] A. Djouadi and G. Moreau, [1303.6591](#). 26, 34, 35, 49
- [94] B. Dumont, S. Fichet, and G. von Gersdorff, *JHEP* **1307** (2013) 065, [[1304.3369](#)]. 26, 28, 34, 83, 84
- [95] G. Cohan, S. Fichet, and G. Moreau, *in preparation*. 27, 29
- [96] K. Nakamura *et al.*, **Particle Data Group**, *J.Phys.* **G37** (2010) 075021. 27
- [97] CMS Collaboration, Tech. Rep. CMS-PAS-HIG-13-005, CERN, Geneva, 2013. 30, 31, 32, 48
- [98] G. Belanger, B. Dumont, U. Ellwanger, J. Gunion, and S. Kraml, *Phys.Rev.* **D88** (2013) 075008, [[1306.2941](#)]. 30, 31
- [99] F. Boudjema, G. Cacciapaglia, K. Cranmer, G. Dissertori, A. Deandrea, *et. al.*, [1307.5865](#). 31
- [100] K. Arnold, J. Bellm, G. Bozzi, M. Brieg, F. Campanario, *et. al.*, [1107.4038](#). 31
- [101] ATLAS Collaboration, *Phys.Lett.* **B726** (2013) 88–119, [[1307.1427](#)]. 31, 32
- [102] M. Farina, C. Grojean, and E. Salvioni, *JHEP* **1207** (2012) 012, [[1205.0011](#)]. 34
- [103] R. Godbole, S. Kraml, M. Krawczyk, D. Miller, P. Niezurawski, *et. al.*, [hep-ph/0404024](#). 34
- [104] E. Accomando *et. al.*, [hep-ph/0608079](#). 34
- [105] B. Grzadkowski, J. F. Gunion, and J. Kalinowski, *Phys.Rev.* **D60** (1999) 075011, [[hep-ph/9902308](#)]. 38
- [106] B. Grzadkowski, J. Gunion, and J. Kalinowski, *Phys.Lett.* **B480** (2000) 287–295, [[hep-ph/0001093](#)]. 38
- [107] K. Cheung, J. S. Lee, and P.-Y. Tseng, *JHEP* **1401** (2014) 085, [[1310.3937](#)]. 38
- [108] J. Bernon and B. Dumont, *in preparation*. 38
- [109] ATLAS Collaboration, *HepData* <http://doi.org/10.7484/INSPIREHEP.DATA.A78C.HK44>. 38
- [110] ATLAS Collaboration, *HepData*

- <http://doi.org/10.7484/INSPIREHEP.DATA.RF5P.6M3K>. 38
- [111] ATLAS Collaboration, *HepData*
<http://doi.org/10.7484/INSPIREHEP.DATA.26B4.TY5F>. 38
- [112] S. Dawson, *Nucl.Phys.* **B249** (1985) 42–60. 39
- [113] M. S. Chanowitz and M. K. Gaillard, *Nucl.Phys.* **B261** (1985) 379. 39
- [114] P. Borel, R. Franceschini, R. Rattazzi, and A. Wulzer, *JHEP* **1206** (2012) 122, [[1202.1904](#)]. 39
- [115] J. M. Cornwall, D. N. Levin, and G. Tiktopoulos, *Phys.Rev.* **D10** (1974) 1145. 39
- [116] J. Bagger, V. D. Barger, K.-m. Cheung, J. F. Gunion, T. Han, *et. al.*, *Phys.Rev.* **D49** (1994) 1246–1264, [[hep-ph/9306256](#)]. 39
- [117] J. Bagger, V. D. Barger, K.-m. Cheung, J. F. Gunion, T. Han, *et. al.*, *Phys.Rev.* **D52** (1995) 3878–3889, [[hep-ph/9504426](#)]. 39
- [118] J. Butterworth, B. Cox, and J. R. Forshaw, *Phys.Rev.* **D65** (2002) 096014, [[hep-ph/0201098](#)]. 39
- [119] A. Belyaev, O. J. Eboli, M. Gonzalez-Garcia, J. Mizukoshi, S. Novaes, *et. al.*, *Phys.Rev.* **D59** (1999) 015022, [[hep-ph/9805229](#)]. 39
- [120] A. Ballestrero, G. Bevilacqua, and E. Maina, *JHEP* **0905** (2009) 015, [[0812.5084](#)]. 39
- [121] T. Han, D. Krohn, L.-T. Wang, and W. Zhu, *JHEP* **1003** (2010) 082, [[0911.3656](#)]. 40
- [122] K. Doroba, J. Kalinowski, J. Kuczmarski, S. Pokorski, J. Rosiek, *et. al.*, *Phys.Rev.* **D86** (2012) 036011, [[1201.2768](#)]. 40
- [123] Y. Cui and Z. Han, [1304.4599](#). 40
- [124] A. Freitas and J. Gainer, *Phys.Rev.* **D88** (2013) 017302, [[1212.3598](#)]. 40
- [125] J. Chang, K. Cheung, C.-T. Lu, and T.-C. Yuan, *Phys.Rev.* **D87** (2013) 093005, [[1303.6335](#)]. 40
- [126] J. Alwall, M. Herquet, F. Maltoni, O. Mattelaer, and T. Stelzer, *JHEP* **1106** (2011) 128, [[1106.0522](#)]. 43, 61, 70, 89, 91, 94, 96, 106, 118, 125, 130, 136, 169, 178
- [127] H.-J. He *et. al.*, *Phys. Rev.* **D78** (2008) 031701, [[0708.2588](#)]. 43
- [128] R. Brun and F. Rademakers, *Nucl.Instrum.Meth.* **A389** (1997) 81–86. 45
- [129] J. Brod, U. Haisch, and J. Zupan, *JHEP* **1311** (2013) 180, [[1310.1385](#)]. 49
- [130] K. Cheung, J. S. Lee, and P.-Y. Tseng, *JHEP* **1305** (2013) 134, [[1302.3794](#)]. 49
- [131] CMS Collaboration, Tech. Rep. CMS-PAS-HIG-12-020, CERN, Geneva, 2012. 49
- [132] ATLAS Collaboration, Tech. Rep. ATLAS-CONF-2013-012, CERN, Geneva, Mar, 2013. 50
- [133] CMS Collaboration, Tech. Rep. CMS-PAS-HIG-13-001, CERN, Geneva, 2013. 50
- [134] CMS Collaboration, Tech. Rep. CMS-PAS-HIG-13-002, CERN, Geneva, 2013. 50, 155
- [135] CMS Collaboration, Tech. Rep. CMS-PAS-HIG-13-003, CERN, Geneva, 2013. 50
- [136] CMS Collaboration, Tech. Rep. CMS-PAS-HIG-13-004, CERN, Geneva, 2013. 50
- [137] CMS Collaboration, Tech. Rep. CMS-PAS-HIG-13-020, CERN, Geneva, 2013. 50
- [138] CMS Collaboration, Tech. Rep. CMS-PAS-HIG-13-015, CERN, Geneva, 2013. 50
- [139] CMS Collaboration, Tech. Rep. CMS-PAS-HIG-12-025, CERN, Geneva, 2012. 50
- [140] CMS Collaboration, Tech. Rep. CMS-PAS-HIG-13-019, CERN, Geneva, 2013. 50
- [141] ATLAS Collaboration, Tech. Rep. ATLAS-CONF-2013-080, CERN, Geneva, Jul,

2013. [50](#)
- [142] R. Godbole, C. Hangst, M. Muhlleitner, S. Rindani, and P. Sharma, *Eur.Phys.J.* **C71** (2011) 1681, [[1103.5404](#)]. [52](#)
- [143] R. Godbole, P. Bhupal Dev, A. Djouadi, M. Muhlleitner, and S. Rindani, *eConf C0705302* (2007) TOP08, [[0710.2669](#)]. [52](#)
- [144] P. Bhupal Dev, A. Djouadi, R. Godbole, M. Muhlleitner, and S. Rindani, *Phys.Rev.Lett.* **100** (2008) 051801, [[0707.2878](#)]. [52](#)
- [145] S. Heinemeyer *et al.*, **LHC Higgs Cross Section Working Group**, [1307.1347](#). [53](#), [70](#)
- [146] D. B. Kaplan and H. Georgi, *Phys.Lett.* **B136** (1984) 183. [55](#), [68](#), [135](#)
- [147] D. B. Kaplan, H. Georgi, and S. Dimopoulos, *Phys.Lett.* **B136** (1984) 187. [55](#)
- [148] S. Dimopoulos and J. Preskill, *Nucl.Phys.* **B199** (1982) 206. [55](#)
- [149] H. Georgi, D. B. Kaplan, and P. Galison, *Phys.Lett.* **B143** (1984) 152. [55](#)
- [150] H. Georgi and D. B. Kaplan, *Phys.Lett.* **B145** (1984) 216. [55](#)
- [151] M. J. Dugan, H. Georgi, and D. B. Kaplan, *Nucl.Phys.* **B254** (1985) 299. [55](#)
- [152] B. Bellazzini, C. Csaki, and J. Serra, [1401.2457](#). [56](#)
- [153] K. Agashe, R. Contino, and A. Pomarol, *Nucl.Phys.* **B719** (2005) 165–187, [[hep-ph/0412089](#)]. [56](#), [98](#), [135](#)
- [154] J. Baglio, A. Djouadi, R. Grober, M. Muhlleitner, J. Quevillon, *et. al.*, *JHEP* **1304** (2013) 151, [[1212.5581](#)]. [57](#), [68](#)
- [155] A. J. Barr, M. J. Dolan, C. Englert, and M. Spannowsky, *Phys.Lett.* **B728** (2014) 308–313, [[1309.6318](#)]. [56](#), [57](#), [68](#)
- [156] P. Lodone, *JHEP* **0812** (2008) 029, [[0806.1472](#)]. [56](#)
- [157] M. Gillioz, *Phys.Rev.* **D80** (2009) 055003, [[0806.3450](#)]. [56](#)
- [158] C. Anastasiou, E. Furlan, and J. Santiago, *Phys.Rev.* **D79** (2009) 075003, [[0901.2117](#)]. [56](#), [87](#)
- [159] M. Gillioz, R. Grober, A. Kapuvari, and M. Muhlleitner, [1311.4453](#). [56](#)
- [160] E. N. Glover and J. van der Bij, *Nucl.Phys.* **B309** (1988) 282. [56](#)
- [161] M. J. Dolan, C. Englert, and M. Spannowsky, *JHEP* **1210** (2012) 112, [[1206.5001](#)]. [57](#), [68](#)
- [162] M. Bahr, S. Gieseke, M. Gigg, D. Grellscheid, K. Hamilton, *et. al.*, *Eur.Phys.J.* **C58** (2008) 639–707, [[0803.0883](#)]. [57](#), [106](#)
- [163] R. Grober and M. Muhlleitner, *JHEP* **1106** (2011) 020, [[1012.1562](#)]. [57](#)
- [164] R. Frederix, S. Frixione, V. Hirschi, F. Maltoni, O. Mattelaer, *et. al.*, [1401.7340](#). [57](#), [69](#)
- [165] D. de Florian and J. Mazzitelli, *Phys. Rev. Lett.* **111**, **201801** (2013) 201801, [[1309.6594](#)]. [57](#), [68](#)
- [166] J. Grigo, J. Hoff, K. Melnikov, and M. Steinhauser, *Nucl.Phys.* **B875** (2013) 1–17, [[1305.7340](#)]. [57](#)
- [167] S. Dawson, A. Djouadi, and M. Spira, *Phys.Rev.Lett.* **77** (1996) 16–19, [[hep-ph/9603423](#)]. [57](#)
- [168] S. Dawson, E. Furlan, and I. Lewis, *Phys.Rev.* **D87** (2013) 014007, [[1210.6663](#)]. [57](#)
- [169] **ATLAS** Collaboration, Tech. Rep. ATL-PHYS-PUB-2013-004, CERN, Geneva, Mar, 2013. [57](#)
- [170] M. Cacciari, G. P. Salam, and G. Soyez, *Eur.Phys.J.* **C72** (2012) 1896, [[1111.6097](#)].

- 57, 63, 96, 107
- [171] M. Cacciari, G. P. Salam, and G. Soyez, *JHEP* **0804** (2008) 063, [[0802.1189](#)]. 57, 107
 - [172] R. Contino, L. Da Rold, and A. Pomarol, *Phys.Rev.* **D75** (2007) 055014, [[hep-ph/0612048](#)]. 58, 87
 - [173] M. Gillioz, R. Grober, C. Grojean, M. Muhlleitner, and E. Salvioni, *JHEP* **1210** (2012) 004, [[1206.7120](#)]. 58, 59
 - [174] M. J. Dolan, C. Englert, and M. Spannowsky, *Phys.Rev.* **D87** (2013), no. 5 055002, [[1210.8166](#)]. 58
 - [175] CMS Collaboration, *JHEP* **1306** (2013) 081, [[1303.4571](#)]. 59
 - [176] T. Plehn, M. Spira, and P. Zerwas, *Nucl.Phys.* **B479** (1996) 46–64, [[hep-ph/9603205](#)]. 59
 - [177] A. Djouadi, W. Kilian, M. Muhlleitner, and P. Zerwas, *Eur.Phys.J.* **C10** (1999) 45–49, [[hep-ph/9904287](#)]. 59, 60
 - [178] C. O. Dib, R. Rosenfeld, and A. Zerwekh, *JHEP* **0605** (2006) 074, [[hep-ph/0509179](#)]. 59
 - [179] R. Contino, C. Grojean, M. Moretti, F. Piccinini, and R. Rattazzi, *JHEP* **1005** (2010) 089, [[1002.1011](#)]. 59, 68, 69, 70, 72, 75, 77
 - [180] U. Ellwanger, *JHEP* **1308** (2013) 077, [[1306.5541](#)]. 60
 - [181] M. Moretti, S. Moretti, F. Piccinini, R. Pittau, and J. Rathsman, *JHEP* **0712** (2007) 075, [[0706.4117](#)]. 60
 - [182] L. Randall and R. Sundrum, *Phys.Rev.Lett.* **83** (1999) 4690–4693, [[hep-th/9906064](#)]. 60
 - [183] L. Randall and R. Sundrum, *Phys.Rev.Lett.* **83** (1999) 3370–3373, [[hep-ph/9905221](#)]. 60
 - [184] M. Gouzevitch, A. Oliveira, J. Rojo, R. Rosenfeld, G. P. Salam, *et. al.*, *JHEP* **1307** (2013) 148, [[1303.6636](#)]. 60, 63, 64, 68, 72
 - [185] H. M. Lee, M. Park, and V. Sanz, *Eur.Phys.J.* **C74** (2014) 2715, [[1306.4107](#)]. 60, 61
 - [186] K. Agashe, H. Davoudiasl, G. Perez, and A. Soni, *Phys.Rev.* **D76** (2007) 036006, [[hep-ph/0701186](#)]. 60
 - [187] A. L. Fitzpatrick, J. Kaplan, L. Randall, and L.-T. Wang, *JHEP* **0709** (2007) 013, [[hep-ph/0701150](#)]. 60
 - [188] P. Aquino, <http://feynrules.irmp.ucl.ac.be/wiki/RSmodel> . 61
 - [189] A. Belyaev, N. D. Christensen, and A. Pukhov, *Comput.Phys.Commun.* **184** (2013) 1729–1769, [[1207.6082](#)]. 61, 96, 130, 169, 178
 - [190] G. F. Giudice, R. Rattazzi, and J. D. Wells, *Nucl.Phys.* **B595** (2001) 250–276, [[hep-ph/0002178](#)]. 61
 - [191] M. L. Mangano, M. Moretti, F. Piccinini, R. Pittau, and A. D. Polosa, *JHEP* **07** (2003) 001, [[hep-ph/0206293](#)]. 62, 71
 - [192] J. M. Butterworth, A. R. Davison, M. Rubin, and G. P. Salam, *Phys.Rev.Lett.* **100** (2008) 242001, [[0802.2470](#)]. 63, 70
 - [193] A. Djouadi, R. Godbole, B. Mellado, and K. Mohan, *Phys.Lett.* **B723** (2013) 307–313, [[1301.4965](#)]. 64
 - [194] U. Baur, T. Plehn, and D. L. Rainwater, *Phys.Rev.* **D69** (2004) 053004,

- [[hep-ph/0310056](#)]. 68
- [195] V. Barger, L. L. Everett, C. Jackson, and G. Shaughnessy, [1311.2931](#). 68
- [196] U. Baur, T. Plehn, and D. L. Rainwater, *Phys.Rev.* **D68** (2003) 033001, [[hep-ph/0304015](#)]. 68
- [197] M. J. Dolan, C. Englert, N. Greiner, and M. Spannowsky, [1310.1084](#). 68
- [198] A. Papaefstathiou, L. L. Yang, and J. Zurita, *Phys.Rev.* **D87** (2013) 011301, [[1209.1489](#)]. 68
- [199] B. Cooper, N. Konstantinidis, L. Lambourne, and D. Wardrope, [1307.0407](#). 68
- [200] L. Liu-Sheng, Z. Ren-You, M. Wen-Gan, G. Lei, L. Wei-Hua, *et. al.*, [1401.7754](#). 68, 71
- [201] R.D. Ball *et al.*, **NNPDF Collaboration**, *Nucl.Phys.* **B855** (2012) 153–221, [[1107.2652](#)]. 70
- [202] R. Contino, D. Marzocca, D. Pappadopulo, and R. Rattazzi, *JHEP* **1110** (2011) 081, [[1109.1570](#)]. 70, 136, 137, 148
- [203] C. Degrande, C. Duhr, B. Fuks, D. Grellscheid, O. Mattelaer, *et. al.*, *Comput.Phys.Commun.* **183** (2012) 1201–1214, [[1108.2040](#)]. 70, 130, 146, 169
- [204] J. Espinosa, C. Grojean, M. Muhlleitner, and M. Trott, *JHEP* **1212** (2012) 045, [[1207.1717](#)]. 70
- [205] J. Ellis and T. You, *JHEP* **1306** (2013) 103, [[1303.3879](#)]. 70
- [206] A. Pomarol and F. Riva, *JHEP* **1401** (2014) 151, [[1308.2803](#)]. 70, 83, 84
- [207] M. Ciuchini, E. Franco, S. Mishima, and L. Silvestrini, *JHEP* **1308** (2013) 106, [[1306.4644](#)]. 70
- [208] S. Dittmaier *et al.*, **LHC Higgs Cross Section Working Group**, [1101.0593](#). 70
- [209] S. Dittmaier, S. Dittmaier, C. Mariotti, G. Passarino, R. Tanaka, *et. al.*, [1201.3084](#). 70
- [210] **CMS Collaboration**, *JHEP* **1401** (2014) 096, [[1312.1129](#)]. 75
- [211] **ATLAS Collaboration**, Tech. Rep. ATLAS-CONF-2013-030, CERN, Geneva, Mar, 2013. 75
- [212] M. Cacciari, J. Rojo, G. P. Salam, and G. Soyez, *JHEP* **12** (2008) 032, [[0810.1304](#)]. 78
- [213] K. Hagiwara, R. Peccei, D. Zeppenfeld, and K. Hikasa, *Nucl.Phys.* **B282** (1987) 253. 80
- [214] K. Hagiwara, S. Ishihara, R. Szalapski, and D. Zeppenfeld, *Phys.Rev.* **D48** (1993) 2182–2203. 80
- [215] E. Argyres, A. Lahanas, C. Papadopoulos, and V. Spanos, *Phys.Lett.* **B383** (1996) 63–77, [[hep-ph/9603362](#)]. 80
- [216] S. Fichtel and G. von Gersdorff, [1311.6815](#). 80
- [217] M. E. Peskin and T. Takeuchi, *Phys.Rev.* **D46** (1992) 381–409. 80
- [218] **ALEPH Collaboration, DELPHI Collaboration, L3 Collaboration, OPAL Collaboration, LEP Electroweak Working Group**, *Phys.Rept.* **532** (2013) 119–244, [[1302.3415](#)]. 80, 81
- [219] **DELPHI Collaboration**, *Eur.Phys.J.* **C66** (2010) 35–56, [[1002.0752](#)]. 81
- [220] **ALEPH Collaboration, DELPHI Collaboration, L3 Collaboration, OPAL Collaboration, SLD Collaboration, LEP Electroweak Working Group, SLD Electroweak Group, SLD Heavy Flavour Group**, *Phys.Rept.* **427** (2006) 257–454, [[hep-ex/0509008](#)]. 81
- [221] A. Denner, S. Dittmaier, M. Roth, and D. Wackeroth, *Nucl.Phys.* **B560** (1999) 33–65,

- [[hep-ph/9904472](#)]. [81](#)
- [222] W. Buchmuller and D. Wyler, *Nucl.Phys.* **B268** (1986) 621. [83](#)
- [223] B. Grzadkowski, M. Iskrzynski, M. Misiak, and J. Rosiek, *JHEP* **1010** (2010) 085, [[1008.4884](#)]. [83](#)
- [224] J. Elias-Miro, J. Espinosa, E. Masso, and A. Pomarol, *JHEP* **1311** (2013) 066, [[1308.1879](#)]. [83](#)
- [225] A. Alloul, B. Fuks, and V. Sanz, [1310.5150](#). [83](#)
- [226] M. B. Einhorn and J. Wudka, *Nucl.Phys.* **B876** (2013) 556–574, [[1307.0478](#)]. [83](#)
- [227] J. Ellis, V. Sanz, and T. You, *Eur.Phys.J.* **C73** (2013) 2507, [[1303.0208](#)]. [84](#)
- [228] G. Isidori and M. Trott, [1307.4051](#). [84](#)
- [229] N. Vignaroli, *Phys.Rev.* **D86** (2012) 075017, [[1207.0830](#)]. [87](#), [98](#)
- [230] R. Contino and G. Servant, *JHEP* **0806** (2008) 026, [[0801.1679](#)]. [87](#)
- [231] R. Contino, T. Kramer, M. Son, and R. Sundrum, *JHEP* **0705** (2007) 074, [[hep-ph/0612180](#)]. [87](#), [135](#)
- [232] O. Matsedonskyi, G. Panico, and A. Wulzer, *JHEP* **1301** (2013) 164, [[1204.6333](#)]. [87](#)
- [233] J. Berger, J. Hubisz, and M. Perelstein, *JHEP* **1207** (2012) 016, [[1205.0013](#)]. [87](#)
- [234] A. De Simone, O. Matsedonskyi, R. Rattazzi, and A. Wulzer, *JHEP* **1304** (2013) 004, [[1211.5663](#)]. [87](#)
- [235] J. Aguilar-Saavedra, *EPJ Web Conf.* **60** (2013) 16012, [[1306.4432](#)]. [87](#)
- [236] J. Aguilar-Saavedra, R. Benbrik, S. Heinemeyer, and M. Perez-Victoria, *Phys.Rev.* **D88** (2013) 094010, [[1306.0572](#)]. [87](#)
- [237] G. Cacciapaglia, A. Deandrea, L. Panizzi, N. Gaur, D. Harada, *et. al.*, *JHEP* **1203** (2012) 070, [[1108.6329](#)]. [87](#)
- [238] M. Buchkremer, G. Cacciapaglia, A. Deandrea, and L. Panizzi, *Nucl.Phys.* **B876** (2013) 376–417, [[1305.4172](#)]. [87](#), [88](#), [94](#), [96](#), [98](#), [99](#)
- [239] M. Redi, V. Sanz, M. de Vries, and A. Weiler, *JHEP* **1308** (2013) 008, [[1305.3818](#)]. [87](#)
- [240] F. del Aguila, M. Perez-Victoria, and J. Santiago, *JHEP* **0009** (2000) 011, [[hep-ph/0007316](#)]. [87](#)
- [241] **ATLAS** Collaboration, Tech. Rep. ATLAS-CONF-2013-051, CERN, Geneva, May, 2013. [87](#)
- [242] **ATLAS** Collaboration, Tech. Rep. ATLAS-CONF-2013-056, CERN, Geneva, Jun, 2013. [87](#)
- [243] **ATLAS** Collaboration, Tech. Rep. ATLAS-CONF-2013-018, CERN, Geneva, Mar, 2013. [87](#)
- [244] **ATLAS** Collaboration, Tech. Rep. ATLAS-CONF-2013-060, CERN, Geneva, Jun, 2013. [87](#)
- [245] **CMS** Collaboration, *Phys.Lett.* **B729** (2014) 149–171, [[1311.7667](#)]. [87](#), [89](#), [90](#), [97](#), [98](#), [100](#), [103](#)
- [246] **CMS** Collaboration, Tech. Rep. CMS-PAS-B2G-12-019, CERN, Geneva, 2012. [87](#), [98](#), [100](#), [103](#)
- [247] **CMS** Collaboration, Tech. Rep. CMS-PAS-B2G-13-003, CERN, Geneva, 2013. [87](#)
- [248] **CMS** Collaboration, Tech. Rep. CMS-PAS-B2G-12-021, CERN, Geneva, 2013. [87](#)
- [249] **ATLAS** Collaboration, *Phys.Lett.* **B712** (2012) 22–39, [[1112.5755](#)]. [87](#)

- [250] A. Atre, G. Azuelos, M. Carena, T. Han, E. Ozcan, *et. al.*, *JHEP* **1108** (2011) 080, [[1102.1987](#)]. [88](#)
- [251] A. Atre, M. Chala, and J. Santiago, *JHEP* **1305** (2013) 099, [[1302.0270](#)]. [88](#), [89](#), [98](#)
- [252] N. D. Christensen and C. Duhr, *Comput.Phys.Commun.* **180** (2009) 1614–1641, [[0806.4194](#)]. [88](#), [130](#), [146](#)
- [253] A. Alloul, N. D. Christensen, C. Degrande, C. Duhr, and B. Fuks, [1310.1921](#). [88](#), [130](#), [146](#), [169](#), [178](#)
- [254] A. Belyaev, M. Brown, J. Moreno, and C. Papineau, *JHEP* **1306** (2013) 080, [[1212.4858](#)]. [89](#)
- [255] A. Azatov, O. Bondu, A. Falkowski, M. Felcini, S. Gascon-Shotkin, *et. al.*, *Phys.Rev.* **D85** (2012) 115022, [[1204.0455](#)]. [89](#)
- [256] CMS Collaboration, [1312.2391](#). [90](#)
- [257] M. Cacciari, M. Czakon, M. Mangano, A. Mitov, and P. Nason, *Phys.Lett.* **B710** (2012) 612–622, [[1111.5869](#)]. [91](#), [92](#)
- [258] T. Sjostrand, S. Mrenna, and P. Z. Skands, *JHEP* **0605** (2006) 026, [[hep-ph/0603175](#)]. [91](#), [94](#), [96](#), [118](#), [125](#), [169](#), [179](#)
- [259] E. Conte, B. Fuks, and G. Serret, *Comput.Phys.Commun.* **184** (2013) 222–256, [[1206.1599](#)]. [91](#), [96](#), [115](#), [122](#), [123](#)
- [260] C. Delaunay, T. Flacke, J. Gonzalez-Fraile, S. J. Lee, G. Panico, *et. al.*, [1311.2072](#). [98](#)
- [261] N. Vignaroli, *JHEP* **1207** (2012) 158, [[1204.0468](#)]. [98](#)
- [262] T. Flacke, J. H. Kim, S. J. Lee, and S. H. Lim, [1312.5316](#). [98](#), [99](#), [100](#), [102](#)
- [263] C. Delaunay, O. Gedalia, S. J. Lee, G. Perez, and E. Ponton, *Phys.Rev.* **D83** (2011) 115003, [[1007.0243](#)]. [99](#)
- [264] M. Redi and A. Weiler, *JHEP* **1111** (2011) 108, [[1106.6357](#)]. [99](#)
- [265] K. Agashe, R. Contino, L. Da Rold, and A. Pomarol, *Phys.Lett.* **B641** (2006) 62–66, [[hep-ph/0605341](#)]. [99](#)
- [266] ATLAS Collaboration, Tech. Rep. ATLAS-CONF-2013-072, CERN, Geneva, Jul, 2013. [101](#), [102](#), [103](#)
- [267] H. P. Nilles, *Phys.Rept.* **110** (1984) 1–162. [105](#)
- [268] H. E. Haber and G. L. Kane, *Phys.Rept.* **117** (1985) 75–263. [105](#)
- [269] D. S. Alves, E. Izaguirre, and J. G. Wacker, *Phys.Lett.* **B702** (2011) 64–68, [[1008.0407](#)]. [105](#)
- [270] T. J. LeCompte and S. P. Martin, *Phys.Rev.* **D84** (2011) 015004, [[1105.4304](#)]. [105](#)
- [271] H. K. Dreiner, M. Kramer, and J. Tattersall, *Europhys.Lett.* **99** (2012) 61001, [[1207.1613](#)]. [105](#), [173](#), [178](#)
- [272] B. Bhattacharjee and K. Ghosh, [1207.6289](#). [105](#)
- [273] H. Dreiner, M. Kramer, and J. Tattersall, *Phys.Rev.* **D87** (2013), no. 3 035006, [[1211.4981](#)]. [105](#)
- [274] B. Dutta, W. Flanagan, A. Gurrola, W. Johns, T. Kamon, *et. al.*, [1312.1348](#). [105](#)
- [275] J. Andrea, B. Fuks, and F. Maltoni, *Phys.Rev.* **D84** (2011) 074025, [[1106.6199](#)]. [105](#)
- [276] J. Wang, C. S. Li, D. Y. Shao, and H. Zhang, *Phys.Rev.* **D86** (2012) 034008, [[1109.5963](#)]. [105](#)
- [277] E. Alvarez, E. C. Leskow, J. Drobnak, and J. F. Kamenik, *Phys.Rev.* **D89** (2014)

- 014016, [[1310.7600](#)]. [105](#)
- [278] J.-L. Agram, J. Andrea, M. Buttignol, E. Conte, and B. Fuks, *Phys.Rev.* **D89** (2014) 014028, [[1311.6478](#)]. [105](#)
- [279] T. Gleisberg, S. Hoeche, F. Krauss, A. Schalicke, S. Schumann, *et. al.*, *JHEP* **0402** (2004) 056, [[hep-ph/0311263](#)]. [106](#)
- [280] S. Frixione, P. Nason, and G. Ridolfi, *JHEP* **0709** (2007) 126, [[0707.3088](#)]. [106](#)
- [281] S. Alioli, P. Nason, C. Oleari, and E. Re, *JHEP* **0909** (2009) 111, [[0907.4076](#)]. [106](#)
- [282] E. Re, *Eur.Phys.J.* **C71** (2011) 1547, [[1009.2450](#)]. [106](#)
- [283] S. Frixione, E. Laenen, P. Motylinski, B. R. Webber, and C. D. White, *JHEP* **0807** (2008) 029, [[0805.3067](#)]. [106](#)
- [284] K. Hamilton, *JHEP* **1101** (2011) 009, [[1009.5391](#)]. [106](#)
- [285] J. Pumplin, D. Stump, J. Huston, H. Lai, P. M. Nadolsky, *et. al.*, *JHEP* **0207** (2002) 012, [[hep-ph/0201195](#)]. [106](#), [107](#), [121](#), [131](#), [169](#), [179](#)
- [286] J. Bellm, S. Gieseke, D. Grellscheid, A. Papaefstathiou, S. Platzer, *et. al.*, [1310.6877](#). [106](#)
- [287] **ATLAS** Collaboration, *Phys.Lett.* **B717** (2012) 330–350, [[1205.3130](#)]. [107](#)
- [288] **ATLAS** Collaboration, Tech. Rep. ATLAS-CONF-2011-089, CERN, Geneva, Jun, 2011. [107](#)
- [289] **ATLAS** Collaboration, *Eur.Phys.J.* **C72** (2012) 2173, [[1208.1390](#)]. [108](#)
- [290] **CMS** Collaboration, *Eur.Phys.J.* **C73** (2013) 2283, [[1210.7544](#)]. [108](#)
- [291] **ATLAS** Collaboration, Tech. Rep. ATLAS-CONF-2013-068, CERN, Geneva, Jul, 2013. [109](#), [169](#)
- [292] <https://twiki.cern.ch/twiki/bin/view/AtlasPublic/SupersymmetryPublicResults>. [111](#), [153](#)
- [293] <https://twiki.cern.ch/twiki/bin/view/CMSPublic/PhysicsResultsSUS>. [111](#), [153](#)
- [294] W. Porod, *Comput.Phys.Commun.* **153** (2003) 275–315, [[hep-ph/0301101](#)]. [112](#), [155](#)
- [295] W. Porod and F. Staub, *Comput.Phys.Commun.* **183** (2012) 2458–2469, [[1104.1573](#)]. [112](#), [129](#), [155](#)
- [296] S. Kraml, S. Kulkarni, U. Laa, A. Lessa, W. Magerl, *et. al.*, [1312.4175](#). [113](#)
- [297] **ATLAS** Collaboration, *JHEP* **1310** (2013) 189, [[1308.2631](#)]. [114](#), [116](#), [120](#), [121](#)
- [298] **CMS** Collaboration, *Eur.Phys.J.* **C73** (2013) 2677, [[1308.1586](#)]. [114](#), [116](#), [117](#), [118](#)
- [299] E. Conte and B. Fuks, [1309.7831](#). [115](#)
- [300] E. Conte, B. Dumont, B. Fuks, and C. Wymant, *in preparation*. [115](#)
- [301] **ATLAS** Collaboration, Tech. Rep. ATLAS-CONF-2013-061, CERN, Geneva, Jun, 2013. [116](#)
- [302] **CMS** Collaboration, *Phys.Lett.* **B725** (2013) 243–270, [[1305.2390](#)]. [116](#), [173](#)
- [303] **CMS** Collaboration, *Eur.Phys.J.* **C73** (2013) 2568, [[1303.2985](#)]. [116](#), [173](#)
- [304] S. Chatrchyan *et. al.*, **CMS Collaboration** Collaboration, [1402.4770](#). [116](#)
- [305] **ATLAS** Collaboration, Tech. Rep. ATLAS-CONF-2013-037, CERN, Geneva, Mar, 2013. [116](#)
- [306] S. Chatrchyan *et. al.*, **CMS Collaboration** Collaboration, [1311.4937](#). [116](#)
- [307] **ATLAS** Collaboration, Tech. Rep. ATLAS-CONF-2013-048, CERN, Geneva, May, 2013. [116](#), [119](#), [120](#)

- [308] CMS Collaboration, *JHEP* **1401** (2014) 163, [[1311.6736](#)]. [116](#), [119](#)
- [309] CMS Collaboration, Tech. Rep. CMS-PAS-SUS-13-016, CERN, Geneva, 2013. [116](#)
- [310] S. Kraml, B. Allanach, M. Mangano, H. Prosper, S. Sekmen, *et. al.*, *Eur.Phys.J.* **C72** (2012) 1976, [[1203.2489](#)]. [116](#), [127](#)
- [311] M. Whalley, *Comput.Phys.Commun.* **57** (1989) 536–537. [116](#)
- [312] <http://inspirehep.net/>, see also <http://www.projecthepinpire.net/>. [116](#)
- [313] Y. Bai, H.-C. Cheng, J. Gallicchio, and J. Gu, *JHEP* **1207** (2012) 110, [[1203.4813](#)]. [117](#), [123](#), [124](#)
- [314] <https://twiki.cern.ch/twiki/bin/view/LHCPhysics/SUSYCrossSections>. [118](#), [121](#)
- [315] D. R. Tovey, *JHEP* **0804** (2008) 034, [[0802.2879](#)]. [120](#)
- [316] G. Polesello and D. R. Tovey, *JHEP* **1003** (2010) 030, [[0910.0174](#)]. [120](#)
- [317] C. Lester and D. Summers, *Phys.Lett.* **B463** (1999) 99–103, [[hep-ph/9906349](#)]. [123](#)
- [318] H.-C. Cheng and Z. Han, *JHEP* **0812** (2008) 063, [[0810.5178](#)]. [123](#)
- [319] J. de Favereau, C. Delaere, P. Demin, A. Giammanco, V. Lemaitre, *et. al.*, [[1307.6346](#)]. [124](#), [169](#), [179](#)
- [320] CMS Collaboration, Tech. Rep. CMS-PAS-BTV-09-001, CERN, 2009. Geneva, Jul, 2009. [125](#)
- [321] CMS Collaboration, Tech. Rep. CMS-PAS-BTV-11-001, CERN, Geneva, 2011. [125](#)
- [322] C. Duhr and B. Fuks, *Comput.Phys.Commun.* **182** (2011) 2404–2426, [[1102.4191](#)]. [125](#)
- [323] M. L. Mangano, M. Moretti, F. Piccinini, and M. Treccani, *JHEP* **0701** (2007) 013, [[hep-ph/0611129](#)]. [125](#)
- [324] I. Sfiligoi, D. C. Bradley, B. Holzman, P. Mhashilkar, S. Padhi, and F. Wurthwein,, “The pilot way to Grid resources using glideinWMS.” 2009 WRI World Congress on Computer Science and Information Engineering, Vol. 2, pp. 428–432. [126](#), [127](#)
- [325] R. Pordes, D. Petravick, B. Kramer, D. Olson, M. Livny, A. Roy, P. Avery, K. Blackburn, T. Wenaus, F. Wurthwein, I. Foster, R. Gardner, M. Wilde, A. Blatecky, J. McGee, and R. Quick, *Journal of Physics: Conference Series* **78** (2007), no. 1 012057. [126](#), [127](#)
- [326] M. Drees, H. Dreiner, D. Schmeier, J. Tattersall, and J. S. Kim, [[1312.2591](#)]. [127](#)
- [327] M. Papucci, K. Sakurai, A. Weiler, and L. Zeune, [[1402.0492](#)]. [127](#)
- [328] R. Francis, M. Frank, and C. S. Kalman, *Phys.Rev.* **D43** (1991) 2369–2385. [128](#), [129](#)
- [329] K. Huitu, J. Maalampi, and M. Raidal, *Phys.Lett.* **B328** (1994) 60–66, [[hep-ph/9402219](#)]. [128](#), [129](#)
- [330] K. Huitu, J. Maalampi, and M. Raidal, *Nucl.Phys.* **B420** (1994) 449–467, [[hep-ph/9312235](#)]. [128](#), [129](#)
- [331] K. Babu and R. N. Mohapatra, *Phys.Lett.* **B668** (2008) 404–409, [[0807.0481](#)]. [128](#), [129](#)
- [332] CMS Collaboration, Tech. Rep. CMS-PAS-EXO-12-059, CERN, Geneva, 2013. [128](#), [130](#), [131](#), [132](#)
- [333] CMS Collaboration, Tech. Rep. CMS-PAS-B2G-12-010, CERN, Geneva, 2013. [128](#), [130](#), [131](#)
- [334] J. C. Pati and A. Salam, *Phys.Rev.* **D10** (1974) 275–289. [128](#)
- [335] R. N. Mohapatra and J. C. Pati, *Phys.Rev.* **D11** (1975) 566–571. [128](#)
- [336] R. N. Mohapatra and G. Senjanovic, *Phys.Rev.* **D23** (1981) 165. [128](#)

- [337] R. N. Mohapatra, *NATO Adv.Study Inst.Ser.B Phys.* **122** (1985) 219. [128](#)
- [338] **CMS** Collaboration, Tech. Rep. CMS-PAS-EXO-12-017, CERN, Geneva, 2012. [129](#), [132](#), [133](#), [134](#)
- [339] A. Alloul, M. Frank, B. Fuks, and M. Rausch de Traubenberg, *JHEP* **1310** (2013) 033, [[1307.5073](#)]. [129](#), [130](#)
- [340] F. Staub, *Computer Physics Communications* **184** (2013) pp. 1792–1809, [[1207.0906](#)]. [129](#)
- [341] F. Staub, [1309.7223](#). [129](#)
- [342] **CMS** Collaboration, Tech. Rep. CMS-PAS-HIG-12-005, CERN, Geneva, 2012. [130](#)
- [343] **CMS** Collaboration, Tech. Rep. CMS-PAS-EXO-12-060, CERN, Geneva, 2013. [130](#)
- [344] D. B. Kaplan, *Nucl.Phys.* **B365** (1991) 259–278. [135](#)
- [345] Y. Grossman and M. Neubert, *Phys.Lett.* **B474** (2000) 361–371, [[hep-ph/9912408](#)]. [135](#)
- [346] T. Gherghetta and A. Pomarol, *Nucl.Phys.* **B586** (2000) 141–162, [[hep-ph/0003129](#)]. [135](#)
- [347] R. Contino and A. Pomarol, *JHEP* **0411** (2004) 058, [[hep-th/0406257](#)]. [135](#)
- [348] D. Pappadopulo, A. Thamm, R. Torre, and A. Wulzer, [1402.4431](#). [136](#), [141](#), [145](#)
- [349] S. R. Coleman, J. Wess, and B. Zumino, *Phys.Rev.* **177** (1969) 2239–2247. [136](#)
- [350] J. Callan, Curtis G., S. R. Coleman, J. Wess, and B. Zumino, *Phys.Rev.* **177** (1969) 2247–2250. [136](#)
- [351] G. Bozzi, B. Fuks, B. Herrmann, and M. Klasen, *Nucl.Phys.* **B787** (2007) 1–54, [[0704.1826](#)]. [153](#)
- [352] Y. Nomura, M. Papucci, and D. Stolarski, *Phys.Rev.* **D77** (2008) 075006, [[0712.2074](#)]. [153](#)
- [353] G. Hiller and Y. Nir, *JHEP* **0803** (2008) 046, [[0802.0916](#)]. [153](#)
- [354] B. Fuks, B. Herrmann, and M. Klasen, *Nucl.Phys.* **B810** (2009) 266–299, [[0808.1104](#)]. [153](#)
- [355] T. Hurth and W. Porod, *JHEP* **0908** (2009) 087, [[0904.4574](#)]. [153](#), [158](#)
- [356] A. Bartl *et. al.*, *Phys.Lett.* **B679** (2009) 260–266, [[0905.0132](#)]. [153](#), [158](#)
- [357] G. Hiller, J. S. Kim, and H. Sedello, *Phys.Rev.* **D80** (2009) 115016, [[0910.2124](#)]. [153](#)
- [358] A. Bartl *et. al.*, *Phys.Lett.* **B698** (2011) 380–388, [[1007.5483](#)]. [153](#), [158](#)
- [359] M. Bruhnke, B. Herrmann, and W. Porod, *JHEP* **1009** (2010) 006, [[1007.2100](#)]. [153](#), [156](#), [158](#)
- [360] M. Mühlleitner and E. Popenza, *JHEP* **1104** (2011) 095, [[1102.5712](#)]. [153](#)
- [361] A. Bartl *et. al.*, *Phys.Rev.* **D84** (2011) 115026, [[1107.2775](#)]. [153](#), [158](#)
- [362] B. Fuks, B. Herrmann, and M. Klasen, *Phys.Rev.* **D86** (2012) 015002, [[1112.4838](#)]. [153](#)
- [363] B. Fuks, [1401.6277](#). [153](#)
- [364] M. Ciuchini, A. Masiero, P. Paradisi, L. Silvestrini, S. Vempati, *et. al.*, *Nucl.Phys.* **B783** (2007) 112–142, [[hep-ph/0702144](#)]. [154](#)
- [365] Y. Amhis, *et al.*, **Heavy Flavor Averaging Group**, [1207.1158](#). [155](#)
- [366] M. Misiak, H. Asatrian, K. Bieri, M. Czakon, A. Czarnecki, *et. al.*, *Phys.Rev.Lett.* **98** (2007) 022002, [[hep-ph/0609232](#)]. [155](#)

- [367] F. Mahmoudi, *JHEP* **0712** (2007) 026, [[0710.3791](#)]. [155](#)
- [368] **LHCb** Collaboration, *Phys.Rev.Lett.* **111** (2013) 101805, [[1307.5024](#)]. [155](#)
- [369] **CMS** Collaboration, *Phys.Rev.Lett.* **111** (2013) 101804, [[1307.5025](#)]. [155](#)
- [370] **CMS and LHCb** Collaboration, Tech. Rep. CMS-PAS-BPH-13-007, CERN-LHCb-CONF-2013-012, CERN, Geneva, Jul, 2013. [155](#)
- [371] F. Mahmoudi, S. Neshatpour, and J. Orloff, *JHEP* **1208** (2012) 092, [[1205.1845](#)]. [155](#)
- [372] **LHCb** Collaboration, *Phys.Rev.Lett.* **111** (2013) 191801, [[1308.1707](#)]. [155](#)
- [373] S. Descotes-Genon, T. Hurth, J. Matias, and J. Virto, *JHEP* **1305** (2013) 137, [[1303.5794](#)]. [155](#)
- [374] T. Hurth and F. Mahmoudi, [1312.5267](#). [155](#)
- [375] **BaBar** Collaboration, *Phys.Rev.Lett.* **93** (2004) 081802, [[hep-ex/0404006](#)]. [155](#)
- [376] **Belle** Collaboration, *Phys.Rev.* **D72** (2005) 092005, [[hep-ex/0503044](#)]. [155](#)
- [377] T. Huber, T. Hurth, and E. Lunghi, *Nucl.Phys.* **B802** (2008) 40–62, [[0712.3009](#)]. [155](#)
- [378] T. Hurth and F. Mahmoudi, *Nucl.Phys.* **B865** (2012) 461–485, [[1207.0688](#)]. [155](#)
- [379] J. Beringer *et al.*, **Particle Data Group**, *Phys.Rev.* **D86** (2012) 010001. [155](#)
- [380] F. Mahmoudi, *Comput.Phys.Commun.* **178** (2008) 745–754, [[0710.2067](#)]. [155](#), [159](#)
- [381] F. Mahmoudi, *Comput.Phys.Commun.* **180** (2009) 1579–1613, [[0808.3144](#)]. [155](#), [159](#)
- [382] P. Ball and R. Fleischer, *Eur.Phys.J.* **C48** (2006) 413–426, [[hep-ph/0604249](#)]. [155](#)
- [383] K. Hagiwara, R. Liao, A. D. Martin, D. Nomura, and T. Teubner, *J.Phys.* **G38** (2011) 085003, [[1105.3149](#)]. [155](#)
- [384] S. Heinemeyer, W. Hollik, F. Merz, and S. Penaranda, *Eur.Phys.J.* **C37** (2004) 481–493, [[hep-ph/0403228](#)]. [156](#)
- [385] A. Bartl *et al.*, [1212.4688](#). [156](#), [158](#)
- [386] J. Camargo-Molina, B. O’Leary, W. Porod, and F. Staub, *JHEP* **1312** (2013) 103, [[1309.7212](#)]. [156](#)
- [387] J. Camargo-Molina, B. O’Leary, W. Porod, and F. Staub, *Eur.Phys.J.* **C73** (2013) 2588, [[1307.1477](#)]. [156](#)
- [388] O. Buchmueller, R. Cavanaugh, A. De Roeck, M. Dolan, J. Ellis, *et al.*, [1312.5250](#). [159](#)
- [389] J. A. Conley, J. S. Gainer, J. L. Hewett, M. P. Le, and T. G. Rizzo, *Physical Review D* (2011) [[1103.1697](#)]. [159](#)
- [390] S. Sekmen, S. Kraml, J. Lykken, F. Moortgat, S. Padhi, *et al.*, *JHEP* **1202** (2012) 075, [[1109.5119](#)]. [159](#)
- [391] A. Arbey, M. Battaglia, and F. Mahmoudi, *Eur.Phys.J.* **C72** (2012) 1847, [[1110.3726](#)]. [159](#)
- [392] A. Arbey, M. Battaglia, and F. Mahmoudi, *Eur.Phys.J.* **C72** (2012) 1906, [[1112.3032](#)]. [159](#)
- [393] M. W. Cahill-Rowley, J. L. Hewett, A. Ismail, and T. G. Rizzo, *Phys.Rev.* **D88** (2013) 035002, [[1211.1981](#)]. [159](#)
- [394] G. Brooijmans *et al.*, [1005.1229](#). [159](#)
- [395] J. Lee, A. Pilaftsis, M. S. Carena, S. Choi, M. Drees, *et al.*, *Comput.Phys.Commun.* **156** (2004) 283–317, [[hep-ph/0307377](#)]. [159](#)
- [396] J. Lee, M. Carena, J. Ellis, A. Pilaftsis, and C. Wagner, *Comput.Phys.Commun.* **180**

- (2009) 312–331, [[0712.2360](#)]. [159](#)
- [397] J. Lee, M. Carena, J. Ellis, A. Pilaftsis, and C. Wagner, *Comput.Phys.Commun.* **184** (2013) 1220–1233, [[1208.2212](#)]. [159](#)
- [398] A. Arbey and F. Mahmoudi, *Comput.Phys.Commun.* **181** (2010) 1277–1292, [[0906.0369](#)]. [159](#)
- [399] G. Belanger, F. Boudjema, A. Pukhov, and A. Semenov, *Comput.Phys.Commun.* **176** (2007) 367–382, [[hep-ph/0607059](#)]. [159](#), [169](#), [177](#)
- [400] G. Belanger, F. Boudjema, A. Pukhov, and A. Semenov, *Comput.Phys.Commun.* **180** (2009) 747–767, [[0803.2360](#)]. [159](#), [169](#)
- [401] J. Ellis, J. S. Lee, and A. Pilaftsis, *JHEP* **1010** (2010) 049, [[1006.3087](#)]. [160](#)
- [402] A. Arbey, M. Battaglia, and F. Mahmoudi, *Phys.Rev.* **D88** (2013) 095001, [[1308.2153](#)]. [160](#), [169](#)
- [403] A. Arbey, M. Battaglia, A. Djouadi, and F. Mahmoudi, *Phys.Lett.* **B720** (2013) 153–160, [[1211.4004](#)]. [162](#)
- [404] A. Arbey, M. Battaglia, and F. Mahmoudi, *Phys.Rev.* **D88** (2013) 015007, [[1303.7450](#)]. [162](#)
- [405] A. Arbey and F. Mahmoudi, *Phys.Lett.* **B669** (2008) 46–51, [[0803.0741](#)]. [163](#)
- [406] A. Arbey and F. Mahmoudi, *JHEP* **1005** (2010) 051, [[0906.0368](#)]. [163](#)
- [407] G. Belanger, F. Boudjema, S. Kraml, A. Pukhov, and A. Semenov, *Phys.Rev.* **D73** (2006) 115007, [[hep-ph/0604150](#)]. [163](#)
- [408] G. Belanger, F. Boudjema, S. Kraml, A. Pukhov, and A. Semenov, *AIP Conf.Proc.* **878** (2006) 46–52, [[hep-ph/0610110](#)]. [163](#)
- [409] LUX Collaboration, [1310.8214](#). [163](#), [169](#), [178](#)
- [410] Q.-H. Cao, C.-R. Chen, C. S. Li, and H. Zhang, *JHEP* **1108** (2011) 018, [[0912.4511](#)]. [168](#)
- [411] J. Goodman, M. Ibe, A. Rajaraman, W. Shepherd, T. M. Tait, *et. al.*, *Phys.Lett.* **B695** (2011) 185–188, [[1005.1286](#)]. [168](#)
- [412] J. Goodman, M. Ibe, A. Rajaraman, W. Shepherd, T. M. Tait, *et. al.*, *Phys.Rev.* **D82** (2010) 116010, [[1008.1783](#)]. [168](#)
- [413] A. Rajaraman, W. Shepherd, T. M. Tait, and A. M. Wijangco, *Phys.Rev.* **D84** (2011) 095013, [[1108.1196](#)]. [168](#)
- [414] G. Busoni, A. De Simone, E. Morgante, and A. Riotto, *Phys.Lett.* **B728** (2014) 412–421, [[1307.2253](#)]. [169](#)
- [415] G. Busoni, A. De Simone, J. Gramling, E. Morgante, and A. Riotto, [1402.1275](#). [169](#)
- [416] A. Pukhov, [hep-ph/0412191](#). [169](#)
- [417] G. Belanger, F. Boudjema, A. Pukhov, and A. Semenov, *Comput.Phys.Commun.* **149** (2002) 103–120, [[hep-ph/0112278](#)]. [169](#)
- [418] G. Belanger, F. Boudjema, and A. Pukhov, [1402.0787](#). [169](#)
- [419] XENON10 Collaboration, *Phys.Rev.Lett.* **107** (2011) 051301, [[1104.3088](#)]. [169](#)
- [420] XENON100 Collaboration, *Phys.Rev.Lett.* **109** (2012) 181301, [[1207.5988](#)]. [169](#)
- [421] Planck Collaboration, [1303.5076](#). [169](#)
- [422] CMS Collaboration, Tech. Rep. CMS-PAS-EXO-12-048, CERN, Geneva, 2013. [169](#), [182](#)

- [423] A. Arbey, M. Battaglia, and F. Mahmoudi, [1311.7641](#). [169](#)
- [424] S. Ovyn, X. Rouby, and V. Lemaitre, [0903.2225](#). [169](#)
- [425] A. L. Read, *J.Phys.* **G28** (2002) 2693–2704. [169](#)
- [426] W. Barletta, M. Battaglia, M. Klute, M. Mangano, S. Prestemon, *et. al.*, [1310.0290](#). [169](#)
- [427] D. Malling, D. Akerib, H. Araujo, X. Bai, S. Bedikian, *et. al.*, [1110.0103](#). [170](#)
- [428] S. Dimopoulos and G. Giudice, *Phys.Lett.* **B357** (1995) 573–578, [[hep-ph/9507282](#)]. [172](#)
- [429] K. L. Chan, U. Chattopadhyay, and P. Nath, *Phys.Rev.* **D58** (1998) 096004, [[hep-ph/9710473](#)]. [173](#)
- [430] J. L. Feng, K. T. Matchev, and T. Moroi, *Phys.Rev.Lett.* **84** (2000) 2322–2325, [[hep-ph/9908309](#)]. [173](#)
- [431] J. L. Feng, K. T. Matchev, and T. Moroi, *Phys.Rev.* **D61** (2000) 075005, [[hep-ph/9909334](#)]. [173](#)
- [432] J. L. Feng, K. T. Matchev, and D. Sanford, *Phys.Rev.* **D85** (2012) 075007, [[1112.3021](#)]. [173](#)
- [433] J. R. Espinosa, C. Grojean, V. Sanz, and M. Trott, *JHEP* **1212** (2012) 077, [[1207.7355](#)]. [173](#)
- [434] R. T. D’Agnolo, E. Kuflik, and M. Zanetti, *JHEP* **1303** (2013) 043, [[1212.1165](#)]. [173](#)
- [435] M. Carena, S. Gori, N. R. Shah, C. E. Wagner, and L.-T. Wang, *JHEP* **1308** (2013) 087, [[1303.4414](#)]. [173](#)
- [436] G. D. Kribs, A. Martin, and A. Menon, *Phys.Rev.* **D88** (2013) 035025, [[1305.1313](#)]. [173](#)
- [437] E. Hardy, *JHEP* **1310** (2013) 133, [[1306.1534](#)]. [173](#)
- [438] J. Fan and M. Reece, [1401.7671](#). [173](#)
- [439] H. Baer, V. Barger, and D. Mickelson, *Phys.Rev.* **D88** (2013) 095013, [[1309.2984](#)]. [173](#)
- [440] H. Baer, A. Belyaev, T. Krupovnickas, and J. O’Farrill, *JCAP* **0408** (2004) 005, [[hep-ph/0405210](#)]. [173](#)
- [441] D. S. Alves, E. Izaguirre, and J. G. Wacker, *JHEP* **1110** (2011) 012, [[1102.5338](#)]. [173](#)
- [442] C. Han, A. Kobakhidze, N. Liu, A. Saavedra, L. Wu, *et. al.*, [1310.4274](#). [173](#), [179](#)
- [443] Z. Han, G. D. Kribs, A. Martin, and A. Menon, [1401.1235](#). [173](#), [181](#)
- [444] A. Bartl, W. Majerotto, and W. Porod, *Phys.Lett.* **B465** (1999) 187–192, [[hep-ph/9907377](#)]. [174](#)
- [445] A. De Simone, V. Sanz, and H. P. Sato, *Phys.Rev.Lett.* **105** (2010) 121802, [[1004.1567](#)]. [174](#), [175](#)
- [446] A. E. Nelson, N. Rius, V. Sanz, and M. Unsal, *JHEP* **0208** (2002) 039, [[hep-ph/0206102](#)]. [174](#)
- [447] K. Hsieh, *Phys.Rev.* **D77** (2008) 015004, [[0708.3970](#)]. [174](#)
- [448] G. Belanger, K. Benakli, M. Goodsell, C. Moura, and A. Pukhov, *JCAP* **0908** (2009) 027, [[0905.1043](#)]. [174](#)
- [449] E. A. Baltz, M. Battaglia, M. E. Peskin, and T. Wizansky, *Phys.Rev.* **D74** (2006) 103521, [[hep-ph/0602187](#)]. [176](#)
- [450] **WMAP** Collaboration, [1212.5226](#). [176](#)
- [451] LEP2 SUSY Working Group,.

http://lepsusy.web.cern.ch/lepsusy/www/inoslowdmsummer02/charginolowdm_pub.html.
176

- [452] R. Allahverdi, B. Dutta, and K. Sinha, *Phys.Rev.* **D86** (2012) 095016, [[1208.0115](#)]. 177
- [453] H. Baer, V. Barger, P. Huang, and X. Tata, *JHEP* **1205** (2012) 109, [[1203.5539](#)]. 177
- [454] G. Belanger, F. Boudjema, P. Brun, A. Pukhov, S. Rosier-Lees, *et. al.*,
Comput.Phys.Commun. **182** (2011) 842–856, [[1004.1092](#)]. 177
- [455] **XENON100** Collaboration, *Phys.Rev.Lett.* **111** (2013) 021301, [[1301.6620](#)]. 178
- [456] **XENON1T** Collaboration, [[1206.6288](#)]. 178
- [457] G. Belanger, M. Heikinheimo, and V. Sanz, *JHEP* **1208** (2012) 151, [[1205.1463](#)]. 178
- [458] H. M. Lee, M. Park, and V. Sanz, *JHEP* **1303** (2013) 052, [[1212.5647](#)]. 178
- [459] N. F. Bell, J. B. Dent, A. J. Galea, T. D. Jacques, L. M. Krauss, *et. al.*, *Phys.Rev.* **D86**
(2012) 096011, [[1209.0231](#)]. 178
- [460] Y. Bai and T. M. Tait, *Phys.Lett.* **B723** (2013) 384–387, [[1208.4361](#)]. 178
- [461] S. Eidelman *et al.*, **Particle Data Group**, *Phys.Lett.* **B592** (2004) 1–1109. 179
- [462] **ATLAS** Collaboration, Tech. Rep. ATLAS-CONF-2012-147, CERN, Geneva, Nov,
2012. 182
- [463] **ATLAS** Collaboration, *JHEP* **1304** (2013) 075, [[1210.4491](#)]. 184
- [464] **CMS** Collaboration, *JHEP* **1209** (2012) 094, [[1206.5663](#)]. 184